Precision Laser Micromachining of Hollow Core Negative Curvature Fibres

Catarina Cardoso Novo

Submitted for the degree of Doctor of Philosophy

Heriot-Watt University

School of Engineering and Physical Sciences

February 2019

The copyright in this thesis is owned by the author. Any quotation from the thesis or use of any of the information contained in it must acknowledge this thesis as the source of the quotation or information.

Abstract

The principal aim of this work was to develop a novel micromachining strategy for a new class of hollow core silica optical fibre, the Negative Curvature Fibre (NCF). Processing techniques were investigated to increase the physical access to the hollow core (along the length of the fibre) in order to enhance the interaction of chemical species with the light and hence enable practical sensing devices. Because of the unique internal structure of these NCFs, consisting of a fine (sub-micron) silica webbing, a highly precise and controllable machining process was required. Due to the well-known advantages of femtosecond laser machining such as the ability for inscription in any material, small volume removal and the non-thermal nature of the process, resulting in machined structures with an almost negligible heat-affected zone, a new femtosecond laser micromachining process was developed.

A methodology was successfully demonstrated which gives the capability to precisely machine away the solid outer cladding fibre and then controllably remove the silica webbing and expose the hollow core of the fibre. This single step process provides a more direct way of machining a fibre (compared to previously reported hybrid techniques such as laser machining plus chemical etching). Parameter optimisation allowed control of the removal depth, minimisation of re-deposited material and avoidance of damage to the remaining silica web which is very important for NCF due to its guidance mechanism. An NCF, which was machined through to the hollow core, exhibited no significant disruption to the guidance preserving the confinement of light to the hollow core. Hence the laser micromachining strategy presented in this work paves the way to develop new optical sensing devices exploiting the unique properties of these novel fibre geometries.

Acknowledgement

During the journey that was my PhD I had the privilege to know some bright minds I would like to thank.

Dr Jonathan D. Shephard, my primary supervisor, for the opportunity of doing this PhD within the Applied Optics and Photonics group, for the guidance and support and for the fruitful meetings and insights that kept me motivated to see always the bright side.

Professor Robert R. Thomson, my second supervisor, for the support and guidance along this journey.

Dr Debaditya Choudhury, for his availability to work with me on the femtosecond laser related points and for some fruitful discussions about machining.

Dr Richard Carter and Dr Krystian L. Wlodarczyk for the good advices given throughout the years.

Mark Leonard for the SEM support. My colleagues in laboratory G77 of Earl Mountbatten building, my colleagues in the laboratory G23 of David Brewster Building and in particular Jacopo Siliprandi for the insights regarding the G Code.

The last but not the least, I would like to thank my family for all the support and specially João Costa, my husband for the supporting and encouraging words that were always present.

Thank you so much!

ACADEMIC REGISTRY
Research Thesis Submission

Name*:*	Catarina Cardoso Novo		
School:	School of Engineering and Physical Sciences		
Version: *(i.e. First, Resubmission, Final)*	Final	Degree Sought:	Doctor of Philosophy in Physics

Declaration

In accordance with the appropriate regulations I hereby submit my thesis and I declare that:

1) the thesis embodies the results of my own work and has been composed by myself
2) where appropriate, I have made acknowledgement of the work of others and have made reference to work carried out in collaboration with other persons
3) the thesis is the correct version of the thesis for submission and is the same version as any electronic versions submitted*.
4) my thesis for the award referred to, deposited in the Heriot-Watt University Library, should be made available for loan or photocopying and be available via the Institutional Repository, subject to such conditions as the Librarian may require
5) I understand that as a student of the University I am required to abide by the Regulations of the University and to conform to its discipline.
6) I confirm that the thesis has been verified against plagiarism via an approved plagiarism detection application e.g. Turnitin.

* *Please note that it is the responsibility of the candidate to ensure that the correct version of the thesis is submitted.*

Signature of Candidate*:*		Date:	

Submission

Submitted By *(name in capitals):*	
Signature of Individual Submitting:	
Date Submitted:	

For Completion in the Student Service Centre (SSC)

Received in the SSC by *(name in capitals):*			
Method of Submission *(Handed in to SSC; posted through internal/external mail):*			
*E-thesis Submitted (**mandatory for final theses)***			
Signature:		Date:	

Table of contents

List of Abbreviations

AFM	Atomic Force Microscope
Er:YAG	Erbium-doped Yttrium Aluminium Garnet
FIB	Focused Ion Beam
fs	Femtosecond
GLS	Gallium Lanthanum Sulphide
HF	Hollow core Fibre
HC-PBGF	Hollow-Core Photonic Bandgap Fibre
HC-PCF	Hollow Core Photonic Crystal Fibre
IR	Infrared
LPG	Long Period Grating
MEMS	Micro-Electro-Mechanical Systems
MOF	Microstructure Optical Fibre
NA	Numerical Aperture
NCF	Negative Curvature Fibre
Nd:YAG	Neodymium-doped Yttrium Aluminium Garnet
ns	Nanosecond
OFS	Optical Fibre Sensors
PBG	Photonic Bandgap
PCF	Photonic Crystal Fibre
PMD	Polarisation Mode Dispersion
ps	Picosecond
SC-PBG	Solid Core Photonic Bandgap
SC-PCF	Solid Core Photonic Crystal Fibre
SEM	Scanning Electron Microscope
SMF	Single Mode fibre
TIR	Total Internal Reflection
UV	Ultraviolet
Yb:KYW	Ytterbium-doped Potassium Yttrium Tungstate

List of Publications

Conference Paper

C.C. Novo, A. Urich, D. Choudhury, R. Carter, D.P. Hand, R.R. Thomson, F. Yu, J.C. Knight, S. Brooks, S. Mcculloch, J.D. Shephard. *Negative curvature fibres: exploiting the potential for novel optical sensors*, Proceedings of SPIE, 9634, 963454–5 (2015)

Jounal Paper

C.C. Novo, D. Choudhury, B. Siwicki, R. Thomson, J.D. Shephard. *Femtosecond laser machining of Hollow-Core Negative Curvature Fibres,* In preparation

Chapter 1 – Introduction

Creating optical fibre sensors that operate in the infrared region, where most of the molecular vibrational absorptions occur, is of major interest in many fields, such as spectroscopy and medicine [1], [2]. However, the high absorption of silica (the material from which most optical fibres are made) in that region, particularly for wavelengths longer than 3 μm, is prohibitively high [2] and makes the realisation of solid core silica optical fibre based sensors in the mid-infrared (MID-IR) a significant challenge. Hence, there has been a drive to develop non-conventional silica fibres to address this shortfall.

Particularly promising results in this field are based on hollow core fibres, since these fibres allow guidance in the infrared region (not possible with conventional solid core fused silica fibres) by dramatically reducing the overlap of the light with the glass. This is achieved by having a relatively complex photonic structure surrounding the hollow core which, by a range of guiding mechanisms dependent on the specific structure used, effectively traps light in the core providing low loss guidance above the region where bulk silica does not transmit. Such fibres are more broadly referred to as Photonic Crystal Fibres (PCF) or Hollow Core Microstructured Optical Fibres (HC-MOF). Among these, a new class of fibres, the hollow core Negative Curvature Fibres (NCF), have emerged which show great promise by having low loss, favourable guidance characteristics and a relatively simple photonic structure [3], [4]. Figure 1.1 shows a Scanning Electron Microscope (SEM) picture of an NCF exhibiting the hollow core, the cladding web and the solid cladding.

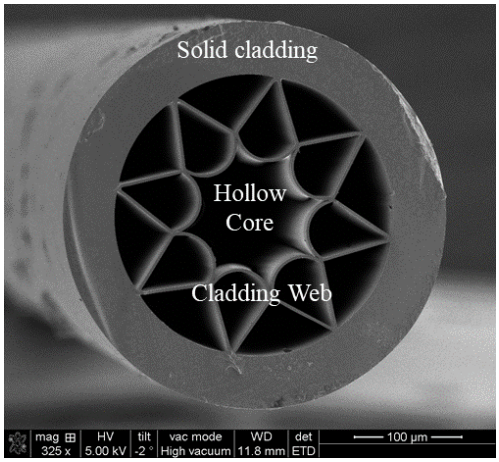

Figure 1.1 SEM picture of a cross section of an NCF fibre.

The microstructured web (cladding web, Figure 1.1) is of major importance for NCF due to the guiding mechanism of the light. Guidance in the hollow core is achieved through an inhibited coupling between light that propagates in the fibre core and light that propagates in the glass of the cladding tubes or in the glass interstices between the cladding tubes and the glass wall [5], [6]. Also, the wavelengths that are guided are strongly dependent on the thickness of the core wall or capillaries [7] as will be described in Chapter 2, section 2.1.4.

It is important to develop a new fabrication route in order to achieve the full potential of the unique properties of these fibres and to realise novel optical sensors. A critical challenge of this fabrication is the ability to locally modify the fibre. This is traditionally achieved by polishing, etching and flame tapering on conventional fibres. However, preservation of the fine microstructures is essential to ensure the guidance properties of the NCF are not adversely affected. Consequently, conventional modification techniques are largely unsuitable for application to microstructured fibres and a novel processing route must be developed.

The main challenges when machining this type of fibre are the issues of hole tapering associated with laser drilling of the fibres, since when this happens the microstructure of the fibre may be deformed (for example [8]). There are other methods, such as multi-step processes to achieve the core of the fibre, for example, FIB (Focused Ion Beam) and laser machining [9], laser machining and chemical etching [10] and [11] or water assisted femtosecond laser machining of fibres [12]. In this case, the realisation of these methods is not simple, expensive, time consuming and requiring handling of chemical substances. Also, the structures reported in the literature are relatively small (i.e. 50 μm diameter features reported in [13]) and since most of the structures are tapered or the depth is enhanced by chemical substances, the depth achieved is not always controllable.

So, the main objective of this thesis is to overcome the above-mentioned challenges, developing a new fabrication route that will achieve the full potential of the unique properties NCF to ultimately realise novel optical fibre sensors. A distinct manufacturing route is proposed in which femtosecond laser machining is employed. Using this technique, it is possible to achieve precision of machining, address the issues of the

feature size, achieve cleanliness of processing and most importantly to machine the internal structures whilst preserving the unique guiding capabilities. This will also allow the opportunity to create active fibre components to address a range of sensing applications which will contribute to the adoption of these hollow core fibres instead of using these as passive components. The possibilities with the machining strategy proposed are the possibility to allow potential any shape to be machined into a microstructured optical fibre (since it is governed by a digital scanning pattern), to enable the preservation of the cladding web and depth control and to allow the potential to modify the core wall (which is not possible by other methods). These characteristics open up a new path for chemical sensing, for example, combining the important guidance properties of NCF, allowing the infrared region detection and the detection of selective species, not only by optical properties (wavelength) but also due to the possibility of incorporating selective membranes on the core walls or even Bragg gratings.

Femtosecond laser machining has been proposed previously for the modification of hollow core fibres where holes were drilled laterally through the cladding to increase access to the hollow core. In principle this will enhance the interaction of the measurand (substance to be detected) with the light and improve the response time of the device [14].

Hence, the aim of this work is to develop a novel fabrication route in order to produce structures that may subsequently be developed into a functional component for a range of novel applications, developing a robust machining strategy using the femtosecond machining. Femtosecond laser machining is chosen as it has advantages including the ability for inscription in any material type without pre-processing or special core doping and its inherent flexibility of being a non-thermal process which results in structures with an almost negligible heat-affected zone [15]. The method proposed in this work is also a robust processing method of the NCF, not reported before in the literature.

The interesting potential of the NCF associated with the advantages of femtosecond laser machining results in a promising solution for the development of novel silica based optical fibre sensors for the MID-IR region. Ways of functionalizing the NCF in order to develop devices capable of chemical sensing will be explored with femtosecond laser

machining. The initial proposed machining strategy for this type of fibre consists of 4 stages, as can be seen in Figure 1.2:

1. Ablating the bulk of the solid cladding, Figure 1.2 a);
2. Approaching the cladding web, Figure 1.2 b);
3. Removal of the fine cladding web structure, Figure 1.2 c);
4. Removal or modification of the core wall, Figure 1.2 d).

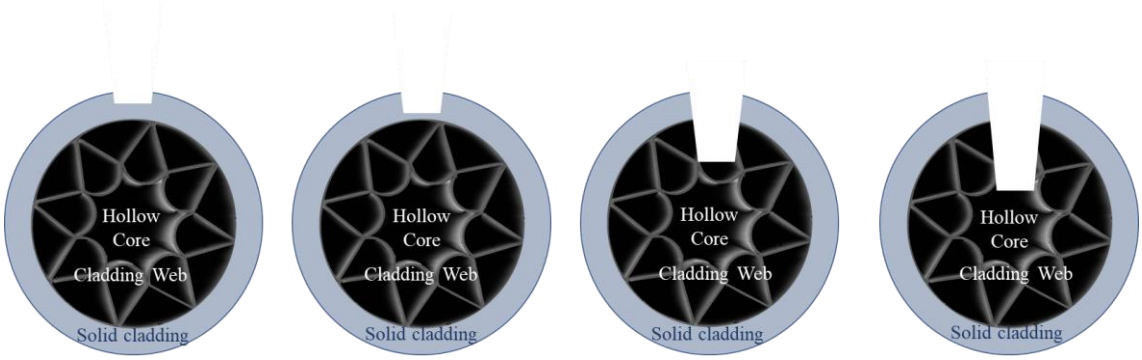

a) b) c) d)

Figure 1.2. Proposed scheme for the femtosecond laser machining of NCF showing the four stages of the proposed machining strategy: a) b) c) and d) correspond to stages 1, 2, 3 and 4 respectively.

Previous work uses femtosecond lasers to increase the access of a measurand to the hollow core e.g. [16], [13]. However, the proposed machining strategy (and its study) in this work is different and unique given that it allows enhanced precision and control in terms of depth achieved and the definition of the machined structure geometry while maintaining the cladding web without damage. Additionally, it will provide the ability to directly write a wider range of geometries (that is governed by a scanning strategy) into the fibre in comparison to simple hole drilling which comprises the majority of work previously reported.

This thesis is organised in the following chapters which provide a comprehensive review of the state-of-art of hollow core fibres (and the strategies previously attempted for their modification) and a detailed description of the development and evaluation of a novel femtosecond laser machining protocol for NCF:

- In Chapter 2, the literature review will present an overview of non-conventional fibres such as MOF, PCF and NCF. Detail will focus on NCF including

applications and potential for MID-IR sensing. The femtosecond laser machining of fused silica and optical fibres will be also reviewed.

- In Chapter 3, the femtosecond laser methodology will be presented and the initial tests regarding machining parameters such as pulse energy, scanning speed, scanning strategy and number of laser passes is reported. The initial tests presented were done in a fused silica, single mode fibre SMF-28 (SMF) and NCF. A comparison between SMF and NCF will be presented with regards to the initial machined structures.
- In Chapter 4, a new femtosecond laser scanning approach will be presented. The aim of the experiments reported in this Chapter was to develop a better depth control of the machined structures and ensure that the laser is on focus for each laser pass. Tests with NCF will be presented as well as its results regarding the depth achieved and machining quality.
- In Chapter 5, the optimisation of the laser scanning technique developed in Chapter 4 will be shown. This was to overcome a lack of repeatability detected in the results reported in Chapter 4. A new machining protocol was tested and implemented on NCF successfully modifying the fibre and accessing the hollow core whilst preserving the fine microstructure of the cladding web.
- In Chapter 6, an analysis of the results obtained in Chapter 5 is reported regarding the optical output of a machined fibre and comparing this to the output of a non-machined fibre in terms of light and power output. A mechanical method, machining the NCF with a diamond saw, will also be presented here for comparison.
- Finally, in Chapter 7 the general conclusions will be presented. The machining strategies will be summarised, and emphasis will be on the machining strategy that delivered the best results. Further work will also be presented.

Chapter 2 – Literature Review

The need for devices that perform fast, reliable and in-situ measurements commanded the fast development of Optical Fibre Sensors (OFS) technology [17]. Most common applications of optical fibre sensors include the measurement and monitoring of strain, temperature, displacement, bending or torsion, vibration and acceleration, rotation, chemical or gas detection and current or voltage [18]. OFS generally can be classified regarding the localisation of the sensor (intrinsic or extrinsic), the operating principle (intensity phase, frequency or polarisation) and the application (physical, chemical and bio-chemical) [19].

These sensors have a number of advantages over conventional (electrical) sensors, such as, immunity to electromagnetic interference, compact and lightweight, high sensitivity, large bandwidth, inability to conduct current (e.g. useful in environments with potential explosion risk), robust and resistant to harsh environments. They also enable in-situ distributed and remote sensing capability [19], [20].

However, there is a challenge for optical sensing: its ability to detect and discriminate specific molecules. This can be achieved by analysing the absorption or transmission spectrum resulting in a "molecular fingerprint". This effect is localised in the infrared wavelength range of 2-25 μm and it is characterised by the strong vibration absorption lines of various molecules. Measuring in this region with optical fibre sensors can have applications in spectroscopy and medicine [2].

The main difficulty of developing OFS in this region arises due to material absorption limitations. Although fused silica is the most common optical fibre material and has good mechanical and chemical durability, unfortunately, it is limited by high attenuation (rising to greater than 60 dB/m) at wavelengths longer than 3 μm [2]. Therefore, the use of solid core silica fibres for sensor devices, at theses wavelengths, is not feasible.

Alternative optical materials have been explored, such as the chalcogenide glasses, Gallium Lanthanum Sulphide (GLS), As-S [21] and As-Se [21], and Fluoride glasses such as ZBLAN [22].

The GLS in particular was widely investigated because it is transparent for wavelengths up to 5 μm [23], it has a high refractive index (2.3-2.5) which is useful for non-linear applications [23] and can be readily doped with rare earth ions [23]. The implementation of chalcogenide and fluoride glass fibres for practical application has been limited due to the difficulty of fabricating low loss single mode glass fibres from such materials [2] particularly when compared to the mature state of silica fabrication.

Hence, hollow core waveguides and fibres have recently arisen as a promising alternative transmission medium in this spectral range because the guidance mechanism can circumvent material absorption problem of silica at mid-IR wavelengths [2]. In particular microstructured hollow core silica fibres have been shown to be a viable alternative for guidance in the IR spectral region (studied from 800 nm up to 4.5 μm with a minimum attenuation of 24.4 dB/km at around 2400 nm) [3].

Although hollow core fibres are of great interest as a platform for OFS, novel ways of modifying and functionalizing these fibres must be developed in order to manufacture an optical fibre sensor device that can work in the "molecular fingerprint" wavelength region. In this thesis, the method used to functionalise the fibres was femtosecond laser machining, due to its advantages such as the ability for inscription in a wide range of material types without pre-processing or special core doping and its inherent flexibility of being a non-thermal process resulting in structures with an almost negligible heat-affected zone [15]. This allows high precision micromachining necessary for removal and modification of the delicate internal structures of the microstructured silica hollow core fibres without compromising the optical guidance.

In this review Chapter, microstructured optical fibres and photonic crystal fibres will be presented. Among them it will be shown why one such fibre, the Negative Curvature Fibre (NCF), arises as a promising fibre for sensing in the MID-IR. The state-of-the-art for femtosecond laser machining of fused silica and optical fibres will also be reviewed.

2.1 Microstructure Optical fibre (MOF) and Photonic Crystal Fibres (PCF)

Microstructure Optical Fibres (MOF) are a family of optical fibres that comprise many optical fibre types with different waveguide properties [24] and the first was fabricated in 1974. MOFs with a periodic microstructure of air holes are often referred to as Photonic Crystal Fibres (PCFs). These fibres emerged in the 1990s as a new class of optical waveguides with great potential and unprecedented properties owing to the flexibility in tailoring optical waveguiding parameters and the capacity to adapt and suit a wide range of applications [24]. The first PCF was demonstrated in 1996 [25] by J. C. Knight *et al*. The first sensor developed based on a PCF was performed in 2000 [26].

Some other materials such as soft glass (chalcogenide) have been studied as alternative glasses for mid-IR. However, not only the development of the stack-and-draw fabrication technique is not well-established as for silica as (since they exhibit a rather steep viscosity-temperature profile) [27] but they also present low mechanical stability (when compared to silica). [28]

There are generally two different mechanisms of guiding light [29] with an overview in Figure 2.1:

i. *Index guiding*: similar to conventional fibres, the light is guided in a higher index core by modified total internal reflection (TIR) from a low effective index cladding:
   - Properties: endlessly single mode, capable of small and large mode area, high numerical aperture, high birefringence, high nonlinear coefficient and dispersion management.

ii. *Bandgap guiding*: for a specific range of frequencies the light is confined in a low index core as it cannot propagate across the surrounding photonic crystal cladding:
   - The Photonic bandgap (PBG) guidance: this can be observed in PCFs with a hollow core, Hollow Core Photonic Crystal Fibres (HC-PCF) [30] or more specifically Hollow Core Photonic Bandgap Fibres (HC-PBGF) or with a solid core [29].

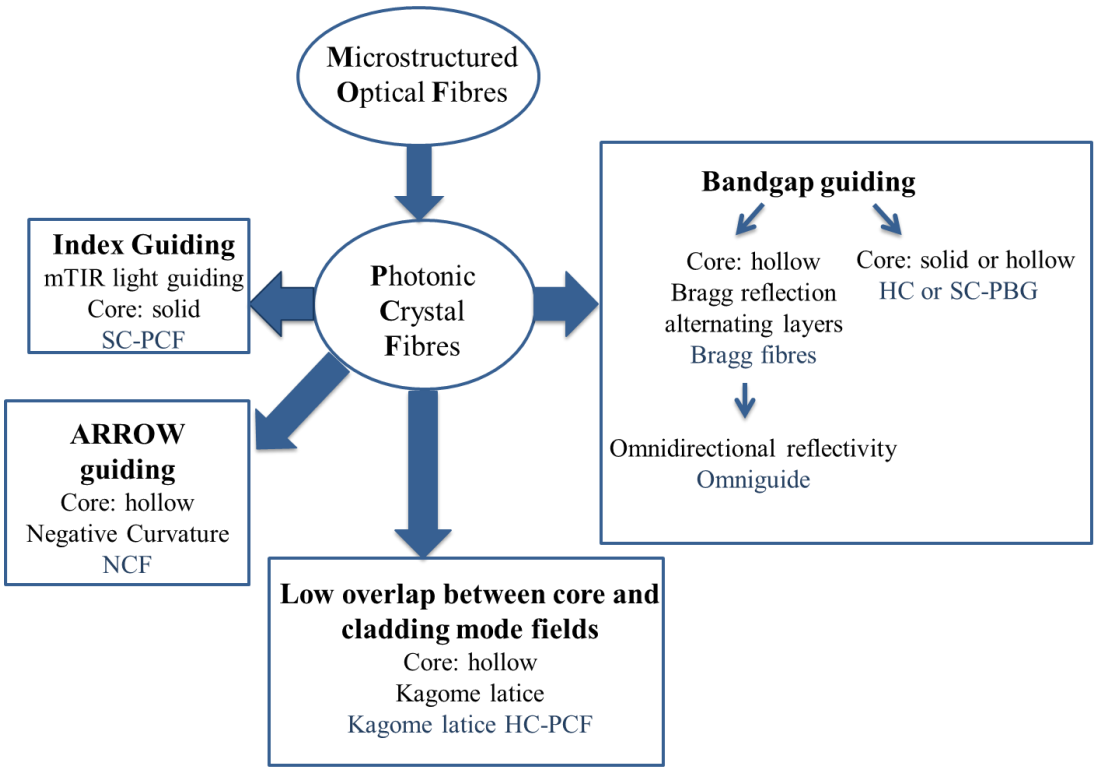

Figure 2.1 Summary of the classification of the PCFs according to the guiding mechanism.

In general, PCFs guide by only one guiding mechanisms although a hybrid (index guiding plus bandgap guiding) has been used in photonic crystal slabs [29]. The HC-PCF can guide light also due to an inhibited coupling between the core guided modes and modes associated with the cladding. This shows higher propagation loss but guides over much broader wavelength ranges [31].

There are other important types of HC-PCF with slightly different guiding mechanisms to that of HC-PBGFs such as the Kagome Lattice HC-PCF [30] and Negative Curvature HC-PCF also known as the Negative Curvature Fibre (NCF) [32]. In Figure 2.1, a summary of the classification of the PCFs according to the guiding mechanism is presented.

The fibre fabrication process of silica based HC-PCFs is a process now well established and employs a "stack and draw" method which reduces the transverse dimensions of the structured preform down to optical dimensions with no need of further processing [33]. This technique is capable of producing long lengths of the fibre and allows the number of guiding modes to be controlled through adjustment of the final core size [33]. However,

the stacking process of complex geometries (done by hand) is an inherently a slow process [27].

The losses in HC-PCFs are limited by the same mechanisms that limit loss in conventional fibres: absorption, Rayleigh scattering, confinement loss, bend loss and variations in the fibre structure along the length [33]. Nevertheless, these losses may be reduced below the conventional levels because the majority of light travels in the hollow core in which scattering and absorption could be very low [33] and it overcomes the material absorption limits by minimising the interaction of light with the glass material. HC-PCFs have many advantages including [33]:

- ✓ Produce lower optical transmission loss than conventional solid core fibres at wavelengths where the bulk material is highly absorbing (at MID-IR wavelengths);
- ✓ Exhibit substantially higher laser induced damage thresholds compared to conventional solid core fibres, being suitable for delivery of high peak power beams for applications such as laser machining;
- ✓ Promising in relation to the nonlinear optical processes in gases. A HC-PCF can be constructed as a gas cell with diffraction free and only loss limited performance (preliminary experiments have shown that HC fibres filled with hydrogen can act as cell for stimulated Raman scattering experiments [33], [34];
- ✓ Potentially suitable for trace gas detection or monitoring or as gain cells for gas lasers.

PCFs have been reported as promising alternative for both applications in optical communications and optical fibre sensing. The microstructured silica-air cladding fibres with fluid-filled cores have been considered for many applications such as gas and liquid sensors [23], biosensing, pressure, transverse force, strain sensing and bend sensing [35]. Structural health monitoring is also another area that has seen the application of PCFs [26]. The main attractiveness of applying PCF in this field (among other fields) is that by varying the size and location of the cladding holes and/or the core it is possible to tune the fibre transmission spectrum, the mode shape, the non-linearity, dispersion, air filling fraction and birefringence to values that are not achievable with conventional optical fibres. Also, since there can be air holes it is possible to propagate the light in air or to

add liquid or gases into the air holes. These characteristics enable a well-controlled interaction between light and sample leading to sensing applications not possible with standard optical fibre. For example, Sagnac interferometers are common for PCF-based fibre optic sensors due to their high extinction ratio, short length of fibre needed (when compared with SMF), and they exhibit high insensitivity to temperature [26].

The following sub-section will show a summary of the waveguiding mechanisms for HC-PBGFs, Bragg fibres, Kagome fibres and how these fibres were important for the implementation of the NCF. The NCF will be presented, as well a summary of the work done to date with such fibres.

2.1.1 Hollow Core Photonic Bandgap Fibre (HC-PBGF)

An example of a HC-PBGF can be seen in Figure 2.2. The light propagation in HC-PBGFs occurs within the hollow core while the surrounding periodic array of air holes [33] or a dielectric multilayer in the case of Bragg fibres [36] reflects the electromagnetic field.

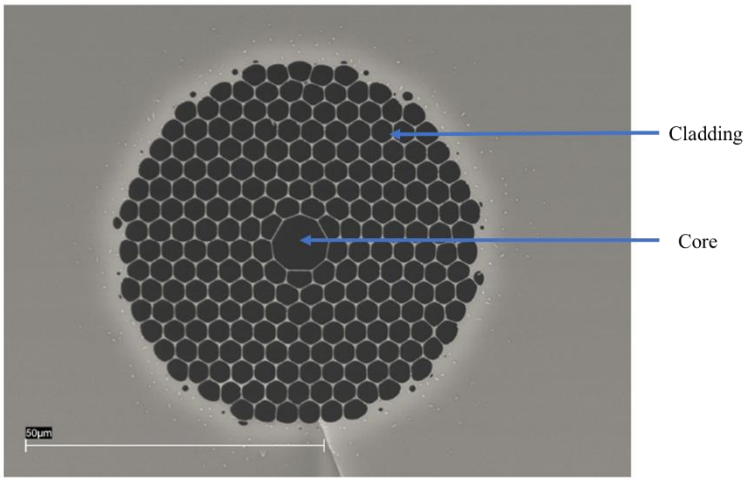

Figure 2.2 Cross section of a HC-PBGF [37].

The PBG effect depends on the structure (size and spacing) of the periodic dielectric layers and allows light confinement in a low index medium, such as air or another gas [38]. The guiding of the light occurs due to the guidance at a low-index "defect" site within the photonic crystal lattice (cladding). At a certain frequency, the band gaps appear in a range of values of the propagation constant β in which it is expect propagating

modes and they are surrounded by propagating modes at higher and lower values of β. The band gap occurs for values of propagation constant $\beta<k$ (vacuum wavevector) and so can be used to trap light in an air core. Since the range of $k > \beta$ for which bandgaps occur is limited, only a limited range of wavelengths can be expected to be guided in the hollow core [39], [40]. The fabrication of a PBG fibre becomes more difficult at shorter wavelengths e.g. a PBG fibre for 850 nm is more difficult to realise since the dimensions of the fibre microstructure have to be reduced compared to fibres for 1550 nm [39].

The PBG effect can also occur in a solid core fibre and light propagates in a low index defect. Solid core PBG fibres consist of an array of high index cylinders in a low index background and a low index defect – core in which light propagates. These fibres have a low loss transmission spectra for several windows and the light is confined to the core by a photonic bandgap of the cladding [41].

2.1.2 Bragg Fibres: The "Omniguide" Fibre

There is another interesting group of HC-PBGFs known as Bragg fibres [36]. These fibres were proposed in 1970's [25]. Bragg fibres consist of a core surrounded by layers. These layers are of alternating high and low refractive index, Figure 2.3. The light is confined to the core by Bragg reflection of the alternating layers, which approximately form a Bragg grating and have a one-dimensional bandgap [36]. There is one class of Bragg Fibres named Omniguide fibres [42] which guide the light within a hollow core by concentric multilayer films with the property of omnidirectional reflectivity. A large hollow core is surrounded by a multilayer omnidirectional mirror that confines light as a hollow metallic waveguide. The multilayer cladding of the fibre has a photonic band gap that confines light in a certain frequency range and it is determined by the periodicity. Reference [42] mentions that with only 17 layers surrounding the hollow core, the radiation losses of the TE_{01} mode is better than 0.001 dB/m. The mode exhibits high suppression of the nonlinearities and losses of the cladding material due to the strong confinement in the core. The scheme of an Omniguide fibre can be seen in Figure 2.3 [42].

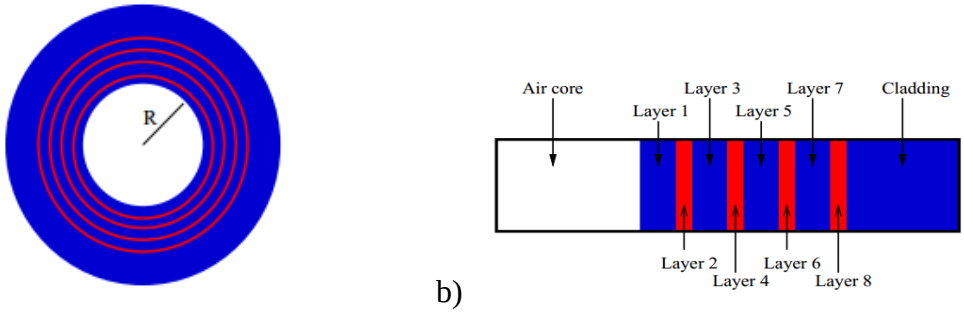

a) b)

Figure 2.3 a) Omniguide fibre with a large hollow core of radius R surrounded by a multilayer omnidirectional mirror and b) scheme of the layers [42].

2.1.3 Kagome Lattice HC-PCFs

Kagome lattice HC-PCFs have a conventional circular core-cladding boundary [30] or can also have a hypocycloid core-shape [43]. An example of this fibre can be seen in Figure 2.4 [44].

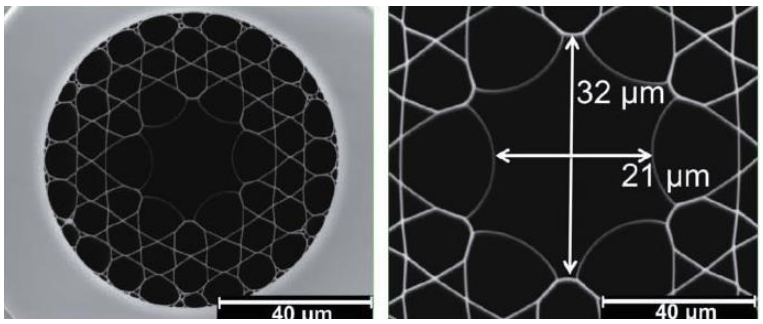

Figure 2.4 Example of a Kagome fibre [44].

These fibres show broad optical transmission bands with relatively low loss [30]. They have also been proposed as an ideal structure to reduce the large material losses in polymer PCFs. Although there are various suggestions to the guidance mechanism of these fibres, such as low cladding density of states, low overlap between core and cladding mode fields and high-order bandgaps, the nature of guidance of these fibres is not fully understood [30]. Some work points to the low overlap between core and cladding mode fields [45] whilst other work suggests that the photonic guidance relies on a mechanism similar to Von Neumann-Wigner bound states of the Schrödinger equation within a continuum [46]. The fibre guided modes in these fibres interact weakly with the cladding modes due to the rapid phase modulation of the latter. Due to this guiding

mechanism Kagome lattice HC-PCF exhibit broad transmission regions with relatively low loss covering the spectral range from the infrared up to the UV [47].

2.1.4 Negative Curvature Fibres

A systematic numerical and experimental study of the effect of the negatively curved hypocycloid-core in a Kagome-lattice HC-PCF on the fibre transmission loss and its modal properties was also reported in 2013 [43]. The negative curvature refers to the contour of the core-cladding interface when compared to the curvature of the outer diameter of the fibre. An SEM picture of the fibre can be seen in Figure 2.5.

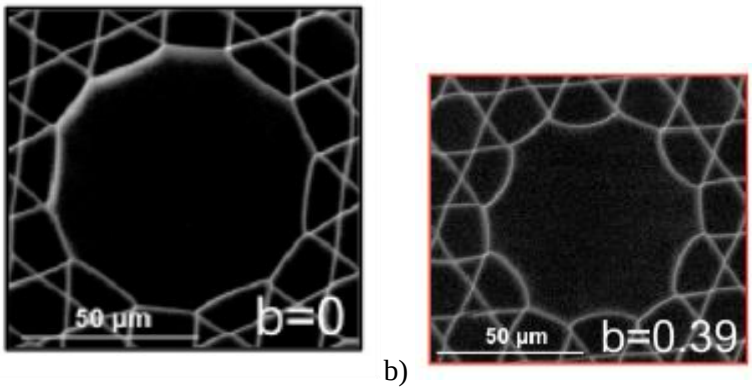

a) b)

Figure 2.5 SEM picture of the hypocycloid-core Kagome latticed hollow core PCFs being a) the fibre with a b parameter of 0 and b) the fibre with b parameter of 0.39 (increased curvature) [43].

The results showed that increasing the core-surround curvature is of the most importance because the confinement loss decreases several orders of magnitude. The parameter b on the picture denotes the curvature of the hypocycloid like core defined and has the ratio between *d* and *r*, where *d* is the distance between the top of the arc and the chord joining the nodes connecting the inward arc to its two nearest ones and *r* is the half of the chord length. The parameter b=0 corresponds to an almost circular core. A more than tenfold reduction in the fundamental core-mode power overlap with cladding silica can be achieved and it is possible to obtain a near single mode guidance. Fibres with enhanced negative curvature demonstrated 17 dB/km at 1064 nm and the results indicated that the transmission loss of NCF could outperform the HC-PBGF [43].

As described above the Kagome lattice is a complicated structure and requires stacking many layers of capillaries during preform fabrication. In contrast, an HC-PCF with a much less complex design, the NCF [4], was first proposed in [47] and [2] (2011 and 2012). The NCF have emerged as promising fibres due to the realisation of a Kagome fibre with a negative curvature core boundary that exhibited a lower attenuation than the regular ones. Following this discovery, several experiments were done to confirm the significance of core wall shape in the reduction of attenuation in such fibres [48]. Reference [4] also mentions this fibre is promising for optical devices that enables the low loss mid-IR guidance in a silica-based fibre showing capability to be laser machined.

It has been shown that the negative curvature of the core boundary has an important role in decreasing the optical loss both in hypocycloid Kagome Lattice fibres [49] and in NCF [47]. It was demonstrated that in the case of a silica NCF it was possible to guide the light in the IR spectral range (above 3.5 μm) where the loss of silica glass is very high [3].

The NCF light guiding mechanism is based on the Anti-Resonant Reflecting Optical Waveguide (ARROW) phenomenon. All wavelengths which are not in resonance with the core wall are reflected into the core and propagate with low loss. This structure behaves in a similar way to a Fabry-Perrot resonant cavity [3], [48], [7], [50], [51], [52]. The resonant frequencies that cannot be confined in the core and leak away to the cladding region where they are strongly attenuated. The wavelengths that are guided are strongly dependent on the thickness of the core wall or capillaries. For example, for guidance at 1030 nm and 1064 nm a suitable wall thickness is in the range of 910 ± 50 nm [7]. The glass curvature surrounding the core has an impact on the leakage loss, bend loss and coupling between the core mode and cladding modes [25].

The combination of the antiresonance (critical role) in the glass at the core boundary and a wavenumber mismatch between the core and the cladding modes inhibits the coupling between modes and this is why silica NCF have been demonstrated with low loss transmission of the order of 10 dB/km and usually lower losses can be obtained for larger core diameters [25].

The first report of a fabricated NCF with the simplified cladding structure was in 2011 [47] with a silica fibre showing transmission above 3.5 µm. This was closely followed by work where CO_2 laser delivery was demonstrated at a wavelength of 10.6 µm using a hollow core NCF made of chalcogenide glass [53]. The loss in this fibre was however relatively high, around 11 dB/m. The work proved that the light was well localised in the core and the results showed promise for delivery of CO_2 laser radiation. However, the authors mention that further improvement of the technology and design of the fibres is needed to reduce the optical loss bellow 1 dB/m. In Figure 2.6 an electron microscopic photography is presented [53].

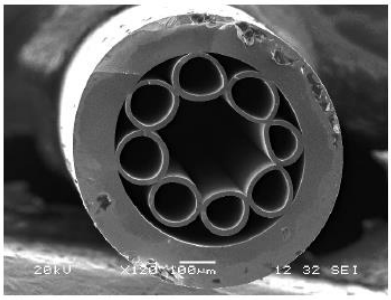

Figure 2.6 Electron microscopic photography of the fibre cross section of the negative curvature fibre with a cladding of eight capillaries [53].

The first demonstration of a low loss NCF was in 2012 [2] which demonstrated a silica NCF (see Figure 2.7) for a transmission in the MID-IR with a minimum attenuation of 34 dB/km at 3.05 µm. Notably, above 4 µm the fibre also had a transmission band, but the fibre did exhibit considerable bend loss for bending diameters lower than 40 cm [2].

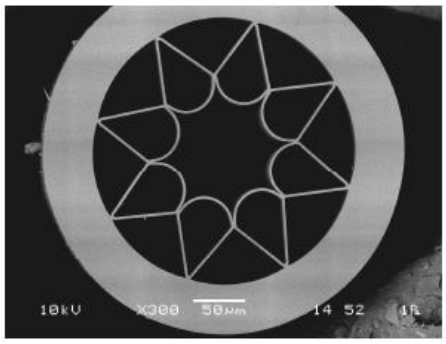

Figure 2.7 Scanning electron micrograph of a fibre cross section of a NCF with low loss guidance at 3.05 µm [2].

Since the geometry has such a strong impact, different configurations were proposed. The cross section of two different NCF designs can be seen in Figure 2.8.

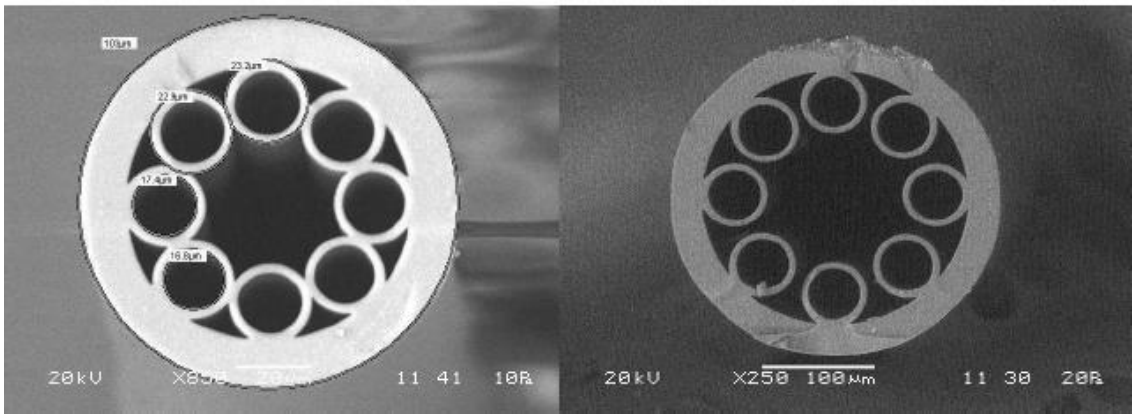

Figure 2.8 Negative curvature fibre cross sections showing slightly different designs: (left) with touching capillaries in the cladding and (right) with no touching capillaries [32].

The purpose of having a design with non-touching capillaries is to remove the additional resonances in the transmission bands. In Figure 2.9 it is possible to see the output of an NCF with touching capillaries with clear guidance at the contact points between the capillaries. Here the NCF with non-touching capillaries allows reduced loss in transmission bands due to the lack of additional optical resonators in the cladding. [54].

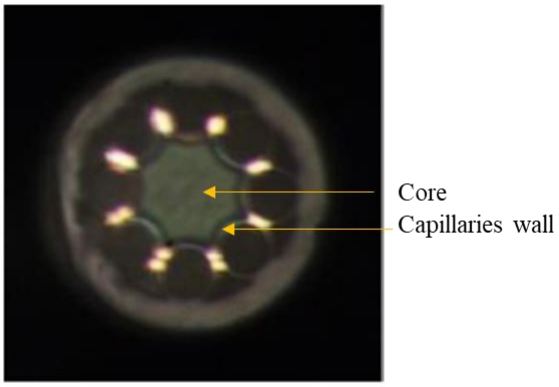

Figure 2.9 The output of NCF with touching capillaries excited by visible light [54].

In [54] light propagation through a silica NCF with transmission bands at 4.5, 5.8 and 7.7 µm, in a region where silica has extremely high material loss, was demonstrated. The authors introduced a separation between the cladding capillaries to remove the additional resonances in the transmission bands. The total loss was at least three orders of magnitude lower than the loss of silica glass.

The authors confirm a very weak coupling of the air core modes with the cladding structure. The NCF with non-touching capillaries in the cladding decreases the loss level in the transmission bands due to an absence of additional optical resonators in the cladding. The authors suggest that in order to decrease the loss level in the required spectral range it is necessary to carry out an optimisation of the NCF structure by optimizing the air core diameter, the number of capillaries in the cladding and the outer and inner diameters of the capillaries [54].

The authors also mention that it is more difficult to fabricate the NCF with touching capillaries in the cladding because at the relatively high drawing temperatures the silica glass viscosity is reduced, and surface tension effects tend to straighten the capillary walls. This makes it more difficult to maintain a negative curvature geometry in the core boundary [54].

In 2014, numerical simulations showed that the bending losses of the HC-ARF were strongly influenced by their geometrical structure and an HC-ARF exhibiting a bend loss of 0.25 dB/turn or, 1.6 dB/m at a wavelength of 3.35 μm and a bend radius of 2.5 cm, was fabricated and demonstrated. The attenuation of this fibre was < 200 dB/ cm over 600 nm in mid-infrared spectral range measured by the cut-back method. The authors mention that it is possible to neglect the impact of silica absorption since the advantage of the design with non-touching capillaries regarding the attenuation (which is the case) is that it is probably greater in the near-infrared spectral range [55]. Also in this reference, the authors studied the impact of the gap separation between the non-touching capillaries and concluded that the more separated are the non-touching capillaries, the more beneficial it is in terms of bending losses, but a balance is required to produce a fibre with low bending loss and low transmission losses.

There are other studies that explore a potentially improved design of the NCF more generally referred to as hollow core antiresonant fibres (HC-ARF), as seen in Figure 2.10. This design consists on adding extra antiresonant glass elements within the air cladding region of an HC-ARF.

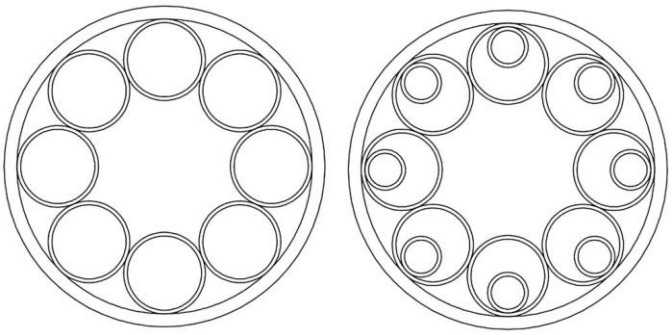

Figure 2.10 Non modified NCF on the left and modified NCF or HC-ARF on the right [56].

The authors used numerical simulation to compare fibre structures with and without the additional cladding elements in the near and MID-IR regions and proved that this new design contributes to the reduced bending losses at MID-IR and in lower attenuation in the near IR due to the reduction of leakage loss. In the non-modified NCF, the attenuation is limited by the coupling to the voids in the cladding and in the case of the modified HC-ARF, the coupling is supressed due to the additional antiresonant elements within the cladding void. [56]

In 2017, the measurement of resonant spectral bend loss of a series of HC-ARF was performed, since these fibres are important for applications in delivery of high power ultra-short laser pulses for industrial applications [57]. In this study, the impact of the fibre geometry was also clear, and it was observed that the sensitivity to bend diameter is dependent on the ratio between the cladding and core structure size and that the exact position of the loss bands is highly dependent on the orientation of the fibre structure with the bend plane [57]. When the core diameter ratio (i.e. the cladding diameter divided by the core diameter) is reduced from 0.70 to 0.43, by decreasing the cladding capillary diameter, the minimum bend diameter is decreased from 160 mm to approximately 15 mm at a wavelength of 800 nm [57].

In summary the geometry of the NCF has a direct impact on the performance of the fibres:

- the negative curvature increases confinement,
- the low loss region can be selected using the geometry,
- the gaps between the tubes/capillaries (touching or non-touching capillaries) increase confinement and bandwidth,

- additional capillaries (addition of another tube inside the existing one) improve the field confinement and reduces bend loss,
- capillary parameters can be used to decrease the bend loss.

All these characteristics allow the possibility to tailor and control the guidance proprieties of the NCF or HC-ARF and hence increase the use and application of such fibres [25].

Due to the interest of NCF and HC-ARF for high power infrared light new fabrication routes, as an alternative to the stack and draw technique, are being developed. In 2016, R.R. Gattass *et al* demonstrate an infrared-sulphide based chalcogenide glass NCF fabricated through extrusion. The aim was to overcome limitations of the manual assembly process currently used to build the preform i.e. time-consuming, labour intensive and restriction of the configurations that can be fabricated. The fibres made by the extrusion technique showed <1 dB /m for 2-5 μm window, determined through a cut-back method with a Fourier-Transform Infrared (FTIR) spectrometer [27].

The extrusion process consists on heating a bulk piece of glass close to the softening point and pushing it through a die to form a preform. This is drawn down into a fibre in a second step, where the glass is heated again and stretched into a fibre. This process takes advantage of the ability to process a soft-glass at low temperatures to extrude the preform [27]. However, the main limitation of this type of fibre manufacturing is the lack of accuracy which is possible to fabricate the final structure. As mentioned above, with the stack-and-draw fabrication route there is an established commercial base from which it is possible to ensure a range of tubes with tight tolerances, as for silica. For soft glasses the same is not completely true although the work in progress may be leading towards that development [27].

The application of this process with fused silica would be difficult due to the high temperatures required to achieve a suitable viscosity for the process to occur. For example, the softening temperature of fused silica is 1585 °C when the viscosity is $10^{7.6}$ poises which means this is the temperature at which glass can deform under its own weight (as in accordance with the datasheet of the fused silica used in this work, Fused

Silica Corning 7980, Industrial Grade, [58]). In contrast the softening temperature for the glass used in work of reference [27] (soft glass) was approximately 200 °C.

NCF can be applied to a variety of applications: pulse delivery [7], [59], [6] surgical applications [5], sensing [32], [60] and microscopy [61]. NCF have also been applied in the study of gas-light interaction, stimulated Raman scattering in H_2 and C_2H_2 gas lasing [48]. An NCF was also used to present the onset of pulse breakdown with low repetition-rates in a mode-locked Ytterbium fibre laser [62].

The delivery of high energy microsecond pulses from an Er:YAG laser through a silica NCF at 2.94 µm has been reported in 2013 [59]. Since the fibre was made from silica it also had good mechanical and chemical robustness and was biocompatible [59]. The lowest attenuation reported was 0.06 dB/m at 2.94 µm and pulses up to 195 mJ were delivered [5]. The delivered fluence exceeded that required for removal of biological tissue demonstrating the potential of such NCF for minimally invasive surgical procedures [63]. A cross section of the NCF designed for 2.94 µm guidance is presented in Figure 2.11 [5].

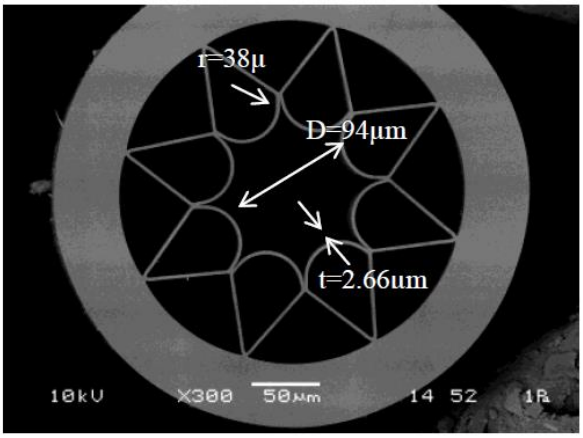

Figure 2.11 SEM picture of the fibre cross section of an NCF designed for guidance at 2.94 µm [5].

High energy green nanosecond and picosecond pulse delivery though a negative curvature fibre for precision micromachining was demonstrated by Jaworski *et al*. [6] when the authors present an anti-resonant guiding, low loss NCF for the efficient delivery of high energy short and ultrashort (nanosecond and picosecond) pulsed laser light in the green spectral region. The NCF showed an attenuation of 0.15 dB/m and 0.18 dB/m at

532 and 515 nm respectively. The authors also showed that NCF provided robust transmission of nanosecond (ns) and picosecond (ps) pulses with energies of 0.57 mJ and 30 µJ respectively. It was possible to achieve a single-mode, stable output whilst maintaining the spectral and temporal properties of the source laser beam. The authors showed the practical application in precision micro-machining and marking of metals and glass.

Also in 2013 [7], high average power picosecond and nanosecond pulse delivery at 1030 nm and 1064 nm respectively through a NCF was demonstrated. The SEM image of the NCF is shown is Figure 2.12. In this work, successful transmission of ps pulses with an average power more than 36 W, 7 times greater than previously reported with a hypocycloid-core Kagome lattice HC-PCF was reported [49]. The delivered pulse energy and average powers are of the level required for precision micro-machining applications.

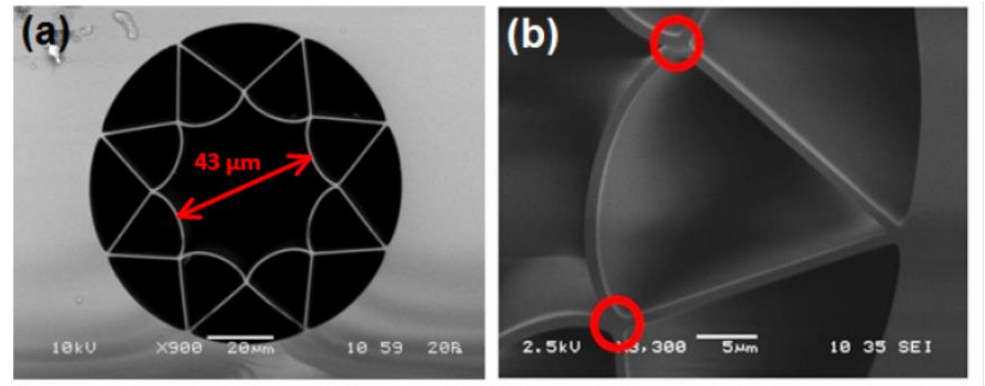

Figure 2.12 SEM image of the negative curvature fibre used in reference b) as well as picture of the capillary forming the negative curvature of the fibre core wall. The cladding nodes, marked as a circle, behave as independent waveguides supporting their own lossy modes [7].

In 2015 work carried out to assess the dispersion performance of NCF in comparison to HC-PCF showed that the addition of the complicated photonic crystal cladding increases the waveguide dispersion slope and that is the reason why NCF shows lower dispersion in comparison with the HC-PCFs. The main reason for the low dispersion slope for the NCF is the strong light localisation in the air core in comparison to HC-PCFs [64].

In order to establish the reason for the difference between the dispersion characteristics of HC-PCF and NCF, the optical properties of the model waveguide structures was numerically analysed. A dielectric tube made of silica glass suspended in air was

modelled that can be considered as an HC-PCF core-cladding boundary with continuous rotational symmetry, having the dielectric tube with a core diameter of 78 µm and the wall thickness of 2.7 µm. The second structure modelled consisted of a dielectric tube with negative curvature boundary made of silica glass, Figure 2.13.

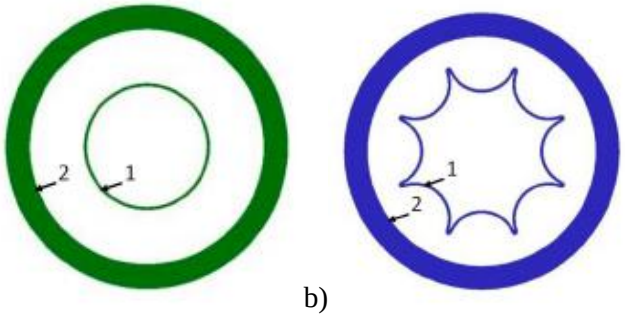

a) b)

Figure 2.13. a) The HC-PCF showing the core-cladding boundary being 1 the glass capillary and 2 the region of boundary condition (190 µm diameter) and b) the NCF with 1 being the glass capillary and 2 the region of boundary condition with 190 µm diameter.

The wall thickness of the air core modes was the same as in the case of the dielectric tube. In this study model waveguides were used and can be considered has hollow fibres without the microstructured cladding and the waveguide loss and dispersion curves for the model waveguide structures were calculated. The values of the Group Velocity Dispersion (GVD) were very similar and the dispersion slopes are very small in both cases, approximately 0.01 ps nm^{-2} km^{-1}. However, an example of a known value for real HC-PCFs of dispersion slopes can be as higher as 29 ps nm^{-2} km^{-1} [64], [65]. The authors mention that this increase in dispersion slope happens due to the addition of the complicated microstructured cladding to the dielectric tube. The light localisation mechanism of the tube in the case of the NCF model avoids the addition of the complicated microstructured cladding web. The authors mention that only two factors strongly influence the waveguide properties of the HC-PCF and NCF which are the shape of the core cladding boundary and the microstructured cladding [64]. Also, the NCF was shown to be promising in terms of femtosecond pulse delivery [64].

The study of the dispersion characteristics of an NCF was also done using the spectral and auto-correlation measurements of femtosecond pulses at the input of the fibre. The NCF fibre used had 8 circular cladding rings (non-touching capillaries) and a 21 µm core.

The measurements were done in two regimes of the femtosecond laser operation: 255 fs autocorrelation duration that corresponds to approximately 4 nm bandwidth and 180 fs autocorrelation duration with approximately 7 nm of bandwidth using a femtosecond laser with 748 nm central wavelength, repetition rate of 76 MHz and more than 1 W of average power. In the first case the Dispersion was 7.7 ps nm^{-1} km^{-1} and in the second case the dispersion was 6.5 ps nm^{-1} km^{-1} using 10 m of fibre length [64].

In comparison, SMF-28 has a value ≤ 18.0 ps nm^{-1} km^{-1} for wavelength 1550 nm and ≤ 22.0 ps nm^{-1} km^{-1} for wavelength 1625 nm. The dispersion slope value (zero dispersion slope) is ≤ 0.092 ps $nm^{-2}km^{-1}$ [66] and the zero dispersion wavelength is between 1304 nm to 1324 nm. Although the wavelength is different, the fibres have a different behaviour regarding dispersion, showing the NCF lower dispersion value.

Further studies on the dispersion were performed in 2016 [50] in terms of their suitability for beam delivery of both high power and ultrashort pulse lasers. Two NCF fibres were investigated: one NCF was designed to operate at 1030 nm with 15 µm of core diameter, the other NCF was designed for dual wavelength delivery at 515 nm and 1030 nm with 38 µm of core diameter. The experimental set-up is based on the dispersive Fourier transform spectroscopy and the technique is based on measuring the phase difference between Fresnel reflections at the input and output surfaces of the fibre. Mirrors were used because the core of the NCF is hollow and there are no useable Fresnel reflections. The fibres showed a dispersion of 2.17 ± 0.25 ps $nm^{-1}km^{-1}$ (fundamental mode) and 4.69 ± 0.17 ps nm^{-1} km^{-1} for the first order mode at 1030 nm. The dispersion of the fundamental mode is lower than the first order mode as expected. Regarding the double wavelength fibre the dispersion measurement was 3.81 ± 0.03 ps nm^{-1} km^{-1} for the fundamental mode at 1030 nm [50]. The dispersion of the fibre designed for guidance at 515 nm is greater than the one for the fibre designed for guidance at 1030 nm. This is probably due to the result of the larger overlap between the core mode and cladding (due to the smaller core). This overlap may be correlated to the complex loss mechanism of NCF fibres however, the authors mention further work should be done to understand this dependence. As the dispersion is low, these fibres show feasibility for guiding high peak power ultrashort pulses for industrial and telecommunication applications [50].

In terms of dispersion, authors in [67] mention that a dispersion of 100 ps nm^{-1} km^{-1} is relatively low and to compare the dispersion values of the NCF with HC-PBG fibre. Reference [67] shows a method to obtain dispersion measurements from spectral domain low coherence interferograms of a hollow core PBG fibre with a 7 cell core geometry designed for operation at 1550 nm (2.5 m long). The highest dispersion measurable was about s 1000 ps nm^{-1} km^{-1} [67]. Another example can be seen in reference [65] where the authors shown an all fibre chirped pulse amplification using an HC-PBGF. The dispersion of this fibre was approximately 1146 ps nm^{-1} km^{-1} at 1560 nm (10 m length) using the modulation phase-shift method. These results are clearly higher than the ones obtained for the NCF [65].

Reference [60] shows another example where the NCF also present a very low dispersion slope when compared to HC-PBG fibre. The dispersion value of HC-PBG fibre at 760 nm reaches 100 ps nm^{-1} km^{-1} (and 200 ps nm^{-1} km^{-1} at 870 nm) with a slope dispersion of approximately 7 ps nm^{-2} km^{-1}. The NCF shows a dispersion parameter of 5 ps $nm^{-1}km^{-1}$ across the spectrum of 680-750 nm and only 0.01 ps nm^{-2} km^{-1} of slope. This contributes to the feasibility of NCF for multiphoton spectroscopy and microscopy applications, since a low dispersion parameter in that spectrum makes the fibre appropriate for the purpose of multiphoton excitation of biological fluorophores [60].

In 2014 work was done regarding the acoustic sensitivity of the NCF, theoretically and experimentally and comparing it to the conventional fibre SMF-28 [32], [68]. The experimental set-up was based on the Michelson fibre interferometer, using as a light source a 1550 nm Distributed Feedback Laser with a narrow linewidth. The NCF fibre was coupled to one of the ports of a conventional 3dB coupler forming the sensing arm of the interferometer. The other end of the NCF was coupled to a fibre pigtailed Faraday rotator mirror (FRM) and the sensing fibre was placed in a water filled chamber (eliminating the temperature-induced phase shift). A diagram of the set-up can be seen in Figure 2.14.

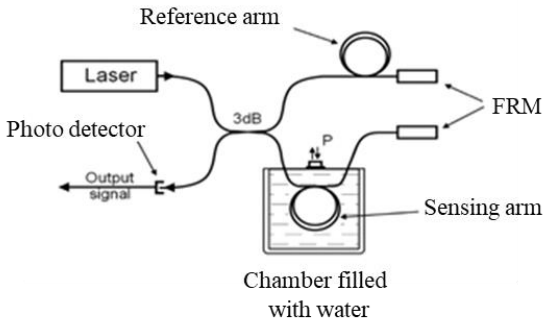

Figure 2.14 Scheme of the set-up adapted from reference [68].

The pressure of the chamber could be varied in the range of 0-50 kPa and the variations of the relative phases of the light passing though the two fibre arms were observed by counting the fringes in the output signal interferometer. The NCF sensor response to acoustic pressure was measured to be -340.1 dB re 1 μPa^{-1} similar to the theoretical value -337.7 dB re 1 μPa^{-1}. The response of the sensor was about 6 dB higher when comparing to be SMF-28 fibre [68]. It should also be highlighted that the NCF used had separated capillaries similar to fibre shown in Figure 2.8 (right side).

In 2017, the application of an NCF in an all-fibre multiphoton fluorescence sensor set-up was presented [60]. Since the dispersion parameter of the fibre did not exceed the value of 5 ps $nm^{-1}km^{-1}$ across the optical spectrum of 680-750 nm it was suited for the purpose of multiphoton excitation of biological fluorophores, being to the authors knowledge the first time an NCF was used in an optical fibre sensor set-up for multiphoton fluorescence experiments [60]. The NCF used had eight separated or non-touching capillaries. The authors compare this fibre with an HC-PBGF and showed that the NCF presents dispersion-free spectral bandwidth at 680-750 nm and hence provided a superior solution for the multiphoton fluorescence excitation of endogenous fluorophores. The total fluorescence emission signal of the tested solutions induced by the 730 nm pulses transmitted though NCF was 6 to 9 times stronger when compared to the fluorescence induced with 780 nm pulses transmitted thought the commercial HC-PBGF. However, the authors mentioned the sensor (which combined hollow core fibres with solid core fibres) required improvements in terms of collection efficiency, due to the absence of additional fibres in the fibre ring and a very large dead volume between the GRIN lens (graded-index) and collection fibres, see Figure 2.15.

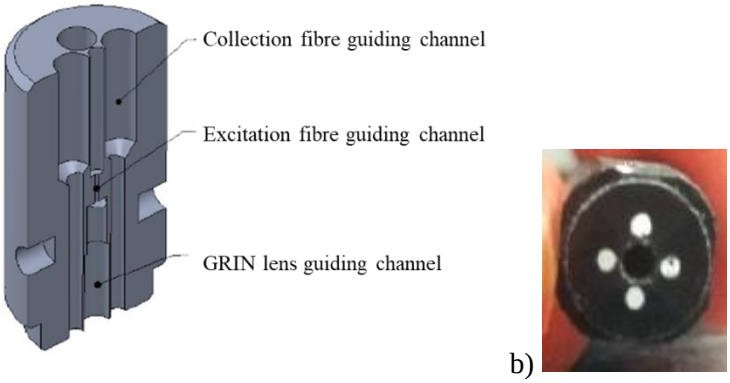

Figure 2.15 a) Diagram of the device cross section and b) photograph of the sensor detection face both adapted from reference [60].

The transmission of high-energy laser pulses is essential for the efficient induction of the Non-Linear Optical Phenomena and as the transmission of this pulses though optical fibres is difficult due to the pulse temporal broadening caused by dispersion, the common solutions would be dispersion compensation systems or using HC-PBGF or both. However, dispersion compensating systems are bulky set-ups and the HC-PBGF only maintains the dispersion parameters in a narrow optical bandwidth (this is problematic if the optical spectrum of two photon absorption cross section of biological fluorophores is considered). Being so, the authors mentioned the proposed sensor is an interesting alternative to current sophisticated solutions [60].

In Table 2.1, a summary of the different type of fibres is provided for comparison and some of the key properties are presented.

Hollow Core PCF	Guidance Mechanism	Simple cladding	Suitable for IR guidance	Suitable for MID-IR
Photonic Bandgap	Bandgap guiding	x	✓	✓
Omniguide fibres	Omnidirectional reflectivity	✓	✓	x
Hollow Core PCFs	Various mechanisms	x	✓	✓
Kagome lattice	Low overlap between core and cladding mode fields	x	✓	✓
Negative Curvature	ARROW guiding	✓	✓	✓

Table 2.1 Hollow core fibres, respective mechanism and characteristics.

2.2 High Precision Machining

It is clear from the discussion above that NCF provide an excellent potential to develop silica glass optical based sensors (and other devices) particularly in the infrared spectral region where bulk silica has very high absorption. The hollow core and negative curvature geometry enable infrared transmission and delivery of ultrashort and high peak power pulses. Nevertheless, in order to realise any practical device then hollow core optical fibres must be modified in order to add functionality e.g. access portal for sensing species. The relatively simple cladding structure of the NCF, compared to other PCFs, allows the prospect of a simpler post-processing of the fibre to modify or functionalise the fibres for development of novel devices. However, to preserve the microstructure of the fibre and not significantly disrupt the guidance, a highly precise and controllable modification technique needs to be developed. Additionally, a technique that allowed flexibility of the geometries which can be machined into the NCF would be highly

desirable as this would enable more complex or bespoke devices tailored to a specific application. Therefore, in this work the modification of an NCF via femtosecond laser processing is investigated.

In the next sub-section, a general overview of techniques used for the machining of glass and fused silica will be reviewed and in the following sub-sections, femtosecond laser machining, fused silica laser optical breakdown and examples of machining of fused silica and optical fibres with femtosecond lasers will be presented.

2.2.1 Overview of glass machining techniques

One conventional machining method used for processing glass is that of single point diamond turning [69] such as milling and grinding (use of an abrasive grain) [69]. The single point diamond turning is a technique that is well suited to generate nanosurfaces [69] on a smaller scale than the machining slots created with the femtosecond in this work (in this work, slots with depths of about 130 µm can be achieved and areas of about 338 µm (solid cladding ablated) or 350 µm wide (solid and web cladding ablated) (x-direction) and 100 or 150 µm long (y-direction) can be achieved).

For precision microhole drilling and cutting lasers are widely used in aeronautic, automobile, semiconductor, and biomedical industries. Aircrafts engine turbine blades, combustion chambers and microfluidic devices are just a few examples of the applications. In contrast, the current fabrication method for microhole drilling [70] and patterning of nanostructures for the microelectronic industries is photolithography [71]. Although photolithography provides high resolution and precision, it requires advanced facilities and numerous process steps, hazardous wet chemicals [71] and is often limited by material type and geometry [70]. Also, it relies on a physical mask [71] being made for every geometry change, rather than the digital template used by laser processing, hence photolithography is much less flexible than a direct write laser process. Whilst lithography is well suited to mass production of many identical parts (as for example mentioned in reference [72]), as in electronics industry, it is less suited to making custom or bespoke devices.

Reference [73] mentions that electron beam lithography is widely used for nanopatterning of fused silica substrates. However, to fabricate the nanoimprint templates with this technique requires several processing steps (such as electron-beam exposure, development of resist, oxygen plasma etching, Cr etching, resist stripping, fused silica dry etching and Cr wet etching). Hence, the authors purpose an alternative technology for performing atom cluster and atomic processing of fused silica by FIB lithography. The authors point out the main advantages of this process are the high patterning flexibility, high resolution and relatively simple processing steps (this eliminates many lithography steps required by electron beam lithography) and the direct pattern is possible. With FIB the authors mention it is also possible to optimise the surface properties if the ion beam probe current and the ion beam fluence is varied [73].

An example of patterning fused silica substrates, (coated with a layer of 15 nm of Cr) is shown in Figure 2.16 (from reference [73]). In this study, increasing the ion beam fluence causes the sputtering rate of fused silica to decrease non-linearly and the sputtering rate increases with the increase of the beam current, until it reaches a maximum (0.307 μm^3/nC for ion beam current of 1.3 nA), then it decreases with further beam current increments [73]. The processing parameters for the 10 by 3 µm areas were: acceleration voltage of 30 kV, emission current of 1.8 µA and objective aperture with nominal diameter of 50 µm. The ion beam current was 101 pA and the results are shown in Figure 2.16 [73].

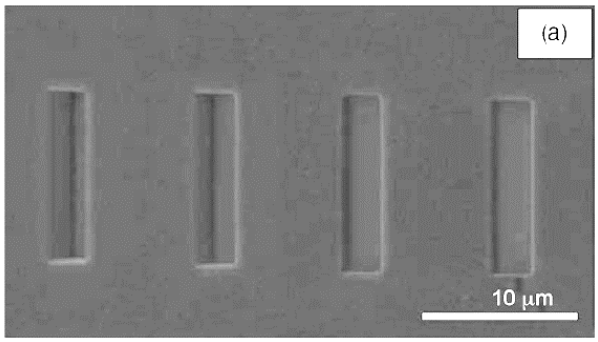

Figure 2.16 SEM picture of the trenches in fused silica produced by FIB (viewing angle of 45°) done with ion fluence of: 2.02 nC/ μm^2 (average depth of 0.39 µm and 0.429 µm measured with Dektak^{3}ST surface profilometer and Atomic Force Microscope, respectively), 4.04 nC/μm^2 (0.71 and 0.711 µm), 8.08 nC/ μm^2 (1.385 measured with AFM only) and 12.12 nC/ μm^2 (1.947 measured only with AFM) (from left to right) [73].

The experiments were performed on a dual beam SEM/FIB system, with an FIB column, a gas injection system for conducting beam-induced deposition or performing gas assisted etching (GAE) and lithography software. Before processing with FIB, a 15 nm layer of Cr was deposited on the top surface by thermal evaporation to limit the surface charging effects during the electron beam and ion beam exposure. The effects of ion fluence and ion beam current were studied regarding surface morphology and depth profile and so three different features were produced. The frequencies applied in X and Y directions were 300 Hz and 3 Hz for the fabricated features: rectangular trenches with an area of 10 by 3 µm, rectangular trenches with 20 by 10 µm area and nanogrooves [73].

The actual dimensions of the four rectangular trenches were 11.41 by 3.43 µm which the authors attributed to the destructive nature of the ion beam, software accuracy errors or the angle dependence topography. For the 20 by 10 µm, used to study the ion fluence and ion beam current dependent surface morphology and to verify the ion fluence dependent sputtering rate, two sets of these were done with different ion fluences and ion beam currents. The first set had an ion fluence of 0.61 and 2.73 nC/µm^2 and the second one had a beam current of 5.2, 101, 366, 1.3 and 5.4 nA, with 20 min exposure time. In Figure 2.17 and 2.18, the results of the trenches with 20 by 10 µm using an ion fluence of 0.61 and 2.17 nC/µm^2 are presented [73].

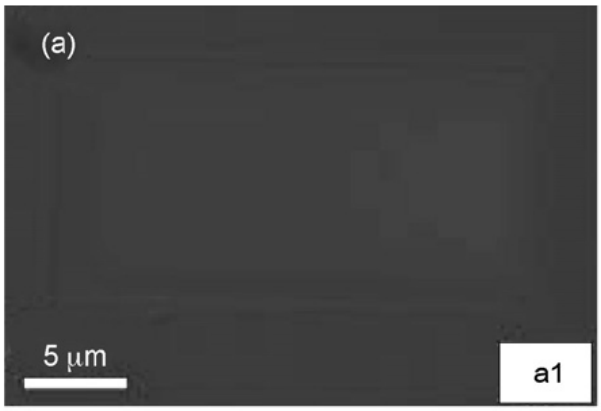

Figure 2.17 SEM images of the results of the trenches with 20 by 10 µm using an ion fluence of 0.61 nC/µm^2 with depth 0.098 µm [73].

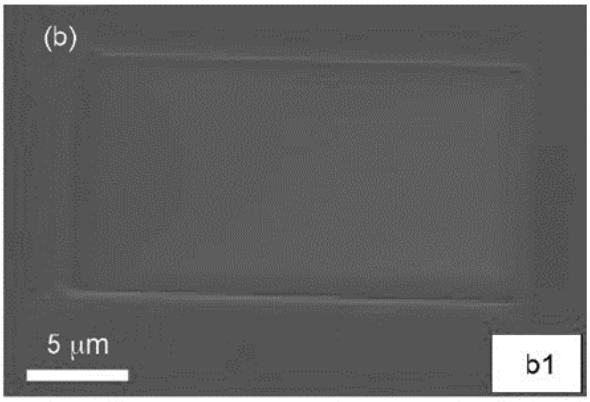

Figure 2.18 SEM images of the results of the trenches with 20 by 10 µm using an ion fluence of 2.17 nC/µm^2 with depth of 0.364 µm [73].

Four groups of nanogrooves were produced using an ion probe of 5.2 pA and the grooves were milled with different ion fluences (group I: 1.07 nC/µm^2, group II: 2.08 nC/µm^2, group III: 3.12 nC/µm^2 and group IV: 5.20 nC/µm^2), Figure 2.19. [73]

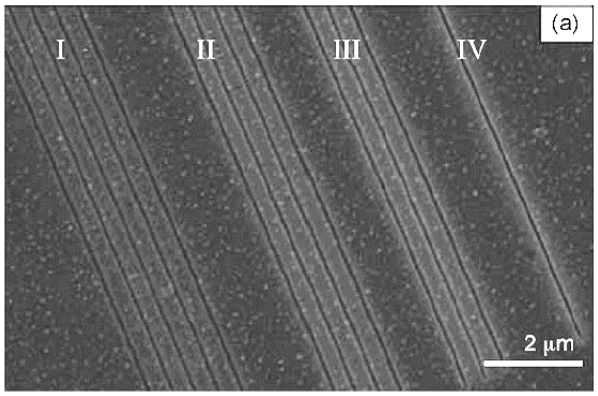

Figure 2.19 Four groups of grooves produced in fused silica with milling time of 1, 2, 3 and 5 min (respectively for groups I to IV) [73].

The depth of the nanogrooves showed some deviation of the groove width and depth within each group and the authors attribute this to the in-homogeneity of the deposited Cr layer and its roughness (9.01 nm) although they refer further studies should be done to determine the dependence of the effects of the Cr layer on the quality of the nanofeatures. The average milled depth of each group of grooves increased from 54 to 192 nm as a result of the increase in milling time from 1 to 5 min.

The structures achieved with the FIB milling have smaller dimensions to those required in this work as can be seen by Figures 2.15-2.18. However, the effect of layering and the

quality of the machined structures requires further studies and this is a multistep process (requires an additional layer of Cr to be deposited on the surface).
For the machining of optical fibres the most commonly used techniques are the laser based ones (these will be discussed in following sub-section), lithography (as seen above, it is a multistep method), micromachining by dry etching (which is time-consuming and has low selectivity etching) and focused ion beam (FIB) (the main drawbacks can be processing time and high cost) [74].

2.2.2 Laser machining

In laser machining, there are considerable differences when machining with nanosecond (ns), picosecond (ps) or femtosecond (fs) laser pulses. If ns pulses laser is used, formation of melting and recast layers are an issue and quality is also limited due to the uncontrolled re-deposition of the melted material [70]. If ps lasers are used and parameters are not carefully optimised cracks and a heat affected zone in the surrounding area can result from high energy input and thermally induced stresses [70]. However, fs laser micromachining has been shown to have none of the detrimental effects associated with the longer pulsed systems and therefore can achieve exceptional results when used for drilling, milling and cutting [70]. It shows low heat input and the reduction of melt component of material removal [70].

When comparing fs and ns regimes, it is possible to achieve finer, more energy-effective and more material independent structuring with fs laser pulses. In fs laser processing, the non-linear absorption behaviour confines the induced changes to the focal volume making possible micromachining structures within the bulk of material and allows processing of materials transparent to the laser radiation. This provides a more precise method of material removal (compared to ns or ps pulsed lasers) and may not require any post processing [75] although another established route for processing is femtosecond laser machining followed by chemical etching [10] and [11].

The concentration of energy within a single pulse is sufficiently high to cause detachment from the material without any heat transfer to the surrounding material due to the short pulse duration [75]. The combination of this non-linear absorption, spatial confinement

and the translation of the sample relative to the focus volume allows complex, non-planar or three-dimensional, devices to be fabricated in a wide range of materials [76]. The main drawbacks of fs laser are the cost and relatively large size of the systems and that they need regular maintenance [76]. Also, some authors mention that another drawback of femtosecond laser machining is the slow process speed [77] although this could be circumvented to some degree in a practical process by using parallel processing with multiple beams from a single laser source [78], [79]. Some advances using ultrashort pulsed laser in a parallel processing configuration (with a spatial modulator) include the possibility of achieving a high throughput, flexible and precise processing of materials at industrial scales, as in the study mentioned in reference [78].

Femtosecond laser machining can be used for most materials, such as metals, semi-conductors and dielectrics (crystals glasses, ceramics) with micrometre and sub micrometre scale micromachining accuracies and negligible heat effects. Therefore, it is attractive for the processing of transparent materials and can enable three-dimensional micromachining. The mechanism of the femtosecond laser-matter interaction differs among metals, semiconductors and transparent materials [80]. This happens since metals absorb visible and near infrared light due to the large number of free electrons which does not happen for semiconductors and transparent dielectrics since the electrons are in bound states in these materials [80].

The most common laser system used for micromachining is the Ti:Sapphire laser with a titanium-doped Sapphire crystal as the gain medium and has a centre wavelength near 800 nm. A typical set-up comprises a microscope objective or a lens to focus the light on the sample and the sample is mounted on a three-axis translation stage where the position is scanned relative to the laser focus to perform the machining [81]. The first demonstrations of microstructuring in bulk glass using femtosecond laser pulses occurred in 1996 [81].

The topic of fs laser machining is broad due to the wide range of materials for which it is applicable. However, as in this work all the optical fibres used are composed of fused silica the review will be restricted to prior examples of fs laser machining in silica.

Nevertheless there is extensive literature on this as silica is one of the most studied materials due to its relatively simple composition and excellent optical properties [82].

2.2.3 Femtosecond laser machining of fused silica: optical breakdown

The focused pulses of the femtosecond laser are the key tool to modify the physical and chemical properties of materials in three dimensions at a sub-micrometer scale. These physical and chemical modifications depend on the laser parameters, the material composition and the focusing conditions that can be at the surface or within the bulk [82]. When the fused silica is exposed to femtosecond pulses at the surface, it undergoes breakdown, which is surface damage and/or material removal or ablation [82]. If fused silica is exposed to femtosecond pulses inside the bulk (usually more than tens of micrometres below the surface) there can be three different regimes according to laser fluence [82]:

- at low radiance (low fluence): it is possible to create local densification and colour centres creating an isotropic refractive index change [82]. This is suitable for waveguide fabrication [83].
- at intermediate irradiances: formation of nanogratings leading to anisotropic refractive index change and birefringence [82]. In this regime it is possible to use the femtosecond laser with association to the chemical etching process [83].
- at high irradiance, voids with a low refractive index core and a high refractive index shell are formed [82]. This is used for direct laser ablation [83].

The produced structure depends on laser parameters (such as pulse duration, wavelength, energy and repetition rate), on the material parameters such as bandgap and thermal properties and on the numerical aperture of the focusing objective. However, if the conditions are the same such as numerical aperture of 0.65, 100 fs pulses, at 800 nm in fused silica, it is possible to achieve three different morphologies changing only the incident laser energy: isotropic refractive index changes can be produced if the threshold energy is about 40 nJ to 150 nJ, a birefringent refractive index change can occur with an energy of about 150 to 500 nJ and voids can be formed from approximately above 500 nJ [81].

Laser-induced breakdown is a process where a transparent material is first transformed into an absorbing plasma by the strong laser pulse and the subsequent absorption by plasma of the laser energy causes heating that leads to irreversible damage to the target material. The nonlinear processes that cause breakdown are avalanche ionisation and multiphoton ionisation [84]. For non-UV wavelengths, the absorption mechanisms are different from absorbing materials (metals and semiconductors) and transparent dielectric materials (glasses and plastics). For these, absorption derives from nonlinear processes though laser-induced optical breakdown [84].

The optical breakdown induced in transparent materials by femtosecond laser pulses has been studied recently [81]. The femtosecond pulse focused inside the bulk of a transparent material causes the intensity in the focal volume to become high enough to cause absorption through nonlinear processes, leading to optical breakdown in the material. The absorption is strongly non-linear [85], and the breakdown can be localised in the focal volume inside the bulk of the material without affecting the surface. The localised permanent structural changes in the sample caused by the energy deposited in the material enable the micromachining of a three-dimensional structures inside the bulk of the glass [85]. For pulse widths from continuous wave to few tens of picosecond, the breakdown mechanism is avalanche ionisation, started from the seed electrons. But, for ultrashort pulse widths (less or equal to 1 ps) multiphoton ionisation determines the breakdown threshold behaviour. Also, ultrashort pulses have precise breakdown thresholds and negligible thermal diffusion [84].

In dielectric materials, such as fused silica, the conduction band is initially empty. Electrons from the valence band are transferred in the conduction band by nonlinear ionisation process to start the laser heating. The initial generation of conduction electrons occurs by the photo-ionisation process and this is dependent on the laser field and material. When the photo-ionisation is initiated the seed electrons excite into the conduction band and then absorb the laser energy [86]. When the kinetic energy of the conduction electrons exceeds a critical value, an avalanche ionisation process is initiated as the electrons further ionise other bound electrons in the valence band. The ionised dielectric medium then has a time varying electron density in the conduction band. The deposited laser energy is transferred to the lattice and thermomechanical relaxation and

ejection processes occur depending on the amount of absorbed laser energy density [81], [84], [86].

As mentioned previously, there is extensive literature regarding the femtosecond laser machining of fused silica [82] and some examples of femtosecond laser machining of bulk silica will be presented here.

In reference [83] the fabrication of shape-controlled microchannels in fused silica by femtosecond laser irradiation is presented. The author proposes the technique of femtosecond laser irradiation followed by chemical etching because of its simplicity and ability to produce three-dimensional structures with high aspect-ratios as an alternative to the conventional combination of photolithography and chemical etching. The authors mention this last combination technique has the limitation of the fabrication of two dimensional patterns on the surface and that to create a three-dimensional structure several layers of glass substrate must be processed individually and then fused together. This results in a complex and multi-step method. The method of combined laser and chemical etching is therefore maskless enabling a fast prototyping of new complex devices and the authors also state that the femtosecond laser-based technologies can be a solution for the fabrication of microfluidic channels integrated with optical circuits. The etching process is a combination of the diffusion of the acid into the irradiated region and the etching of fused silica that is in contact with the acid. There is a fast diffusion of acid into the irradiated region causing an etching of material along the diffusion path [83]. Usually this technique shows microchannels with a conical shape and the longer the channels are the more pronounced the conical shape. This can be related to the fact that the etching process is self-terminated due to the exhaustion of the acid in the microchannels and the difficulty to refresh it [83]. To overcome this undesired feature, it is possible to do the etching on both sides of the microchannel. Higher concentrations of acid are related to lower aspect ratio due to a fast lateral etching and delays the self-termination, increasing the channel length [83].

Reference [83] shows the irradiation of a reverse cone (with respect to the one normally obtained) with the femtosecond laser combined with chemical etching method obtaining microchannels with uniform and cylindrical shape. The authors used a second harmonic

of a cavity-dumped Yb:KYW oscillator that provides 350 fs laser pulses and up to 1 MHz of repetition rate. The irradiated line was produced using 150 nJ of pulse energy at 1030nm, polarisation orthogonal to the irradiated path, 600 kHz of repetition rate, using a 0.6 NA microscope objective beam diameter of about 1 µm and 1 cm/s translation speed. The etching process was performed in an ultrasonic bath of 20 % solution of Hydrofluoric acid (HF) in water for 3 hours at 35 ±1 °C. The Figure 2.20 shows the line produced with the laser and the after the chemical etching.

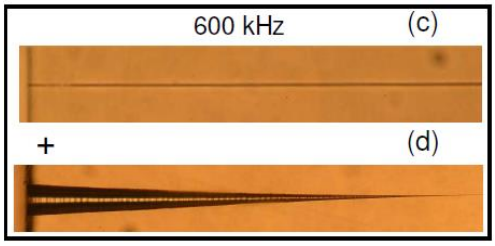

Figure 2.20 Microscope image on the line produced using the fs laser (top) and the microchannel obtained after the chemical etching with 1.5 mm (bottom) [83].

The compensation for the conical shape is shown in Figure 2.21. The authors introduced a modification to the method above by irradiating a different structure with a laser modified conical surface and also a straight line forming the axis of the cone [83].

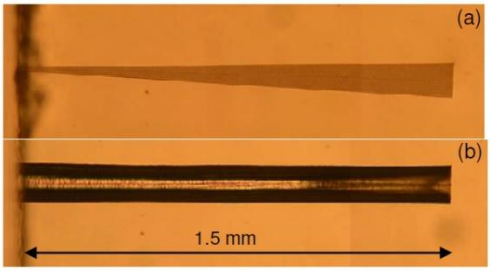

Figure 2.21 Microscope image of the conical spiral on the substrate and the etched microchannel with diameter of 100 µm and 1.5 mm length [83].

The authors noted some nano-cracks formed by irradiation of successive overlapping arcs and these contribute to the etching mechanism (provides paths for the acid diffusion). The spirals were done by keeping the laser in focus while the sample is moved by a suitable software driving a 3 axis air-bearing translation stage. The authors used 600 kHz of repetition rate, allowing 1 cm/s of processing speed but 1 mm/s was used for the conical spiralling to allow a higher control of the shape with the effective z speed lower than the tangential one (although it is not uniform it was calculated to be 20 µm/s) [83].

Improvements to these results were also performed by producing a longer channel of 4 mm, overcoming the main drawback of this technique (limited length of microchannels, 1.5-2 mm). Conical spirals were written back to back with each one 2 mm Figure 2.22 [83].

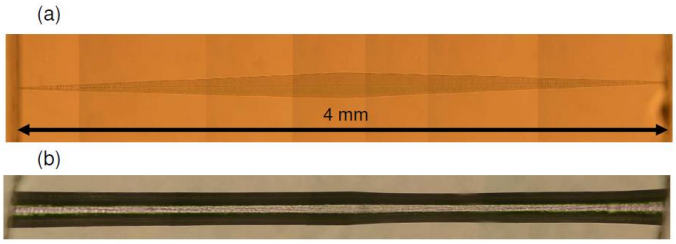

Figure 2.22 Microscope image of the double spiral irradiated above and below the cylindrical microchannel achieved by etching the above structure [83].

This method requires the use of chemical reagents (Hydrofluoric acid is particularly hazardous and requires specialist handling) combined with the femtosecond laser (multistep method). The shape obtained with this method improved with the conical inscription, but it requires complex structures to be performed with the laser. As a consequence, the result is not a homogeneous hole with the longest dimension obtained of 4 mm. Furthermore, the application of this method to optical fibres would be very difficult if, for example, a lateral hole through the fibre is required. Additionally, this would be particularly difficult for microstructured fibres since, for example, it would be difficult to predict how the acid would react when in contact with the fine cladding web which means the predictability of the process (or control of depth achieved) would be compromised.

Reference [87] presents a method for creating a three-dimensional optical splitter with U-grooves for fibre alignment, using fused silica glass and near-infrared femtosecond laser pulses. Also, writing of periodic patterns with the femtosecond laser such as submicron line and dot patterns inside the glass applicable to three-dimensional optical memory is presented. The authors used a Ti;Sapphire laser with 100 fs of pulse width, at 800 nm and 1 kHz of repetition rate. The laser beam was guided into a microscope and focused by 20× objective with NA of 0.42. The glass samples were placed on a computer-controlled stage and the average power of the laser was controlled with neutral density

filters. Using 1 kHz and 100 fs pulses, it was possible to obtain the optical splitter and the U grooves for the passive fibre alignment.

The line and the dot grating with the period of 2 µm were written inside the fused silica using a pulse energy of 320 nJ and a 50× microscope objective. For the U grooves (for passive alignment in the one input and two output ports of the splitter) a pulse energy of 30 µJ and a scanning speed of 500 µm/s were used. Each U groove has 126 µm width, 87 µm depth and 700 µm length (tolerance 0.5 µm). The roughness of the bottom surface was ±0.3 µm measured with a Surface Profiling System, Figure 2.23.

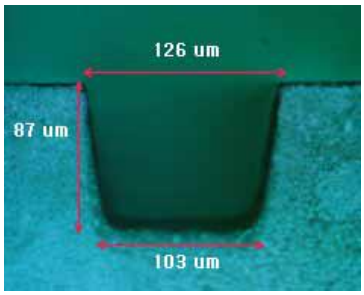

a)

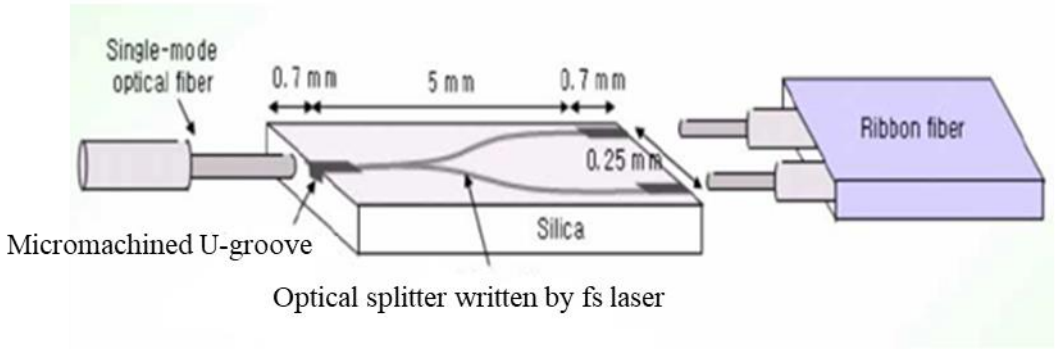

b)

Figure 2.23 a) Side view of the U groove machined with femtosecond laser pulses and b) adapted diagram of the U-grooved optical splitter [87].

This would allow the insertion and alignment of a single mode optical fibre and the waveguide of the optical splitter with engraved U grooves. The authors mention this technique does not require the use of optical fibre array blocks in the active alignment nor etching processes.

Also, the loss is less than 4 dB for two channels, including an intrinsic splitting loss of 3 dB (excess loss of 1 dB as the sum of the propagation loss of the waveguide, the

radiation loss of the 1 by 2 optical splitter and the coupling loss between the optical splitter and fibre) [87]. However, it is possible to see in Figure 2.10 a) that the U groove is not perfectly square.

2.2.4 Femtosecond laser machining of fused silica optical fibres

There are a number of reports on fs laser machining of silica based optical fibres, such as Bragg grating inscription [88], microstructuring of optical fibre [12] and for example the structuring of a Fabry-Perot interferometer [89],[90].

In reference [12] the authors present the experimental results of the femtosecond laser microstructuring of a solid core, single mode optical fibre. They produce micro holes with femtosecond laser pulses in a single step by moving an optical fibre in a pre-programmed structure. The method used was a water-assisted femtosecond laser back side etching of optical fibre. Circular and rectangular holes were drilled from the bottom. The fibre bottom was in contact with water allowing the water to flow into the hole by capillary force. Due to the fact that most of the debris was dispersed into the water, the effects of redeposition and blocking are greatly reduced, and long holes can be obtained [12].

The femtosecond laser worked at 785.5 nm with a pulse duration of 184 fs, 1 kHz repetition rate and an objective lens of 0.4 of numerical aperture. The pulse energy used was 10.4 μJ (higher than in this work, 2 μJ) and a speed of 100 μm/s was used (slower than in this work, 1 mm/s). The fibre used was a single-mode fibre stripped with a diameter of 125 μm [12]. The laser pulses were focused on the bottom of the optical fibre in water and the back side of the fibre was immersed in distilled water. A simplified scheme of this method can be seen in Figure 2.23 a). After the drilling began, the focusing point was moved towards the front surface step by step moving the sample in increments of z in the positive direction. In Figure 2.23 b) and c) it is possible to see the results of this method [12]. Clear, rectangular holes were achieved (100 by 20 μm), Figure 2.24. The authors claim that if fs laser machining in air was used then significant debris and molten material would be expected in and around the holes. Also, when using a higher pulse energy (higher than 10.4 μJ) the authors noticed damage.

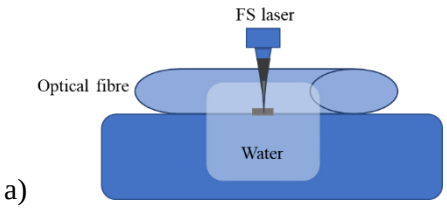

a)

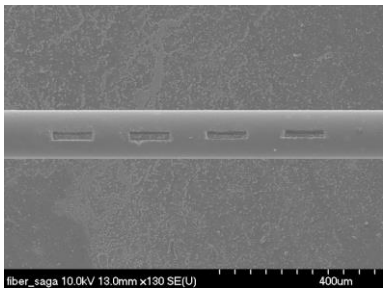

b)

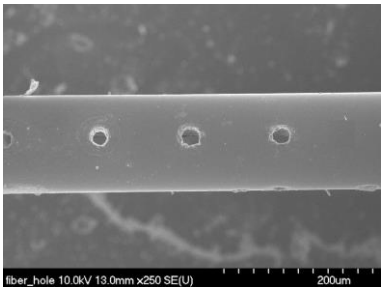

c)

Figure 2.24 a) Simplified scheme of the water assisted fs laser machining of the fibre based and adapted from reference [12] and results of the water assisted femtosecond laser machining of a single-mode solid-core silica optical fibre: SEM image of the optical fibre with b) rectangular shape and c) with a circular shape [12].

The authors present this method of using water assisted fs laser machining has potential for use in fabrication of micro-electronics [12]. However, this additional wet process would potentially add a significant level of complexity particularly if considering scale-up of the process.

Regarding the Fabry-Perot interferometer structure, the reference [89] shows a miniaturised inline Fabry-Perot interferometer fabricated on a single mode optical fibre (SMF-28) with a femtosecond laser. The authors present the fibre inline interferometer structure with an open cavity formed by one step micromachining, a micronotch. The fabrication of the device was done with a home integrated femtosecond laser with 1 kHz of repetition rate, at 800 nm and 120 fs. The maximum output of the laser was approximately 1W, but a combination of wave plates and polarizers were used to reduce the laser power to 20 mW and after this, several neutral density filters were used to reduce the laser power further. The laser beam was then directed to an objective lens with an NA of 0.45. The fibre was mounted in a computer controlled translation stage with 5 axes and resolution of 1 µm [89].

The interference signal of the fibre Fabry-Perot was continuously monitored and a tunable laser source was connected to one of the input ports of the 3 dB fibre coupler. The output port of the coupler was connected to the device under fabrication. The tunable laser scanned continuously though its wavelength range (1475-1575 nm) at the rate of 1 nm per step (controlled by the computer). The signal from the device at each wavelength step was recorded by an optical power meter and the fabrication finished when a well-formed interference pattern was achieved. A cavity of 30 μm length with 72 μm of depth (passing the fibre core) was produced and this was done close to the end of the fibre to avoid bending induced breakage. The device performed with a loss of 16 dB which is a result of the light scattering loss at the laser ablated surface and the non-perpendicular surface orientation regarding the fibre axis (meaning that the machined surface is not flat), as can be seen in Figure 2.25 [89].

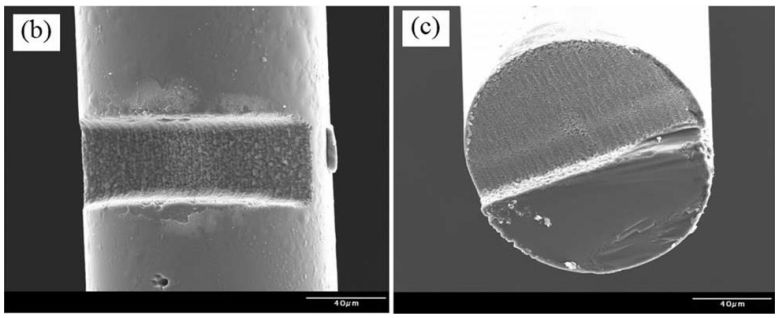

Figure 2.25 SEM pictures of the fibre inline Fabry-Perot interferometer (top view and cross section) [89].

The authors propose that the surface roughness can be reduced if a) the laser scanning steps are reduced, but this will increase the fabrication time and, b) the non-perpendicular surface can be minimised if the stages are adjusted. Nevertheless, the fringe visibility exceeded 14 dB which the authors considered adequate for sensing applications [89].

A further reference shows micro Fabry-Perot interferometers in silica fibres using the femtosecond laser machining [90]. This was shown in single mode and photonic crystal fibres. The laser used was an in house built chirped pulse amplified Ti;sapphire laser system with a high pulse energy (up to 100 μJ for 100 fs pulses) and a repetition rate of 1-5 kHz. The light was reflected from a dichroic mirror and focused to the silica fibre using an objective lens with 50× magnification and 0.65 NA. A light emitting diode was used to illuminate the sample so that the sensor after ablation can be monitored in real

time using a charge-coupled device camera attached to a phase-contrast optical microscope. A computer-controlled translation in 3 axis was used with 100 nm resolution in x, 125 nm in y and 7 nm in z. The experimental conditions were 800 nm wavelength with a pulse width of 120 fs and 1 kHz of repetition rate. The spot size was approximately 5 µm and the pulse energy was approximately 20 µJ. The fibres were mounted on the translation stage and the speed was 300 µm/second. A single pass exposure over an area of 80 µm by 30 µm was done and this was repeated several times to create the ablated Fabry Perot cavity [90]. With the SMF, Figure 2.26, the interferometric fringes are useful for sensing but the fringe visibility is low.

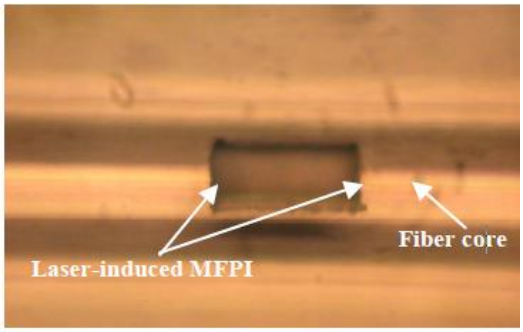

Figure 2.26 Optical micrography of micro Fabry-Perot interferometer on single mode fibre presenting 80 µm length of cavity [90].

The possible cause for this is the surface of the cavity that shows sputtered debris that adhered to the surfaces machined, contributing to rough surfaces and light scattering. However, the authors mention that optimizing the laser ablation process using the etching technique may present a solution for this problem [90].

The results with the PCF, Figure 2.27 present slightly better high-quality fringes than those for SMF fibre with the fringe visibility of the PCF based micro Fabry-Perot interferometer showing improvement by a few dB. This may happen due to the fact that: a) the PCF is entirely made from undoped fused silica that may reduce the sputtered debris therefore decreasing the scattering of light and b) due to the cladding of the PCF that is composed by a two dimensional photonic crystal structure with air holes distributed along the fibre that allows the heat and pressure from the laser ablation to diffuse quickly, which leads to the reduced thermal damage on the cross-section of the fibre [90].

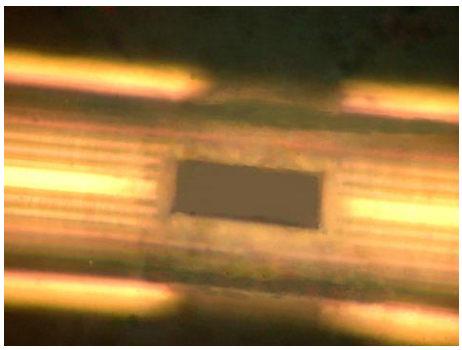

Figure 2.27 Optical micrography of micro Fabry-Perot interferometer on PCF fibre presenting 75 μm length of cavity [90].

Regarding the responses of the sensor, the PCF based micro Fabry-Perot interferometer showed smaller strain sensitivity (0.0045 nm/με) than the SMF one (0.006 nm/με) (in accordance with the theoretical analysis) and both sensors show a high strain sensitivity and low temperature sensitivity. In this reference, some advantages of microstructured fibre was presented for a better quality of fringes for Fabry-Perot interferometer applications. The dimensions achieved were of 80 μm by 30 μm with 80 or 75 μm depth (small structures machined).

Other work reports inscribing of slots on the cladding of a Hollow Optical Fibre (HOF), with the femtosecond laser to obtain stronger mode coupling and wider bandwidth [88]. The HOF used in this experiment had a 6 μm air hole diameter, a ring core surround with a 2 μm thickness and a 125 μm cladding diameter. The fibre cladding was ablated using a femtosecond laser in a systematic way to produce periodic corrugations. The laser used was a Ti:Sapphire laser with a centre wavelength of 785.5 nm, 184 fs of pulse duration and 1 kHz of repetition rate. The average power was 3.59 mW and a microscope objective lens of 20× with 0.4 of numerical aperture was used. The slots were done using a point-by-point method and a corrugated fibre with 15 slots was fabricated in the centre of a 1 m long fibre. The dimensions of the corrugations were controlled such that a pitch of 550 μm and a depth of 13 μm were fixed while the width could vary: 30, 40, 80, 90 and 150 μm [88].

The diameter of the focused laser was 5 μm and the single scan of the laser beam ablated the fused silica cladding to a depth of 6.5 μm. Linear corrugated LPGs were inscribed perpendicular to the fibre axis using a motorised laser beam scanning system. The number of scans used precisely controls the width of the slots. The authors noted an

interesting aspect: the depth of the corrugation in the hollow core fibre was significantly shallower than those of conventional on-side corrugated single mode fibre, LPG, which could be attributed to the unique stress distribution in the hollow optical fibre with the air holes (in contrast to the solid SMFs), Figure 2.28 [88].

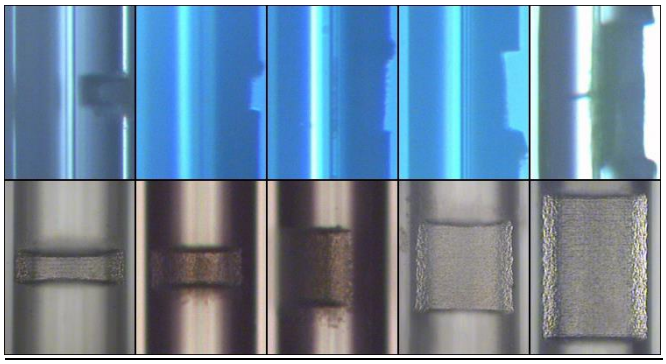

Figure 2.28 Top and side views of the corrugated HOF: 30. 40, 80, 90, 150 μm respectively from the left to the right [88].

The slots have roughness on the surface due to the non-flat top beam mode and relatively small beam area of the femtosecond laser and it is noted that further optimisation of the laser parameters and the scanning mechanism is needed to reduce surface roughness and scattering loss [88].

It was possible to fabricate a broadband LPG on a HOF by using femtosecond laser pulses to achieve a broad bandwidth and a strong band rejection efficiency achieving insertion losses of less than 1dB, a FWHM of up to 190 nm and a maximum coupling strength of 8.5 dB. Therefore, the corrugated HOF-LPG has potential for wide-band rejection filter applications in communications due to their strong mode coupling with flexible control of the rejection range [88].

This work is a good example of the machining with the femtosecond laser on a hollow core fibre, since the LPG were achieved and the machining was well defined. However, the fibre geometry is different and much less complex than that of the NCF and the purpose of the machining process is also different in that the aim was not to reach or access the hollow core.

More generally, the previous work reported above shows that fs laser machining is a promising method for modification of silica based optical fibres. The geometries reported with femtosecond lasers are holes (small dimensions), grooves or they are performed in fibres with a different geometry and guiding properties to the NCF used in this work. Hence in this work, fs laser machining of hollow core silica NCF is explored and a different machining strategy was proposed to the most commonly used percussion drilling techniques without the use of chemical etching. The aim was to avoid strongly tapered structures, as seen in the previous reference [83] and to provide a more flexible and controllable route to achieve a very clean (i.e. without debris) and well-defined structure in NCF whilst preserving the underlying microstructure of the fibre. Additionally, the aim was to provide a method to precisely control both the depth and shape of the machined structures where the geometry is readily controlled by the laser scanning strategy. In the next Chapter, the femtosecond laser methodology will be presented and the initial tests regarding machining parameters will be reported.

2.3 Summary

In this literature review, an overview of the microstructured optical fibres with emphasis on NCF was presented. It was pointed out the impact of the geometry on the properties of NCF and the reasons why this type of fibre is attractive for a number of applications (as for example the low dispersion). A general overview of the methods of machining glass was presented and as well as the femtosecond laser machining of bulk fused silica and optical fibres. Previous work reporting the use of novel laser machining techniques to access the core of microstructured optical fibres will be presented in Chapter 5 to provide a direct comparison with the results.

Chapter 3 – Femtosecond laser methodology

3.1. System Characterisation of Femtosecond Laser

The femtosecond laser used for the laser machining experiments throughout this work was a Hurricane from Spectra-Physics. It has an operation range from 780 nm to 820 nm, a maximum theoretical pulse duration of 130 femtoseconds (fs), an output power of 910 mW and a maximum of 5 kHz of repetition rate. The specified beam diameter at the laser output is 6 mm as in accordance to the manual. Since the laser system was already in use, a bespoke laser set-up was constructed to perform both a detailed parameter investigation on bulk silica and subsequently perform laser machining of features on solid core silica optical fibres and hollow core negative curvature silica optical fibres. This new laser set-up consisted of the implementation of a new beam path, to allow the independent operation of the laser between separate experiments with the minimum of interruption to the existing experiment, with the contribution of Dr Debaditya Choudhury, from Institute of Photonics and Quantum Sciences.

3.1.1. System set-up

From the laser output to the machining lens, the beam passes through several optical components to both guide and condition the beam, Figure 3.1.

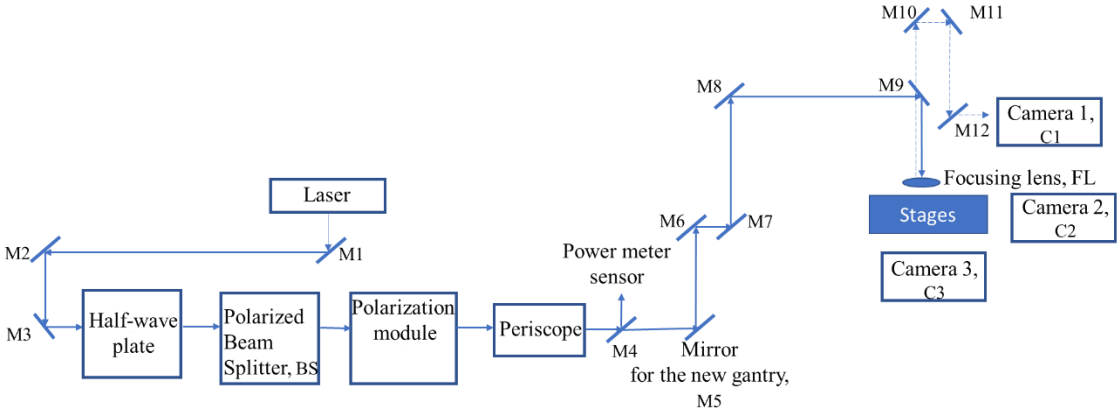

Figure 3.1 Simplified scheme of the femtosecond laser set-up used in this work. The arrows show the beam direction and the dashed line shows the reflected light from the beam to the camera 1.

Three mirrors guide the beam to a half-wave plate and polarised beam splitter (BS) for power adjustment using a servo controller (Thorlabs) to rotate the waveplate. Following power adjustment stage, the beam passes through a polarisation control module before entering a periscope RS99/M (Tip/Tilt Rotation Beam Steering Assembly, Metric, Thorlabs). A flip mirror, M4, allows the beam to be diverted to a Thorlabs S320C sensor connected to the power meter.

Another flip mirror, M5, is positioned to allow the independent operation of two optical beam paths. The beam passes through four more mirrors that direct the beam to an independent gantry. Ring-actuated SM1 Iris Diaphragms SM1D12D (Thorlabs) are used to assist the alignment of the laser beam, therefore they are placed between mirrors along the entire set-up. Opening or closing the iris aperture can help to identify if the beam is centred, with the help of a cage alignment target with an IR fluorescing alignment disc. The alignment of the laser is critical for the machining process, so it was performed prior to any experiments. It was also checked regularly by observing the focal position on the Camera 1, C1 or/and with an IR card that allows visualisation of the beam.

At the end of the optical path there is a lens C11TME-B with an effective focal length of 6.24 mm, 0.4 of numerical aperture (NA) and anti-reflecting coating (AR) from 600 to 1050 nm to collimate or focus the beam (Thorlabs). The mirrors used in this set-up are PF10-03-P01 protected Silver Mirror, 6.0 mm Thick, of 1" diameter (Thorlabs).

There are three cameras positioned to monitor the machining process: DCC1545M High Resolution USB 2.0 CMOS, 1280 × 1024, Monochrome Sensor (C1, C2 and C3). There are also:

- two 6.5× Zoom Lens with 12 mm Fine Focus MVL6X12Z, and two 1.33× Extension Tube for 6.5× with two C-Mount Adapter for 6.5×;
- the lens from which the focal position is found is a 150 mm focal length one with 1" diameter and anti-reflection coating from 400-700 nm (AC254-150-A, Thorlabs) with 12× Zoom Lenses MVL133 and 12× Zoom Lens Extension Tubes MVLCMC (Thorlabs).

The sample was fixed on the motorised stages (Aerotech, Inc) controlled by a computer via NView software with resolution 0.1 μm in x, y and z and an acceleration of 120 mm/s^2.

To perform the machining with the femtosecond laser custom G Code was written. Examples of the G Code use can be seen in Appendices and will be referred when appropriate. To locate the focus of the laser on the surface of the sample, the reflected beam from the sample passes through the back side polished mirror, M10 and M11 (PF10-03-P01 protected silver mirror of 1" diameter Thorlabs) directly above the sample and is steered to Camera 1, C1, DCC1545M, Figure 3.1. In Figures 3.2, photographs of the set-up including labels that allows the correspondence to the diagrams are presented.

a)

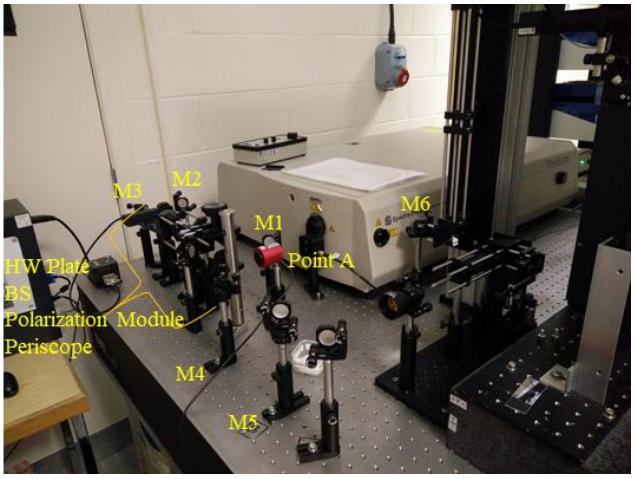

b)

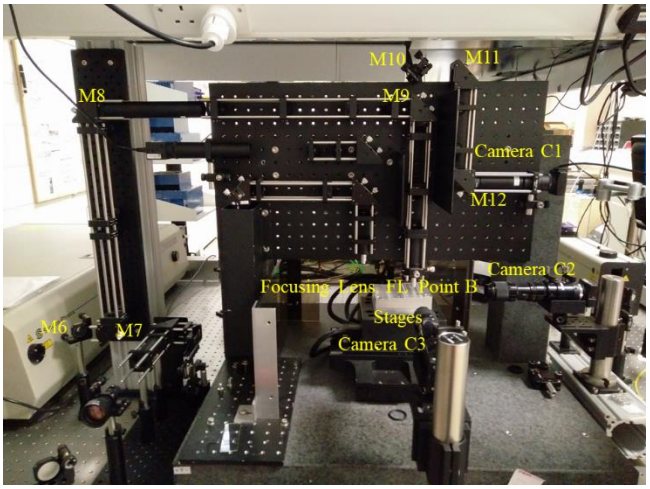

Figure 3.2 The experimental set-up: a) the femtosecond laser is shown along with the optical components such as the polarisation module and periscope and b) the new gantry. The various optical components are marked with abbreviations or names and Point A and Point B refers to the points were the power was measured.

The power at the machining end of the optical path and at the beginning of the optical path was measured with a PM100D power meter (Thorlabs). The sensor used at the end of the optical path was a S122C (Thorlabs). An overall loss of 30% of power through the optical components was measured, between point A, mirror M4 and point B, at the end of the optical path, after the machining lens. This loss was found as the ratio between the power measured in point A and point B. This power loss was measured regularly throughout the experiments to ensure that the power at the sample (used for machining) was well defined.

The cameras 2 and 3 were positioned in such a way that would allow the visualisation of the direction of the negative curvature fibre in a posterior application, this means a lateral view and a front view being the top view given by Camera 1. However, this idea was very difficult to realise and it was not developed further. Instead the fibre was analysed after the machining and not during the process. The reflected laser light is used to find the focal positions for the processing and it also allows for process monitoring. Since the beam is a Gaussian beam, if the light reflected presented a well-defined circular beam shape this means the focal position was found, Figure 3.3.

a) 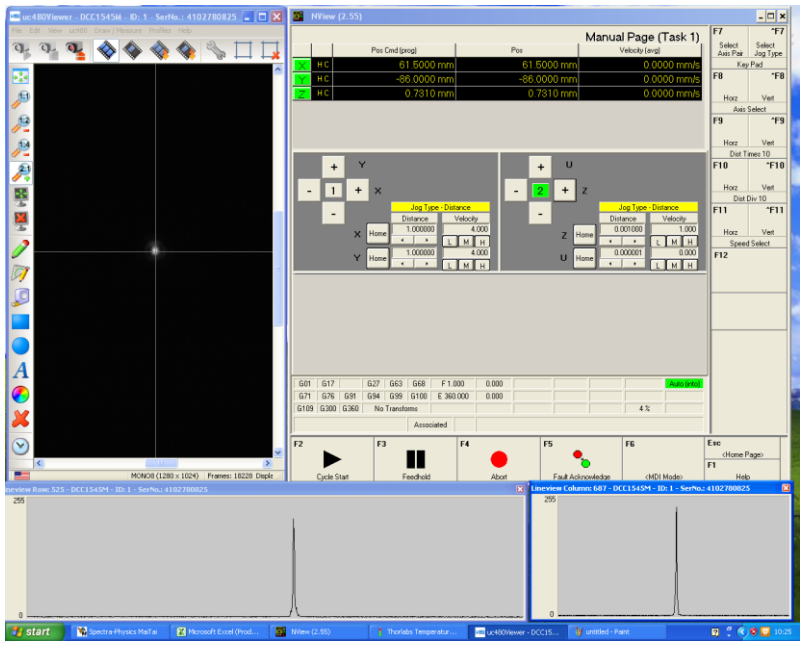

b) 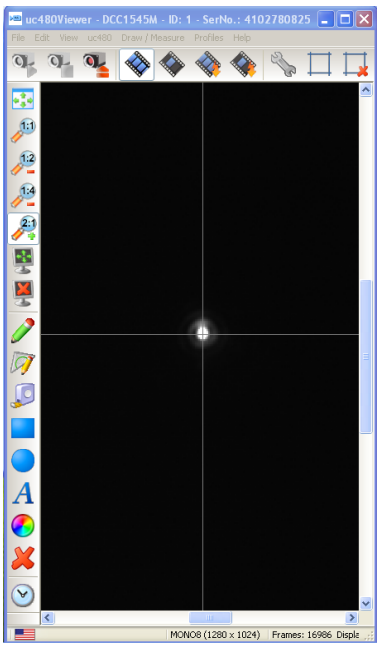

Figure 3.3 a) Print screen of the controlling computer monitor, showing the reflected beam light spot at the left and the NView program at the right. The graphs shown in the bottom part of the monitor show the peak that proves the laser was on focus. If the z position moves away 1 µm the peak height will decrease and b) print screen showing the reflected beam spot with different camera settings to be more evident the focal position (well defined circular beam spot).

There are other methods to find the focal position, since it is a crucial step during the machining. The following will present them and explain the use of the method chosen. The focal position is the position which is associated with the minimum waist diameter and some conventional methods for finding this position can be:

a) The use of a guide beam and requires the adjustment of the specimen's position to minimise the waist of the beam in z -scan experiments. This method is limited to simple fabrication processes that do not need high accuracy;
b) The modification of the specimen to find the focal position such as placing the sample on a worktable and performing test spots on the sample surface while adjusting the worktable height or measuring the beam to detect the electromagnetic field;
c) The use of a confocal system or other auto focusing systems to measure a curved surface.

However, the signal processing of these methods is difficult and requires an auxiliary laser or confocal sensor [91].

In reference [91] an alternative method, simple, with high accuracy and similar to the one used in this work is presented. The authors mention a feedback system with a charge-coupled device CCD camera, a beam splitter and a mirror to focus a laser beam onto the surface of a work piece. The method for collecting data involves the use of an optical system that allows positioning of the specimen at the focal spot (i.e. the position corresponding to the smallest part of the laser's spot), therefore the system proposed in this paper is called focus finder [91].

For the calibration method applied to the focus-finder system to determine the spot size in the focal position, a mirror and a quarter-wave plate were placed in parallel to the beam splitter surface (opposite to the beam profiler) and a blocking plate is installed at the focusing lens on the side of the specimen (to prevent beam reflection). The reflected beam is measured by the CCD camera and inferred to have a beam size corresponding to the focal position (D_{focus}). After this measurement, the blocking plate installed near the focusing lens is removed and reinstalled at the mirror side, so that the beam reflected from the specimen is received by the beam profiler. The specimen is moved until the beam size is equal to D_{focus} (this corresponds to the focal position) [91].

The authors refer that this method, when compared to the conventional ones has advantages such as the simple implementation, the fact that the specimen can be easily positioned at the focal position, the scan amplitude is adjustable and the CCD camera can also be used to monitor the laser beam profile. This one is important because changes in the laser beam can affect the machining quality. This method works because the sample surface does not work as a mirror, so the reflected beam is not identical to the incident beam, and on the CCD is obtained the actual profile of the reflected beam from the specimen. The alignment is also crucial in this method because it affects the results. However, one disadvantage of this method is that it is difficult to measure the diameter of the laser beam accurately, since there is an inaccuracy of the laser beam when using a CCD camera. Since the laser beam is gaussian, the laser beam size can depend on the laser power. Increasing the laser power, decreases the irradiance of the beam at the edges. The beam diameter is the distance across the centre of the beam for which the irradiance or intensity equals to $1/e^2$ and the spot size is defined as the radial distance from the central point of maximum irradiance to the point at which the irradiance decreases by a factor of

$1/e^2$. So, to measure with accuracy, it is important that the CCD camera is adjusted to the optimal laser power [91].

Therefore, in this thesis, the diameter of the laser beam was measured using the beam intensity profile and it is explained in the following section.

3.1.2. Beam diameter and alignment

This characterisation was done measuring the beam intensity profile. The laser power was measured with a detector with increments of 0.2 mm in x distance, maintaining the same z and y position. After that, the power was normalised and a Gaussian fitting was performed to the data.

The beam radius was defined as the distance from the beam axis where the optical intensity drops to $1/e^2$ (13.5%) of the value on the beam axis. After applying the fitting of the intensity profile of a Gaussian beam, (see equation 3.1) [92]:

$$I(r) = I_0 \exp\left(\frac{-2r^2}{w^2}\right) \tag{3.1}$$

where $I(r)$ is the intensity measured at $1/e^2$, I_0 is the maximum beam intensity at r=0, r is the beam radius and w is the beam radius at which the amplitude is (equation 3.2):

$$I = I_0 \exp(-2) \tag{3.2}$$

The diameter calculated was then 7.58 mm.

It was then possible to achieve the w_0, the beam waist diameter, the diameter of the laser spot on the sample using equation 3.3 [93]:

$$2w_0 = \frac{4\lambda}{\pi} \times \frac{F}{d} \tag{3.3}$$

Where λ is the wavelength, F is the effective focal length and d is the laser diameter at the microscope objective. Since the clear aperture is 5 mm, smaller than the diameter of the beam which was 7.58 mm, d is 5 mm, because the aperture in this case defines the

diameter. Being so, the beam waist after the final focussing lens, Figure 3.1, was calculated as 1.26 μm (with equation 3.3).

3.2. Laser Parameter Investigation

To find the optimal parameters for machining slots into the fibre, initial trials were carried out on fused silica microscope slides. Investigations into both laser parameters and scanning strategies were carried out prior to the fibre machining.

The scanning patterns were achieved by moving the stages (and consequently, the sample) relative to the fixed laser beam. Focal position was also controlled by raising or lowering the sample relative to the focussed laser beam. All the experiments were done with a 5 kHz repetition rate.

3.2.1 Fused silica

In this work, fused silica was used as a starting point since the fibre are made of fused silica. The fused silica used was Corning 7980, HPFS, standard grade. The data regarding the fused silica can be found in reference [58]. Fused silica is one of the most studied materials due to its relatively simple composition and excellent optical quality. When the fused silica is irradiated by femtosecond pulses focused at the surface, fused silica undergoes optical breakdown resulting in damage and/or material removal via an ablative process [82].

a) Focal position

As mentioned previously, one of the important aspects when machining with a femtosecond laser is to accurately determine focal position in relation to the sample surface. Scanning lines across the sample whilst varying the axial position of sample relative to the laser beam (z position) was used to determine to focal position (see Figure 3.5). This study was done in collaboration with Jacopo Siliprandi of the Institute of Photonics and Quantum Sciences.

Initial tests to determine the optimal speed for the z position experiments were carried out on fused silica glass slides. Four sets of lines (1 mm long) were machined at speeds of 0.5, 1.0, 1.5 and 2 mm/s and a repetition rate of 5 kHz, 0.1 µJ pulse energy and at a wavelength of 795 nm. When the speed is increased the machined lines become less marked, due to the decrease of the pulse overlap (explained in next section), hence the speed chosen for the z position experiments was 0.5 mm/s.

Using the optimal 0.5 mm/s speed, a parameter map was produced with different pulse energies. Lines were marked onto the silica surface as the z position was changed. As the z position is translated there is point at which marking begins on the surface (when the spot size is small enough to provide sufficient fluence for ablation) as the z position is continually changed the sample moves through the laser focus and then out of focus and eventually the fluence drops below the ablation threshold. The number of lines were counted from the point at which lines first become visible (Z1) to where they disappear (Z2). The powers used were 0.500, 0.600. 0.700. 0.800, 0.900 mW, corresponding to 0.1, 0.12, 0.14, 0.16 and 0.18 µJ pulse energy. 200 lines above and 200 lines below were performed, with 0.015 mm above and 0.015 mm bellow and a total depth of 0.03 mm. The lines were long as 1 mm and the distance between the lines was 50 µm. In Figure 3.4, it is possible to see a diagram illustrating the different places of focus, and in Figures 3.5 and 3.6 two sets of the same pulse energy are shown. The G Code example of this experiment can be found in Appendix A.

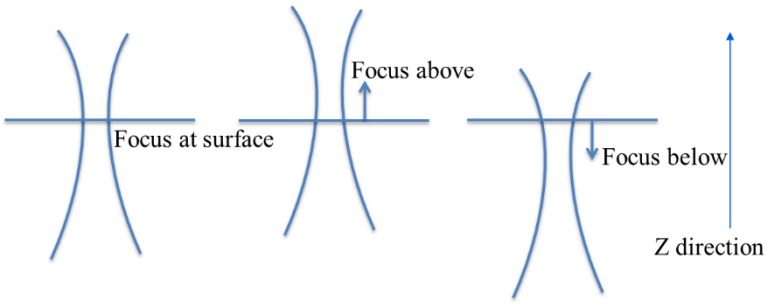

Figure 3.4 Diagram illustrating the different places of focus in this experiment.

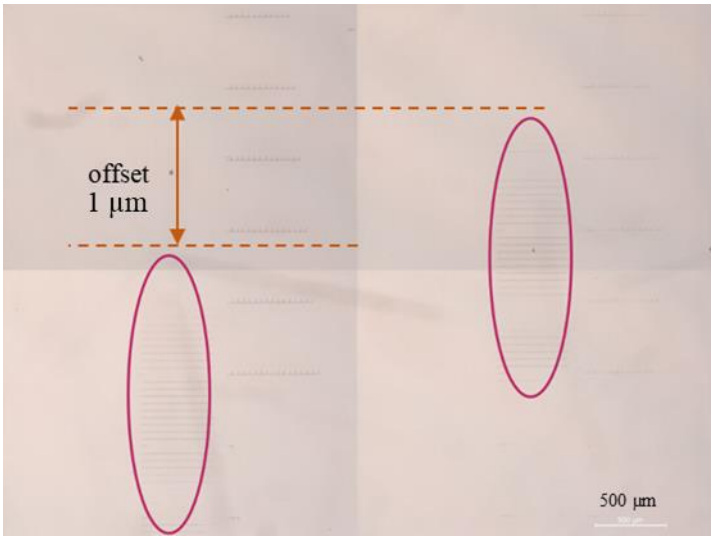

Figure 3.5 Two sets with the same pulse energy: 0.1 µJ, and marks beside the sets. The ellipses highlight areas where the lines are visible.

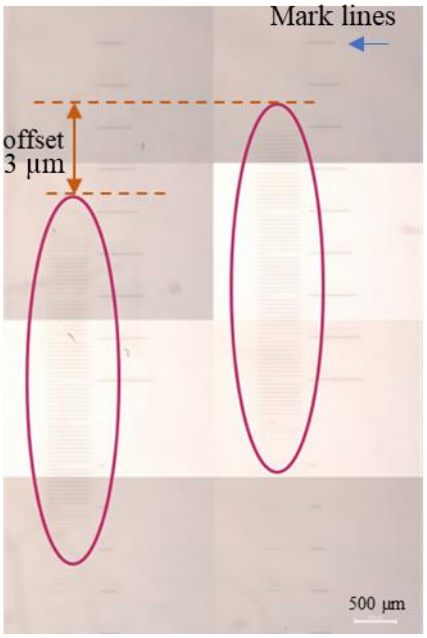

Figure 3.6 Two sets with the same pulse energy: 0.18 µJ, and marks beside the sets. The ellipses highlight areas where the lines are visible.

The sets were done in duplicate with no change in power and the same G Code yet it was possible to see an offset between the sets of lines: this offset was 1 µm in the case of the 0.1 µJ set, Figure 3.4 and 5 µm in the case of 0.16 µJ (values referring to the Z1 position, initial counting of lines)

A likely cause for this offset is the thermal effects on the stages (due to continued movement during several minutes for each set of lines) causing a small expansion in both the stages and the sample due to the mechanical movement. The reference [94] mentions that the temperature profiles on machine tools during the machining processes can be an issue and that in the case of cutting, when the cutting velocity is increased, the temperature of the contact zone, work piece and tool also increases, being this referred to a contact machining. However, if we plot the delta Z against the pulse energy we confirm that increasing energy increases the distance between Z1 and Z2, Figure 3.7.

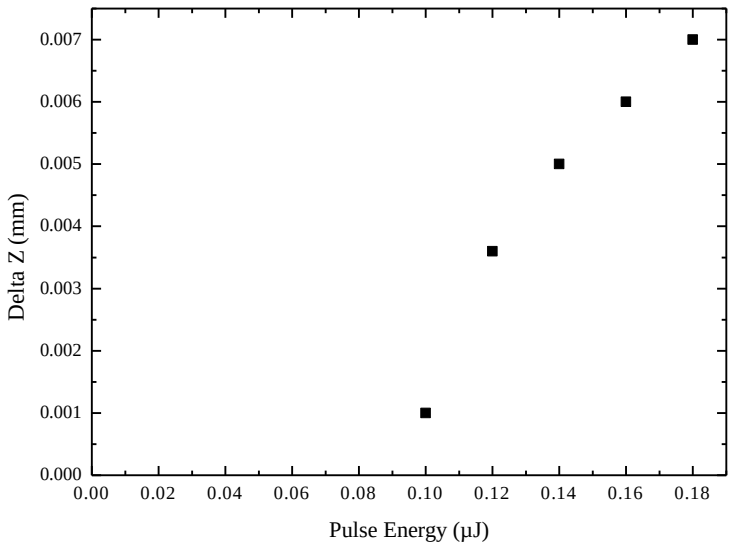

Figure 3.7 Delta z against the pulse energy.

It is therefore possible to conclude that pulse energies below 0.1 µJ of should not be used as the machining is not well defined at that power. Also, the thermal effect of the stages should be considered during subsequent trials.

b) Fused silica slides study

Since the stages are motorised and controlled by the computer via NView software bespoke G Code was machined to machine the samples. More information about the G Codes used can be seen in Appendix B.

To establish appropriate parameters for machining slots into a silica fibre a study of the laser inscription patterns on flat fused silica slides was carried out prior to the fibre

inscription. The pattern consisted of a square with horizontal and vertical lines, to scan over a determined slide area, Figure 3.8. The typical spacing used is 0.5 µm in both x and y axis.

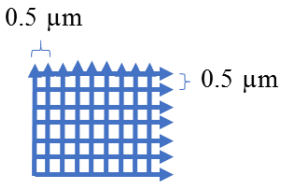

Figure 3.8 Simplified example diagram of the scanning pattern.

In this study, several conditions were considered such as the number of passes performed by the laser (referred to as "*layers*" in the Figure caption, Figure 3.9), speed of scanning and power. To do the layers, the focal position was not changed in these experiments, meaning the focal position was the same as for the first layer. The layers were employed to enable structures with the desired depth to be generated by repeating the scanning procedure several times [81]. All the trials were done with a repetition rate of 5 kHz. The stages have a removable part of metal and the slide was glued on this part with nail varnish which facilitated the removal of the slide from the stages (using acetone). The results can be seen in Figures 3.9 -3.12.

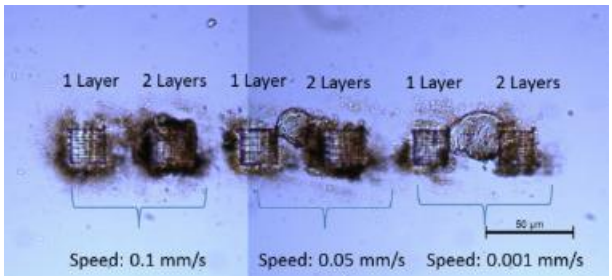

Figure 3.9 Square patterns machined into a fused silica glass slide at 1.5mW, pulse energy of 0.30 µJ at different speeds: 0.1, 0.05 and 0.001 mm/s with a spacing of 5 µm between adjacent lines in the scanning pattern.

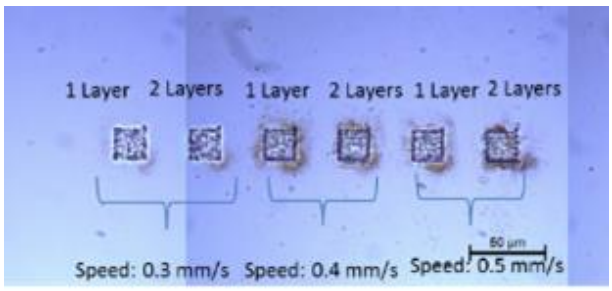

Figure 3.10 Square patterns machined into a fused silica glass slide at 1.5mW, pulse energy of 0.30 µJ at different speeds: 0.3, 0.4 and 0.5 mm/s with a spacing of 5 µm between adjacent lines in the scanning pattern.

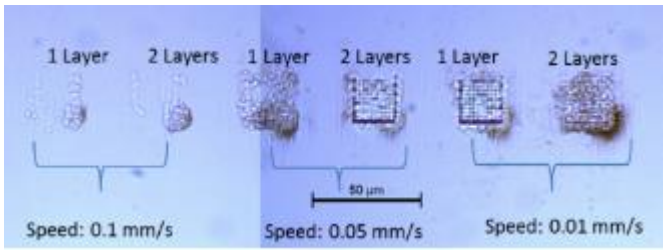

Figure 3.11 Square patterns machined into a fused silica glass slide at 1.3mW, pulse energy of 0.26 µJ at different speeds: 0.1, 0.05 and 0.01 mm/s with a spacing of 5 µm between adjacent lines in the scanning pattern.

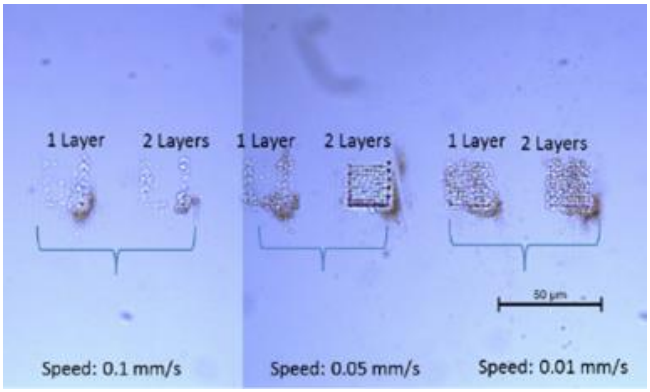

Figure 3.12 Square patterns machined into a fused silica glass slide at 1.0mW, pulse energy of 0.20 µJ at different speeds: 0.1, 0.05 and 0.01 mm/s with a spacing of 5 µm between adjacent lines in the scanning pattern.

Analysis of Figures 3.9-3.12 indicates that 0.30 µJ is the most appropriate energy to machine the squares, since below that value the pulse energy is not sufficient to define the square into the glass.

The squares were also machined with different speeds and for each speed the number of layers was investigated. With a lower speed, higher damage of the material is achieved as we compare Figures 3.10 and 3.11, for the same power (pulse energy) with different speeds. This damage is observed in Figure 3.10 as the squares are not perfectly defined in the fused silica glass, showing undesired effects around the machined structure.

The scanning speed is directly correlated with the pulse overlap. For scanning speeds of 0.1, 0.05 and 0.001 mm/s the corresponding pulse overlap is 98.42%, 99.21% and 99.98%. For scanning speeds of 0.3, 0.4 and 0.5 mm/s the correspondent pulse overlap is 95.24 %, 93.67 % and 92.08%. In Figure 3.13, a simplified scheme of the pulse overlap concept is shown where the spot to spot distance d_{spot} is calculated as the scanning speed divided by the repetition rate and the spot overlap (*SpotOverlap*), equation 3.4 [95]:

$$SpotOverlap = \left(1 - \frac{d_{spot}}{2w}\right) \times 100 \tag{3.4}$$

Where w is the the beam radius.

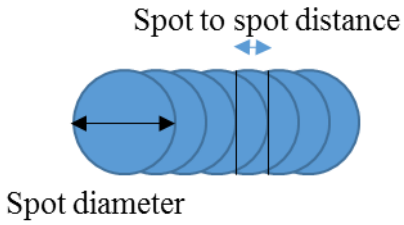

Figure 3.13 Scheme of the pulse overlap where the dots represent the laser beam spot.

The scanning speed influences the overlap of the pulses, for higher speeds, the pulse overlap decreases and the pulses are more separated. For low speeds, the pulse overlap increases being almost coincident [81]. In reference [96] it is possible to find 99.9% overlap. In this paper, the laser used was a regenerative amplified Ti:Sapphire femtosecond laser operating at 800 nm with a repetition rate of 200 kHz and maximum average power of 400 mW (2 µJ pulse energy maximum). The pulse duration was 160 fs and the beam was focused 450 µm inside fused silica using a microscope objective of NA 0.50. The sample was also translated along three orthogonal axes by computer controlled stepping motors and the writing speed was 0.1 mm/s [96]

In reference [83] where the fabrication of shaped-controlled microchannels in fused silica using a femtosecond laser and chemical etching is performed, it is possible to find a pulse overlap of 98.33%. The laser used was a diode-pumped femtosecond ytterbium and a second harmonic (515 nm) of a cavity-dumped YB-KYM oscillator providing 350 fs laser pulses was used. The pulse energy used was 150 nJ, at 600 KHz of repetition rate and the speed used was 1 cm/s. The microscope objective had a numerical aperture of 0.6 and the beam diameter was about 1 μm [83].

It is possible to find different machining parameters for different applications, in the literature. Previous experiments carried out with fused silica slides used pulse energies of 10 μJ and above [97]. In this work pulse energies above 0.30 μJ were not tested, since it was possible to see considerable thermal effects for 0.30 μJ at the slowest speeds, Figure 3.4. The equipment used in [97] was also a Ti:sapphire with 5 kHz of repetition rate, with a central wavelength of 800nm and with 150 fs of pulse duration. However, the machining was performed in a different way, doing parallel rows of discrete small holes as opposed to a milling modality used here where there is a high pulse-to-pulse overlap.

Other work with fused silica has been carried out. In reference [98] the authors use a femtosecond laser to fabricate silica molds and patterned surfaces combined with a chemical etching step and demonstrate that femtosecond laser processing of fused silica allows high-resolution, high aspect-ratio silica molds which are interesting for microsystems. The process consisted of five steps: laser exposure, mould chemical etching, making of the release coating, mould filling, and curing and release of the molding. In the laser exposure step, the substrate is exposed to low pulse energy, typically from 120 to 220 nJ. The focusing objective had a numerical aperture of 0.45 and these conditions were considered because no ablation occurs, instead internal modifications on the silica take place leading to a localised enhanced susceptibility to wet chemical etching. The substrate was translated in the three-dimensions under the laser beam and the patterns were created by stitching laser affected regions together. Two different laser systems were used: to produce holes an oscillator (t-Pulse 500, Amplitude Système based Yb-KGW crystals) emitting 550 fs pulses at 9.4 MHz and at 1030 nm was used. An acousto-optic modulator (AOM) was used to reduce the repetition rate. The repetition rate used was 860 kHz, the specimen was mounted on a Physik-Instrument stages and the scanning

speed was 1 mm/s. To produce more complex structures such as microchannels carved out from the glass surface and trenches a Ti: Sapphire emitting 100 fs pulses at 250 kHz was used. The writing speed was 2 mm/s and the energy used was 200 nJ per pulse. The specimens were also mounted on a translation stages and moved under the microscope objective.

In reference [99] a regeneratively amplified Ti:sapphire femtosecond laser was used to create an optical birefringence in an isotropic glass medium. The authors used fused silica and borosilicate glass. The laser used was a Ti:sapphire femtosecond pulsed laser (Spectra-Physics, Hurricane), with 125 fs pulse width (full width at half maximum) and 1 kHz of repetition rate. The pulse energy was adjusted with the combination of a half-wave plate and a thin film polarizer and the reduction of energy was achieved using neutral-density filters to avoid photo-damage to the polished glass plate. The pulse energy used was between 0.45 and 0.9 μJ. The laser was focused inside the glass with 3 μm diameter and using a microscope objective of 0.4 NA and 20×. There was a monitored x-y translation stage with linearly controlled motion along the z direction to adjust the focus of the laser inside the glass and the laser was focused 600 μm below the surface of the glass plates. The polarisation direction of the beam was fixed and the sample was rotated with respect to the polarisation directions of the laser beam.

The results presented here are in accordance with the literature, being that the better results are achieved for a scanning speed of 0.1, 0.05 and 0.001 mm/s corresponding 98.42%, 99.21 % and 99.98% pulse overlap when compared to 0.3, 0.4 and 0.5 mm/s (once these present less defined squares on fused silica). However, it is possible to see considerable thermal effects for 0.30 μJ at the slowest speeds with the squares having a surrounding region which is not very defined. These results show a square machined using a scan pattern with horizontal and vertical lines and these scanning lines are clearly visible in the resultant surface. To achieve a more efficient ablation of the material, *i.e.* an even and smother structure, it was proposed to decrease the distance between adjacent lines in the scan pattern. In the next set of experiments, the distance between scan lines was reduced from 5 μm to 2 μm, both in x and y directions, Figures 3.14 and 3.15.

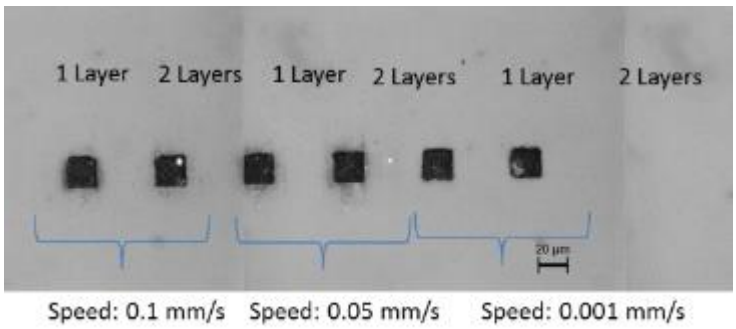

Figure 3.14 Square patterns machined in fused silica glass slide at 1.5mW, 0.30 µJ at different speeds: 0.1, 0.05 and 0.001 mm/s with a spacing of 2 µm between adjacent lines in the scanning pattern.

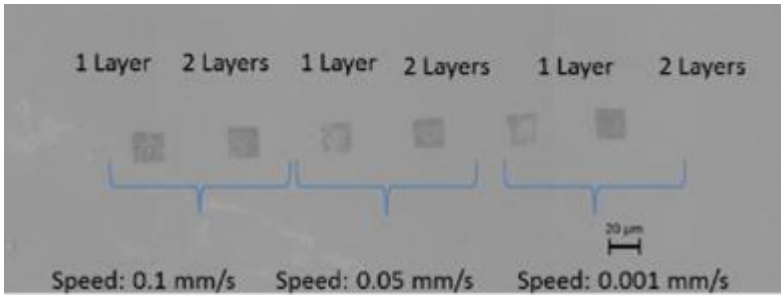

Figure 3.15 Square patterns machined in a fused silica glass slide at 1.3mW, 0.26 µJ at different speeds: 0.1, 0.05 and 0.001 mm/s with a spacing of 2 µm between adjacent lines in the scanning pattern.

The results with 1.5 mW and 0.30 µJ show better definition of the square pattern in the silica than with 0.26 µJ for both spacing in x and y used. However, it was deemed that using a line spacing of 5 microns was the most suitable for machining of squares in the silica slides due to the reduced thermal effect observed. Also, using 1 layer seems to provide a well-defined pattern hence this was chosen over 2 layers as 1 layer provides a faster process. These parameters were deemed to be sufficient to define a square machined area in silica and hence were then applied to an SMF 28 fibre.

3.2.2 Single Mode Fibre SMF-28

To perform the machining on the fibre, two G Codes were written: the first one was the *Find the Fibre* i.e. to distinguish between the microscope slide surface and the fibre surface and to enable the focal position of the fibre. The *Find-The-Fibre* G Code can be

seen in Appendix C. The second G-Code contained the information of the structure to be machined on the fibre and can be found in Appendix B. The distinction between the slide and the fibre surfaces was done by analysing the reflected light from the laser as suggested in reference [91].

The laser operated at low power (approximately 0.200 mW) and by analysing the light reflected on camera 1 it was possible to find the focal position. As the microscope slide and the fibre have different focal positions, it was possible to distinguish which surface was in focus. Running the program *Find the Fibre* using the z position of the slide, when it laser starts scanning the fibre, as the fibre has a different focal position, the camera will detect the surface and the bright focal spot shown in Figure 3.3 will disappear, Figure 3.16.

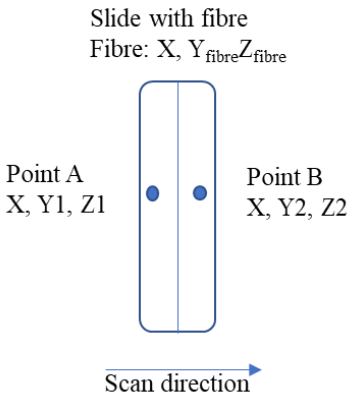

Figure 3.16 Scheme showing the *Find the Fibre* program: it goes from Point A to Point B. The slide has a different focal position from the fibre and when the laser scans the slide the bright focal point is shown on the CCD camera. When the laser scans the fibre, the bright spot disappears when it is possible to see the laser is on the fibre.

A scheme of the machining protocol can be seen in Figure 3.17. Trials with single mode fibre SMF-28 and later with negative curvature fibre (see section 3.2.3) were performed. The samples were analysed with a Leica Microscope (optical) and an Alicona microscope (optical) InfiniteFocus model. The measurement of depth was performed using this microscope which uses a z-scanning technique to achieve the depth measurement as in accordance with the Alicona Manual.

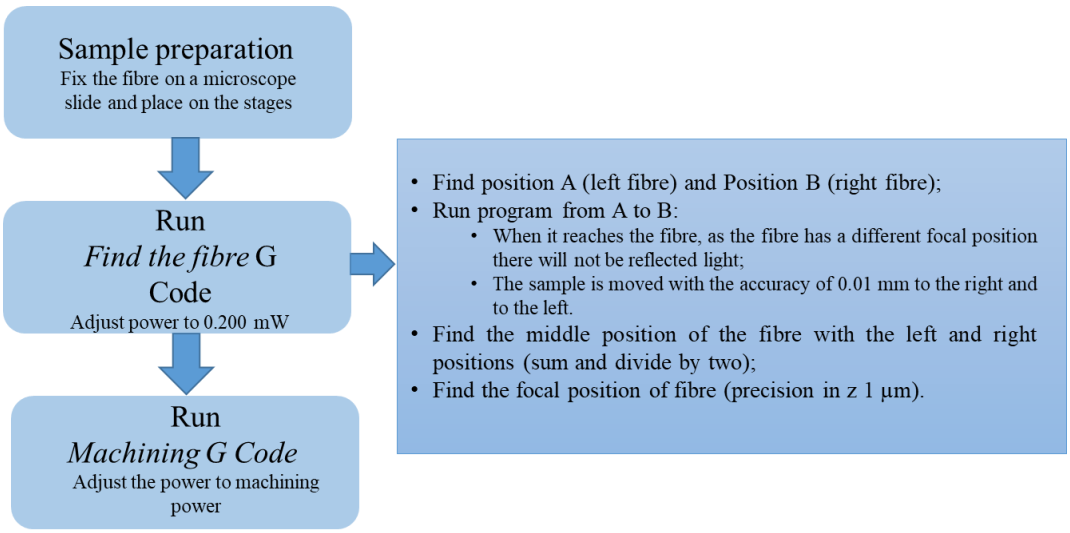

Figure 3.17 Machining protocol used for machining fibres with the femtosecond laser.

For the SMF-28 trials, the fibre was stripped with a conventional mechanical fibre stripper (fibre stripping tool from Thorlabs, typical cladding/coating: 125 µm / 250 µm). After this, the fibre was placed on a microscope slide and fixed with tape. The stages have a removable part of metal and the slide was glued on this part with nail varnish which facilitated the removal of the slide from the stages (using acetone).

Three squares were machined at different speeds with the top square (in the images below) being machined using the highest speed and the lower square is machined using the slowest speed, Figure 3.18.

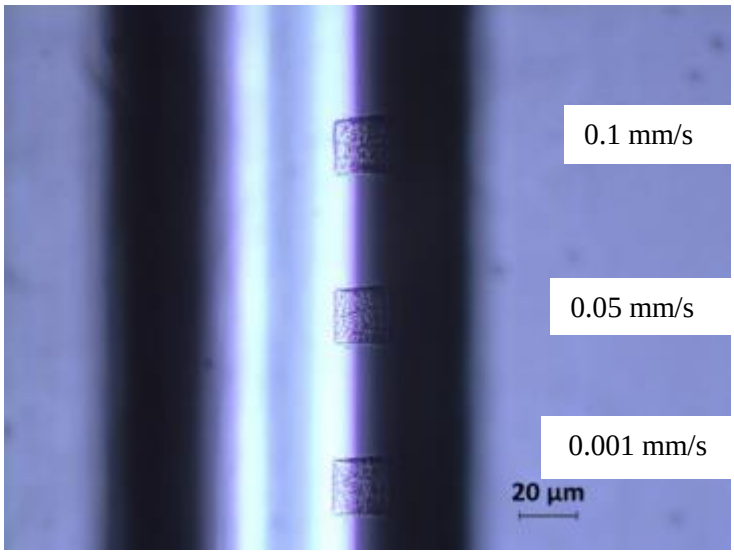

Figure 3.18 Square patterns machined into an SMF-28 machined with power 1.2 mW, 0.24 µJ and speed: 0.1, 0.05 and 0.001 mm/s.

The spacing between adjacent lines was 5 microns, since this spacing produced minimal thermal effect on the slides (as discussed above in section 3.2.1, part b). The speeds of 0.1, 0.05 and 0.001 mm/s, corresponding 98.42%, 99.21 % and 99.98% pulse overlap, where chosen as a starting point with different pulse energies. These speeds showed good results and the corresponding pulse overlap is in accordance with the literature, as for example in in reference [96] it is possible to find 99.9% overlap, as mentioned previously.

The speeds 0.1, 0.05 and 0.001 mm/s were used in following experiments to investigate increasing power and pulse energy. The following pulse energies were performed: 0.38, 0.42, 0.46, 0.50 and 0.54 µJ. Example results for 0.38 µJ and 0.54 µJ are presented in Figures 3.19 and 3.20.

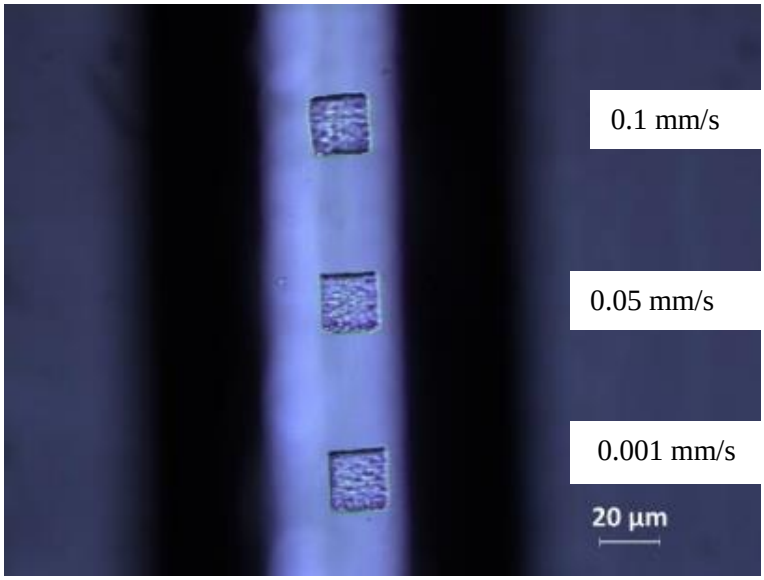

Figure 3.19 Square patterns machined into an SMF-28 with a power of 1.9 mW, 0.38 µJ and speeds of 0.1, 0.05 and 0.001 mm/s.

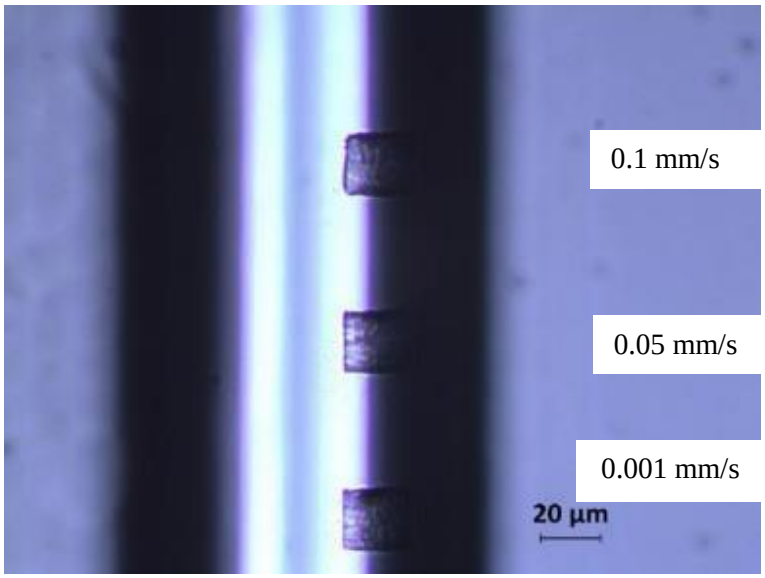

Figure 3.20 Square patterns machined into an SMF-28 with a power of 2.7 mW, 0.54 µJ, speed 0.1, 0.05 and 0.001 mm/s.

The results from Figures 3.19 and 3.20 show that the first square, which has the highest speed, is less well defined and has edges that are not straight or sharp with any of the pulse energies used. Also, increasing the pulse energy to 0.54 µJ produces better defined machined squares.

Consequently, higher pulse energies were tested, such as 0.60, 0.80, 1.0, 1.2, 1.4, 2.0, 4.0, 6.0, 8.0 µJ to determine if a limit could be reached. The speeds were 0.1, 0.05 and 0.001 mm/s (presented from top to bottom). In addition to the procedure used in previous experiments, the fibre was also cleaned with a Kimwipe and isopropanol before analysing to remove any debris around the squares after machining. The results with pulse energies of 1, 2 and 8 µJ are presented in Figures 3.21-3.23.

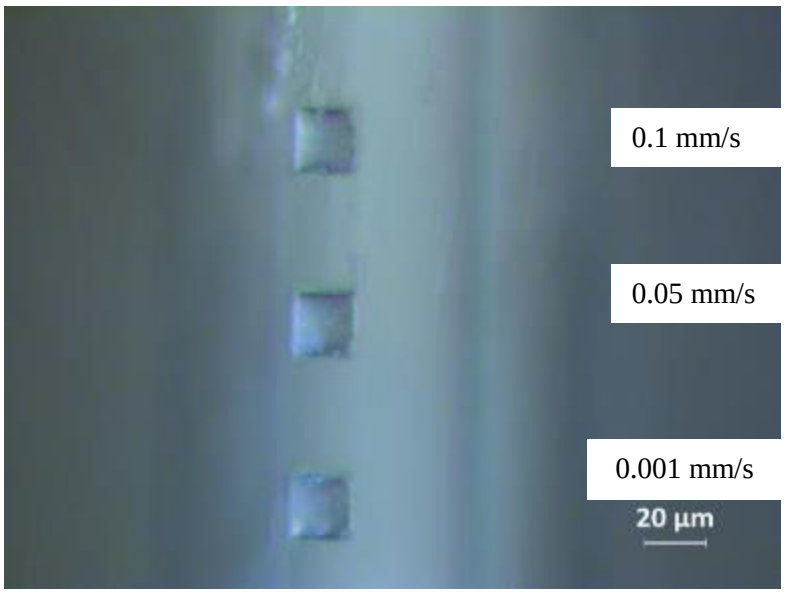

Figure 3.21 Square patterns machined into an SMF-28 with a power of 5 mW, 1.0 µJ and speed 0.1, 0.05 and 0.001 mm/s.

It was observed that the fibre position rotated during the process which results in the squares being off centre in Figures 3.22. 3.23. Nevertheless, the results are promising and show that for higher powers/pulse energies it is possible to inscribe well-defined structures on the fibre.

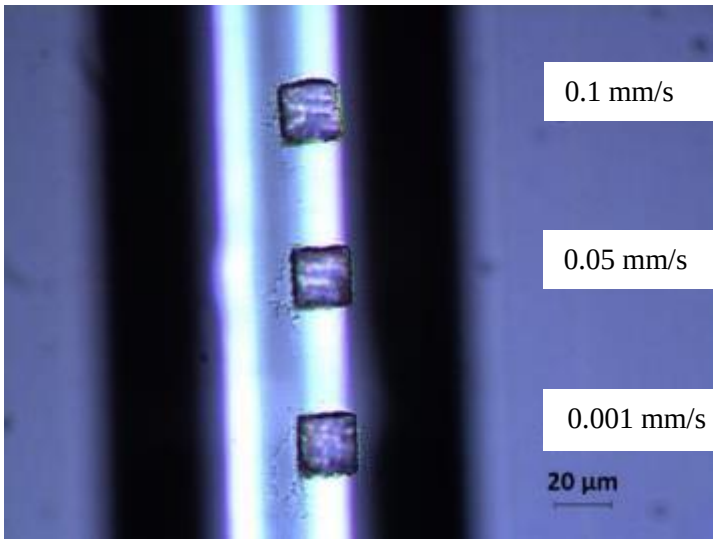

Figure 3.22 Square patterns machined into an SMF-28 with a power of 10 mW, 2.0 µJ speed 0.1, 0.05 and 0.001 mm/s.

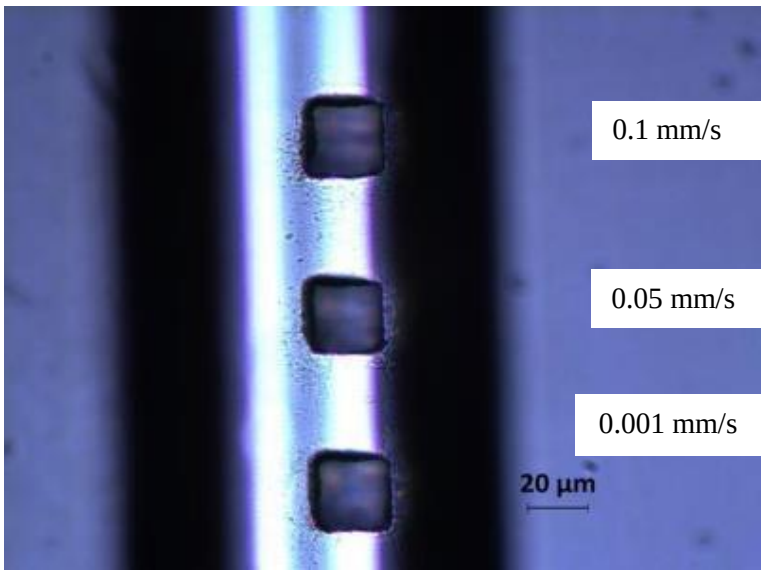

Figure 3.23 Square patterns machined into an SMF-28 with a power of 40 mW, 8.0 µJ speed 0.1, 0.05 and 0.001 mm/s.

It could be useful to compare the depth of each square and correlate it with power and speed. Again, since the squares are not centred on the fibre, making an accurate measurement of the depth was difficult. Therefore, efforts to ensure that the squares were centred on the fibre were made.

Methods to fix the fibre to reduce the rotation were performed. First the fibre was fixed with glue along its entire length (in this case nail varnish was used as it is easily removed with acetone after machining). However, with this method, accurate determination of the fibre position (using the above-mentioned G-Code, Appendix C) was not possible because the glue impaired the reflection of the laser of the mounting slide and fibre, making it difficult to focus on these surfaces. Therefore, the fibre was fixed with glue leaving the region used for machining (a few mm) clear, Figure 3.24.

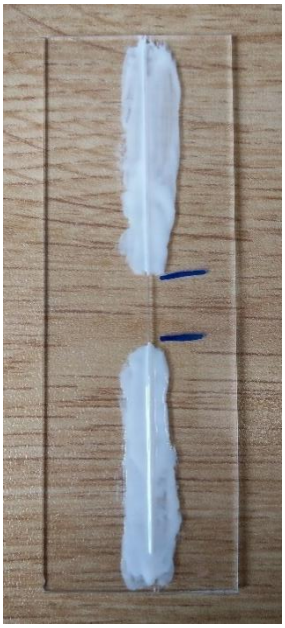

Figure 3.24 Fibre fixed on the microscope slide with glue and the region marked with the blue lines is the machining region.

This provides a secure fixing during the machining process without interfering with the alignment or machining processes. It also allows easy removal of the fibre after machining as the nail varnish is readily removed using acetone and this is applied in a region away from the laser machined section.

Initially SMF-28 was tested with this approach and showed improved results with well-aligned and centralised machining patterns. The pulse energies tested were: 0.60, 1.0, 1.4, 2.0, 6.0, 10.0, 14.0 μJ. The results for 1.0, 2.0, 6 and 14 μJ are shown in Figures 3.25-3.27. The speeds were 0.1, 0.05 and 0.001 mm/s (presented from top to bottom).

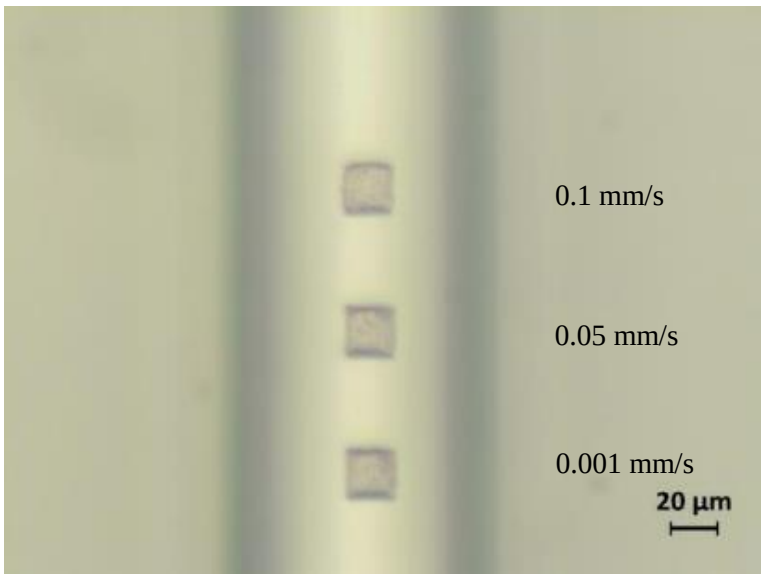

Figure 3.25 Well-aligned square patterns using the improved glue fixation method machined into an SMF-28 with a power of 5 mW, 1.0 µJ speed 0.1, 0.05 and 0.001 mm/s.

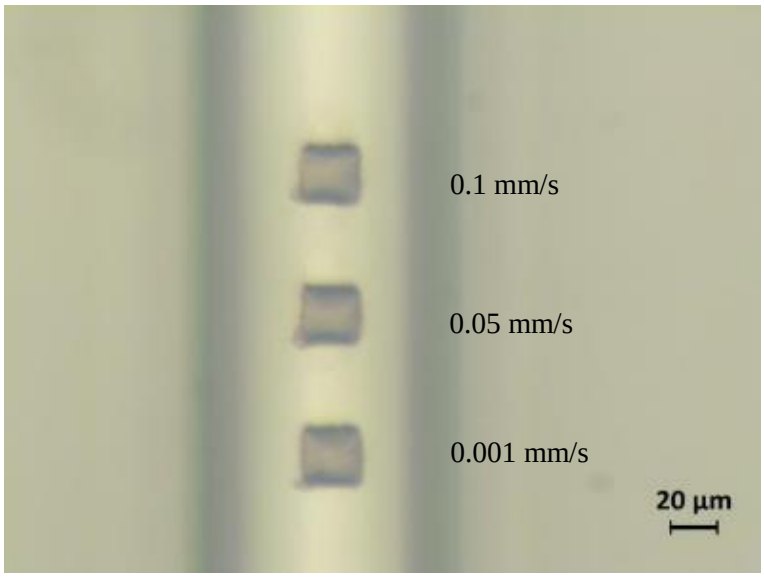

Figure 3.26 Well-aligned square patterns using the improved glue fixation method machined into an SMF-28 with a power of 30mW, 6.0 µJ speed 0.1, 0.05 and 0.001 mm/s.

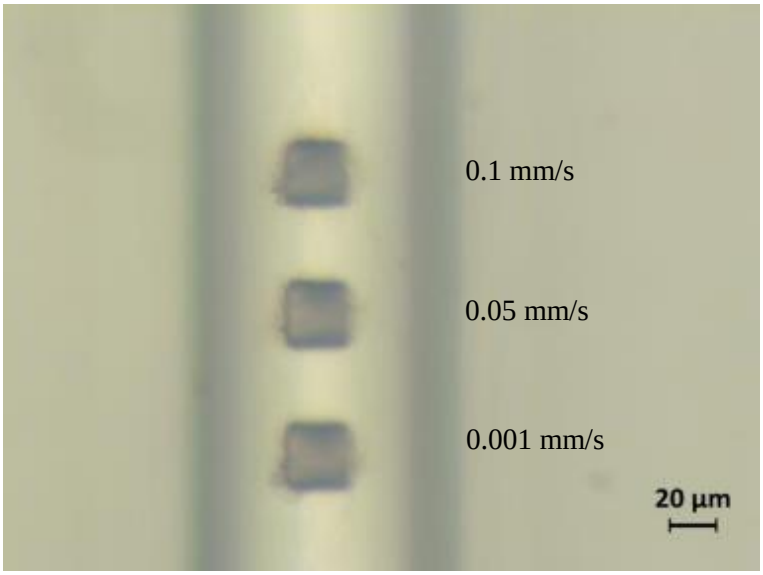

Figure 3.27 Well-aligned square patterns using the improved glue fixation method machined into an SMF-28 with a power of 70mW, 14 µJ speed 0.1, 0.05 and 0.001 mm/s.

Since this method of fixing the fibre showed good results with a wide range of pulse energies tested for SMF-28 it was then transferred for use on the NCF.

3.2.3 Negative Curvature Fibre (NCF)

This fibre was striped mechanically with a metal sheet blade to remove its polymer jacket. This particular NCF is designed for 1µm guidance and has a core diameter of 43 µm [7] and a cladding thickness of 40 microns [7], as shown in Figure 3.28.

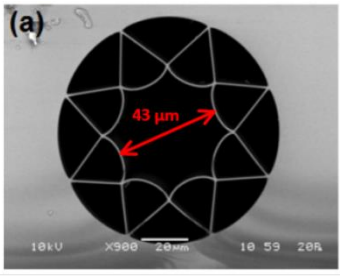

Figure 3.28 SEM image of the NCF [7].

The NCF used in this work was produced by the group of Professor Jonathan Knight at the University of Bath. The speeds used were 0.1, 0.05 and 0.001 mm/s (presented from top to bottom) and a line spacing of 5 µm was used for all patterns. The pulse energies performed were: 0.60, 1.0, 1.4, 2.0, 6.0, 10.0, 14.0 µJ. Figures 3.29-3.31 show the results of the machined squares at pulse energies 0.60, 1.0 and 6.0 µJ.

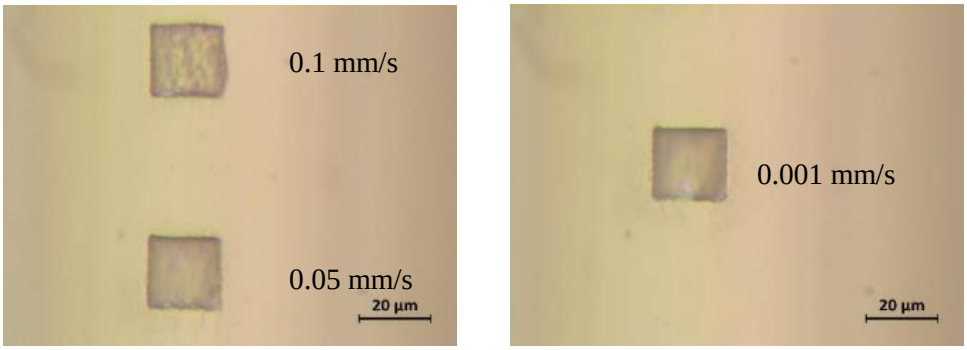

a) b)

Figure 3.29 Square patterns machined into an NCF with a power of 3 mW, 0.60 µJ speed a) 0.1, 0.05 and b) 0.001 mm/s.

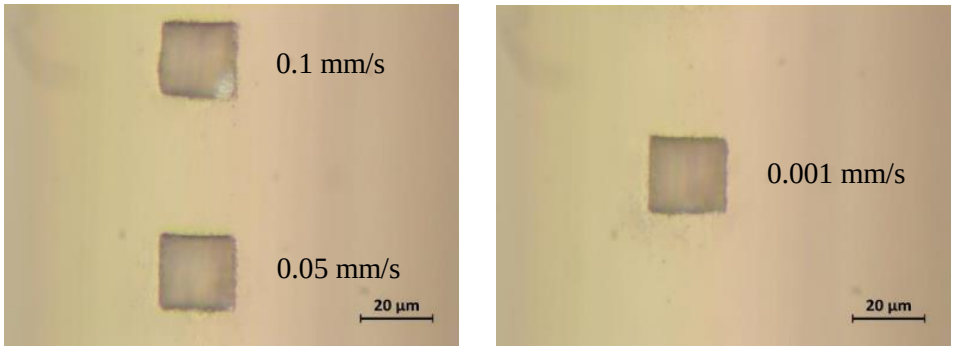

a) b)

Figure 3.30 Square patterns machined into an NCF with a power of 5 mW, 1.0 µJ speed a) 0.1, 0.05 and b) 0.001 mm/s.

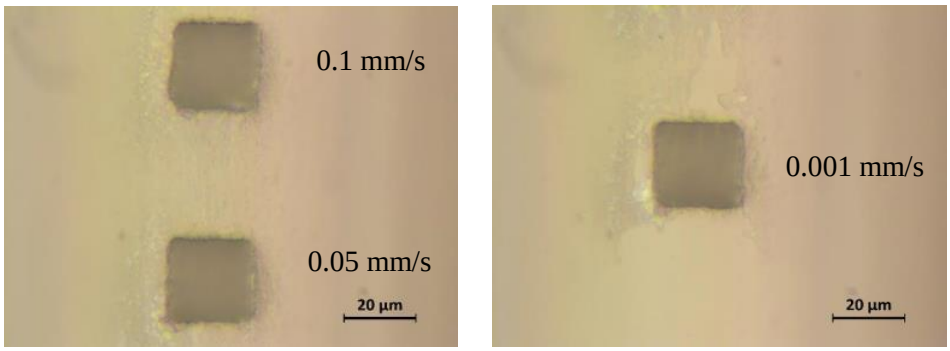

a) b)

Figure 3.31 Square patterns machined into an NCF with a power of 30 mW, 6.0 µJ speed a) 0.1, 0.05 and b) 0.001 mm/s.

Table 3.1 shows the depth achieved for the squares at different pulse energies for the two types of fibres with one single pass.

			SMF	NCF
Power (mW)	Pulse energy (µJ)	Square speed (mm/s)	Depth (µm)	
3	0.6	0.1	2.23	2.44
		0.05	4.35	4.2
		0.001	4.03	4.55
5	1	0.1	3.95	7.00
		0.05	5.12	6.35
		0.001	5.42	6.95
7	1.4	0.1	8.58	7.15
		0.05	9.14	8.51
		0.001	7.42	9.24
10	2	0.1	10.38	11.58
		0.05	10.47	10.85
		0.001	10.76	12.41
30	6	0.1	20.69	20.52
		0.05	20.47	21.97
		0.001	19.78	21.68
50	10	0.1	24.72	29.22
		0.05	26.01	30.74
		0.001	27.6	30.81
70	14	0.1	34.75	34.4
		0.05	33.41	33.26
		0.001	33.65	33.95

Table 3.1 Results of the depth measurement for the squares at different pulse energies for the two types of fibres with one single pass. The objective had a magnification of 20×, a vertical resolution of 0.05 µm and a lateral resolution of 0.88 µm, accordingly to the Alicona microscope manual.

Figures 3.32 and 3.33 show the relation between the pulse energy and depth measured.

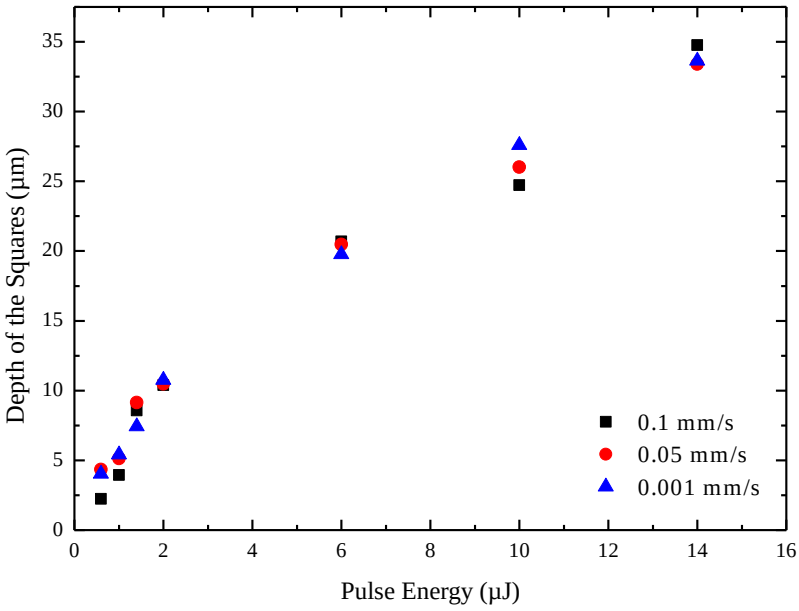

Figure 3.32 Depth of the squares machined into SMF for one pass of the laser.

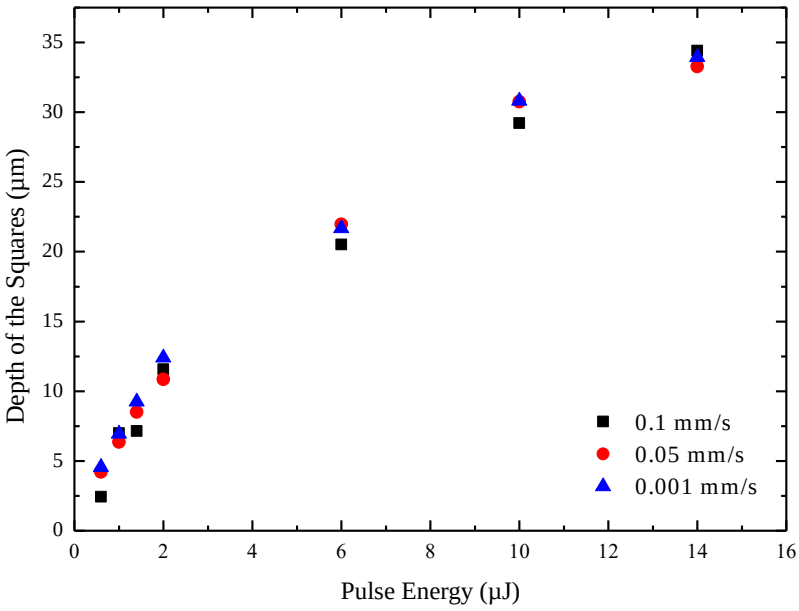

Figure 3.33 Depth of the squares machined into the NCF for one pass of the laser.

This measurement was performed using the Alicona z-scanning process. Representation of typical output from the measurement is shown in Figure 3.34. It is possible to see a similar tendency of the results when comparing the depth of the squares machined with one passes for SMF and for NCF.

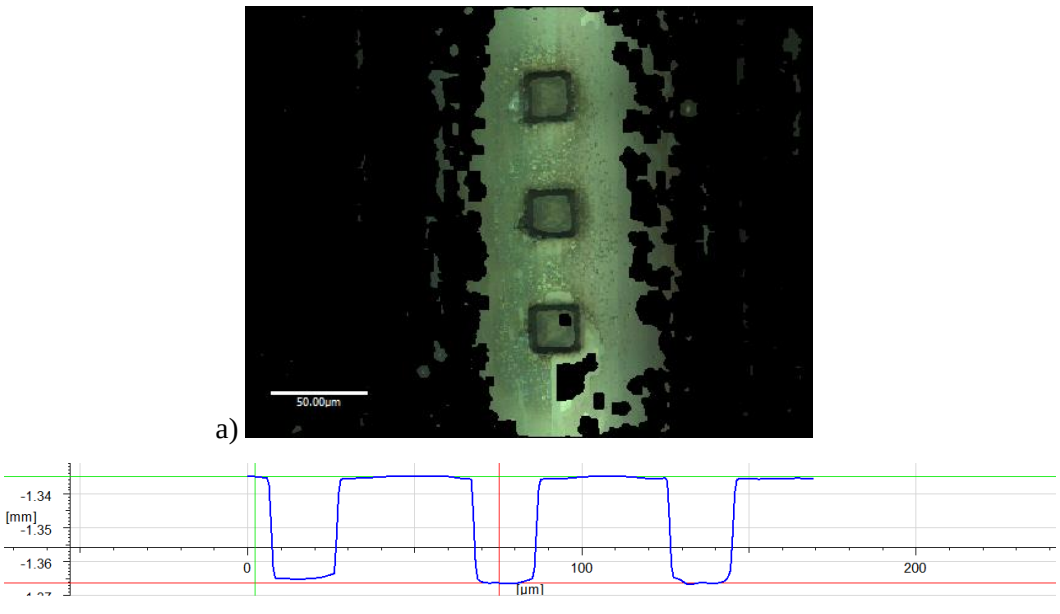

Figure 3.34 a) Example of a measurement done with Alicona microscope a) NCF image under the Alicona microscope and b) depth profile output of the three squares machined on the NCF.

Above 2.0 µJ it was possible to see some undesired thermal effects around the squares. The squares machined at 0.001 mm/s appear to be better defined than those machined at 0.1mm/s. With 0.001 mm/s speed the pulse overlap is 99.98 % compared to 98.42% with 0.1mm/s, indicating that a higher pulse overlap produces a better structure. The machining of squares in NCF and SMF was successful once good squares were machined using a single pass of the laser. However, as the aim from the machining process was to reach at least 50 µm depth (to remove all the cladding of the NCF see Chapter 1, Figure 1.1), it was important to find how deep the removal is for one pass and to find if by repeating the procedure deeper structures could be machined.

For the experiments described above for both the SMF and NCF, a single pass (layer) scanning pattern was used. To see if the number of laser passes influences the depth of the structures, two passes were performed. This test was done for SMF-28 as well as for NCF. Depth measurements were performed with an Alicona microscope.

First, the scanning pattern was repeated (without changing the focal position). However, it was found that increasing the number of passes did not change the depth (as measured with Alicona microscope). This effect was also noticed in reference [100] where the effects of the repeated fabrication are also discussed. The authors used the femtosecond laser to fabricate microchannels with high aspect ratios in glass. The authors drilled in

water and in air and noticed that drilling in air multiple times did not increase the aspect ratio: increasing the drilling attempts did not change the diameter of the channel and the length of the channels were not increased. What happed was a decrease in the length, especially for the case of drilling two times for nearly 50% and this decrease was attributed to the fact that when the hole is drilled for the second time, the solid part of the hole was ablated but as the hole is too long, the ablated materials cools down and solidifies on the wall of the hollow channel drilled last time. Therefore, the solidified material blocks the hollow hole and decreases the length of the hole [100].

This solidified material may also change the focal position. It could be that after the first pass has removed material the laser will not be in focus on the silica for the second pass. This indicates that changing the number of passes without adjusting the focal point does not work. To compensate for this change in surface position the depth of the structures achieved with one pass was measured and that value was used to adjust the focal position for the second pass. To find the correct focal position is of major importance since the removal of the material only occurs if the laser is in focus [75]. Also, the calculated depth of focus of this system is ± 0.5 µm, measured as the distance to both sides of the beam waist over which the beam diameter grows by 5% and the Rayleigh range is 1.5 µm defined as the distance from the beam waist of diameter to the position where it is the square root of 2 multiplied by the beam waist diameter. [92]

The results for SMF-28 and the NCF with two passes are shown in Figures 3.35-3.40. The squares were carried out with scanning speeds 0.1, 0.05 and 0.001 mm/s (showed from top to bottom) and for pulse energies 0.60, 1.0 and 6.0 µJ.

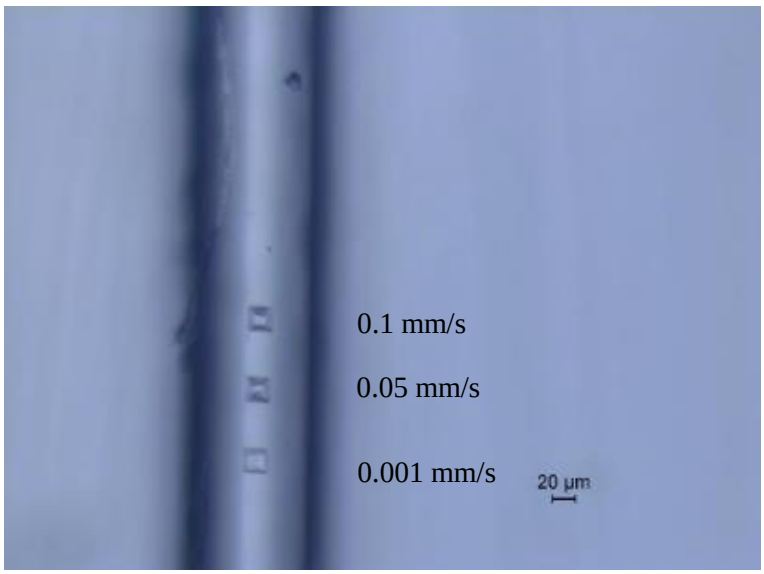

Figure 3.35 Square patterns machined into an SMF-28 with 2 passes (layers) at a power of 3 mW, 0.6 µJ speed 0.1, 0.05 and 0.001 mm/s.

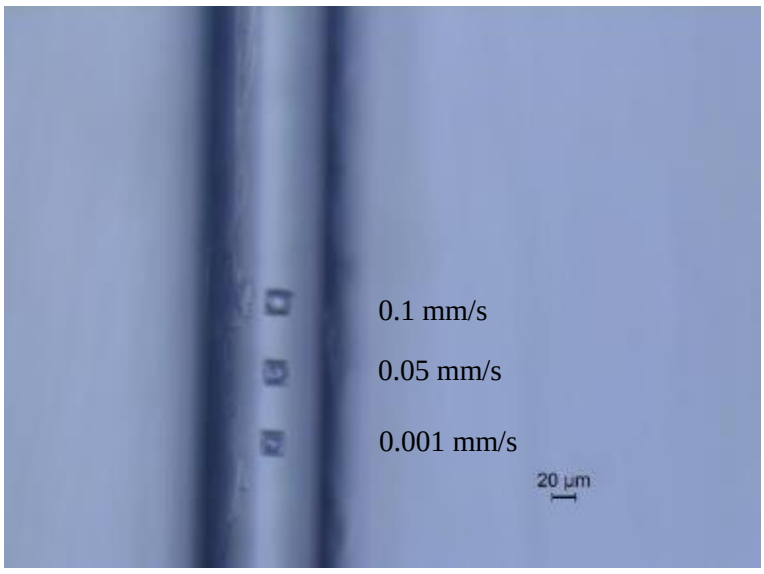

Figure 3.36 Square patterns machined into an SMF-28 with 2 passes (layers) at a power of 5 mW, 1.0 µJ speed 0.1, 0.05 and 0.001 mm/s.

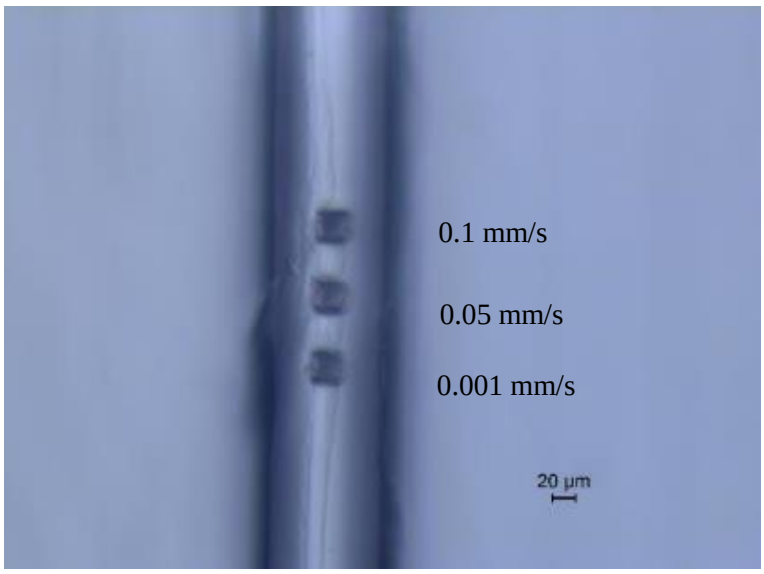

Figure 3.37 Square patterns machined into an SMF-28 with 2 passes (layers) at a power of 30 mW, 6.0 µJ speed 0.1, 0.05 and 0.001 mm/s.

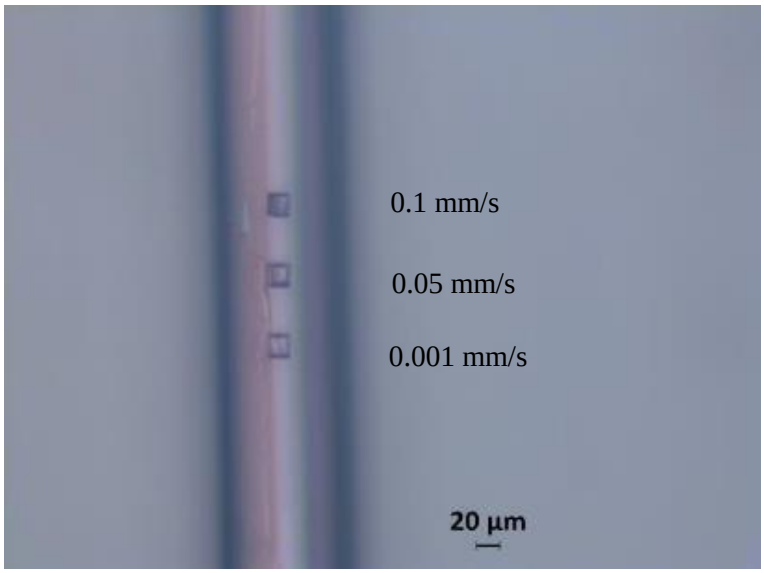

Figure 3.38 Square patterns machined into an NCF with 2 passes (layers) at a power of 3 mW, 0.6 µJ speed 0.1, 0.05 and 0.001 mm/s.

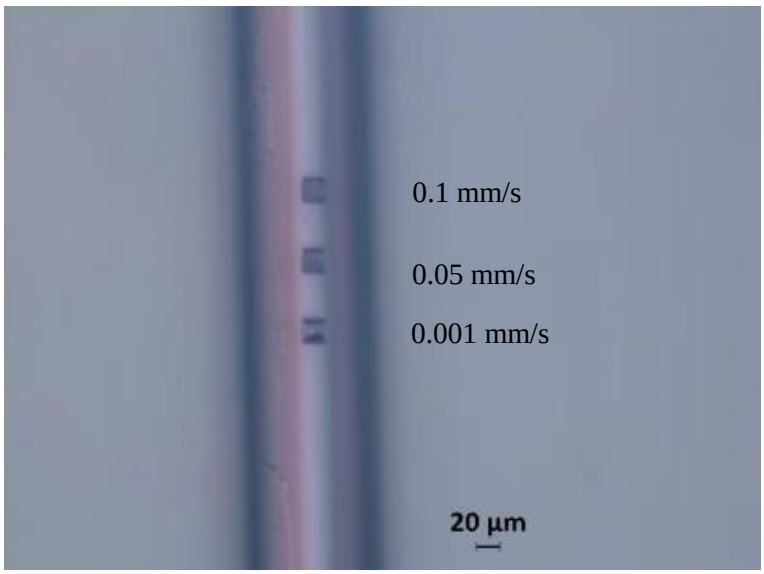

Figure 3.39 Square patterns machined into an NCF with 2 passes (layers) at a power of 5 mW, 1.0 µJ speed 0.1, 0.05 and 0.001 mm/s.

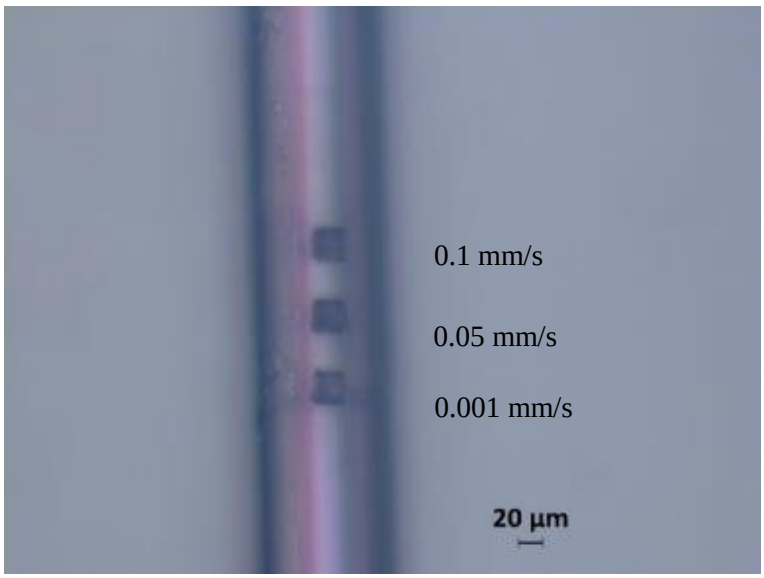

Figure 3.40 Square patterns machined into an NCF with 2 passes (layers) at a power of 30 mW, 6.0 µJ speed 0.1, 0.05 and 0.001 mm/s.

The values of the depth for the two types of fibre after machining with two passes can be seen in Table 3.2 and Figures 3.41-3.42.

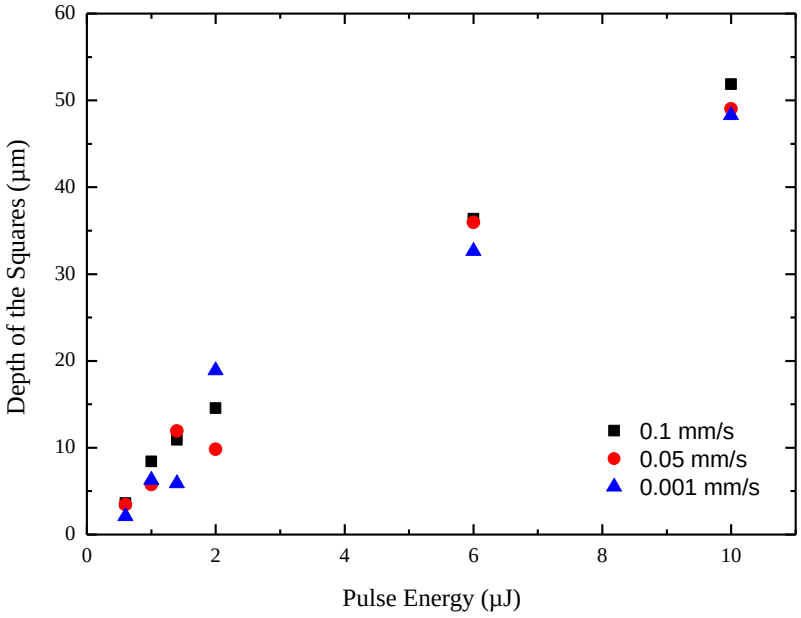

Figure 3.41 Depth of the squares machined into the SMF for two passes of the laser.

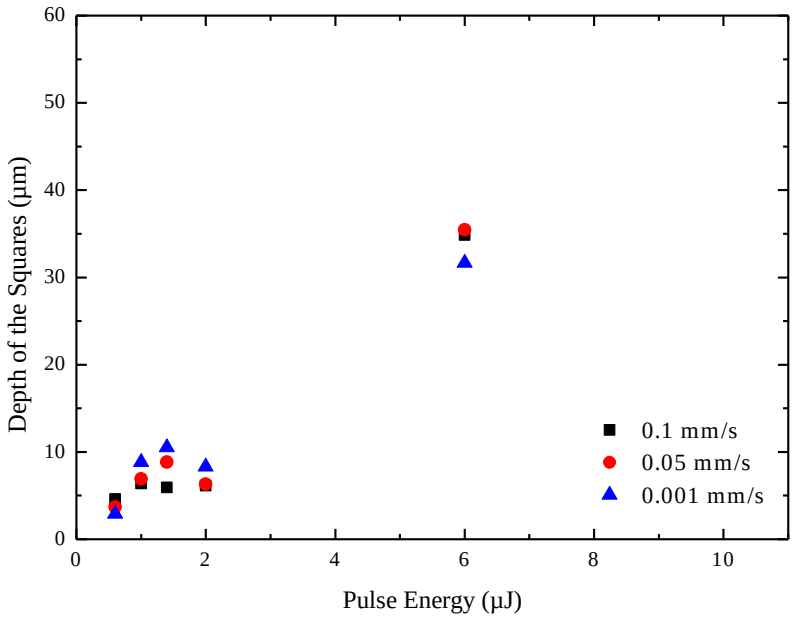

Figure 3.42 Depth of the squares into the NCF for two passes of the laser.

			NCF	SMF
Power (mW)	Pulse energy (µJ)	Square speed (mm/s)	Depth (µm)	
3	0.6	0.1	4.58	3.6
		0.05	3.68	3.45
		0.001	2.91	2.11
5	1	0.1	6.38	8.40
		0.05	6.92	5.76
		0.001	8.82	6.28
7	1.4	0.1	5.94	10.90
		0.05	8.83	11.94
		0.001	10.52	5.88
10	2	0.1	6.14	14.57
		0.05	6.30	9.81
		0.001	8.31	18.90
30	6	0.1	34.87	36.37
		0.05	35.44	35.96
		0.001	31.66	32.65
50	10	0.1	15.74	51.88
		0.05	13.60	49.03
		0.001	8.50	48.30

Table 3.2 Results of the depth measurement for each square and each pulse energy for the two types of fibres with two passes. The objective had a magnification of 20×, a vertical resolution of 0.05 µm and a lateral resolution of 0.88 µm, accordingly to the Alicona microscope manual.

Analysing Figure 3.41, 3.42, 4.33 and 3.32 it is possible to see that the behaviour of the depth of the squares plotted against the pulse energy for SMF and NCF is similar except for the 2 µJ of pulse energy. For this value of pulse energy, for NCF with two passes, the plot does not show the same tendency, showing a decrease of the depth achieved when compared to the same pulse energy for NCF 1 pass, SMF 2 passes and 1 pass.

One possible explanation for this may be related to the operation of the Alicona microscope. This system provides a three-dimensional image by scanning the focal plane through the object, identifying features or edges in each plane and using transmitted light to obtain that information. As the fibres are made of fused silica (transparent), this could result in an unreliable measurement. So, one way to detect if this was the case would be repeating the machining of the sample and re-analysing it on the Alicona microscope.

What would be expectable is the following: low pulse energies, the structures are shallower due to the ablated material that cools down and redeposits on the side wall of the structure, blocking the further ablation process [100]. When the pulse energy is higher, the depth of the structure/squares would increase because the ablated material gains higher temperature and kinetic energy, not cooling down so fast and escaping from a longer structure without redeposition [100].

However, some differences can be seen in the behaviour of the NCF and SMF. The general depth achieved for NCF with 2 passes was not as deep as the depth achieve for SMF 2 passes. Nevertheless, the depth achieved for SMF and NCF with one passes is very similar. The NCF has a hollow core and a silica cladding while the SMF-28 has a bulk core. When the number of passes is 2, this results in a higher depth, so the machined region is near the core, this is, near a medium with a different refractive index and that might explain more pronounced difference with 2 passes. Therefore, the difference of behaviours between the two different fibres could be explained by the differences of the behaviour of light in different refractive index medium, since the deeper the structure is on a hollow core fibre, the nearer it is of the air core medium (different medium, different refractive index).

As the Alicona microscope is an optical one, the light transmitted by the microscope through the different fibres will have a different behaviour due to the refractive index of each medium, accordingly to the Snell's Law, since the refractive index of air is 1 and the fused silica refractive index is around 1.45 as presented in the manufactures datasheet, reference [58].

Snell's law describes the refraction, equation 3.5. when a beam of radiation is incident on an interface between two materials at an arbitrary angle θ with different refractive index (n_1 and n_2), the direction of the propagation of the transmitted [101].

$$n_1 \sin \theta_1 = n_2 \sin \theta_2 \quad (3.5)$$

Another possible explanation can be related to a structural difference due to the femtosecond machining in a bulk silica or hollow core fibre. Authors in reference [88], inscribed slots on a Hollow Optical fibre with a 6 μm air hole diameter, a ring core with a 2 μm thickness and a 125 μm cladding diameter with a femtosecond laser and they noted an interesting aspect: the depth of the corrugation in the hollow core fibre was significantly shallower than those of conventional on-side corrugated single mode fibre, LPG, which could be attributed to the unique stress distribution in the hollow optical fibre with the air holes (in opposite to the solid SMFs).

In this reference [88], the fibre cladding was ablated using a femtosecond laser in a systematic way to produce periodic corrugations. The laser used was a Ti:Sapphire laser with a centre wavelength of 785.5 nm, 184 fs of pulse duration, 1 kHz of repetition rate. The average power was 3.59 mW and a microscope objective lens of 20× with 0.4 of numerical aperture was used. The slots were done using a point-by-point method and the corrugated fibre with 15 slots were fabricated in the centre of a 1 m long fibre. The dimensions of the corrugations were controlled such that a pitch of 550 μm and a depth of 13 μm were fixed while the width could vary: 30, 40, 80, 90 and 150 μm. The diameter of the focused laser was 5 μm and the single scan of the laser beam ablated the fused silica cladding to a depth of 6.5 μm. Linear corrugated LPGs were inscribed perpendicular to the fibre axis using a motorised laser beam scanning system. Knowing the number of scans controls precisely the width of the slots [88].

Although there is a difference in the behaviours (in the case of SMF with 2 passes, deeper structures were achieved when compared to NCF 2 passes), it is still possible to conclude some findings:

- It was not possible to reach the 50 μm cladding region and access the core and structured webbing of the NCF, the depth versus pulse energy is not linear and

there appears to be a levelling off towards 10 µJ. This would suggest that merely increasing pulse energy to machine deeper structure (to access the hollow core) would not be a successful strategy.

- The adjustment of the focal position is very important. For example, if it is expected that with one pass it will be achieved 10 µm of depth this depth should be considered for the next pass. However, this increment corresponding to the depth achieved with one pass might not be the most correct to consider, it might be too much and this would influence the final machining quality.

Reference [102] mentions the importance of maintaining the surface of the workpiece/sample within the focal position of the laser to ensure a high efficiency of the removal of the material and of continuing to adjust the laser focus accordingly to the change of the changes performed in the sample.

Since simply increasing the number of passes did not work (due to fact that when structure is drilled for the second time, the solid part of the structure was ablated and the ablated material cools down and solidifies on the wall of the structure drilled last time [100] leading to a possible change of the focal position) and due to the importance of the adjustment of the focal position, as shown in this work and also reported in [75] and [102]. Optimisation tests considering smaller increments in z directions will be presented in the next Chapter, to increase machining efficiency [102]. In principle, this could enhance the escape of the material from the structure, since less material is removed each time. When the structures or holes become deeper, it is more difficult for the ablated material to escape [100].

The machining procedure was optimised, and new techniques to develop an unambiguous machining of hollow core fibres was developed and it is described in Chapter 4. Small pulse energies will be used as well as a starting point (1 µJ) since high pulse energies in principle increases the depth and when the structure is deeper it is more difficult for the ablated material to escape and this could contribute to rougher structures [100] and also because in this work there was not proven a linear direct relationship between the depth achieved and the pulse energy used.

3.3 Summary

The femtosecond laser set-up was designed and implemented to allow the independent operation of two beam paths. Tests regarding the pulse energy, the scanning speed, the spacing between lines and number of passes/layers were performed.

A first set of trials were carried out with fused silica slides and showed that 5 µm was the optimal spacing between lines (in x and y directions), one layer would be better than two due to thermal effect observed (because the focal position was not adjusted) and the appropriate tested pulse energy would be 0.30 µJ.

Tests were then carried out with SMF-28 and the NCF with the speeds of 0.1, 0.05 and 0.001 mm/s which corresponds to 98.42, 99.21 and 99.98 % of overlap, respectively. Several pulse energies were tested in the range of 0.6 to 10 µJ to correlate pulse energy with the depth achieved for each square. It was possible to measure the depth of each square using the Alicona microscope. The maximum depth achieved was around 51.88 µm for the SMF with 10 µJ with two passes adjusting the focal position but the same did not happen for the NCF, being the maximum depth achieved 35.44 µm for 6 µJ.

This behaviour is not fully understood, with two possible reasons for the difference in the behaviour of light when the light from the Alicona microscope travels in different mediums (the silica and the air), accordingly to the Snell's Law, since the refractive index of air is 1 and the fused silica is around 1.45. Another possible explanation can be related to a structural difference due to the femtosecond machining in a bulk silica or hollow core fibre, since authors in reference [88] noted that the depth of the corrugation in the hollow core fibre was significantly shallower than those of conventional on-side corrugated single mode fibre, LPG, which could be attributed to the unique stress distribution in the hollow optical fibre with the air holes (in opposite to the solid SMFs).

It was not possible to reach the 50 µm cladding region and access the core and structured webbing of the NCF, the depth versus pulse energy is not linear and there appears to be a levelling off towards 10 µJ. This would suggest that merely increasing pulse energy to machine deeper structure (to access the hollow core) would not be a successful strategy

as an opposite from what would be expectable (the higher pulse energy, the depth of the structure/squares would increase because the ablated material gains higher temperature and kinetic energy, not cooling down easily and escaping from a longer structure without redeposition [100]).

Simply increasing the number of passes did not work due to fact that when structure is drilled for the second time, the solid part of the structure was ablated. As a consequence, the ablated material cools down and solidifies on the wall of the structure leading to a possible change the focal position [100]. The adjustment of the focal position is crucial, so optimisation tests considering smaller increments in z directions will be presented in the next Chapter, to achieve a better machining efficiency [102] and quality (uniform machining [102]). This method could enhance the escape of the material from the structure, since less material is removed each time. When the structures or holes become deeper, it is more difficult for the ablated material to escape [100].

Small pulse energies will be used as well as a starting point (1 μJ) since high pulse energies in principle increases the depth and when the structure is deeper it is more difficult for the ablated material to escape and this could contribute to rougher structures [100] and in this work there was not proven a linear direct relation between the depth achieved and the pulse energy used.

In the next Chapter, improved machining of the Negative Curvature Fibre (NCF) with the femtosecond laser to achieved deeper structures will be explored as well as the analysis of the structures machined.

Chapter 4 – New approach for machining Negative Curvature Fibre (NCF) and its characterisation

In this Chapter, the machining of the Negative Curvature Fibre (NCF) with the femtosecond laser will be explored as well as the analysis of the structures machined. The samples were analysed using a Leica Microscope (optical), an Alicona microscope (optical) InfiniteFocus model and with a Scanning Electron Microscope (SEM) at high-vacuum, model FEI Quanta 3D FEG.

Parameter studies of laser power, scan speed and scan path were carried out as a modified machining approach with small incremental changes in z position. Results from Chapter 3 provided the starting parameters for the machining of silica NCF and showed the importance of the adjustment of the focal position between passes and showed the influence of pulse energy in achieving a deeper structure (since the depth versus pulse energy is not linear and simply increasing the pulse energy alone is not sufficient to achieve a deeper structure).

With the aim to further develop a robust machining strategy, for producing structures that may subsequently be developed into functional components for a range of novel applications (as mentioned in Chapter 1), optimisation tests considering smaller increments in z directions will be presented in this Chapter. The aim was to obtain a better depth control and ensure that the laser beam remained in focus for each layer or pass. In principle, the small increments in z will enhance the escape of the material from the structure, since less material is removed each time. When the structures or holes become deeper, it is more difficult for the ablated material to escape [100].

Laser parameters such as pulse duration, repetition rate, wavelength and pulse energy strongly impact the micromachining process in different ways hence it is necessary to carry out systematic parameter optimisations to ensure optimum machining results. Repetition rate influences the modification because of heat accumulation effects. The energy relaxation processes are affected by the pulse duration as this dictates the time to deposit energy within the electronic states of the valence and the conduction bands.

For longer pulsed systems the laser wavelength determines how the energy is absorbed by the material. Pulse energy limits what type of structures can be produced and hence should be carefully controlled to provide sufficient fluence in relation to the material damage threshold to modify the material. This can affect the size and shape of the resulting structures [81].

Fluence and scanning speed of the laser beam are highlighted as the most important factors to control the ablation depth and to obtain a good process quality. The speed has an impact on the overlap of the pulses (for a given repetition rate) on the sample within a certain range. If the scan speed is too high, the pulse overlap decreases, and single ablation spots are separated. However, if the scanning speed is too low, a high pulse overlap occurs. Both extreme cases can result in irregular grooves [81].

The effect of speed on the drilling of holes in glass using the femtosecond laser has been studied [100]. This reference uses a Ti:Sapphire laser, at a central wavelength of 800 nm, capable of producing 100 fs pulses. The laser beam was focused in the fused silica glass sample using a 10× microscope objective with NA of 0.30 and focal length of 8.3 mm. The sample was moved in z direction using a linear motor translation stage. In this reference, the sample was drilled in air or with its rear surface in contact with distilled water. The microchannel was created from the rear surface, focusing the laser on that point and moving the sample in the z direction. To infer about the effect of writing speed, the pulse energy was set at 230 μJ. The speeds tested were 5–10–20–40–80 μm/s and it was noticed that for the holes drilled in air, the diameter decreases slowly as writing speed increases for drilling holes and the length increases until a maximum at 10 μm/s and then becomes small [100]. Therefore, the scanning speed influences the diameter and the length of the holes. In this Chapter the approach will be different i.e. scanning in several z planes as opposed to drilling, starting on the top surface of the sample and using 1 mm/s as a starting point.

For this work, as discussed in Chapter 3, repetition rate, wavelength and pulse direction are fixed with values of 5 kHz, 795 nm and a maximum theoretical pulse duration of 130 femtoseconds. The work is therefore focussed on machining strategy (i.e. scanning geometry, pulse overlap, scanning speed) and pulse energy.

4.1 Scanning Machining Methodology

The new method consisted of scanning horizontal lines of approximately 2 mm in length (in the x direction, transversal, see figure 4.1) across the fibre and 50 µm in the y direction, axial. The fibre is 360 µm in diameter. With the acceleration and deceleration of the stages being 120 mm/s^2 with a scanning speed used of 1 mm/s a length of 8.33 µm is required for the stages to accelerate and decelerate. Therefore, in total a length of 360+8.33 µm (368.33 µm) is needed to ensure the speed is 1 mm/s when the machining of the structure is performed. However, the 2 mm scanning length would safeguard that the stages have time to accelerate and decelerate before passing over the fibre.

Multiple planes at different z positions were performed. Each plane is made on the same x and y coordinates of the fibre but with different z positions, as can be seen in Figure 4.1.

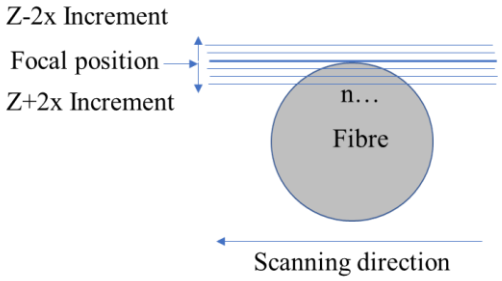

Figure 4.1 Simplified scheme of the machining of the horizontal lines in different z planes with scanning direction.

The distance between the lines was 0.5 µm (y distance). The machining protocol starts with focus above the surface and then the planes are performed. When a plane is completed, there is a translation in the z direction, to perform another set of lines in another z plane, and so on until a certain theoretical depth is achieved. The planes are performed as follows: two planes above the surface, one on the surface and the other set of planes is below the surface. Small increments (of 0.5, 1.0, 2.0, 2.5, and 5.0 µm) in z between each plane were used to ensure a better control of the material removal.

The scanning speed was 1 mm/s corresponding to 84.16% of pulse overlap and the polarisation used was right circular as in accordance with Chapter 3. Also, a pulse energy

of 1 µJ was used to ensure a good quality machining as mentioned before. The analysis was done with both Alicona and SEM microscopes.

The total number of planes refers to the planes above the surface (2), one on the surface and the others below the surface. Increments of 0.5, 1.0, 2.0, 2.5, and 5.0 µm were used as follows:

- Fixed increments: 0.5 µm of increment
    - 13 planes (aim 5 µm depth)
    - 23 planes (aim 10 µm depth)
    - 53 planes (aim 25 µm depth)
    - 103 (aim 50 µm depth)
- Increased increments:
    - 1.0 µm of increment, 53 planes (aim 50 µm depth)
    - 2.0 µm of increment, 26 planes (aim 50 µm depth)
    - 2.5 µm of increment, 21 planes (aim 50 µm depth)
    - 5.0 µm of increment, 11 planes (aim 50 µm depth)

The "WHILE" function in the G-Code allowed the desired number of planes to be carried out (Line 63) adding the increment in z below the surface (Line 65). The number of planes was dictated by the increment and depth required, for example, to achieve a depth of 25 µm it is needed 10 planes of 2.5 µm increment below the surface.

```
(Line 62)  $aaa=0
(Line 63)  WHILE $aaa LE $numberzplanes
(Line 64)  $DO0.X = 0
(Line 65)  G1 Z ($posz1+$incrementz*$aaa)
(Line 66)  dwell 0.1
           …
           END WHILE
```

The example of the G Code used can be found in Appendices D and E. The writing of lines was controlled using another "WHILE" function. This function allowed the movement of the laser from the origin to the initial point (right hand of the fibre) with the shutter off. Once the laser was on the right hand position the shutter is opened and the sample is moved from the right to the left. Appendices D has the code for machining

planes above the surface and E has the code for machining planes on the surface and below. Each plane takes approximately 8 min to perform.

Initially, for each structure, 3 cleaving lines were machined on the middle of the fibre with 6 µJ, one on the focal position of the fibre and the other two with adjusted z position by 20.5 µm and 41µm.

4.2 Results from Scanning Machining Methodology

In Figure 4.2 and 4.3 the results for 13 planes (aiming for a total depth of 5 µm) and 23 planes (aiming for a total depth of 10 µm) are presented.

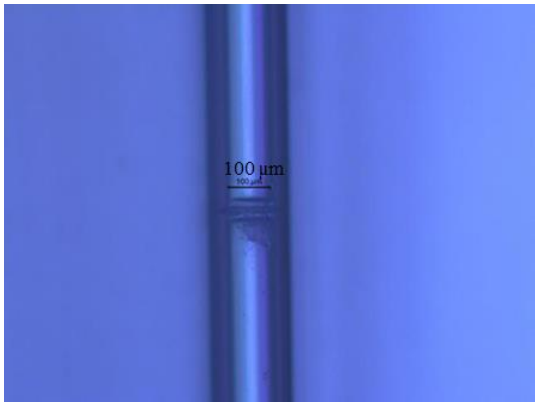

Figure 4.2 Rectangle machined in an NCF using scanning lines with 13 planes. Cleaving lines were machined through the middle of rectangle to allow controlled cleaving.

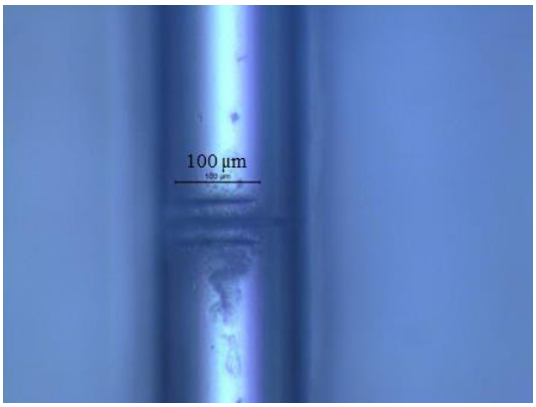

Figure 4.3 Rectangle machined in an NCF using scanning lines with 23 planes. Cleaving lines were machined through the middle of rectangle to allow controlled cleaving.

The depth measured with Alicona microscope depends on the site it is measured but the deepest point for these structures (measured above the cleaving line) was 13.48 and 22.32 µm respectively with 0.05 µm resolution. The objective used had a magnification of 20×, a vertical resolution of 0.05 µm and a lateral resolution of 0.88 µm.

In Figure 4.4 and 4.5, the results for 53 planes (aiming for a total depth of 25µm) and 103 planes (aiming for a total depth of 50 µm) are presented. The depth measured with Alicona microscope depends, once again, on the site it is measured. The actual machined depth measured was 30.53 µm and 65.04 µm respectively with 0.05 µm resolution. These Alicona depth values provide a reasonable indication of the depth, as the Alicona measurement is highly dependent on the surface of the site being measured. Highly scattering surfaces provides lower signal return

a) 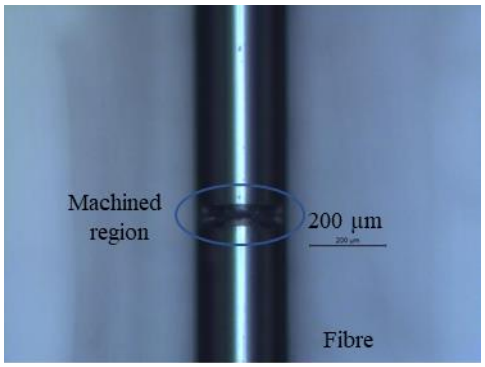

b) 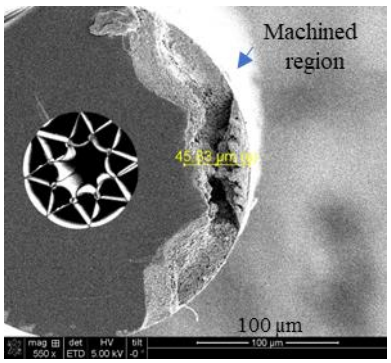

Figure 4.4 a) Top image of the fibre showing the machined structure and b) SEM picture (after cleaving) of the fibre cross section for 53 planes in z.

a) 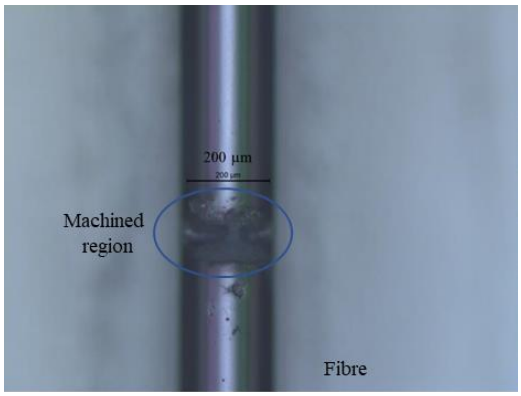

b) 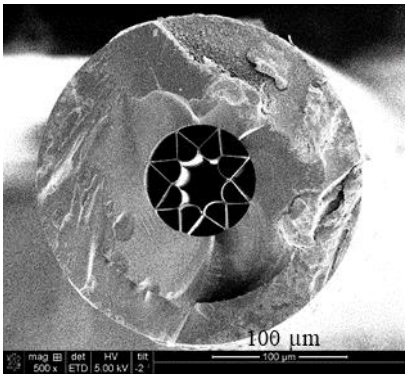

Figure 4.5 a) Top image of the fibre showing the machined structure and b) SEM picture (after cleaving) of the fibre cross section for 103 planes in z.

However, more accurate results can be obtained by analysing with the SEM after the cleaving of the fibre, as shown in Figures 4.4 and 4.5. With small increments (0.5 µm) a clean and well-defined structure without noticeable re-deposition is achieved with 13 and 23 planes, Figure 4.2 and 4.3. Increasing the number of planes, and consequently the depth, it is possible to see some re-deposition on the top of the fibre and with 103 planes there is a considerable amount of re-deposited material on top of fibre and the machining is not well-defined, Figure 4.5 b).

Due to this effect, it was decided to increase the increment, therefore reducing the number of planes performed to obtain a well-defined structure with less re-deposition on top. This deposition may be related to the fluence. The fluence is directly proportional to the pulse energy and by increasing the number of planes the total cumulative pulse energy on a particular region of the fibre is increased and hence the total energy input per unit area is increased. It is known that at high fluence, the formation of a dense, high temperature plasma is formed and the material is removed in plasma, liquid and vapours phases. The molten material is expelled due to the plasma expansion and then vaporisation process and results in debris or droplets condensing or re-depositing on the surface of the fibre [81]. The fluence is the laser pulse energy divided by the effective focal spot area. The authors in reference [103] also mention that high ablation rates at high fluences can cause significant recast formation. The following Figures show the results for the increased increment experiments (Figures 4.6, 4.7 and 4.8).

a) 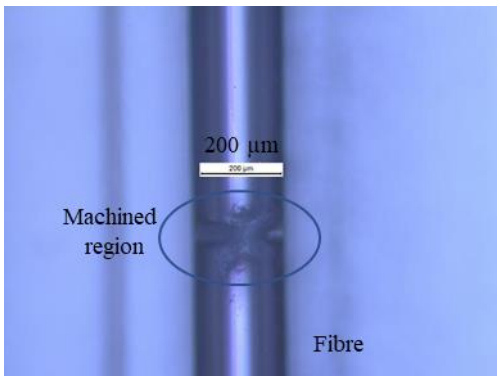

b) 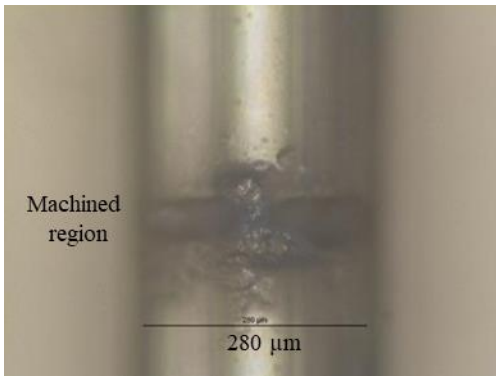

Figure 4.6. a) Machined structure with 1.0 µm increment in z and b) machined structure with 2.0 µm increment in z.

a) 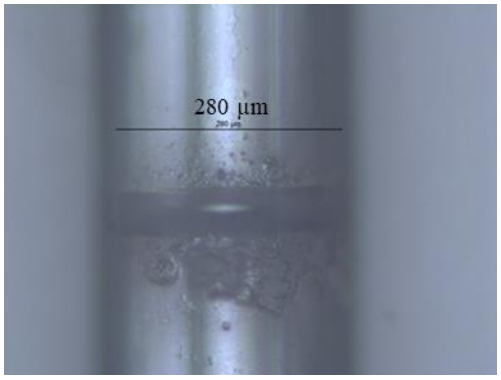

b) 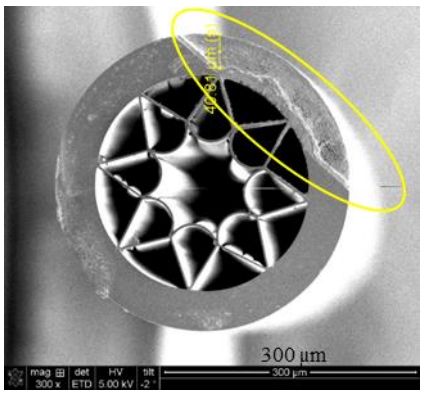

Figure 4.7. a) Top image of the fibre showing the machined structure and b) SEM picture (after cleaving) of the fibre cross section using 2.5 µm increment. The yellow ellipse shows the machined region is irregular.

a) 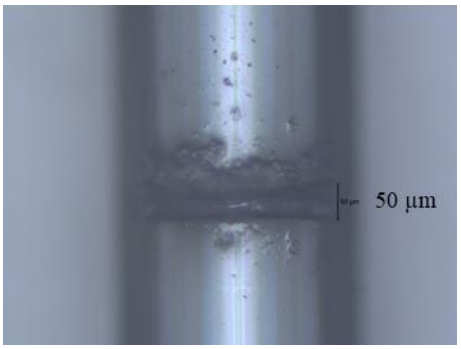

b) 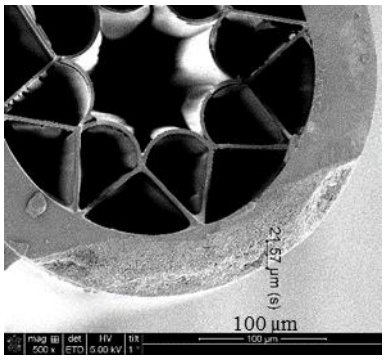

Figure 4.8. a) Top image of the fibre showing the machined structure and b) SEM picture (after cleaving) of the fibre cross section using 5 µm increment.

Increasing the increment to 2.5 µm provided a compromise between having a small z increment whilst relieving the cumulative pulse energy effects. A smaller increment to ensure a good machining quality but having too many increments can adversely affect re-deposition. Since there are less planes to be performed, there is less cumulative pulse energy, therefore less fluence applied to the machined site. However, there is an effect not fully understood that contributes to an irregular machined structure, Figure 4.7 b), as highlighted by the yellow ellipse. One of the possible reasons for this may be that the machining of the fibre has started not on the highest point of fibre which means that the machining was initiated in the wrong starting position leading to an uneven machining. These issues are discussed later in this chapter where the repeatability of the process is considered, and the further improvement will be shown in the following Chapter.

Since it was possible to achieve approximately 50 µm depth with 23 planes, it was decided machine a further 8 planes. An experiment with 2.5 µm increments was performed with

31 planes in z where nominally 2 planes were above the fibre top surface, 1 plane was on the top surface and the remaining 28 were below. Using this strategy, it was possible to reach a measured depth of 50 µm, Figure 4.9. The results shown in this Figure are very promising since it was possible to machine away all the cladding without causing damage to the web structure of the NCF. However, Figure 4.9 b) shows again that the machined region is not straight (yellow ellipse). It was also necessary to see if the cleaving lines influenced the results therefore the subsequent experiments were carried out without the cleaving lines.

a) 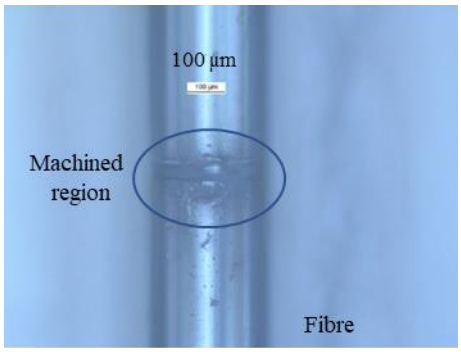

b) 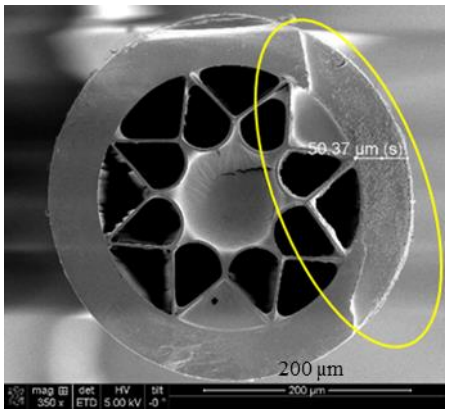

Figure 4.9. a) Top image of the fibre showing the machined structure and b) SEM picture of after cleaving the fibre cross section using 2.5 µm increment and 31 planes. The yellow ellipse shows the machined region is irregular.

To improve on the previous results i.e. to increase the machined depth and to achieve the web cladding machining, some experiments were done with the same number of planes (31) combined with a smaller structure (of 10 planes) with a sample increment of 2.5 µm.

The smaller structure (used for machining of the cladding web) consisted of lines 1 mm (in x) over a length of 50 µm (in y) using the same pulse energy, 1 µJ. Each plane with this dimension took approximately 4 min to perform. The results shown in Figure 4.10 are very promising and provide evidence that the proposed machining strategy (discussed in this section and given in Figure 4.1) for the NCF is valid. Recalling the Figure 1.1 from the Chapter 1, it is possible to see that the third machining stage, the webbing removal stage was achieved. In Figure 4.10, the combination of 31 with the 10 smaller planes is shown.

a) 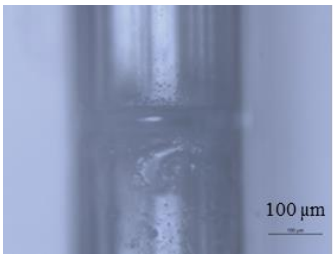

b) 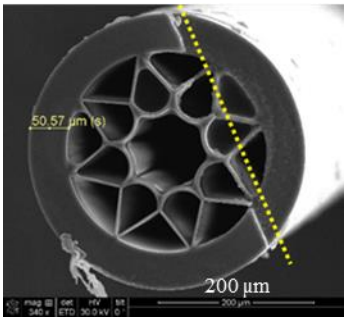

c) 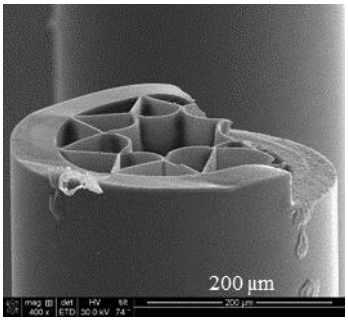

Figure 4.10. a) Top image of the fibre showing the machined structure and b) SEM picture (after cleaving) of the fibre cross section using 2.5 µm increment and 31 planes followed by a second and smaller structure of 10 planes with a 2.5 µm increment in z and c) different perspective of the same machined region of the NCF fibre. The dashed dots show how the machining structure seems to behave in a clear and straight line and provide a smoother machined structure.

Also, in Figure 4.9 b) it is possible to see that the machining was not even across the full width of the fibre, being irregular as highlighted by the yellow ellipse. This contrasts with the machining shown in Figure 4.10 b) where it is possible to see a 'straight line' of the machined region across the full fibre width.

To obtain a 3-dimensional hole, some researchers adopted multistep methods such as water assisted femtosecond laser machining [12] or femtosecond machining whilst translating the fibre perpendicular to the laser beam, followed by heat treatment and subsequent etching in a dilute aqueous hydrofluoric acid (HF) solution [83], [104]. Simply drilling is not sufficient to achieve high precision, high quality and high processing efficiency [81]. However, with the scanning lines method proposed here not only is the machining done perpendicularly to the laser beam, but several increments in z are employed to optimise the removal efficiency.

Regarding the pulse energy chosen, in Chapter 3 some different pulse energies were tested such as: 0.6, 1, 1.4, 2, 6, 10, and 14 µJ. However, as mentioned previously small pulse energies were chosen to improve the machining quality (high pulse energies in principle increases the depth but when the structure is deeper it is more difficult for the ablated material to escape and this could contribute to rougher structures [100]) and also because there was not proven a linear direct relation between the depth achieved and the pulse energy used.

To investigate whether 1 µJ was the optimal pulse energy it was decided to increase the pulse energy to 2 µJ. To investigate using a larger pulse energy 31 planes (for cladding machining) followed by 10 planes (for webbing machining) with a 2.5 µm of increment was performed. The results are shown in Figure 4.11.

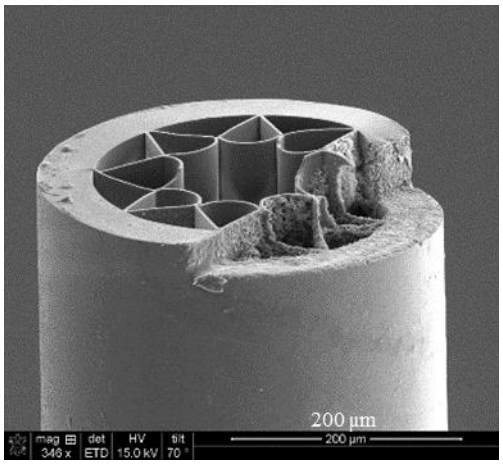

Figure 4.11. Combined structure of 31 planes followed by 10 planes with a 2.5 µm increment in z and a pulse energy of 2 µJ.

Since the increase of the pulse energy to 2 µJ showed a positive result, 31 planes followed by 15 planes and 31 planes followed by 20 planes to see if deeper structures could be achieved (Figure 4.12). In Figure 4.13 it is possible to see a top view of the machined structure under the SEM.

In Figure 4.12 a) the webbing was removed in part, but this could have occurred during the cleaving of the fibre. Figure 4.12 b) shows that using with 31 plus 20 planes the machined region is not well defined with noticeable re-deposition. One possible explanation for the damage shown in Figure 4.13 around the machined slot could be again that the fluence was too high (as stated above).

a) 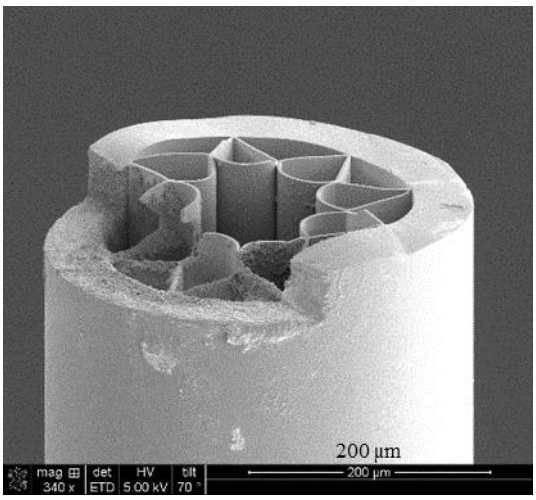

b) 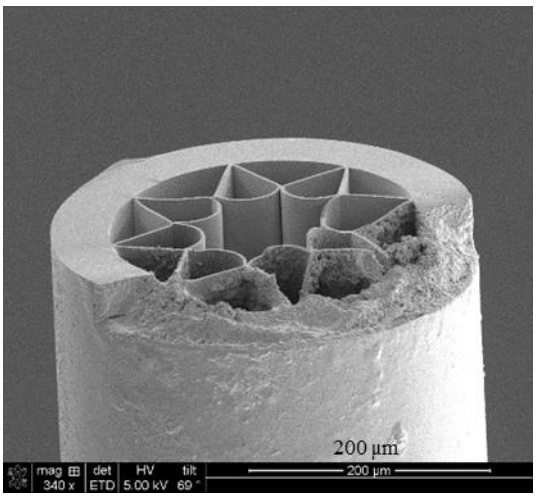

Figure 4.12. a) SEM image of a combined structure of 31 planes followed by 15 planes with a 2.5 µm increment in z and a pulse energy of 2 µJ and b) SEM image of a combined structure of 31 planes followed by 20 planes with a 2.5 µm increment in z and a pulse energy of 2 µJ.

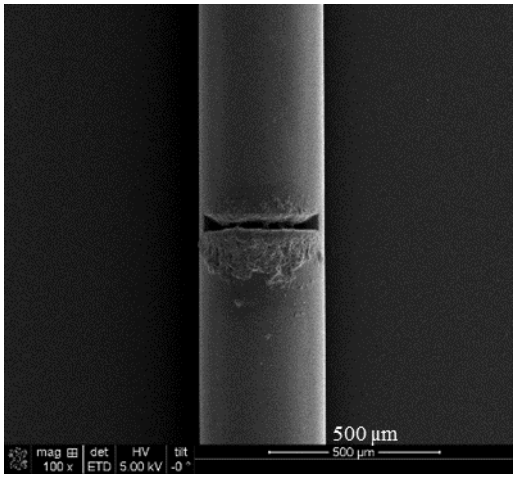

Figure 4.13. a) Top view SEM image of a combined structure 31 planes followed by 15 planes with a 2.5 µm increment in z and a pulse energy of 2 µJ.

To assess the repeatability of the machining protocol the combined structure of 31 with 15 planes with 2.5 µm of increment with 2 µJ was repeated. From the image in Figure 4.14 the results are noticeably different (see Figure 4.12 a) and the machined region is not well defined.

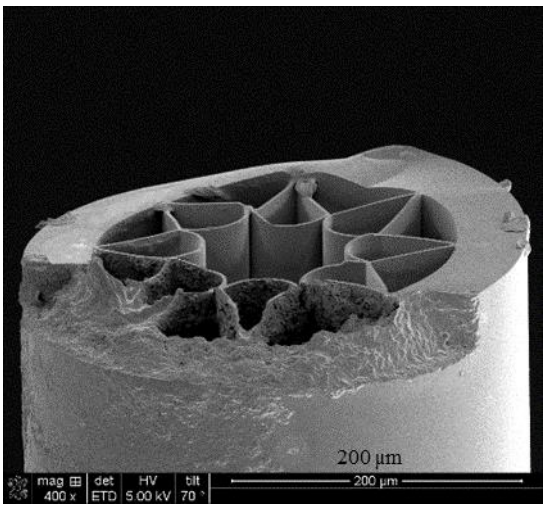

Figure 4.14. a) Repetition of the combined structure of 31 planes followed by 15 planes with a 2.5 µm increment in z and a pulse energy of 2 µJ.

Some possible causes for this above-mentioned issue are:

a) Heating of the stages during processing: This could cause an influence due to conduction of the heat to the sample (as suspected in Chapter 3 section 3.2 and subsection 3.2.1, part a);

b) Accurate location of the position where the machining starts: In the above method the middle position of the fibre is found and used as the starting point for machining. In order for this to work this starting point should be the highest point on the fibre (relative to the laser beam focus). If this is not accurately located then the machining would initiate in the wrong starting position which could lead to an uneven machining across the fibre width. In Chapter 5 improvements to the machining protocol are presented to alleviate such issues.

4.3 Discussion in context of published work

The scanning method proposed here has not previously been applied to the fs laser machining of optical fibres. Some references use the translation in z to machine structures in three-dimensions, such as microchannels [105], [106], drilling holes in glass [100] and waveguides [107], [108] and a more recent work reports the use of a Tunable Acoustic Gradient Index lens to achieve different focal positions [102]. The multi-step scanning methodology has also been reported for the FIB machining [109] and details of these references will be demonstrated below.

The translation in z axis, more specifically the scanning in z was reported recently as a way to achieve precise control of the laser beam position to accomplish optimal efficiency [102]. The authors suggest scanning the laser focal point along the optical axis using an acoustically driven variable focal length lens. They report higher machining rates in a range of defocus distances and noticed a more significant effect when the laser energy was increased achieving a threefold increase in the machining rate of the silicon [102].

The experimental set-up consisted of a Nd:YVO_4 laser, at 355 nm, 15 ns of pulse duration. A Tunable Acoustic Gradient Index lens focus the laser light onto a substrate (500 µm thick silicon water, using a microscope objective of 5× and NA 0.13. The tunable lens is an ultrafast vari-focal device with a lens power that varies sinusoidally with the oscillation frequency (140 kHz) and results in an adjustable focus position after the objective (scanning range). The spacing between pulses was 1 µm. and the repetition rate was 1 kHz. The passes were performed by a bidirectional line scanning over the whole square using a 15× microscope objective and a Nd:YAG laser of 355 nm and 30 ps. A similar set-up was also used for machining of Kapton with thickness of 135 µm. The scanning range was from 0.45-1.21 m^{-1} of lens optical power, and from 0.73-2.09 mm for the 5× microscope objective and 0.09-0.27 mm for the 15× microscope objective. A square hole (200 × 200 µm) was machined in a 500 µm thick silicon wafer with and without z scanning. Without z scanning, four passes are needed to perform the square hole and with scanning the machined rate was approximately doubled with the machining being 88% complete after 2 passes and 100% complete after 3. Without scanning and after four passes the average rate machining was of 9.04 $\times 10^8$ mm^3 per pulse and the machining rate was 2.50×10^7 mm^3 per pulse using a lens power of 1.06 m^{-1}. Also, using 0.7 m^{-1} of lens power, 3 passes were needed and using 1.21 m^{-1} only two passes were needed. However, the authors noticed that the increase of the machining rate brought some degradation on the machining quality (poor lateral resolution and wall angle) [102]. This conclusion can be compared to the work shown in this thesis where an optimal increment in z is needed in order to have a compromise between machining rate and a high quality machining.

Also regarding the scanning methodology showed in this Chapter, it is possible to see the application of a multistep scanning method to obtain a predictive divergence

compensation approach on the Focused Ion Beam (FIB) machining to create three-dimensional structures [109].

Although the commercial FIB systems present a bitmap milling method for the fabrication of complex structures, the milling depth for each pixel is controlled by the local colour of the input map and the fabricated structures diverge from the original design. This happens due to atom redeposition, the overlap effect of the ion beam and the variation of the sputter yield under different angles. These causes are intrinsic to the nature of the FIB machining mechanism. Therefore, this reference shows a predictive divergence compensation approach [109] that allowed the correction of the fabricated divergence using a pre-generated corrected bitmap and a rapid technique for achieving three-dimensional structures with high precision [109].

The structures performed were: a parabolic structure with 2.5 µm of amplitude and 10 µm of width, two hemispherical structures of radius 5 µm and 500 nm and a sinusoidal structure of period 5 µm and amplitude 0.9 µm (filled with platinum before cross-sectioning). These were fabricated on a P-type silicon substrate and the system used was a dual beam FIB system with gallium liquid-metal ion sources working with an acceleration voltage of 30 kV. The beam diameter (FWHM) was 50 nm and the ion current was 1 nA. The number of scanning passes for each bitmap was calculated having in account several parameters such as the sputter yield at a zero degree, the coefficient which compensates the ion beam overlap, the ion current and the electron charge [109].

The authors mentioned that using a multi-pass scanning reduces the re-deposition caused by secondary scattered atoms (due to the incident ion beam), since this way some deposited atoms can be removed by the next scanning pass being also beneficial for the formation of an uniform shape at the bottom of the groove [109].

Although the machining methodology in reference [109] is different from the one used in this work, as well as the machined substrate, this is a good example of the step scanning methodology, since the re-deposition effect that happens during the FIB milling can be compared with the one that occurs during the laser machining. Both machining methods improved with the scanning methodology. As mentioned above, in section 4.1 it was

decided to reduce the number of planes performed (therefore the number of steps) to obtain a well-defined structure with less re-deposition on top being this deposition related to the fluence [81] as explained above.

The translation in z of the sample with respect to the laser is also reported for producing microholes in soda lime glass [105] and in silica glass [106]. However, these methods (shown below) are different from the method used in this work since they are water-assisted and the translation movement was used to define a structure but not additionally to control the depth achieved. Also, the dimensions of the structures are much smaller than the structures achieved in this work.

Reference [105] shows longitudinal and transverse microholes drilled in soda-lime glass by water assisted ablation with femtosecond laser pulses. The wavelength used was 800 nm at 1 kHz of repetition rate and the laser beam propagated along the z direction. The lens used to focus the beam had a numerical aperture of 0.50 NA. The soda-lime sample was mounted on a computer-controlled x, y and z translation microstage with 0.1 µm resolution. During the drilling, the rear surface was in contact with deionised water. The pulse duration was 380 fs and the pulse energy used was 1.4 µJ. To obtain the three-dimensional microchannel, first a longitudinal microhole was drilled for the inflow of the water. The laser focus was positioned at the rear surface of the sample and then moved through the sample along the z direction step by step. The translation step was 1 µm and about 50 pulses irradiated on each paused spot [105].

The microhole was elongated due to the inflow of the water achieving a hole diameter of 3 µm. When the hole reached a length of 35 µm (A to B in Figure 4.15) the translation direction was changed to -x producing a transverse microhole of 20 µm. (B to C, Figure 4.15). When this step was achieved, the translation was changed to -y producing another microhole of 20 µm, (C to D, Figure 4.15) resulting a three-dimensional microchannel of one longitudinal and two transverse holes. The authors achieved the drilling of the microchannels, controlling the translation direction [105].

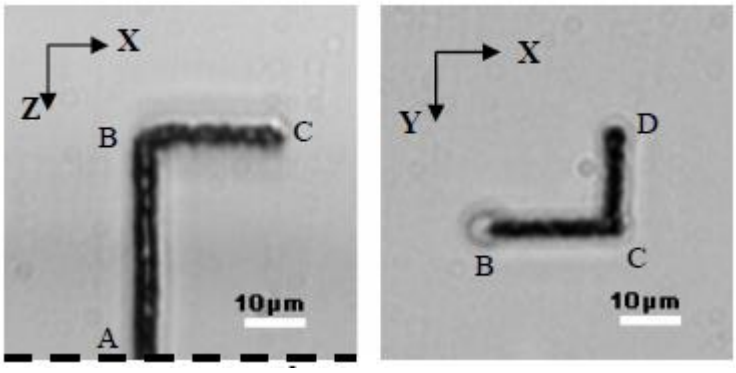

a) b)

Figure 4.15 Drilled microchannel at 1.4 µJ pulse energy: a) side view and b) top view. The beginning of the drilling was at point A, for A to B the translation was in the z direction, B to C in the x direction and C to D in the y direction [105].

In reference [106] the production of three-dimensional holes with the femtosecond laser pulses in a single step is shown, moving the silica glass in a preprogramed structure. Distilled water was also used, due to its advantages: the effects of blocking and re-deposition of the ablated material can be reduced and the aspect ratio of the hole can be increased. The dimensions of the holes were 4 µm in diameter and 200 µm in depth. Similar to the method above, with a combination of parallel and perpendicular channels, the authors could produce three-dimensional holes. The main disadvantage of this water assisted method is that when the length of the channel increases, the debris can no longer be ejected from the microchannel which may cause clogging and termination of the microchannel [110]. Also, the water adds and additional complication to the machining protocol and would be more difficult to scale-up.

The method of translating the sample in three axes is also performed to inscribe waveguides in different positions of a substrate [108] to fabricate a fan-out device. The authors used an ultrafast-laser waveguide-inscription that allows each core of a multicore optical fibre to be addressed by a single mode fibre held in a fibre V-groove array. The authors used a three-dimension fabrication capability to demonstrate the coupling between the fibre-groove array consisting of a one-dimensional array of fibre and a multicore optical fibre consisting of a two-dimensional array of cores. The laser used was also a Ti:Sapphire laser at 800 nm and to fabricate the waveguides the pulse train was focused 200 µm below the surface of a multi-component (predominantly silica glass) mounted to an automated Newport linear travel x, y and z translation stages. The

waveguides were created by translating the substrate material in 3 dimensions through the focus of the laser beam. The speed was 400 μm/s and the pulse energy used was 1.3 μJ. For waveguides 1 and 4 the middle connecting section required a 50 μm translation in the z axis, a 350 μm translation in the x axis and a 20 mm translation along the y-axis. For waveguides 2 and 3, the middle section required no z-axis translation, a 100 μm translation along the x axis and a 20 mm translation along the y axis. The final device length was 25.0 mm along the y-axis [108]. The aim of the work shown in this reference is to fabricate waveguides in different positions of the substrate and to do that the translation in z is performed. Being so, this work is an example of the use of the femtosecond laser machining on silica glass using the translation in z.

As a conclusion for this method comparison, the importance of translating the focal position to accomplish optimal efficiency has been reported where a method to scan in different z positions with a Tunable Acoustic Gradient Index lens was shown in a silicon wafer [102]. This reference is a good example of the importance of optimising the scanning method in order to obtain a good quality machining was shown.

The value of a multi-pass scanning is presented in reference [109]. Although the reference uses a FIB machining method, the authors noticed that, it is important reduce the re-deposition caused by scattered atoms and it is possible to do so by doing several scanning passes is useful to remove the scattered atoms and to achieve a uniform shape.

The translation in z of the sample with respect to the laser has been reported previously but this was used to produce microholes (in soda lime glass [105] and in silica glass [106]). These are water-assisted and the translation movement was used to define a structure (and not to improve the depth achieved).

4.4 Summary

A new machining strategy was presented in this Chapter 4 which consisted of scanning lines in x (2 mm) along a certain distance in y (50 μm). This scanning lines method was repeated for several planes in z. Each plane is made on the same x and y coordinates of the fibre but with different z positions. The distance between the lines was 0.5 μm (y

distance). The machining protocol starts with focus above the surface and then the repeated planes are performed. When a plane is completed, there is a translation in the z direction then the next z plane is scanned, and so on until a certain theoretical depth is achieved. Small increments (of 0.5, 1.0, 2.0, 2.5, and 5.0 μm) in z between each plane were investigated to optimise the material removal.

The best results obtained with regards to both the depth achieved and the quality of the machined structures where the scanning lines were machined in repeated planes with small increments in z and low pulse energy. The small increments in z ensured a better control of the material removal to achieve deeper structures. The most promising results were done using 2.5 μm increment for 31 planes machined in the cladding and 2.5 μm increment for the 15 planes machined on the cladding web at 2 μJ.

Unfortunately, a lack of repeatability was observed (some machining areas were smooth others were irregular, for the same experimental conditions) and hence a modified protocol was investigated and is reported in Chapter 5.

The translation in z of the sample with respect to the laser has been reported previously but this was used to produce microholes (in soda lime glass [105] and in silica glass [106]). These methods are different from the methodology here since they are water-assisted and the translation movement was used to define a structure not to increase or control the depth achieved. Also, the dimensions of the structures reported in [105] and [106] are smaller than the structures achieved in this work.

The importance of translating the focal position to accomplish optimal efficiency has also been reported where a method to scan in different z positions with a Tunable Acoustic Gradient Index lens was shown [102] in a silicon wafer. In this reference the importance of optimising the scanning method in order to obtain a good quality machining was shown. A compromise between the machining quality and the machining rate was presented, and it was observed that increasing the machining rate brought some degradation of the machining quality (poor lateral resolution and wall angle. Without scanning, and after four passes, the average rate machining was of 9.04×10^{8} mm^3 per pulse and the machining rate was 2.50×10^{7} mm^3 per pulse using a lens power of 1.06 m^{-1}.

This can be compared to the work shown in this thesis where a study to optimise the increment in z was needed in order to have a compromise between the machining rate and quality.

Also reported in the literature is the value of a multi-pass scanning [109]. Although the reference uses a FIB machining method, the authors noticed that, in order to reduce the re-deposition caused by scattered atoms, doing several scanning passes is useful to remove the scattered atoms and to achieve a uniform shape (this re-deposition is comparable to the deposition observed by laser machining on the fibres).

Chapter 5 – Improved protocol for machining of slots in Negative Curvature Fibre

In this Chapter, a specific machining technique employing a more robust protocol (compared with the process described in Chapter 4) with the aim of improving repeatability and definition of the machined slots in the NCF is described. The repeatability of the scanning lines with increments in the z axis will be assessed and improved results for machining of the NCF will be shown. The samples were analysed with a Scanning Electron Microscope (SEM) at high-vacuum, model FEI Quanta 3D FEG.

5.1 Modification of Machining Protocol

Previous work [12] reports the difficulty to drill a straight sided hole directly in a bulk transparent material and obtaining a three-dimensional hole requires multi-step methods [12]. An example of this is femtosecond laser machining followed by heat treatment and subsequent etching in a dilute aqueous hydrofluoric acid (HF) solution [83], [104]. It has been shown that simple drilling is not sufficient to achieve high precision, high quality and high processing efficiency [81] and also does not provide a route to machining more complex shapes in to fibres such as the NCF. The process described in Chapter 4 was shown to not have the necessary repeatability. The proposed causes for the lack of repeatability are:

a) Thermal effects of the translation stages: the stages tend to heat during the process resulting in a small (order of microns) dimensional change or expansion. This also could affect the sample via heat conduction (as observed in Chapter 3);
b) Locating the position where the machining starts: the middle position of the fibre was found (using the *Find the Fibre* code) and used as the starting location for machining on the assumption that the fibre is perfectly round. However, locating the top surface or the highest position on the fibre is more critical particularly when using very small z increments and with a small focal volume. If a reliable starting point isn't used the repeatability of the results will be affected and non-symmetrical machining result through the fibre structure occurs.

Therefore, modifications to the machining protocol were made in order to address points a) and b). These changes consisted of:

1. An additional step during the *Find the Fibre* program: after finding the middle position, the stages were moved 5 µm left and right to see if the laser is in focus on the highest part of the fibre. If the laser is not on focus on the highest part of the fibre, a change in the peak focal position (as shown in Chapter 3, Figure 3.4) will be noticed. This is possible to distinguish because the reflected beam light spot, which is circular, will appear non-circular and the peak height will also change. (see Figure 3.4 a) and b) from Chapter 3)
    a. If the laser is focused on the highest part, when moving away either side from that spot the laser will be out of focus, the peak height will decrease and the beam reflected light will be non-circular (Figure 3.4 a and b from Chapter 3).
    b. In a similar way, if the laser was not in focus in the highest part, when moving away to left or right a change in the peak position will happen: the peak height will increase when moving away to left or right and the reflected beam light will appear as a circular spot. This way is possible to see the highest point and determine where is the focal position.

2. Increasing the precision of finding the focal position from 1 µm to 0.1 µm. However, this option is not practical. As explained in Chapter 3, Figure 3.4, the focal position is observed using a camera to monitor the reflected beam and the and the height peak of the focal position. Decreasing the increment in z for 0.1 µm means that changes in the circular shape of the focal position are too small to be assessed.

3. An additional step was performed to deal with the thermal expansion: before running the machining program, a routine called *Heat the Stages* was performed. This runs for approximately 15 min with the shutter off to allow movement of the stages in x, y and z. The movements of the stages follow that of the machining pattern (along 0.100 mm in y and 1.000 mm in x) and it also does two planes with 2.5 µm increment in z. This step was used as a precaution, to allow the stages to

warm up due to the movements in x, y and z. This program is shown in Appendix F. A scheme of these changes on the protocol can be found in Figure 5.1.

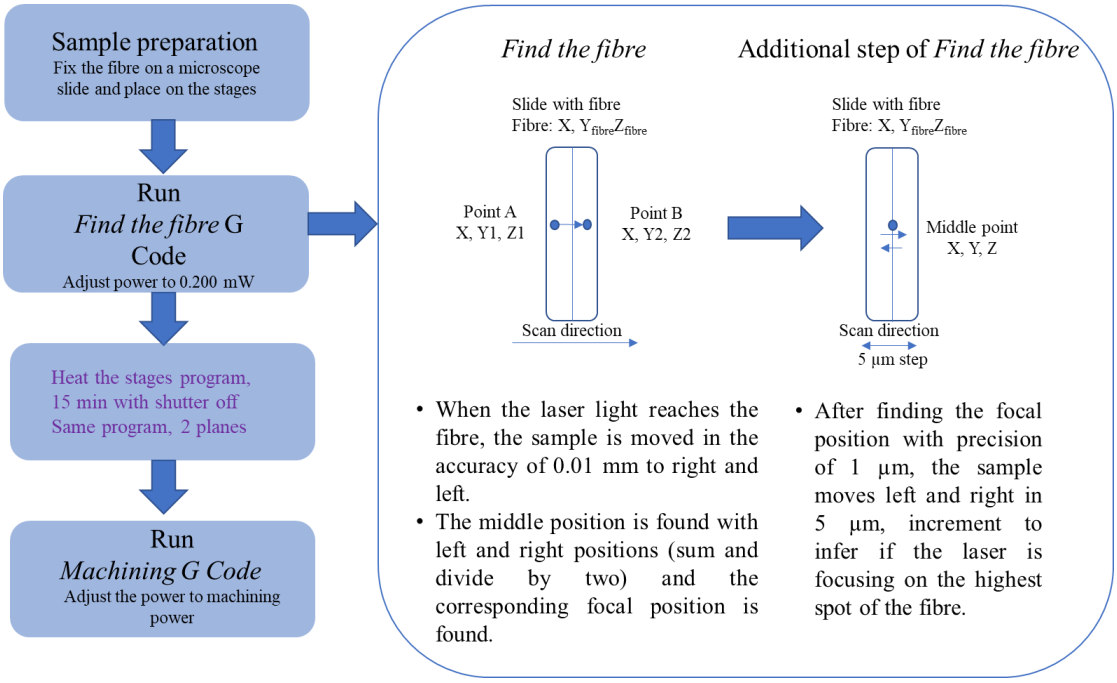

Figure 5.1 Scheme of the new procedure for machining NCF. The additional steps are adding the *Heat the Stages* program and an improvement of the *Find the fibre* procedure.

The machining of the scanning lines with increments in z position is done with increments of 2.5 µm in z with a line spacing of 0.5 µm and a speed of 1 mm/s corresponding to 84.16% overlap.

The dimension of the scanning lines was adjusted accordingly to the desired structure size: for example, a longer structure (along the axis of the fibre) was performed with 0.100 mm or 0.150 mm in y. The dimension in x was sufficient to ensure that the stages have time to accelerate and decelerate. In some cases, 1.000 mm of travel in x was used but it was deemed that between 0.400 and 0.500mm would be sufficient. The fibre used, had a diameter of approximately 360 µm. The acceleration and deceleration of the stages was 120 mm s^{-2} and the scanning speed used (1 mm/s). Based on this, the distance needed for the stages to accelerate and decelerate was calculated as 8.33 µm. The example of the G Code of the structures can be consulted in Appendices D and E.

Since this method requires several planes, it also requires more machining time (which also depend on the length of the lines):

a) if the planes have 1.000 mm in x and 0.100 mm in y it takes approximately 8 min:
    - So, in order to reach the cladding, it will be needed 6h and 15 min (including *heat the stages* program);
b) If the planes have 0.400 mm in x and 0.150 mm in y it takes approximately 6 min:
    - So, in order to reach the cladding, it will be needed approximately 5h and to reach the core approximately 6h;
c) If the planes have 0.500 mm in x and 0.100 mm in y it takes approximately 4 min:
    - In case of reaching the cladding, it is 3h30 min and to reach the core it will take 4h.

5.2 Results of the NCF Machined with the New Protocol

5.2.1 Machining of NCF for guidance at 3 µm

In Figure 5.2, the cross section of an NCF for guidance at 3 µm is shown. The fibre was produced by the group of Professor Jonathan Knight at the University of Bath. The fibre has an inner diameter (measured with the SEM microscope) of approximately 256 µm (excluding the solid cladding), a core diameter of 94 µm. The thickness of the solid is 50 µm.

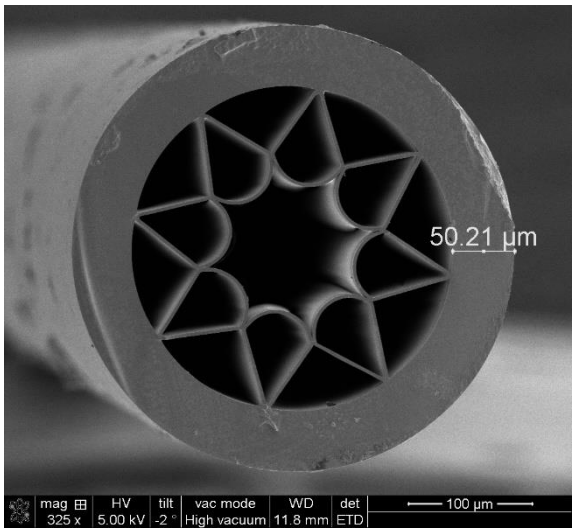

Figure 5.2 SEM picture of an NFC fibre for guidance at 3 µm fabricated at University of Bath.

It has been shown previously (in Chapter 4) that the best results were obtained for pulse energies of 2 µJ and 1 µJ and these were again repeated with the new protocol, Figure 5.3 and 5.4.

a) 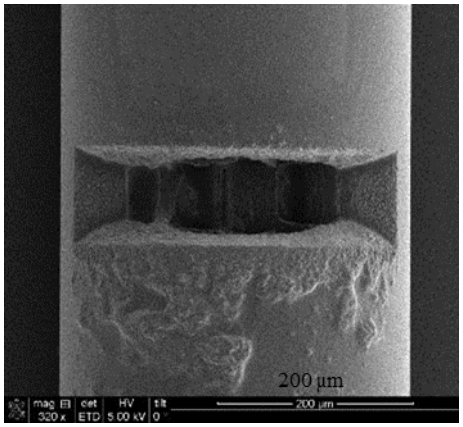

b) 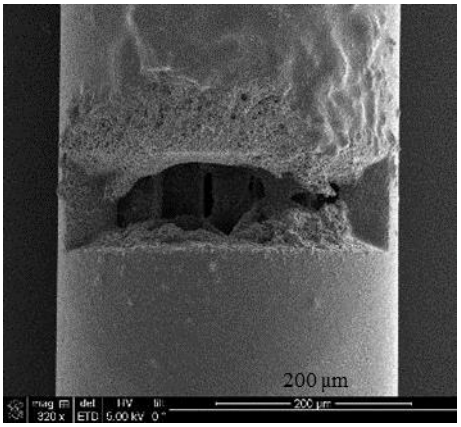

Figure 5.3 a) and b) Two different machining experiments using the same pulse energy of 1 µJ. As it can be seen, there is noticeable material deposition on the fibre and the results are not repeatable.

a) 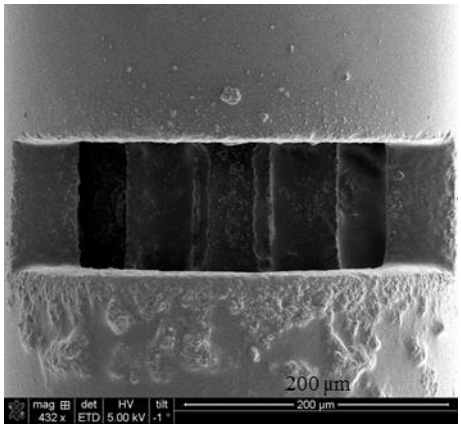

b) 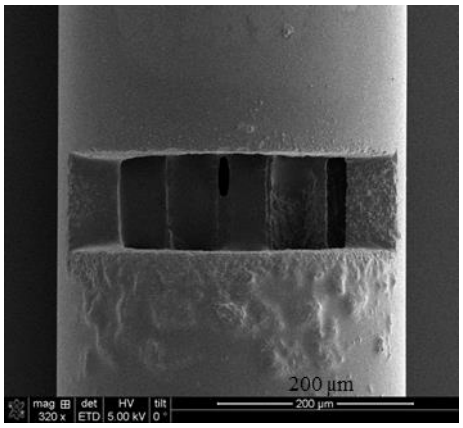

Figure 5.4 a and b) Two different machining experiments using the same pulse energy of 2 µJ. Improved consistency is achieved in comparison with the result using 1 µJ and less re-deposited material is observed on the fibre.

Figure 5.3 a) and b) show two different machining experiments using the same pulse energy and in Figure 5.3 b) it is possible to see more deposited material on top of the fibre and on top of the structure.

As is shown in Figure 5.4 the best results were obtained for a pulse energy of 2 µJ as in this regime there is adequate energy to expel the material from the cladding without re-

deposition. As in accordance with reference [81], usually, for drilled holes, high fluences are needed to allow material expulsion in order to give enough kinetic energy for the ejected particles to escape from the hole [81]. The fluence was calculated using the total laser pulse energy divided by the effective focal spot area. The beam radius calculations are shown in Chapter 3, subsection 3.1.2 and it was calculated using the definition that the beam radius is defined as the distance from the beam axis where the optical intensity drops to $1/e^2$ (13.5%) of the value on the beam axis.

With 1 µJ pulse energy corresponding to 79.82 J/cm^2 the fluence was not enough to expel the material entirely from the machined region in the cladding and also there is significant re-deposited material around the machined region. This is particularly evident in Figure 5.3 b). However, with 2 µJ of pulse energy and a fluence of 159.64 J/cm^2 the structure is clean without any material deposited on around the machined structure.

The dimensions used in the G Code were 1.000 mm in x and 0.100 mm in y. These experiments were performed with one plane located on the top surface of the fibre (as located using the revised *Find the Fibre* program) followed by 43 planes below the top surface of the fibre. In order to ensure that the top surface was machined the process was started using 2 planes above the location of the top surface. A simplified diagram of this overall process can be seen in Figure 5.5.

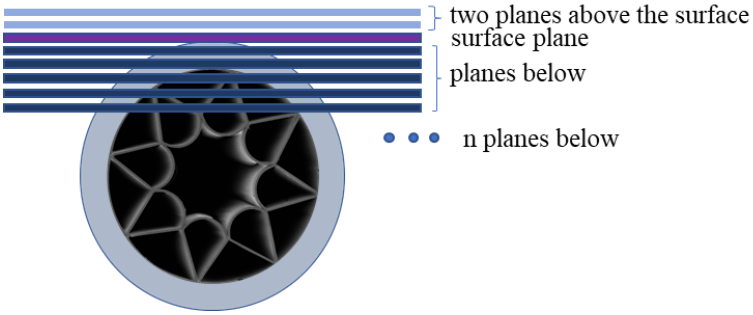

Figure 5.5 Simplified diagram of the machining process (not to scale) showing the two planes above the surface (light blue), one at the surface (purple) and several (n planes) below (dark blue).

Using 43 planes below the top surface was considered as a feasible starting point because the best results shown in Chapter 4 were obtained using 28+15 plains (noting that the +15 planes have smaller dimensions in x and y than the preceding 28 but all with the same

increment in z of 2.5 µm). With 43 planes below the surface, the region that was intended to be machined was the entire cladding web reaching a theoretical depth (form the top surface) of 107.5 µm (43 planes × 2.5 µm) depth, leaving the cladding web edges intact, Figure 5.4 showing the experimental result and Figure 5.6 showing a diagrammatic representation of planned machining result. With 53 planes it was expected that the core would be reached being the theoretical depth 132.5 µm. Figure 5.6 b). As mentioned above all the tests were performed with 2 planes above and one on the surface, but to simplify the results refer only to the number of planes below the top surface.

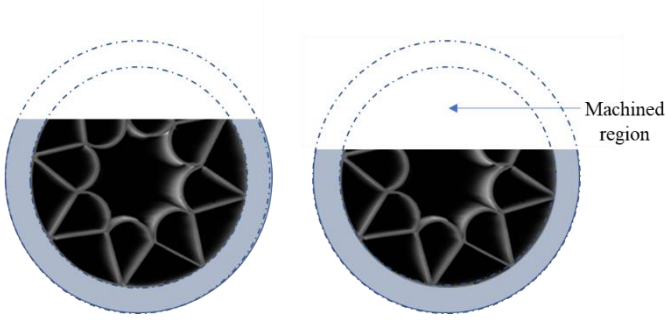

a) b)

Figure 5.6 Simplified diagram) showing the machining result that should be expected using a) the 43 planes and b) 53 planes.

Analysing Figure 5.7 a) and b) it is possible to see the exposed NCF cladding web structure. Figure 5.7 c) confirms the machining has reached part of the cladding web structure.

a) 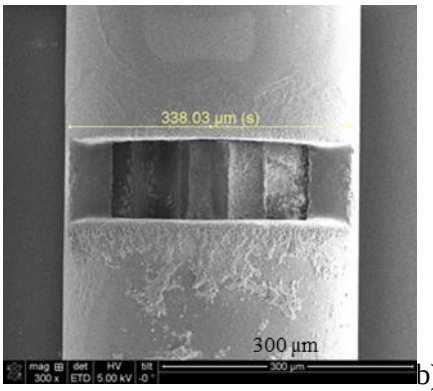

b) 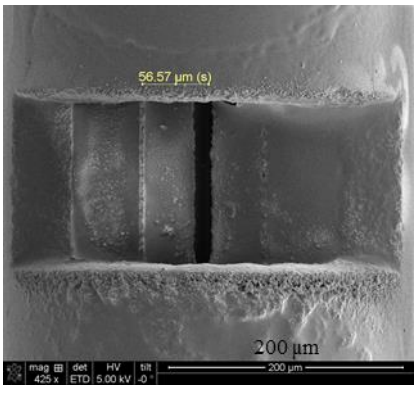

c) 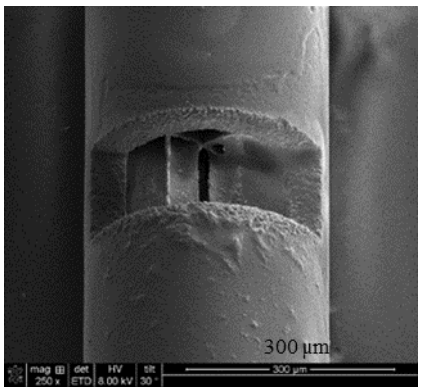

Figure 5.7 Machining performed with 43 planes below the surface: a) first trial with 0.100 mm in y and 0.500 mm in x and, b) second trial with increased dimension in y (0.150 mm) to allow better visualisation and c) different point of view of the second trial.

Having chosen the optimal pulse energy, tests with 43 and 53 planes below the surface were performed to check if the protocol changes were effective in ensuring the repeatability of the results and obtaining a well-defined and clean machined structure. The dimensions on the G Code used were 0.500 mm in x and 0.100 mm in y or 0.400 mm in x and 0.150 mm in y (the larger length in y was used to make it easier to observe the depth achieved using the SEM).

The fibre has an inner diameter (measured with SEM microscope) of approximately 256 µm (without the solid cladding) and a core diameter of 94 µm the difference will give 162 µm. If we divide 162 by 2 and sum the cladding thickness, 50 µm, Figure 5.2, it will give the minimum value it is needed to ablate to reach the core of 131 µm. With 53 planes machined below the surface, the expected depth would be 132.5 µm and hence should be enough to machine to the hollow fibre core.

Figures 5.8 a) and b) suggest that the exposed part of the web structure is the region at the bottom of the hollow core and Figure 5.7 c) confirms that the machined depth has reached the core, showing the bottom part of the cladding web. This result shows that by applying the revised protocol a methodology to machine the NCF in order to reach and expose the hollow core is possible as proposed by the original machining strategy (Chapter 1, Figure 1.1). This machined region is well-defined and there is little or no damage to the delicate web structure. Additionally, re-deposited material has been minimised.

Furthermore, the results from Figure 5.7 and 5.8 show the new protocol is effective, since the method is repeatable and shows well defined machined structures or slots. This was achieved by ensuring that the point where the machining starts is the highest point on the fibre (near the middle of the fibre) as opposed to using the exact middle of the fibre.

a) 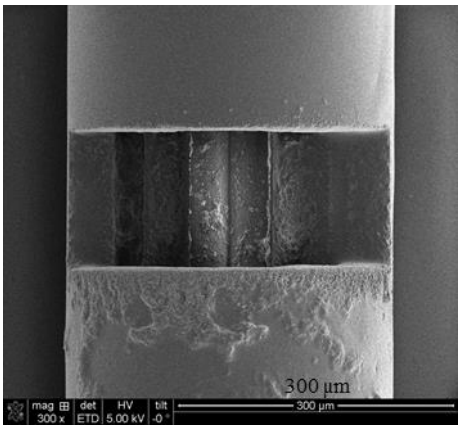

b) 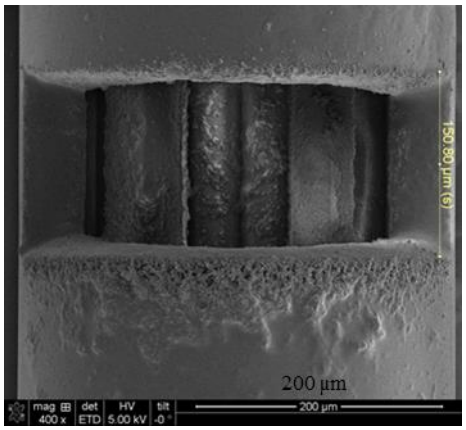

c) 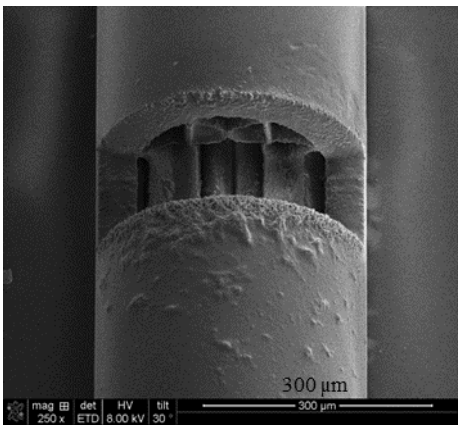

Figure 5.8 Machining performed with 53 planes below the surface. a) first trial with 0.100 mm in y and 0.500 mm in x and, b) second trial with increased dimension in y (0.150 mm) to allow better visualisation and c) different point of view of the second trial.

After these successful results, trials with 58 planes were also performed. The aim of this experiment was to reach a depth of 145 µm to assess if this would be a better result than that obtained with 53 planes below the surface (a depth of 132.5 µm).

It should be noted that the position where the machining is performed in terms of the orientation of the cladding web with respect to the incident laser will have an influence on the machining process. To make sure the machining is performed always in the same position with respect to the cladding web 3 machining trails were performed on the same fibre with the different depths, Figure 5.9.

As can be observed in Figure 5.9 a) and b), the structure performed with 58 planes is shallower than the calculated expected depth of 145 μm. This was due to an unexpected drop of laser power during the machining process. Therefore, a repetition of the structure with 58 planes was done and in Figure 5.10 it is possible to see the 43 planes, the 53 planes and the repetition of 58 planes.

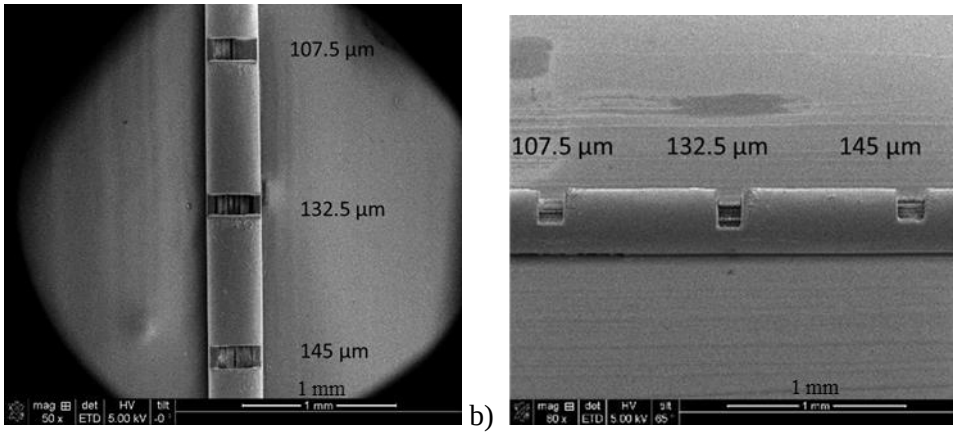

Figure 5.9 Three slots on the same fibre with different planes to achieve different theoretically depths: 43 planes achieving a calculated depth of 107.5 μm; 53 planes achieving a calculated depth of 132.5 μm and 58 planes achieving a calculated depth of 145 μm a) and b) different angle view.

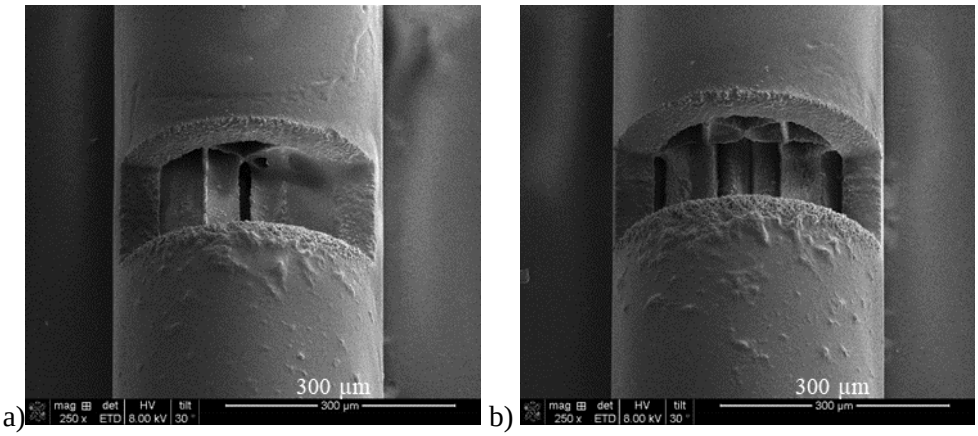

c) 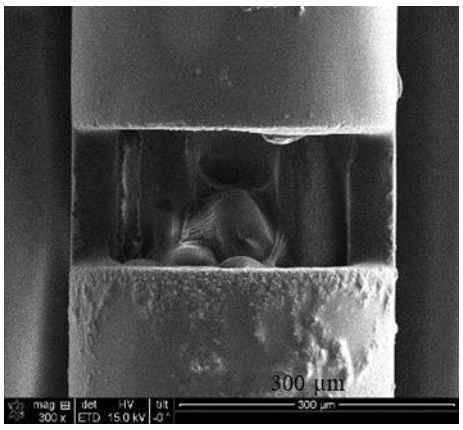

d) 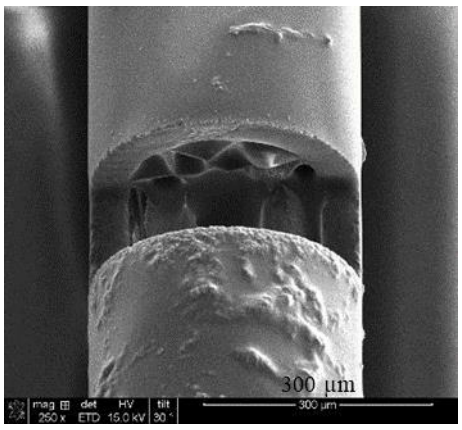

Figure 5.10 Machined structures on NCF with a) 43 planes, b) 53 planes and c) and d) with 58 planes below the surface.

The results above suggest machining with 53 planes is better than with 58 planes below the surface, although both structures reach the core. With 58 planes there is noticeably more deposited material on the top of the structure, as it is evident on Figure 5.7 c). Also, with 53 planes there is less debris around the structure. The fluence is directly proportional to the pulse energy however, by increasing the number of planes the total cumulative energy input over the machined area is also increased resulting in more ejected and re-deposited material. It is known that at high fluence, the formation of a dense, high temperature plasma is formed and the material is removed in plasma, liquid and vapours phases. The molten material is expelled due to the plasma expansion and then vaporisation process and results in debris or droplets condensing or re-depositing on the surface of the fibre [81].

It is only possible to get an accurate measure of the depth machined using the SEM by cleaving the fibre. However, this was not done in this case since cleaving could damage the fragile cladding web structure. Nevertheless, in the images in Figure 5.10 it is clearly observed that machining has removed the solid cladding and exposed the cladding web and the hollow core. In Figure 5.11, there is a scheme of the top view of the fibre showing the machining fibre when the machining reached the top part of the cladding web a) and when the machining reached the bottom part of the cladding web, b) corresponding to Figure 5.10 a) and b) machining with 43 and 53 planes

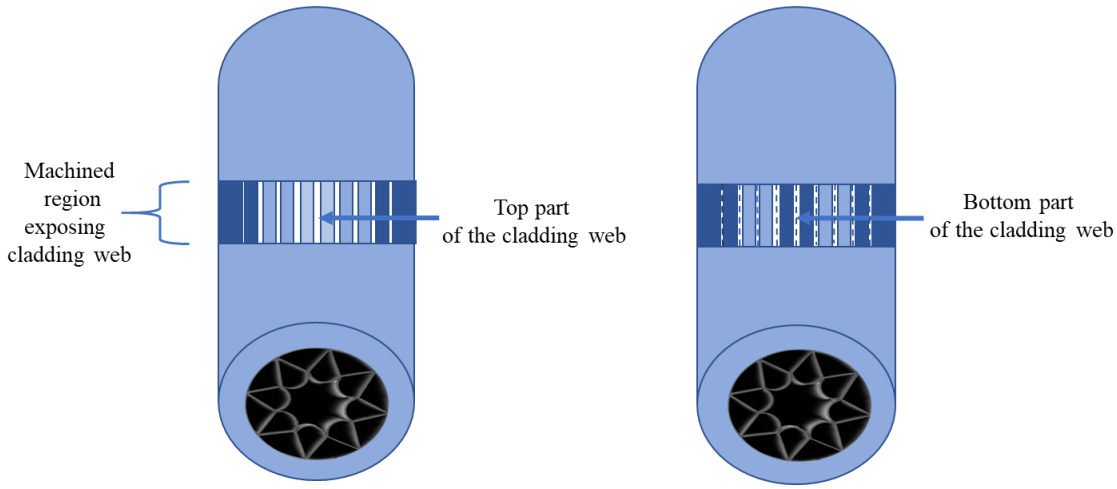

Figure 5.11. Scheme of the machining when the machining reached the top part of the cladding web a) and when the machining reached the bottom part of the cladding web b).

5.2.2 Machining of NCF for guidance at 1 µm

An SEM image of the fibre used for guidance at 1 µm can be seen in Figure 5.12. The fibre was produced at the University of Bath by the group of Professor Jonathan Knight. The core and external diameter are 21 µm and 157 µm and respectively (as opposed to 94 µm and approximately 360 µm for the 3 µm guidance fibre described above, core and external diameter respectively).

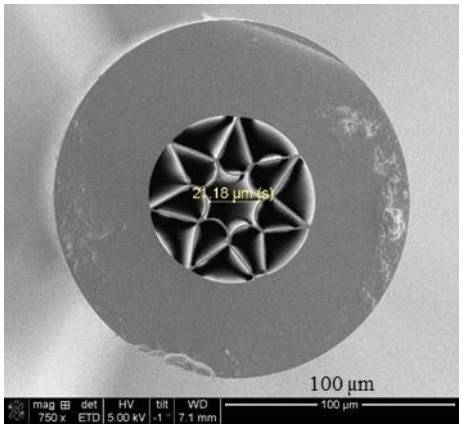

Figure 5.12. SEM picture of the NCF cross section for 1 µm guidance used in this work with an external and core diameter of 157 µm and 21 µm respectively.

The initial trails were aimed to ablate to a depth of 69.5 µm. This time, the external diameter considered was the approximate 160 µm. With each plane increment being 2.5 µm by preforming 29 machined planes the theoretical ablated depth would be

72.5 µm, Figure 5.13 and 5.14. Regarding machining time, for the planes with dimensions 0.400 mm by 0.150 mm, each plane takes 6 min and if 58 planes are done this means in total 6h and 15 min.

The Figures 5.13 and 5.14 verify that the method can be applied for the 1 µm guiding NCF by translating the protocol used for the NCF guiding at 3 µm. However, in Figure 5.12 b) it is possible to see that machining went below the hollow core. Also, the structure shows more damage in the machined area and some debris around the structure compared to the results obtained for the 3 µm NCF.

a) 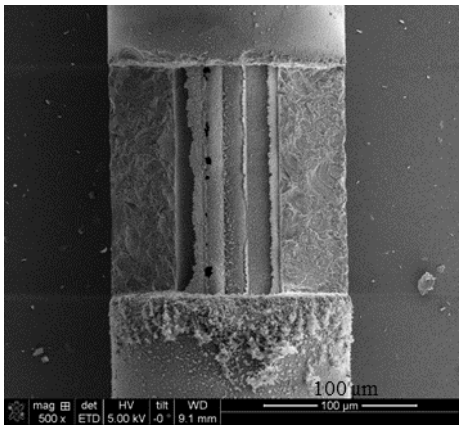

b) 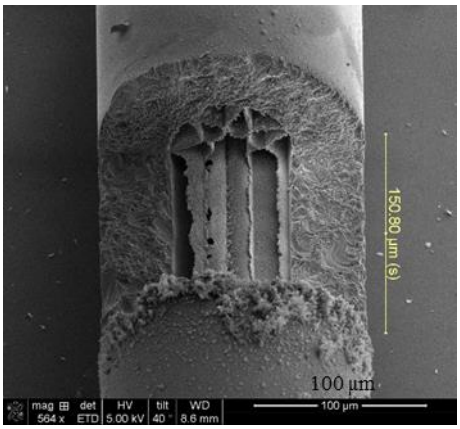

Figure 5.13 NCF for 1 µm guidance machined with 29 planes below the surface with 2.5 µm increment in z: a) top view and b) view with an angle.

a) 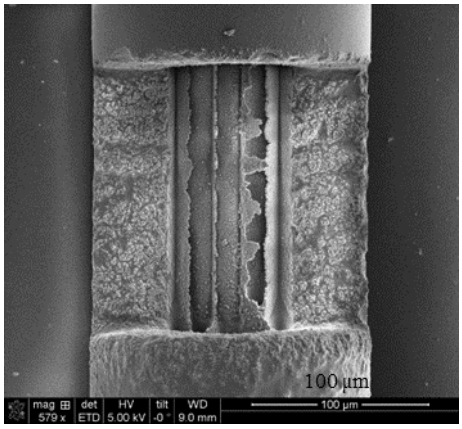

b) 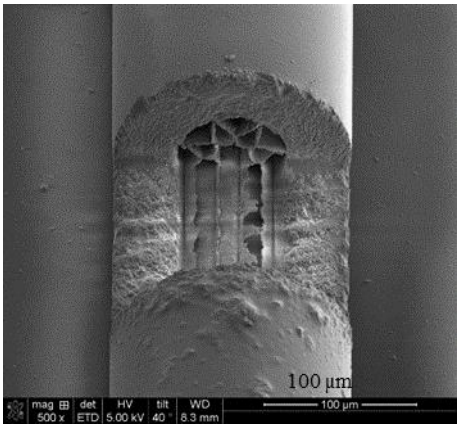

Figure 5.14 Repetition of machining the NCF for 1 µm guidance with 29 planes below the surface, with 2.5 µm, increment in z: a) top view and b) view with an angle.

5.3 Discussion in context of published work

In this section, a comparative analysis of the results with the literature regarding the machining of microstructured or hollow core fibres and its results is exposed regarding the fabrication of holes or microchannels in silica fibres.

Femtosecond laser machined microchannels in Hollow Core Photonic Bandgap Fibres (HC-PBGF) and Suspended-core Holey Fibres (SC-HF) has been reported [8]. Both fibres were fabricated in-house by the stack-and-draw technique. The fibres have an outer diameter of 205 µm, a core diameter of 14.4 µm, a cladding pitch of 4.5 µm and an air filling factor of 94% [8].

The femtosecond laser used was an amplified mode-locked Ti:sapphire laser providing 110 fs duration pulses at 800 nm and a repetition rate of 1 kHz. The diameter of the laser output is 2 mm and passes through a 200 µm diameter aperture. There is also a plano-convex lens pair and a 50× objective with 0.55 of numerical aperture and 10.1 mm of working distance. The spot size at the focal position is 2 µm. The pulse energy used was 13 µJ. The fibres were mounted in V-grooves on a three-dimensional nano-translation stage. A CCD camera imaging though the microscope objective was used to have visual confirmation of focusing [8].

The micromachining was done at the outset, close to focus and decreased gradually as the channel tip moved away from the focus, Figure 5.15 a). The result is a narrowing of the channel beyond the laser focus and with tapering continuing to the hollow core, Figure 5.15 b). The machining was discontinued soon after the core had been breached (to avoid damaging the microstructured cladding beyond the core). Two scoring lines were also inscribed, on each the side of the fibre, to allow the cleaving in the precise spot for analysis. The channel diameter tapers from 20 µm at the fibre surface to a few microns at the core (the total depth is similar to the radius of the fibre). In Figure 5.15 it is possible to see an SEM image of the microchannel done in the HC-PBGF. The authors noticed damage to the microstructure which was more severe at the interface between the solid silica cladding and the microstructured region (debris was also visible) but the channels contained less debris in the remainder of the microstructured cladding as it tapers gradually to the core [8].

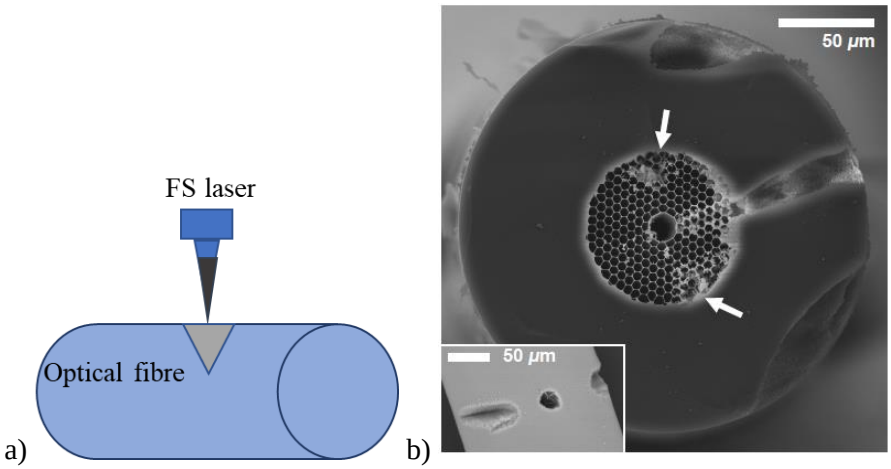

Figure 5.15 a) Simplified scheme of the machining process based on the description of reference [8] and b) SEM image of a microchannel fabricated in HC-PBGF where the arrows show the damage caused by laser scoring. The smaller picture shows the microchannel and the scoring lines in uncoated fibre [8].

The quality of the microchannel machined in coated fibres (i.e. with the polymer jacket in place as opposed to being stripped prior to machining) is similar to the uncoated ones with respect to the depth achieved and the laser-induced damage. The ability to do microchannels in coated HC-PBGF is an advantage concerning device implementation. However, the polymer ablation rate exceeds the fused silica one and as a result the channel entrance appears considerably rougher at the polymer surface. The HC-PBGF was spliced to conventional single mode fibre by arc fusion splicer and each open fibre was places in a gas-tight, windowed interface to allow the filling with acetylene at atmospheric pressure. The diffusion of acetylene was demonstrated though these microchannels and in the case of the two microchannels inscribed in HC-PBGF the out-diffusion rates increased [8].

The work performed in this reference [8] allowed to reach the core of the fibre, however the dimensions of the hole are smaller when compared to the dimensions obtained by the method exposed in this work. Also, the tapering effect happens in this reference due to the way the holes are performed and the damage to the microstructure occurs being more severe at the interface between the solid silica cladding and the microstructured region. Nevertheless, the holes performed by this method allowed the increase of the out-diffusion rates when the diffusion of acetylene was performed after filling the HC-PBG fibre with acetylene.

In reference [16] a gas pressure sensor based on an antiresonant reflecting guidance mechanism in a hollow core fibre (HCF) with an open microchannel has been experimentally demonstrated. The microchannel was machined with femtosecond laser drilling on the ring cladding of the HCF [16]. The sensor has a part with an HCF spliced between two single-mode fibre (SMF) sections and with a microchannel passing through the ring cladding of the HCF in a direction perpendicular to its core. The HCF employed consisted of a 25 μm diameter and a ring-cladding with a thickness 50 μm. The HCF section was spliced to the SMFs using a Fujikura 80S fusion splicer [16].

The femtosecond machining was carried out at a wavelength of 800 nm, with a pulse width of 120 fs and pulse energy of 2 μJ (similar to the one used in this work) at a repetition rate of 1 kHz (in this work was 5 kHz). A microscope objective lens of 20× was used to focus the laser beam. A linear translation stage was used and the scanning speed was 2 μm/s over a total distance of 20 μm, parallel to the fibre axis [16]. After one scanning cycle, the laser beam focus was shifted 10 μm perpendicular to the fibre axis, for the next scanning cycle. These scanning cycles can be compared to the z planes used in this work. After 4 scanning cycles, a V shaped microchannel was fabricated in the cladding of the HCF, allowing the air core pressure equivalent to that of the external pressure. A diagram of the designed pressure sensor and a side and top view of the microchannels created by fs laser machining is shown, Figure 5.16 [16].

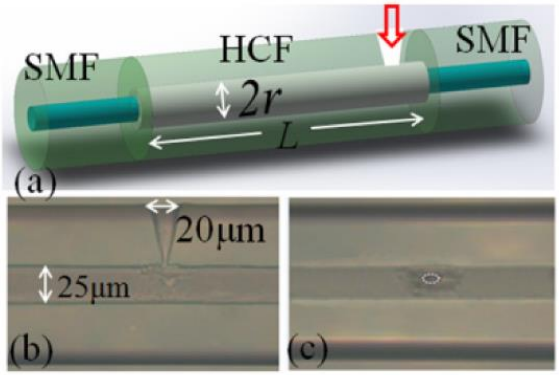

Figure 5.16 a) Pressure sensor showing the two types of fibres, SMF and HCF, b) and c) Microscopy images of the microchannel done with the femtosecond laser machining, side view and top view [16].

The proposed sensor was tested and exhibits a high-pressure sensitivity of 3.592 nm/MPa and a low temperature cross-sensitivity of 7.5 kPa/°C [16]. In this reference, the technique used with the femtosecond laser was very similar to the technique used in this work. The scanning cycles where the laser beam focus was shifted 10 μm perpendicular to the fibre axis, for the next scanning cycle, can be directly compared to the planes used in this work (in this work, the planes were done using a shift or increment in z of 2.5 μm). This reference used a simple fibre: Hollow Core Fibre with 25 μm diameter and a ring-cladding with a thickness 50 μm and the scanning cycles where the laser beam focus was shifted 10 μm perpendicular to the fibre axis worked well to reach the core in this fibre.

However, the planes used in this work use a small increment in z which allow improved precision and better overall quality of the machined structure when comparing Figure 5.16 c) and 5.10 b) for example, working very well with a cladding web. Using larger increments (such as 10 μm as used in [16]) is not suited to removal of the fine microstructured cladding present in fibres such as the NCF. As mentioned in previous results, the increment which allows better machining quality is 2.5 μm although larger increments were also studied (see Chapter 4, sub-section 4.1).

The main advantage of the improved protocol for fs laser machining reported in this Chapter (small increments in z) is the possibility to carry out ablation of the solid cladding while preserving the underlying cladding web structure. Additionally, this advantage opens the possibility to use the improved fs laser machining protocol with other fibres with a much more complicated cladding web such as HC-PBGF or Kagome fibres.

In reference [13] side holes were drilled in four different types of fibre for process development and gas sensing measurements: multi-mode fibre, single mode fibre, HC-PCF and NCF (Bath-HC-PCF). Solid core, single mode and multi-mode fibres were used to evaluate the drilling depth. The system used showed 1 kHz of repetition rate, 100 fs pulses at 790 nm, 1.8 mJ of pulse energy. The authors refer that the ultrafast machining of silica glass typically uses less than 1 μJ. The laser was focused to a 3 μm spot diameter using a 20×, 0.4 NA long working distance objective lens. The side holes were drilled with additional 500 μm long side-hole trenches to cleave and perform the imaging of end-face.

The laser focus remained fixed during the hole fabrication and the fibre sample was traversed below with a high accuracy motion stages controlled by the computer. The side holes were machined using a real-time fibre transmission to indicate when the fibre core was achieved being on the set-up a separate laser coupled into the fibre core. The hole was then performed translating the spot deeper in discrete steps while a photodiode collected transmitted light. The authors noticed the transmitted intensity decreased at 14 µm stage depth for the multi-mode fibre while the single mode fibre transmission decreased at 35 µm. Since these positions were 23 µm above the core, the laser spot removed material is deeper than the indicated by the encoder. Being so, this offset was used to account for the laser depth of focus. Regarding the NCF, a 50 µm diameter side hole was drilled and for the HC-PCF a 38 µm diameter hole was drilled, Figure 5.18. The choice of the hole diameter was made in order to allow the drilling to achieve deeper positions since the authors mention that the depth to diameter ratio was dependent on the numerical aperture of the laser focus (directly proportional).

The NCF was tested for methane absorption measurements and showed the capability of gas detection using side-holes [13]. The NCF used and a side hole drilled on the fibre can be seen in Figure 5.17. However, in Figure 5.17 it is possible to see significant damage on the cladding web structure in comparison to the process used in the thesis and shown in Figures 5.7 and 5.8, for example. Although the authors mention that the cleaving of the fibre after drilling can lead to breakage, the features or holes are smaller than the structures machined in this work.

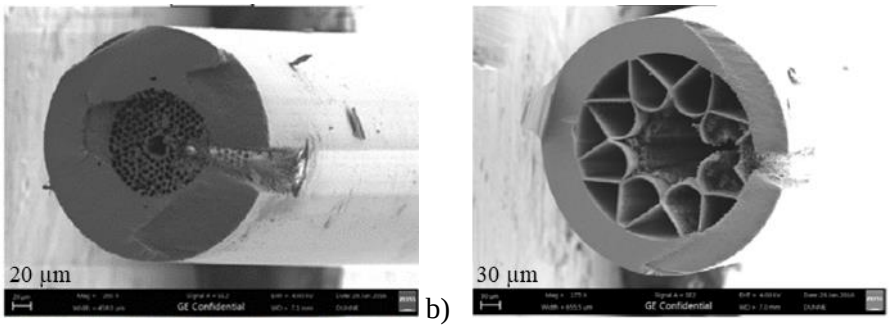

Figure 5.17 SEM image of the side holes drilled on a) HC-PCF and b) NCF [13] adapted from [13].

Nonetheless, the authors have translated the laser spot deeper in discrete steps while a photodiode collected transmitted light, an auxiliary laser was used to measure the

transmitted power and the obtained holes have a conical or V-shape. With this method, (applying a drilling modality) making a larger or more complex structure would not be feasible.

In reference [111] fs laser machining was explored to produce a variable pressure fibre gas cell in a HC-PBGF. Micrometer diameter radial channels were drilled in a HC-PBGF and through these microchannels the core of the fibre was filled with a gas. The fibre cell was formed by fusion splicing and sealing the ends of the fibre to a standard step-index fibre [111]. A commercial, regeneratively amplified Ti:Sapphire laser (Spectra-Physics, Hurricane) capable of 90 fs, 1 mJ, 800 nm at 1 kHz was used. The pulse energy used for drilling the holes was 80 nJ. The lens used was a Zeiss Neofluar 0.9 NA multi-immersion objective. The fibre was held in an index-matching fluid of refractive index of 1.45 and translated through the focus objective at a speed of 1 μm/s with Newport PM-500 stage at 100 nm step sizes. The function of the index-matching fluid was to reduce aberrations from tightly focusing into the cylindrical fibre and also to assist debris removal [111].

The light was circularly polarised to produce a more rounded hole, according to the authors in [111] and [112]. However, reference [113] mentions that the beam polarisation was found to have little effect on the machining results of fused silica.

This method was first tested on a solid core Corning SMF-28E fibre, translating the step-index fibre upward though the laser focus and the drilling performed from the surface to the core on the fibre. The pulse threshold pulse energy was 50 nJ [111].

As the presence of multiple glass-air interfaces constituted a problem when using this method in a HC-PBG fibre, index-matching fluid was continuously pumped though the core and the surrounding capillaries of the fibre during the drilling, to overcome scattering and optical aberrations due to the different surfaces. Also, the use of the fluid adds the advantages of removing debris within the fibre and due to this process, the drilling in HC-PBGF was done from the core to the surface, so the ejected debris would be swept down the capillaries and go out of the fibre [111].

After the drilling the index-matching fluid was removed by flushing the air-core and surrounding capillaries multiple times with methanol and nitrogen gas. Several pulse energies were testes from 50-180 nJ and no increase of the diameter was obtained with an increase of the pulse energy. At higher pulse energies there was more structural damage hence 80 nJ was the pulse energy chosen [111]. In Figure 5.18 the experimental scheme is shown and in Figure 5.19 an example of the fibre drilled hole is presented.

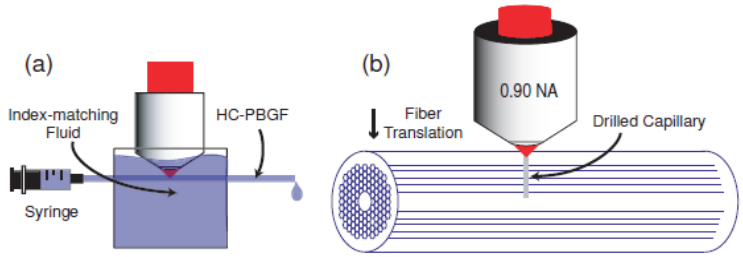

Figure 5.18. a) Experimental set-up for fs laser-drilling. b) Schematic showing the drilling orientation [111].

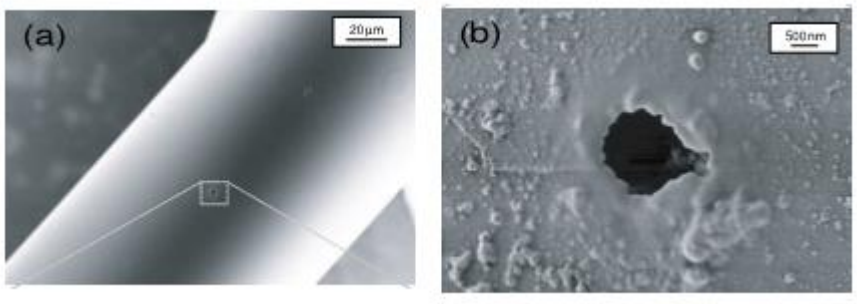

Figure 5.19 a) SEM image of the fs laser drilled holes in HC-PBGF with 80 nJ pulses b) magnified image of the drilled capillary formed in the side of the fibre [111].

The loss due to a single drilled microchannel was measured to be approximately 0.35 dB [111] meaning that for a larger number of holes the loss may not be practical for the majority of applications. Some authors mention that the drilling induced losses for meter long sensors should be less than 0.1dB per channel to be in an appropriate range [14]. Also, high pressure application needs to be investigated, since a compact tunable source or tunable pulse compression following a fibre laser is needed. However, at low pressures the system showed the potential for spectroscopic and gas sensing applications [111]. The holes produced are relatively small (approximately 1.5 µm diameter) and the edges are not particularly clean or smooth (see figure 5.19). The process of filling the hollow

core fibre with fluid adds an additional complexity to the process (similar to that of photolithography). The attraction of fs laser machining is that it should be a relatively simple, single stage process with no need for wet chemicals and post processing.

Other examples of fs lasers for the drilling of lateral microchannels in HC-PCF have been described [14]. The fibre was tailor made for gas sensing applications in the infrared region, from 1.5 to 1.7 μm. The aim of laser-drilled lateral microchannels was to enable access of the gas to the light guiding core to obtain a faster response of the sensor [14]. A mode-locked Ti:Sapphire laser, coupled to a Ti:Sapphire amplifier which provides pulses of 120 fs lengths at 780 nm with a repetition rate of 1 kHz, was used for microchannel fabrication. A microscope equipped with an optical monitoring system that allows the fibre adjustment and monitoring of the drilling process was used for final beam forming and focusing. The laser beam was collimated with a microscope objective 10/0.1 and the fibre was fixed in a Teflon ® V-Groove on a 4 D translation stage that allows the control of the fibre position. The fibre transmission was continuously monitored during the drilling process with an IR-LED as light source and an optical power meter as a detector [14]. The conditions used to obtain the microchannels in Figure 2.14 d) were 50 mW and 100 ms of drilling time [14].

The sensor consisted of two pieces of a HC-PBGF with laser drilled lateral microchannels housed separately in glass tubes (chambers) and attached by thermal splicing to FC-plug terminated SMF. The single fibre sensors were joined by SMF to a spatial distributed sensor line to allow the measurements. The authors used white light spectroscopy as the interrogation method and principal component analysis as the data analysis tool and showed the ability to use this sensor line for the quantitative and distributed measurement of gas mixtures [14]. The HC-PBGF and the experimental set-up are presented in Figure 5.20.

When the coating of the fibre was maintained during the machining process to give more robustness to the fibre (i.e. prevent breakage), the authors noticed that the laser beam was not able to penetrate the fibre and major destruction in the cladding and the photonic structure were noticed, Figure 5.20 c). With the coating of the fibre removed, better results were achieved, Figure 5.20 d), for the same drilling parameters [14]. The authors

mention that it was possible to improve the quality and reliability and process speed moving the focus down: the drilling would start at a position of 30 µm above the outer cladding and would stop at a focus position close to the boundary and within the cladding tube [14].

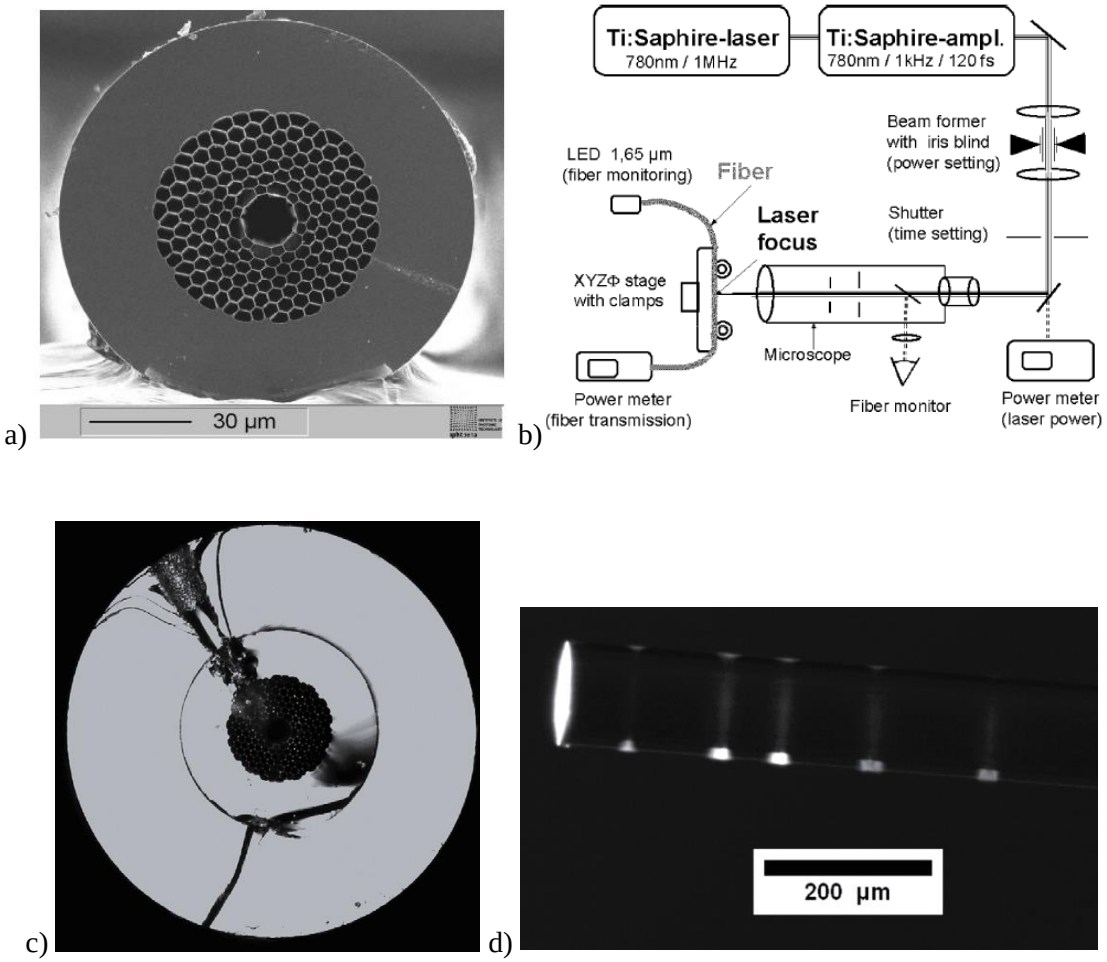

Figure 5.20. a) SEM image of the HC-PBGF form which the gas sensor was constructed for operation in the infrared region of 1.5 to 1.7 µm, b) experimental set-up for drilling lateral microchannels in these HC-PBGF, c) picture showing the channel drilled in acrylate coated fibre and d) channels in the fibre without acrylate cladding (both for the same experimental parameters) [14].

Although the work in reference [14] is showing the use of the femtosecond laser to do the lateral channels, the achieved holes are single drilled, and the range of possible machining geometries is not wide. The results itself, while allowing access to the light guiding core, they show some irregularities along the length of the channel, with a non-even inscribed structure (relatively rough), common of single hole drilling. Also, the use of this type of

fibre and not NCF difficult to increase the range of geometries, since the cladding is more complex.

One contributing factor to the production of conical shaped holes obtained in most cases reported above is related to the Gaussian intensity profile of the laser beam and enhanced thermal losses at the walls of the hole. This leads to the laser radiation interaction at grazing incidence with the walls increasing the area of interaction and therefore, decreasing the effective fluence [81]. However, the numerical aperture also has an influence. In reference [114] the authors affirm that during the fabrication of a sub-micrometer sized void array in fused silica using a femtosecond laser, the void shape was narrower and longer when the numerical aperture used was higher than 0.9 NA [114]. Other authors also mention that when using a higher beam numerical aperture such as 0.6 submicron damages in the form of voids can occur. When using an aperture in the range of 0.25-0.50 [115], [96] a strong permanent birefringence over a transverse size of a few microns is observed [96] not producing deep structures. Arrays of conical submicrometric holes were also produced in bulk silica using a focused fs laser beam (NA = 0.45) combined with chemical etching [115]. Here, the modified structure is formed near the bottom surface of the sample and then chemically etched in the tapered region, clean, circular submicrometer diameter holes can be produced [115]. Additionally, when the laser beam is translated parallel to this bottom surface then submicrometer-wide channels can be created [115].

The method described in this thesis uses an NA = 0.4 but it enables larger machined areas due to x and y scanning strategy and the translation in z (small increments in z). This can be used to machine wide channels without the use of chemical etching or water assisted debris removal. It is the proposed that the flexibility of this novel machining protocol will allow the machining of a range of structures and geometries not feasible using the drilling methods most commonly reported to date. This has the potential to lead to the ability to make a new class of fibre components needed for the full implementation of novel hollow core microstructured fibres as photonic devices.

Alternative approaches have also been considered for drilling microchannels in fibres. In [9] a fibre was drilled using ultraviolet laser micromachining of a cylindrical hole of the

acrylate polymer coating and subsequent FIB milling of the silica cladding. Although the femtosecond laser drilling is faster than the FIB milling, it leaves undesired particles and structural changes in the light guide when compared to the clean material removal from the FIB process [9]. Since FIB is not suitable for drilling though the top polymer [9], due to the damage on the polymer by the incident ion beam [116] it is usually only used on bare fibre [9]. The most common problems in the polymer are the heating damage, breaking due to thermal expansion, the re-deposition of the material and the curtain effect (which happens when the energetic ions reach the surface of the material and the removal of the material creates excessive heating of the surroundings leading to undesired damage and holes on the surface). Although these problems can happen with all types of materials, in polymer it is more adverse [117].

The FIB uses a focused ion beam to obtain functional nanostructures by the removal of the material or deposition with an accuracy of nanometer level [118]. The beam of high energy ions bombards the substrate atoms where the collision transfers sufficient energy to the substrate atoms to overcome the surface binding energy causing the physical sputtering effect [119]. The beam can be smaller than 3.5 nm and the beam-position accuracy and stable operation condition are advantageous [118].

If compared to another method used in nanofabrication such as electron beam lithography, the FIB allows a higher material removal rate. However, when using the FIB process re-deposition can occur where some scattered atoms which are knocked out by the incident ion beam adhere to the sidewall of the nanostructures, leading to a different final shape to the desired one. The number of atoms ejected per incident ion is called the sputter yield and this is dependent on the ion incident angle. Due to these facts, that are inherent of the process, when using the FIB and in order to find the most suitable machining parameters, the approach used is trial and error, which is expensive and time-consuming [118].

As bare fibre is not practical for handling, the laser micromachining removes the polymer coating prior to FIB milling of the underlying silica. A lateral hole was drilled into the hollow core with no need for post chemical processing, with near zero damage to the microstructures and no transmission losses [9]. The laser used was a Nd:YAG laser (Lumentum Q201-D) with 532 nm output with a single pass beta barium borate and Pelin-

Broca prism to generate 266 nm pulsed output. The conditions used were 10 ns of pulse width and 20 µJ pulse energy at 500 Hz pulse frequency. The beam was focused with a 5× microscope objective onto the HC-PCF acrylate jacket. The hole drilled on the polymer coating had a diameter of 120-180 µm to expose the bare silica without heating or melting the fibre and at the same time giving strength to the fibre [9].

With the silica exposed, the silica cladding was drilled using a FIB milling. This was performed with an adapted SEM to monitor the process. The sample was tilted 52 º for direct facing the ion column, in the centre of the stage and with 15 mm from the electron column. The FIB drilling required 30 min to reach the core. To drill 10 µm diameter hole the drilling rate was 1 µm per minute. The beam current used was 7 nA being approximately 10 times faster in microstructure regions taking 30 min to reach the hollow core (dimensions of the fibre 10±1 µm hollow core diameter, 120±2 µm cladding and 220±30 µm acrylate polymer coating) [9]. The authors show there is no deformation or contamination in the HC-PCF light guide and therefore the transmission loss remained unchanged after the FIB process. In Figure 5.21 it is possible to see a stripped hole in the jacked before and after drilling a 10 µm diameter and approximately 55 µm deep hole from the silica surface to the hollow core [9].

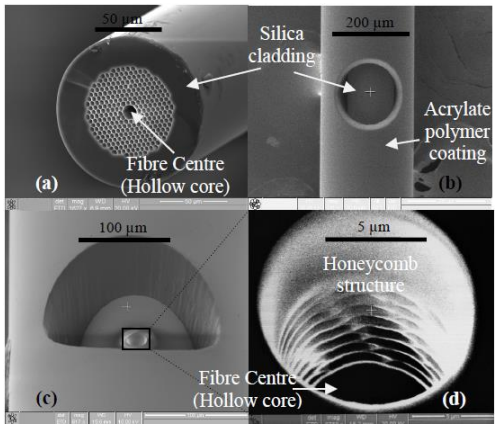

Figure 5.21 SEM and FIB images of the a) cross section of cleaved fibre, b) hole in acrylate coating before the FIB milling, c) FIB milling after 5 min and d) FIB milling completed showing the honeycomb structure [9].

The approach described in the reference [9] combines two different and expensive processes: the ultraviolet laser micromachining for the polymer coating and, the focused ion beam milling in silica cladding of HC-PCFs as opposed to the work presented in this

chapter that only uses a single step (femtosecond machining) after the removal of the polymer jacket with a blade. Being so, the method presented in this work is simpler requiring only a machining process although it still requires mechanical removal of the fibre jacket in the region where the fs laser machining is performed.

The structures or holes achieved in this reference [9] are very small (10 μm diameter and approximately 55 μm deep hole from the silica surface to the hollow core) when compared to the structures achieved in this work (where total depths of 132.5 μm are achieved, for example). Additionally, the scanning strategy used in the work of this thesis dictates the final geometry which enables the possibility of making larger more complex geometries which gives more flexibility to the process.

Regarding time comparison between the FIB machining and femtosecond laser machining, as mentioned above, reference [9] mentions that the FIB milling speed depends on the substrate and size of the hole. In the example shown in this reference, to drill a 10 μm diameter hole in solid silica, the drilling rate is approximately 1 μm per minute with a 7 nA beam current and in the case of HC-PCF it takes approximately 30 min to reach the core (it is 10 times faster in microstructure regions) [9]. Although these times are smaller than the ones presented in this thesis, not only the structure is significantly smaller than the structures produced in this thesis, but also the FIB milling is based on a trial and error process to find the most suitable parameters, as mentioned above [118].

To summarize this sub-section, there are some references that report the machining of holes or micro channels in silica fibres to enable the access to the core such as femtosecond laser machined micro channels with the machining done at the outset and decreased gradually as the channel tip moved away; femtosecond laser machining with cycles shifting some micrometres the laser focus to the perpendicular axis (of the fibre); femtosecond laser machining to drill side holes (obtaining V shaped structures) or in alternative combining laser machining with FIB milling. The methodology used in this work allows the use of a single technique (femtosecond laser machining), using small increments in z that allow depth control and shows no damage on the remaining cladding web.

5.4 Summary

The changes implemented to the laser machining protocol (Figure5.1) were shown to be effective in enabling a more repeatable and robust process. The protocol was tested successfully for NCF designed for 3 and 1 µm guidance. Since the fibres present different dimensions, these were considered when adapting the G Codes programs, either in terms of number of planes or dimensions in x and y.

The best results were obtained when using 2 µJ of pulse energy and a 2.5 µm increment in z. For the NCF designed for guidance at 3 µm 53 planes below the surface, one at the surface and 2 above were optimal. For the NCF for guidance at 1 µm and using 27 planes below the surface were optimal. The speed used was 1 mm/s corresponding to 84.16% of pulse overlap (at the used repetition rate of 5 kHz). The dimensions scanned in the x direction must be larger than the external diameter of the fibre to allow for acceleration and deceleration effects. However, it was calculated that only an additional 8.33 µm (in total, for both sides of the fibre) would be required to ensure the speed is uniform at 1 mm/s when the structure is machined. Nevertheless, in some cases, 1.000 mm of travel in x was used but it was deemed that between 0.400 and 0.500mm in x would be sufficient. Being so, the dimensions on the G Code used in most results were initially 0.500 mm in x and 0.100 mm in y or later 0.400 mm in x and 0.150 mm in y (the length in y was increased to make it easier to see the final depth achieved under the SEM).

The literature reports the machining of both holes or microchannels in a range of silica fibres. Even though the aim is similar i.e. enabling access to the core to increase measurand sensitivity, the machining conditions and methods employed were distinctly different from the protocol used in this work:

- Some authors used femtosecond laser machined microchannels in Hollow Core Photonic Bandgap Fibres (HC-PBGF) and Suspended-core Holey Fibres (SC-HF) and the micromachining was done at the outset, close to focus and decreased gradually as the channel tip moved away from the focus resulting in a narrowing of the channel beyond the laser focus and with tapering continuing to the hollow core. The machining was discontinued soon after the core had been breached (to avoid damaging the microstructured cladding beyond the core). The channel

diameter tapered from 20 μm at the fibre surface to a few microns at the core (the total depth is similar to the radius of the fibre) [8].

- Other authors drilled microchannels with fs laser employing four scanning cycles shifting 10 μm the laser focus perpendicular to the fibre axis, for the next scanning cycle, obtaining a V-shaped microchannel with 20 μm diameter and 50 μm depth [16].
- And other authors use only the femtosecond laser machining to drill side holes obtaining a V-shaped structure and some damage on the cladding web [13], [14], [111]. One of the reasons for this conical or V-shaped hole is related to Gaussian intensity profile of the laser beam and enhanced thermal losses at the walls of the hole, that leads to the laser radiation interaction at grazing incidence with the walls increasing the area of interaction and therefore, decreasing the effective fluence [81]. The numerical aperture also has an influence. Some references mention its importance in the shape of the hole: for example reference [114] mentions that the void shape is narrower and longer when the numerical aperture used was higher than 0.9 NA [114]. The method described in this thesis uses an NA = 0.4 but enables larger machined areas due to x and y scanning strategy and the translation in z (small increments in z).
- Alternative examples include the use of the ultraviolet ns laser machining combined with FIB milling to eliminate the polymer jacked and to drill a 10 μm diameter and approximately 55 μm deep hole from the silica surface to the hollow core [9].

The methodology used in this work (when comparing to the work mentioned above in this field) allows the use of a single technique (femtosecond laser machining), using small increments in z that will allow to determine with precision when and where the machining should stop. Therefore, it is highly controllable, and it is possible to stop the process at the particular desired depth. This allows different regions of the underlying microstructure to be removed which give more flexibility when considering future photonic devices. Furthermore, there is no damage on the remaining cladding web in comparison to previous work which is the main advantage of this machining protocol. This is of major importance for these NCF (and indeed other microstructured fibres) since

the wavelengths that are guided and the optical performance of the fibres are wholly dependent on these fine and complex structures

Although this work has been demonstrated on NCF, the advantages of the machining protocol advantage opens the possibility to use it on any type of silica-based fibre in particular those with more complicated cladding web structures, such as HC-PBGF or Kagome fibres.

Chapter 6 – Analysis of the optical guidance of machined NCF and comparative study of a mechanical machining method

In this Chapter, the analysis of the fibre before and after the machining protocol (described in Chapter 5) will be presented. The fibres used for this analysis were NCF for 1 µm guidance. To perform this analysis, a diode laser working in this wavelength was used. The experimental set up is described in the following sub-section as well as the imaging results of the fibre. Additionally, as a comparative study, a mechanical method, namely fine diamond sawing, is also presented in this chapter.

6.1 Experimental Set-up for Optical Analysis of NCF

The laser used had a wavelength of 1064 nm, with 3-3.5 V DC and maximum 1.4 A. The working conditions were 2.3 V and 0.4 A and the measured maximum output was 22.3 mW. The set-up consisted of the laser, two mirrors to guide the beam to a telescope and one lens to focus the laser beam, Figure 6.1:

- mirrors M1 and M2: BB1-E03 - Ø1" Broadband Dielectric Mirror, 750 - 1100 nm;
- telescope BE052-B - Variable Optical Beam Expander, 0.5X - 2X Zoom, AR Coated: 650 - 1050 nm;
- lens with 5 mm focal length C430TME-C (Thorlabs) with NA of 0.16, Mounted Geltech Aspheric Lens and anti-reflecting coating AR: 1050-1620 nm
- micro block 1 where the fibre is placed;
- micro block 2 with the microscope objective 20 X to focus the fibre output to the camera;
- camera Basler 106957-07 to see the output of the fibre with NE60A and NE20A filters.

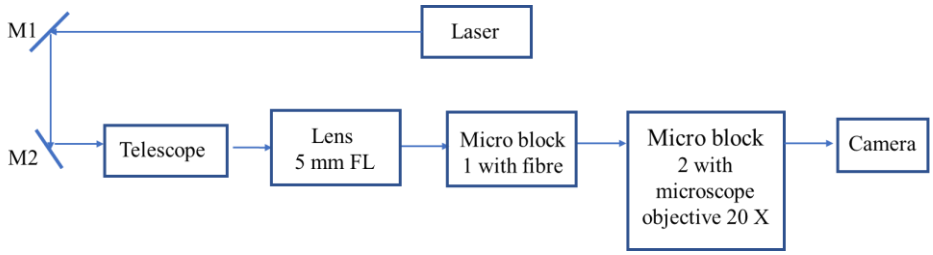

Figure 6.1 Scheme of the experimental set-up for the NCF analysis.

The fibre was placed on a micro block 1 and it was glued to the microscope slide with nail polish, Figure 6.2. A power meter PM100D power meter (Thorlabs), and a sensor S122C (Thorlabs) were used to measure the optical power, between micro block 1 and 2.

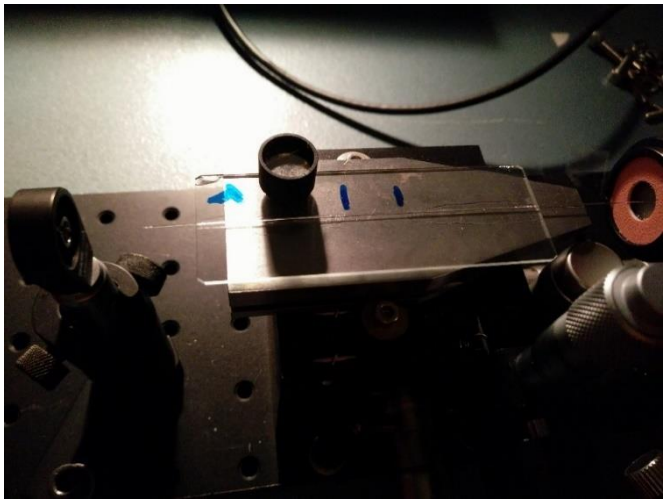

Figure 6.2 Photography showing the microscope slide with the fibre glued, the lens at the left side and the power meter sensor at the right side of the fibre.

The experimental set-up was already in use for another purpose and the laser beam diameter has been previously measured by Dr Bartlomiej Siwicki. It was approximately 418.9 μm by the Full Width at Half Maximum (FWHM) method which was used to calculate the coupling optics for the NCF. Knowing the beam diameter outside the laser with the FWHM method, the conversion of this value for the beam diameter calculated by the $1/e^2$ method was performed, in order to calculate which would be the appropriate lens that matches the numerical aperture of the of the fibre. The value of the diameter using the $1/e^2$ method is approximately 355.8 μm using equation 6.1:

$$2w = 0.8493218 \times FWHM \tag{6.1}$$

where w is the radius of the beam and $FWHM$ the diameter of the beam by the FWHM method [120]. Knowing the beam diameter, it is possible to know which lens is appropriate to couple the laser light into the fibre. The numerical aperture is directly proportional to the input diameter, D, and inversely proportional to the focal length, F , equation 6.2 [121]:

$$NA = D/2F \tag{6.2}$$

The numerical aperture of the fibre is 0.044 and so, using the equation above (6.2), the ideal focal length is approximately 4043 µm. Therefore, the use of a focal lens of 5 mm is appropriate for a proper coupling of the light into the fibre. Also, if the numerical aperture is calculated using the 5 mm of focal lens, the value obtained is 0.0356, very close to the approximate 0.044 of the fibre, as measured by a researcher of Applied Optics and Photonics group, Dr Richard Carter. However, the coupling into the fibre was not simple, since the length of the fibre was short and it was fixed on the microscope slide to avoid potential breakage, being the positioning of the fibre end restricted

The NCF tested is shown in Figure 6.3. It was made for guidance at 1 µm. Unfortunately, it was not possible to test the NCF for 3 µm guidance due to high losses possibly arising from the absorption of the water into the fibre [122]. The absorption spectrum can be seen in Appendix G. Ways to overcome this difficulty can be seen in Further Work section of Chapter 7.

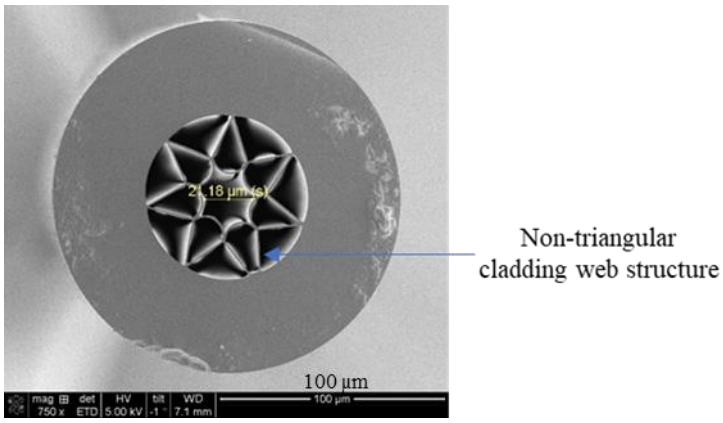

Figure 6.3. SEM picture of the NCF cross section for 1 µm guidance used in this work with a core diameter of 21 µm.

A piece of approximately 11 cm of length of non-machined fibre was used to establish a baseline loss. The power output of the fibre was measured to be 8.20 mW, meaning 36.8% of transmitted power given the laser output directly from the laser of 22.3 mW. Although no cutback measurement was possible due to the short lengths of fibre available this corresponds to an approximate loss of 0.39 dB/cm, calculated as the 10 $\log_{10}$ of the ratio of the power (P_{input}/P_{output}), equation 6.3 [123].

$$Loss\ (dB) = 10 \log_{10}((P_{input}/P_{output}) \quad (6.3)$$

When analysing the power output of the machined fibre with 15 cm length, it was found to be 5.2 mW which is 23.3 %. Again, if we consider the loss, with the machined fibre for this length of fibre it is possible to obtain 0.42 dB/cm. In Figure 6.4 it is possible to see the pictures of the output of a non-machined fibre and of a machined one.

Comparing the losses of the machined (0.42 dB/cm) with non-machined (0.39 dB/cm) fibre, it is possible to see the results are similar although there is some additional loss introduced due to the machining. Using the value of 0.39 dB/cm for an unmachined NCF, the total loss for a fibre 15 cm long would be 5.85 dB compared to 6.3 dB for the machined fibre (15 cm long). Hence, it is possible to find the loss due to the single hole (0.45 dB) which is higher than the work reported in literature that shows a loss due to a single drilled microchannel of approximately 0.35 dB [111] using a HC-PBG fibre. However, it should be noted that the HC-PBG fibre in [111] is a different fibre to the NCF here and it shows a much lower loss overall (0.1 dB/m). The total loss of the unmachined fibre in [111] (which is 33 cm in length) is 0.033 dB. Hence, the single microchannel drilled into the HC-PBG in [111] adds a much larger relative increase in loss compared to that of the hole created in the NCF.

Furthermore, NCF with lower losses has been reported in the literature, such as reference [5] that shows a loss of 0.06 dB/m at 2.94 μm (6.0×10^{-4} dB/cm). The fibre used in this work presents a higher loss, possibly due to the cladding guidance observed in Figure 6.4. Also, since it has been shown in literature (for example, reference [57]) that the web cladding has a strong influence on the light guidance properties (see Chapter 2, sub-section 2.1.4) it is possible that the fact that the web cladding showing a non-perfect triangular “ice cream cone” on the cladding web as in opposite to the rest of the cladding web, may have an influence on the high loss of the fibre, see Figure 6.3

In terms of power output, it is possible to see a decrease in the power output when analysing a machined fibre and a non-machined one. However, from Figure 6.4 it is possible to see that there is light in the cladding in the non-machined fibre (a) and in the machined one there is light in the core with reduced light in the cladding, Figure 6.4 b).

a) 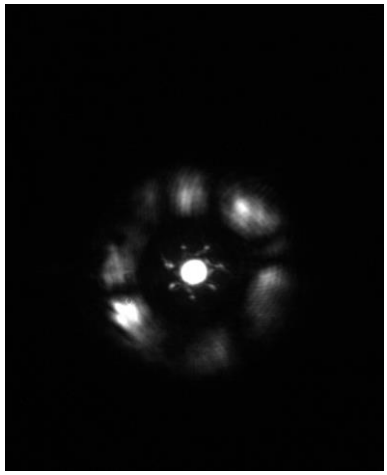 b) 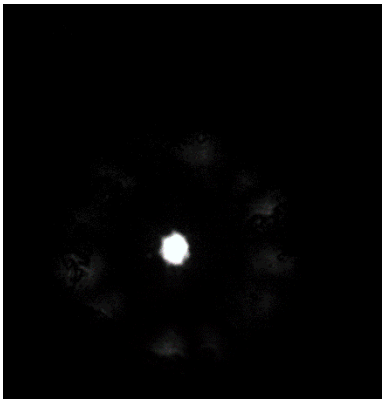

Figure 6.4 Photographs of the light output of a) non-machined fibre and b) machined fibre

As the machining removes a significant portion of the cladding (as described in Chapter 5) it is expected that this will disrupt guidance of any light in the cladding. This implies that the power output measured of the machined fibre with 23.3% transmission is more representative of the light confined and guided solely in the core whereas for the non-machined NCF, with a 36.8% transmission, this represents light guided both in the cladding and the core. It is possible to infer the machining process optimised in Chapter 5 is successful as the light is well confined in the core. This is only possible due to two main aspects: the preservation of the cladding web after the machining process (as shown in Chapter 5) without ingress of debris into the hollow core and the guiding mechanism of the light in this fibre. As detailed in Chapter 2, subsection 2.1.4, the NCF light guiding mechanism is based on the Anti-Resonant Reflecting Optical Waveguide (ARROW) phenomenon. All wavelengths which are not in resonance with the core wall are reflected into the core and propagate with low loss. This structure behaves in a similar way to a Fabry-Perrot resonant cavity [7],[50],[51],[3],[48],[52]. Therefore, providing the core wall is preserved before and after the machined region good confinement in the core should be preserved.

This initial result provides a proof-in-principle that the new machining protocol can be applied to machine a slot in the NCF and access the hollow core whilst maintaining light guidance in the NCF. Unfortunately, the fibre used in this instance (the only fibre available at the time of the experiments) has a relatively high loss and therefore future work should be carried out on other NCF and more complex microstructured fibres such

as HC-PBF and Kagome fibre. More details on this can be seen in Chapter 7, in the Further Work section.

6.2 Mechanical Machining Method

An alternative, mechanical process was tested to compare the differences to the femtosecond laser machining protocol. This work was done in collaboration with Neil Ross from the School of Engineering and Physical Sciences. It consisted on machining the fibre with a fine diamond saw and the width of the saw was similar to the length of the structures obtained with the laser: 0.150 mm. The aim was to mimic the structures obtained with the femtosecond laser to see if it would be possible to realise them with a mechanical method, which is cheaper and faster.

6.2.1 Method and results

The fibres were placed on previously made V grooves on a microscope slide. This in turn was fixed to a membrane using UV light that was incorporated on the sawing machine, Figure 6.5 b). The machine used was a DAD 3220 Disco Automatic Dicing Saw, as can be seen in Figure 6.5.

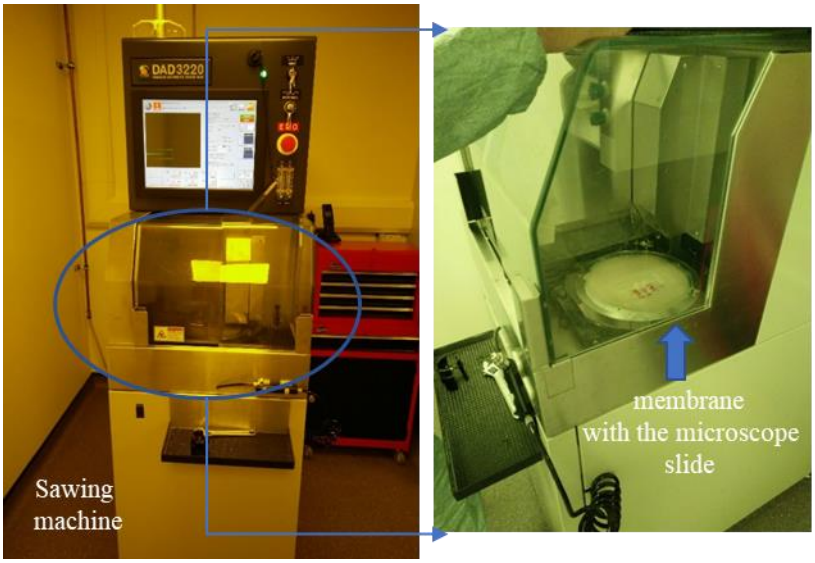

a) b)

Figure 6.5 Sawing machine used in this work and b) photograph showing the membrane with the microscope slide inside the machine

The fibre used was the one presented in Chapter 5, sub-section 5.2.1 (NCF for 3 µm guidance). Glue was added to the grooves (crystal wax, temperature 130 °C) to fix the fibres on the slide. Three fibres were used in order to perform the same depth in different fibres. The feed speed used was 1.5 mm/s at 30000 rpm. To program the different depths in the machine, the surface of the fibre was measured. Then the desired depths were programmed in the sawing machine. Four sets of different depths were tested, Table 6.1. The heights of the surface of the slide and fibres was measured with a Vernier calliper. The initial depths were chosen to correspond with those performed with the femtosecond laser:

- 107.5 µm (corresponding to 43 planes with 0.0025 mm increment in z)
- 132.5 µm (corresponding to 53 planes with 0.0025 mm increment in z)
- 145.0 µm (corresponding to 58 planes with 0.0025 mm increment in z)

Additionally, a number of trials with reduced depth were also performed, Table 6.1.

		Depths (µm)
1	a	107.5
	b	132.5
	c	145
2	a	78.75
	b	91.25
	c	97.5
3	a	53.75
	b	66.25
	c	72.5
4	a	26.88
	b	33.13
	c	36.25

Table 6.1 Depths performed with the sawing machine. The four sets of depths are shown in 1, 2, 3 and 4.

The results of the sawing machining for two different NCF fibres can be seen in Figures 6.6. and 6.7. It is possible to see damage in the web cladding in the 3 different fibres machined with the diamond saw, Figure 6.6, 6.7, and 6.8. However, it should be noted that water was used as a coolant and to wash any debris away.

a) 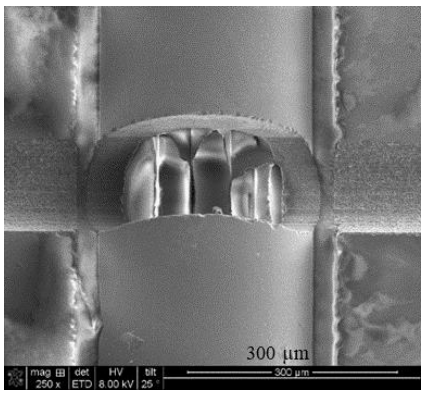

b) 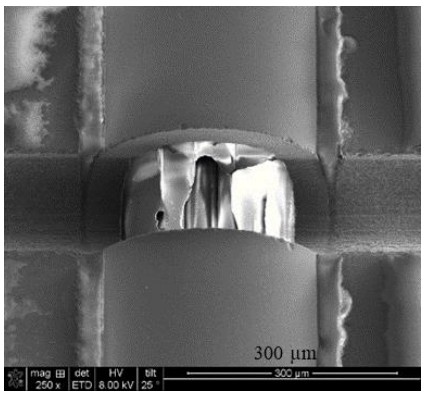

c) 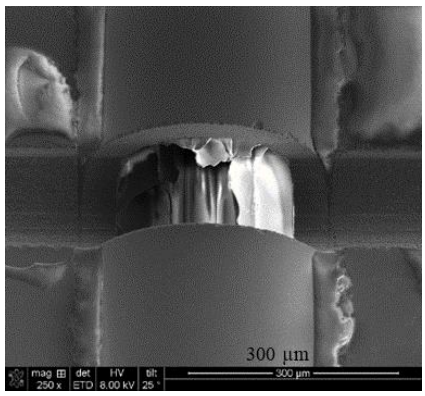

Figure 6.6 SEM image of an NCF fibre machined with the diamond saw. The a), b) and c) correspond to a depth 107.5 µm, 132.5 µm and 145 µm respectively.

a) 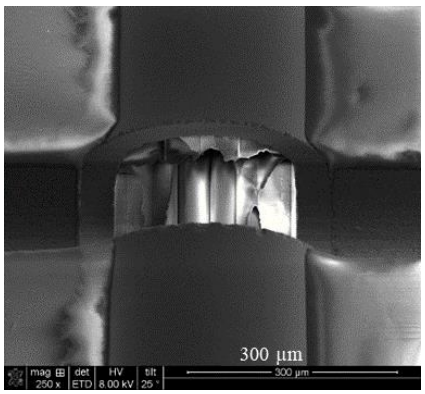

b) 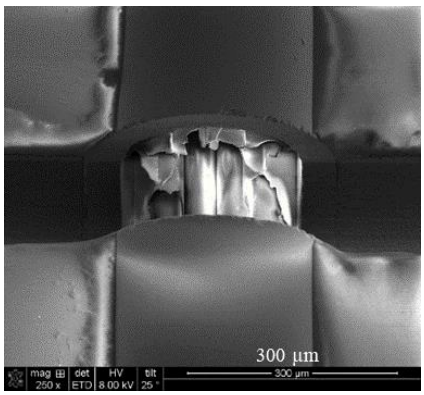

c) 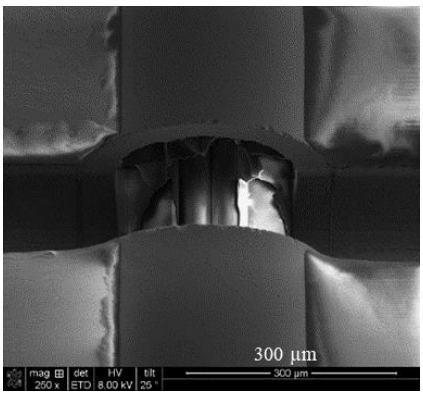

Figure 6.7. SEM image of a second NCF fibre machined with the diamond saw. The a), b) and c) correspond to a depth of 107.5 µm, 132.5 µm and 145 µm respectively.

a) 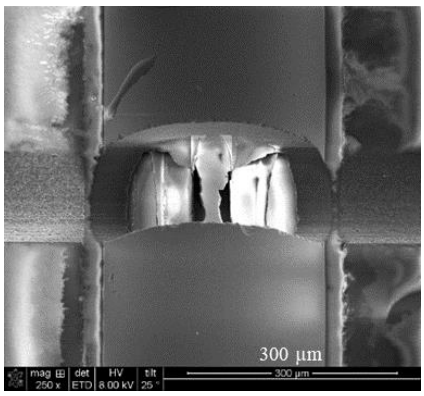

b) 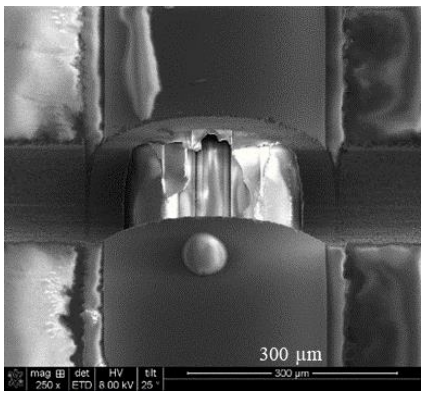

c) 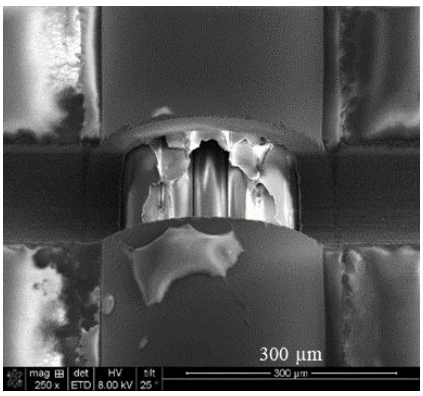

Figure 6.8 SEM image of a third NCF fibre machined with the diamond saw. The a), b) and c) correspond to a depth of 107.5 µm, 132.5 µm and 145 µm respectively.

Also, the depths shown in Figure 6.8 and 6.7 seem deeper than the one in the pictures in Figures 6.6 although the same depth was performed with the saw which indicates that there is a lack of repeatability of the process. One possible reason for this is that as the fibres are fixed with glue to the microscope slide, it is difficult to ensure that this glue is distributed evenly hence can lead to a height difference along the fibre length. Debris is

also visible deposited on top of the fibre, Figures 6.8 b) and c). Results of the other tested depths are presented in Figures 6.9, 6.10 and 6.11, for the same fibre.

a) 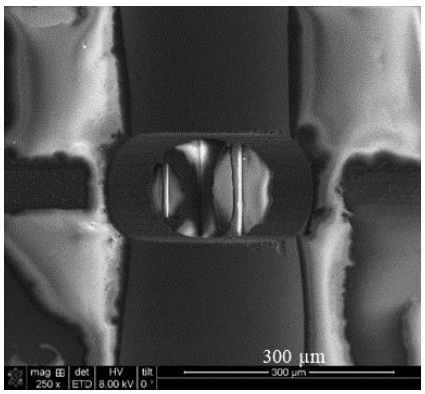

b) 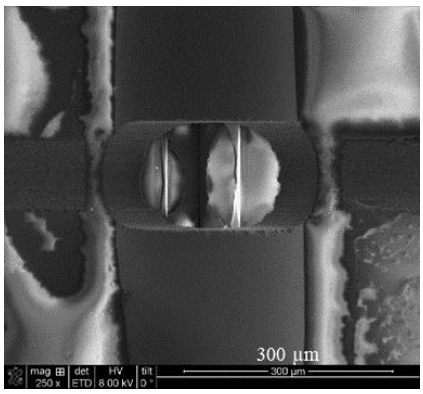

c) 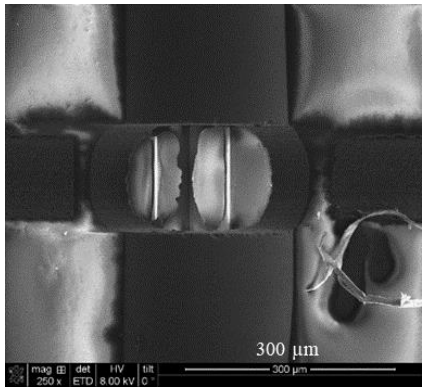

Figure 6.9 Results of one NCF fibre machined with the diamond saw. The a), b) and c) correspond to a depth of 78.75 µm, 91.25 µm and 97.5 µm respectively.

a) 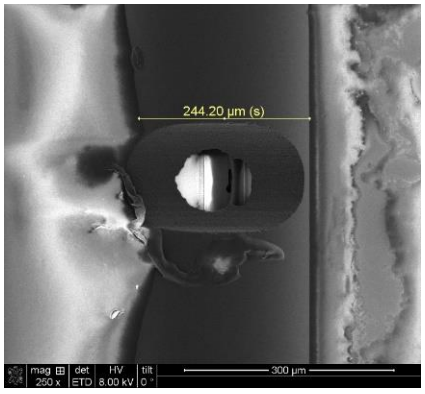

b) 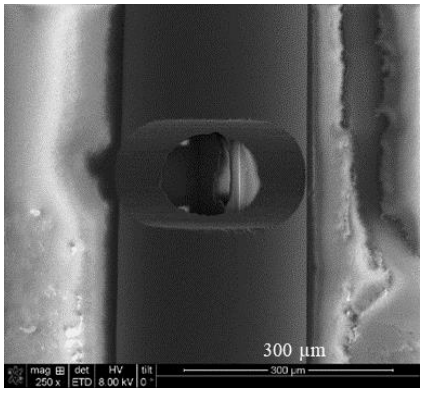

c) 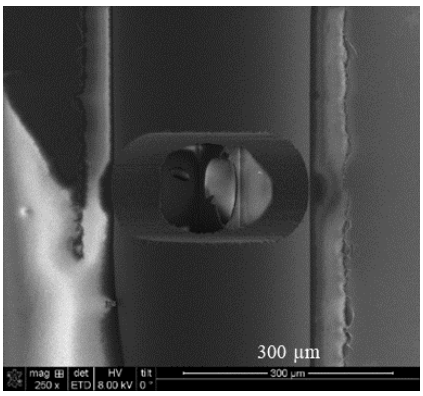

Figure 6.10 Results of one NCF fibre machined with the diamond saw. The a), b) and c) correspond to a depth of 53.75 µm, 66.25 µm and 72.5 µm respectively.

a) 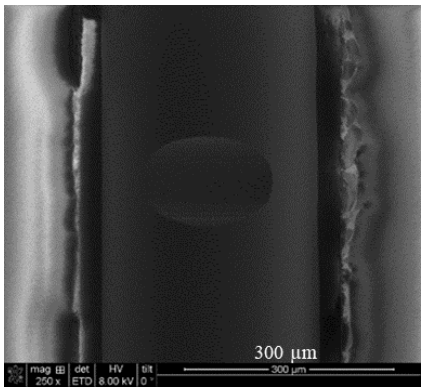

b) 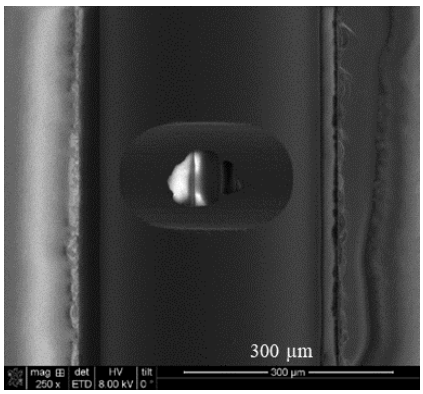

c) 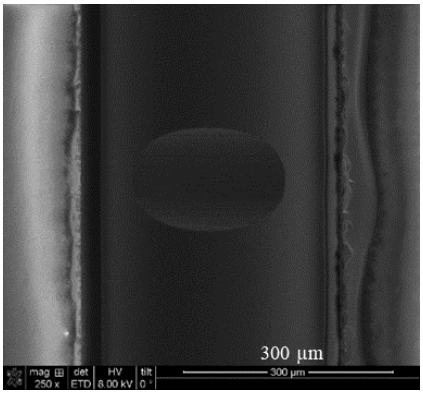

Figure 6.11 Results of one NCF fibre machined with the diamond saw. The a), b) and c) correspond to a depth of 26.88 µm, 33.13 µm and 36.25 µm respectively.

Comparing Figures 6.9, 6.10 and 6.11, for different depths it is possible to see that different depths were successfully achieved. However, the effect mentioned above regarding the fixation method is very pronounced in some cases, as in Figures 6.9 and 6.10 a) where the glue that surrounds the fibre was excessive and was deposited on top of the fibre.

Due to this reason that leads to a lack of repeatability of the process and also due to the fact that the cladding web was damaged, when machining to the same depth as achieved with the femtosecond laser (Figures 6.6, 6.7 and 6.8), this technique was not pursued in this work. Optimisation methods of this process should be considered in Further work, such as, changing the fixation method: for example, not applying the glue where the sawing is performed. Another suggestion may be changing the feed rate since the machining variables also have an influence (feed rate, depth of cut, geometry of the cutting tool). It has been reported that increasing the feed rate damage as cracks propagating into the final cut surface may occur, in silicon [124].

6.2.2 Diamond as a machining tool

Diamond tools have been successfully used for machining nanostructures [125], [126] with applications in ultra-precision machining due to the fact that it is the hardest known material that occurs naturally [125] and due to other favourable properties: toughness, capability to create a nanometric tool cutting edge, high thermal conductivity, low friction and high wear resistance [127].

A study to compare the diamond drilling and laser drilling technique (with a Nd:YAG laser) is reported on reference [128] with the aim to fabricate MEMS device (Micro-Electro-Mechanical Systems) on Pyrex (7740) glass wafer. For this application it is important to fabricate holes usually from 100 μm to 3 mm. The diamond drilling was done with a Computer Numerical Control (CNC) machine tool, with the use of a multi-layered diamond drill using water as coolant and the machining parameters (cutting speed, feed rate, power, wavelength and repetition rate) for both methods were optimised by the Taguchi method (statistical method). The laser machining was performed with an Nd:YAG laser focusing the laser beam on a sample surface through a beam expander. The best conditions for diamond drilling were a spindle speed of 2500 rpm and a feed rate of 0.25 mm/min with mist water as a coolant. The optimised conditions for laser drilling were 3.2 kW and 17500 Hz of frequency and the authors mention that the CNC diamond drilling achieved better edge quality when compared to the laser drilling. This characteristic was analysed using an optical microscope. The authors attribute this result

to the transparency of the glass wafer to the laser wavelength hence there is low absorption of the optical energy and increases the difficulty in removing the glass material [128]. However, the laser used in this reference is a Nd:YAG laser and hence the laser material interaction is different from the ultrafast femtosecond laser used in this work (see Chapter 2, sub-section 2.2).

In the specific case of single point diamond turning, it has been well stablished since the late 1980s, and it is a machining process with ultra-precision used to generate ultra-smooth machined structures with a tight surface form control and good step definition. It is also possible to produce freeform shape optics using a single pass and this advantage makes this method applicable to use as a finishing process (instead of grinding and polishing). [129] It uses large single diamonds sharpened to edge an radius as fine as 100 nm and sometimes it can be down to 20-40 nm [130].

The single point diamond turning is a technology used to fabricate aspheric optics on metals and it works well in glass and ceramic materials [130]. The references [131] and [129] show this technique being performed in calcium fluoride and silicon respectively. The single point diamond turning works accordingly to the brittle-ductile transition but as the diamond tool degrades rapidly due to the wear. This can cause a sudden transition of material removal mechanism from ductile to brittle fracture in the cutting region which leads to deterioration of the quality of the cut [129]. Furthermore, the contact between the workpiece and the tool results in localised high temperatures [129] in contrast to the femtosecond machining which is a non-thermal process [15].

Diamond turning using a multi-tip single crystal diamond tool as a new approach for the fabrication of micro or nanostructures has also been reported [126]. It is achieved by directly replicating pre-fabricated structures on the tip of the diamond tool onto the substrate surface. In this way micro groves, arrays and diffraction gratings have been obtained using micro multi-tip tools fabricated by FIB [126].

Sawing work is presented for example in BK7 glass [132], granite [133] and silicon [134]. Reference [132] shows the characteristics and wear mode of the diamond grits in the cut-off grinding of BK7 glass using a thin diamond wheel. When too high a transverse

velocity was used, the diamond wear pattern showed macro-breakage and the worn wheel surface showed flattened regions, leading to unstable grinding forces, a low gridding ratio and a poor straightness of cut (tested transverse velocities of 50, 100 and 150 mm/min). Reference [134] presents the effects of sawing parameters on wafer topside peeling quality and shows that the blade height is the main factor that influences the peeling quality. This reference also mentions that the diamond sawing technology is the first choice of smart chip production. Diamond blade dicing has also been the principal approach of the semiconductor industry [135]. Reference [133] shows a study to evaluate the loads acting on the diamond grits during the circular sawing of two types of granite with a diamond segmented saw blade and found that the average force acting in each diamond grit was 4% of the diamond compressive strength (measured by a static method) and the wear of the diamond grits was related to the high temperatures generated at the individual cutting points.

6.2.3 Examples of mechanical machining methods applied to optical fibres

Although there is substantial literature on the fine mechanical machining as described above, with respects to the machining of optical fibres the most commonly employed used techniques are still laser based. Other techniques have been reported (as reviewed in Chapter 2) such as lithography (which requires many process steps), micromachining by dry etching (time-consuming and low selectivity etching) and FIB (time consuming and cost-inefficient) [74]. Some of these methods are used in conjunction to perform structures on optical fibres Reference [128] also refers to ultra-sonic glass drilling but indicates that it does not produce good edge quality nor allows positioning accuracy.

The use of a precision dicing saw applied to optical fibres can be seen in reference [136] to fabricate a microcantilever at the end face of an integrated optical fibre [136]. The authors mention the methodology is single-step and rapid, achieving trenches with high aspect-ratio (higher than 10:1). The fabrication is made on a monolithic integrated optical fibre platform which integrally fuses an optical fibre to a planar substrate using Flame Hydrolysis Deposition (FHD) and high temperature consolidation (higher than 1000 °C). The FHD creates a miscible alloy between the optical fibre and the planar substrate. The fabrication of the cantilever was done with a precision dicing saw and a nickel bonded

synthetic diamond blade where the depth of the cut was 800 µm, the rotation speed was 25000 rpm and cutting speed of 0.1 mm/s. These conditions are less pronounced than the ones used in this work (30000 rpm and 1.5 mm/s). Five cuts were made, two parallel and three orthogonal to the fibre and the orthogonal formed air cavities of 59 µm with a single cut and 147 µm with a dual cut and a glass cavity of 65 µm. To obtain a distal cantilever, this structure was cleaved leaving only a single air and glass cavity. The authors mention this paper is the first report of a fibre tip cantilever using this technique and this integrated platform [136]. The depths achieved with a single pass are similar to the depths obtained in this work. It is apparent that the integrated optical fibre may contribute to the robustness of the fibre during sawing. The FHD was used to form a miscible alloy between the optical fibre and the planar substrate and avoid the fixation problem detected in this work due to the glue in excess on top of the fibre. However, this FHD process could present problems for removal and fabrication of novel sensing devices.

The use of laser machining to produce cantilever structures is shown in reference [137], and the combined use of laser machining and FIB milling to achieve these structures can be seen for example in reference [138] and [139]. The interest in cantilever structures is related to the fact that by adding a specific coating it is possible to add sensitivity for temperature, chemical or bio-chemical species. They are also used on Atomic Force Microscopes (the probe tip is attached to a micro-cantilever) [137].

Reference [138] reports the fabrication of micro-cantilevers onto the end of a single mode optical fibre by combining picosecond laser machining and the FIB milling and shows its use as a temperature sensor. The authors mention the FIB technique shows good dimensional control of the features (nm level) with excellent surface finish but that it is also a slow process. On the other hand, there are alternative processes such as femtosecond laser and subsequent etching or photolithography methods that are faster and show potential for mass production [138]. In this reference, the authors show the use of the direct laser machining exploiting its advantages: compared with other fabrication techniques for the same material (fs laser machining combined with chemical etching or using only the FIB machining) the total machining time decreases making this method potentially suitable for industrial production [138].

The authors mention this dual process reduces the polishing time to less than 20 min for cantilevers of these dimensions after the ps laser machining and this also represents a significant reduction of the FIB machining time to form the complete structure. The cantilever was designed to measure deflection over a range of 10 µm using a readout technique and a phase recovery algorithm was used to reduce the interrogation error to 2-3 nm. The temperature experiments showed it could be used as a temperature sensor from 20° C to 500 °C with an average error (root mean square) of ±1.4 °C [138]**.**

The picosecond laser machining operated at a wavelength of 343 nm, a repetition rate of 40 kHz, with 6 ps pulses. The pulse energy used was 10 µJ and the focused spot showed a diameter of 6 µm. The beam was focused on the work piece using a galvanometer scan head to move the focused spot across the fibre and the scanning speed used was 100 mm/s. An in-situ microscope was also used to monitor the process. Initially, the fibre was cleaved, cleaned and mounted on a V-groove holder, the laser beam ablated the top cleaved surface of the fibre and removed the material from the side of the fibre. Then, the fibre was rotated to fabricate the cantilever from that ridge, removing the section beneath it. There is a rotation mount to allow the fibre to be aligned to compensate for the tapering angle caused by the laser beam profile. The resulted cantilever had 110 µm long, 18 µm wide and 8 µm thick [138]**.**

To improve the mechanical sensitivity and to reduce the cantilever thickness the FIB milling was performed. It was a dual beam system with a liquid gallium ion source and a field emission scanning electron microscope. The cantilever was coated with 20 nm of a gold layer (reduces electrostatic charge) and the FIB conditions were: a beam acceleration voltage of 30 keV and a current of 15 nA. A narrow rectangular pattern of 110 µm long and 2 µm wide was used to thin the cantilever and a second cut was performed to eliminate a small connection with the main part (left on purpose during the first cut to form a shield between the cantilever and the fibre core) forming the final cantilever [138]**.**

A similar work is also reported on reference [139] where the authors report a micro-cantilever fabricated with ps laser machining and FIB onto the end of an optical fibre (standard telecommunications optical fibre) but this time it is demonstrated as a liquid pH

sensor. The fibre tip end of the cantilever was coated with a pH sensitive layer and the pH induced deflection was monitored using an interferometric approach (more robust than an intensity-based sensor). The structure forms an optical Fabry-Perot Cavity and measuring the cavity length allowed to infer about the cantilever deflection that arises due to the pH change. Also, since the cantilever is onto the end of the fibre this allows inherent alignment to the readout system (by the fibre core during the fabrication) not requiring post fabrication mechanical alignment [139]. The dimensions of the cantilever are: 112 µm long, 15 µm wide and approximately 1.5 µm thick. In Figure 6.12 it is possible to see the machined cantilever on the end of the optical fibre after the laser machining a) and after the FIB machining b).

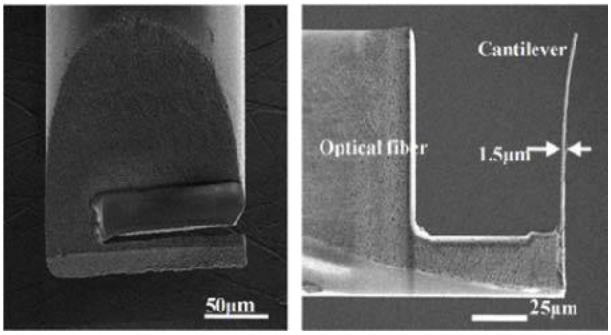

a) b)

Figure 6.12 Cantilever obtained a) after the laser machining and b) after the FIB machining [139].

The detectable pH range was 4.0-10.0 when the cantilever was coated with a functional layer of MHA (16-mercapto-hexadecanoic-1-acid) /HDT (1,6-hexanedithiol) and a range of 4.9-9.0 was detectable when the cantilever was coated with a functional layer of Al2O3/Au. The maximum deflection was approximately 200 nm at a pH of 9.0 using AlO3/Au coatings and 90 nm using MHA/HDT coating at pH 10.0. The detection time is approximately 2 min using the volume of 50 µL. This sensor also presents an advantage of measuring small sample volumes as on opposite to the conventional pH meters (need approximately 50 mL) [139].

6.3 Summary

The results presented in this chapter provide a proof-of-principle that the femtosecond machining process optimised in Chapter 5 provides a successful route to machine NCF, accessing the hollow core whilst preserving guidance in the fibre core.

The non-machined fibre presented 36.8% of transmission and the machined one (with one hole) transmitted 23.3%. However, this value should be more accurate (measuring the core transmission) than the non-machined one since the non-machined had the influence of the cladding transmission.

Regarding the fibre loss, although it was not possible to do a cutback measurement, the calculated loss for the machined fibre is 0.42 dB/cm and for the non-machined one is 0.39 dB/cm. Considering the loss for the machined hole, this is 0.45 dB. Comparing to the literature, the work reported shows a loss due to a single drilled microchannel of approximately 0.35 dB [111] using a HC-PBG fibre although the HC-PGB fibre has much lower loss overall and the microchannel reported in provides a much larger relative increase in loss compared to the hole drilled in the NCF using the optimised fs machining strategy.

The NCF used in this work presents a relatively high loss, when compared to other NCF reported in the literature, reference [5] reports a loss of 0.06 dB/m at 2.94 μm (6.0×10^{-4} dB/cm). The relatively strong guidance in the cladding of the NCF used in here (see Figure 6.3) indicates non-optimal fibre quality. This can be seen in cross section of the NCF where the cladding web shows a non-perfect triangular “ice cream cone” (since the web cladding has a strong influence on the light guidance properties [57]). Due to this observed high loss of the unmachined fibre (and the fact that the NCF used was the only fibre available at the time of the experiments) future work should be carried out on other, lower loss NCF and more complex microstructured fibres such as HC-PBF and Kagome fibre.

An alternative and mechanical process was tested to compare the differences of the mechanical process and the laser machining. It consisted of mechanical removal of

material with a diamond saw with the width of 0.150 mm (creating structures similar to those machined with the laser). It was possible to see damage of the web cladding in all the different fibres for the same set of depths performed and, in some cases, debris was observed on top of the fibres. Also, there was variability in the depth achieved for a given set of machining parameters. This is due to the difficulty in controlling the deposition of the glue which holds the fibre in place prior to machining with the diamond saw. With this method it is therefore difficult to maintain repeatability in the process and preserve the cladding web without damage.

Chapter 7 – Conclusions and Further Work

7.1 Conclusions

In Chapter 3, a new set-up for the independent operation of two beam paths from the Hurricane Ti:Sapphire laser was established. Tests regarding the pulse energy, the scanning speed, the spacing between lines and number of passes/layers for femtosecond laser machining of silica glass were performed. A first set of trials were carried out with fused silica slides. The results show the following optimised parameters:

- 5 μm was the optimal spacing between lines (in x and y directions),
- one layer is better than two due to thermal effect observed (because in these tests the focal position was not adjusted),
- a pulse energy of 0.30 μJ is appropriate.

However, tests performed with optical fibres were more decisive regarding the machining strategy and pulse energy. Tests with SMF-28 and NCF were done, using scanning speeds of 0.1, 0.05 and 0.001 mm/s corresponding to a 98.42, 99.21 and 99.98 % pulse overlap, respectively. Several pulse energies were tested in the range of 0.6 to 10 μJ to correlate pulse energy with the depth achieved for each laser machined square. The main observations/conclusions were:

- ✓ The depth versus pulse energy was not linear with a limit reached as the pulse energy reaches 10 μJ.
- ✓ Machining deeper structures (to access the hollow core) by simply increasing the pulse energy is not a successful strategy. High pulse energies in principle can be used to increase the depth but as the structure becomes deeper it is more difficult for the ablated material to escape [100].

- ✓ Increasing the number of passes (without changing the focal position) did not work due to fact that when a structure is drilled, the solid part of the structure is ablated and as the ablated material cools down it solidifies on the surfaces of the structure leading to a possible change of the focal position [100].
- ✓ The adjustment and optimisation of the incremental change in z axis of the focal position between planes is therefore crucial.

Therefore:

- The above results led to optimisation tests of smaller increments in the z direction in order to achieve a better machining efficiency [102] and quality (i.e. uniform machining [102]). This method could enhance the escape of the material from the structure (as they become deeper, it is more difficult for the ablated material to escape [100]) since less material is removed each time.
- It was decided to use small pulse energies (1 µJ) to minimise the amount of ablated material removed in each pass. This is particularly important when the structure is deeper as it is more difficult for the ablated material to escape and this could contribute to rougher structures [100].

Ways to improve the laser machining were explored in Chapter 4. The strategy consisted of repeatedly scanning lines across the width of the fibre in the x direction (2 mm) for a given distance in y (50 µm). This scanning lines method was repeated for several planes in z. Each plane is made on the same x and y coordinates of the fibre but with different z positions. The distance between adjacent lines was 0.5 µm (y distance). The machining protocol starts with focus above the surface and then the repeated planes are performed. When a plane is completed, there is a translation in the z direction, to perform another set of line in another z plane, and so on until a certain theoretical depth is achieved.

- Small increments (of 0.5, 1.0, 2.0, 2.5, and 5.0 µm) in z between each plane were used to ensure a better control of the material removal.
- The best results obtained with regards to both the depth achieved and the quality of the machined structures were when the scanning lines were machined in repeated planes with small increments in z and a low pulse energy. The small increments in z ensured a better control of the material removal to achieve deeper structures.

- The most promising results were done using 2.5 µm increment for the 30 planes machined in the cladding and the same increment (2.5 µm) for the 15 planes machined on the cladding web at 2 µJ.
- Lack of repeatability was observed (some machining areas were smooth across the width of the fibre whilst others showed an irregular machined depth for the same experimental conditions) and hence a modified protocol was investigated and demonstrated in Chapter 5.

The key changes to the machining protocol were:

- ✓ An additional step during the *Find the Fibre* program: after finding the middle position, the stages were moved 5 µm left and right to see if the laser is in focus on the highest part of the fibre.
- ✓ An additional step was performed to deal with the thermal expansion: before running the machining program, a routine called *Heat the Stages* was performed. This runs for approximately 15 mins with the laser shutter off to allow movement of the stages in x, y and z. This step was used as a precaution to allow the stages to warm up due to the repeated movements in x, y and z.

The dimensions scanned in the x direction must be larger than the external diameter of the fibre to allow for acceleration and deceleration effects. It was calculated that only an additional 8.33 µm (in total, for both sides of the fibre) would be required to ensure the speed is uniform at 1 mm/s when the structure is machined. In some cases, 1.0 mm of travel in x was used but it was deemed that between 0.400 and 0.500mm in x would be sufficient. The dimensions on the G Code used in most results were initially 0.500 mm in x and 0.100 mm in y or later 0.400 mm in x and 0.150 mm in y (the length in y was increased to make it easier to see the final depth achieved under the SEM).

The method presented in Chapter 5 was then shown to be effective in enabling a more repeatable and robust process. The protocol was tested successfully for NCF designed for 3 and 1 µm guidance:

- Best results were obtained when using 2 µJ of pulse energy and a 2.5 µm increment in z. For the NCF designed for guidance at 3 µm 53 planes below the

surface, one at the surface and 2 above were optimal. The speed used was 1 mm/s corresponding to 84.16% of pulse overlap (at the used repetition rate of 5 kHz).

The importance of the focal position to accomplish optimal efficiency has been reported above and in order to address this topic, the method to scan in different z positions with a Tunable Acoustic Gradient Index lens was shown in reference [102] for a silicon wafer. In this reference the importance of the scanning method to obtain a good quality machining when performing machined lines (compared to the machined planes as in this thesis) was shown. The compromise between the machining quality and the machining rate was also presented and it was reported that increasing the machining rate brought some degradation of the machining quality. This compares well to the findings in this thesis which highlights the need for detailed process optimisation in order to have a good compromise between the increment in z and a good quality machining.

To assess the guidance, light output of a machined fibre was compared to the light output of a non-machined fibre in Chapter 6. For the machined fibre, guidance of light was confirmed and the light was well confined in the core. Therefore, this confirmed the applied machining strategy did not disrupt the microstructured cladding to an extent that significantly disrupts the optical confinement in the hollow core.

It was also noted that, for the non-machined fibre, the light was also guided in the cladding. However, as the machining removes a small section of the cladding (Chapter 5), the light guided in this region is scattered and no longer appears at the output end. Consequently, the power output measured for the non-machined fibre (36.8%) should be expected to be higher than that for the machined fibre (23.3%) because for the non-machined fibre the total power output measured is the power in the core and the cladding. However, for sensing (and other) applications, the power guided in the hollow core is critical, hence the machined fibre shows promising performance.

In terms of fibre loss:

- although it was not possible to do a cutback measurement due to the short length of fibre available, the calculated loss for the machined fibre is 0.42 dB/cm and for the non-machined one is 0.39 dB/cm.

- It is possible to find the loss due to the hole and this would be 0.45 dB. However, as discussed above this is an overestimation of the loss due to the hole because for the non-machined fibre significant power is guided in the cladding. Nevertheless, comparing to the literature, the work reported shows a loss due to a single drilled microchannel of approximately 0.35 dB [111] using a HC-PBG fibre.

It would be expected to obtain lower loss with a better performing NCF fibre. NCF with lower losses has been reported in the literature, such as reference [5] that shows a loss of 0.06 dB/m at 2.94 μm (6.0×10^{-4} dB/cm). The fibre used in this work presents a higher loss, possibly due to the cladding guidance observed and mentioned above. The reason for the fibre loss may be related to the fact that the cladding web presents an non-perfect triangular capillary on the cladding (in the shape of an "ice cream cone") and this may have an influence on the light guidance, since the cladding web strongly influences the light guidance properties [57]. Since this fibre was the only available at the time of the experiments, future work should include other NCF and other complex microstructured fibres. More details can be seen in the following section.

An alternative, mechanical process was tested to compare the differences of a more conventional process to the laser machining technique. It consisted of a diamond saw with a width of 0.150 mm (similar to the width of the structures machined with the laser). However, when using this technique, it was possible to see damage in the web cladding in different fibres for the same set of depths performed and, in some cases, significant debris was left on top of the fibres. This indicates that the mechanical material removal process was more aggressive than the laser machining strategy leading to unavoidable damage to the delicate fibre microstructure. Also, consistency of the depth of cutting was difficult to achieve which was a result of not being able to achieve a homogeneous distribution of the glue used to fix the fibre. Overall, this method has shown to be difficult regarding the repeatability of the process, in maintaining the cladding web without damage and it was inferior to the laser machining strategy

7.2 Further work

The developed machining strategy can be an enabling process for different and novel optical devices with different optical applications. Some ideas of further work will be mentioned in this section.

a) **Further investigation of the influence of machining strategy on guidance.** The first approach regarding the laser machining strategy would be to attempt to quantify the effect of removing the cladding by comparing a fibre where just the cladding is machined away to a fibre that is machined deeper through to the core. Also, multiple holes should be machined into a fibre to see the incremental change in loss due to these additional defects. Both these experiments would allow better quantification of the loss due to a single machined hole in the fibre. However, this must be done with an NFC that exhibits overall lower loss (when such a fibre becomes available) and that has light well confined in the core.

b) **Different fibre types.** The application of the machining strategy developed in this thesis could be applied to different hollow core PCFs, for example to PBGF or Kagome fibre, to study how the machined structures influence the guidance of light and how the different fibres behaves when compared to NCF. This would demonstrate the transferability of the developed machining strategy to other fibres and hence it is an opportunity that enables the development of novel optical sensors based on different fibre geometries.

c) **Fibre gratings in hollow core fibres.** Another possibility would be to perform the machining to a depth just above the core wall and then to modify the thickness or completely remove the core wall in this region. By repeating this along the length of the fibre in a periodic way, potentially an LPG (Long Period Grating) could be realised. The increments in z would need to be adjusted carefully, since the thickness of the core wall is small. For guidance at 1030 nm and 1064 nm the wall thickness is in the range of 910 ± 50 nm requiring a sub-micron incremental change in z [7].

Creating an LPG in a hollow core fibre such as an NCF could bring new sensing possibilities. Bringing together the NCF characteristics that allow the possibility to tailor and control the guidance proprieties [25] and the LPG flexibility such as multi-parameter sensor for temperature, bend, strain, chemical and biological compounds [140] new sensing possibilities can be achieved.

LPGs have been written in conventional single mode fibres, index guiding photonics crystal fibres and solid core PBG fibres. The principal mechanism for the LPG formation is refractive index variation of the core (or cladding) through UV photosensitivity, external applied stress, residual stress-relaxation and or glass structural change [141].

Reference [141] also mentions the formation of an LPG in a hollow-core air-silica photonic bandgap fibre using CO_2 laser pulses. The LPG is created via periodic perturbation of the cladding holes which locally changes the waveguide structure of the fibre. This contrasts with LPGs inscribed in solid core fibres in which the main perturbation is on the refractive index of the fibre. LPGs in this kind of hollow core fibre showed a large polarisation dependent loss, a small sensitivity to temperature, bend and external refractive index and a high sensitivity to strain which makes it promising for optical sensors.

Reference [88] reports the fabrication of an LPG in a hollow optical fibre HOF. In this work 15 corrugating slots with various widths are inscribed using the point by point method with a femtosecond laser. The corrugated HOF-LPG showed potential for wide-band rejection filter applications in communications due to their strong mode coupling with flexible control of the rejection range [88]. More details of this reference can be seen in Chapter 2 sub-section 2.2.4 (Femtosecond laser machining of fused silica optical fibres).

d) **Orientation of fibre structure relative to laser beam.** The orientation of the fibre relative to the focussed laser could also be explored. Indeed, to realise some of the structures mentioned above then control of the orientation of the internal fibre microstructure relative to the laser beam will be critical. It would be interesting to test the same machining strategy with different fibre orientations and this could be an even

more relevant aspect if an LPG was to be written. This could be done using the two cameras on the set-up at either end of the fibre, e.g. in the positions of Cameras 2 and 3 from Figure 3.1 in Chapter 3. Cameras 2 and 3 were positioned in such a way that would allow the visualisation of the orientation of the internal microstructure of the fibre. However, in practice this was difficult to perform as the fibre could still twist in the middle of the fibre where the machining was being performed. Hence, a new method to hold the fibre in place for machining would be required. If an optimised holder could be realised that allows alignment of the fibre structure relative to the laser beam using the cameras, then different machining processes could be investigated as shown in Figure 7.1.

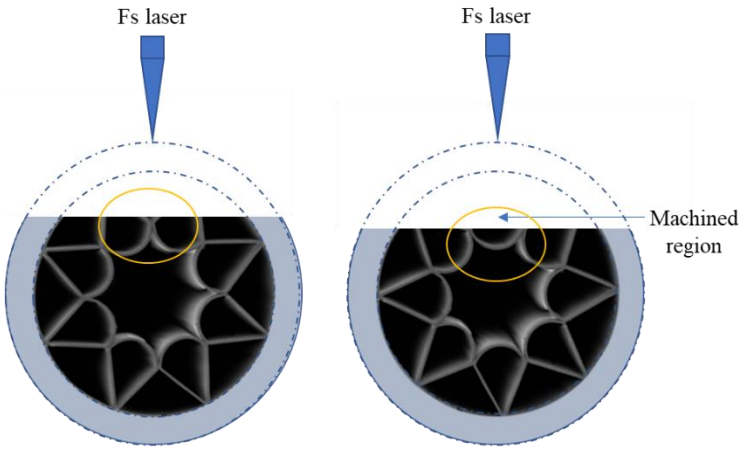

Figure 7.1 The machining strategy applied to different fibre orientations. The orange ellipse highlights the fibre orientation

e) **Species selective devices.** The use of membranes or functional layers for species selectiveness is also a promising topic. If channels for the measurand to flow in the core can be created, using the machining strategy developed in this thesis, incorporation of selective membranes across these openings would provide additional functionality for chemical or biological sensing, Figure 7.2.

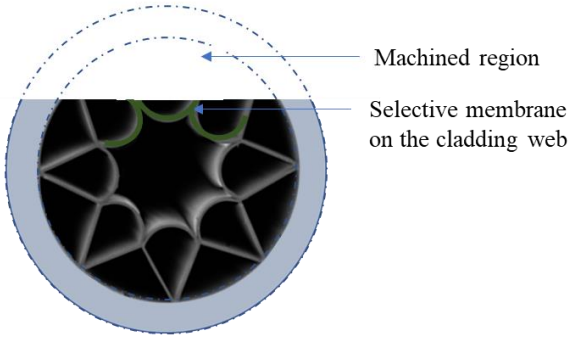

Figure 7.2 Scheme showing an incorporated selective membrane on an NCF machined using the strategy developed in this thesis.

Previous work, such as the one presented in reference [60] has exploited the unique properties of NCF for sensing. In this reference [60] the NCF is used in an optical fibre sensor set-up for multiphoton fluorescence experiments due to its low dispersion of 5 ps nm^{-1} km^{-1} across the optical spectrum of 680-750 nm (more details can be seen in Chapter 2, sub-section 2.1.4 Negative Curvature Fibres). In reference [137] the possibility of using a specific coating for added sensitivity for temperature, chemical or bio-chemical species applied to cantilever structures is reported. Such technology could potentially be transferred to an NCF based sensor.

Also, reference [139] reports on the use of functional layers on cantilevers for pH sensing such as MHA (16-mercapto-hexadecanoic-1-acid) /HDT (1,6-hexanedithiol for a detectable pH range of 4.0-10.0 and a functional layer of Al_2O_3/Au for a pH range of 4.9-9.0 (more details of this reference can be found in Chapter 6, sub-section 6.2.3 Examples of mechanical machining methods applied to optical fibres).

f) **Gas Sensors.** The hollow core of the NCF lends itself to gas detection due to the potential high overlap of the gas with the light in the core. Clearly the machining strategy developed here could provide a viable route to realising such gas sensors. Below, examples from literature will be explained in relation to this.

Previous work, such as reference [14], reports gas sensing experiments on hollow core fibres. In this reference, the fibre was tailor made for gas sensing applications in the infrared region, from 1.5 to 1.7 µm and laser-drilled lateral microchannels were done to enable access of the gas to the light guiding core and to obtain a faster response of the

sensor [14]. The sensor consisted of two pieces of a HC-PBGF with laser drilled lateral microchannels housed separately in glass tubes (chambers) with gas inlet and outlet stubs and attached by thermal splicing to FC-plug terminated SMF. The single fibre sensors were joined by SMF to a spatial distributed sensor line to allow the measurements. The authors used white light source and an optical spectrum analyser (with resolution of 0.2 nm) to interrogate the sensor. The active length of the fibre sensors is 65 cm but they differ from the number and distance of the microchannels sensor 1 in Figure 7.4 has 12 channels and 5 cm of spacing and sensor 2 has 7 channels and 8 cm of spacing). The authors showed the ability to use this sensor line for the quantitative and distributed measurement of gas mixtures [14]. Methane and a mixture of gases (methane, ethene and nitrogen) was also measured since using the white light spectroscopy allowed the ability to distinguish several gases as well as to measure the concentration of gases. The principal component regression (PCR) was used to recalculate the content of the gases in the cells from the absorption spectra. The use of different channel distances also allowed different response time of the sensors, therefore it was possible to identify the chamber and its corresponding gas [14].

The experimental set-up for gas sensing used in this reference [14] can be seen in Figure 7.3 and more details about this reference can be seen in Chapter 5, sub-section 5.3 (Discussion of Machining Results and Comparison with Literature), Figure 5.20.

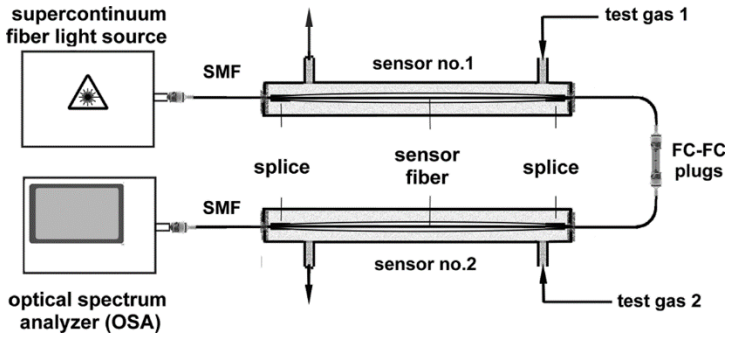

Figure 7.3 Scheme of the experimental set-up for gas sensing [14].

One of the possibilities to test the NCF fibre for gas sensing could be to perform a similar set-up for gas sensing as reference [13]. In this reference [13], an NCF was tested for methane absorption measurements and showed the capability of gas detection using side-holes [13]. The NCF was used due to the low attenuation in the MID-IR. The optical

methods that have been considered for gas sensing are the tunable diode laser absorption spectroscopy and the wavelength modulation absorption spectroscopy. To achieve high sensitivity the gas and laser must interact during several meters hollow fibres such as the NCF enable a long interaction length. Furthermore, due to the possibility to do holes in these fibres, the slow diffusion time (if gas enter only from the fibre ends) can be improved, and the interaction can increase [13]. The scheme of the methane absorption measurement set-up used in this reference [13] can be seen in Figure 7.4.

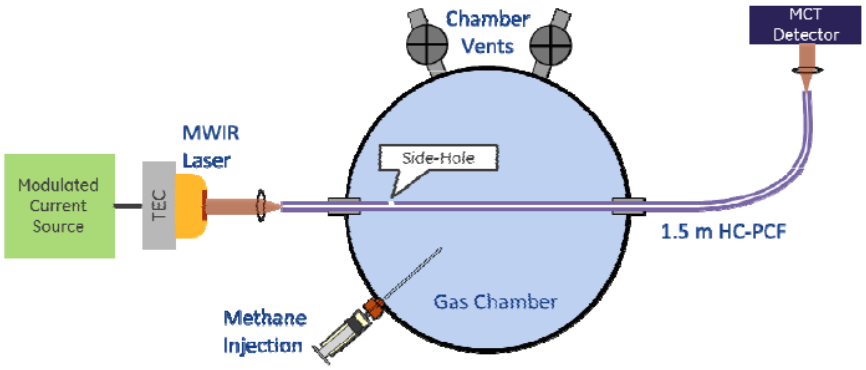

Figure 7.4. The scheme of the methane absorption measurement set-up. [13]

In reference [13], the drilled NCF was placed into a gas test chamber with the fibre end faces outside having also reinforcement tubings and compression fittings sealed around the fibre ports to avoid leaks [13] . A laser was coupled into the fibre (via one external end face) and an interband cascade laser was used to detect the absorption of the gas inside the fibre core (at 3.37 μm). The detector used was an MCT (Mercury Cadmium Telluride) detector. The method used was WMAS-TDLAS (wavelength modulation absorption spectroscopy and tunable diode laser absorption spectroscopy) and known quantities of gas were added to the chamber. The laser wavelength was tuned and modulated for the gas absorption line using temperature and current drives [13]. It was injected 667 ppm of methane into the chamber and the transmitted laser power was monitored to detect the diffusion. The results of the measurements showed strong absorption signals (with the short length of fibre) showing the capability of gas sensing. The authors suggest that sensitivity and response time can be adjusted by the use of a selected fibre length and holes characteristics such as the number, spacing and geometry. [13].

Regarding the difficulties, one of the main difficulties when working in the MI-IR region is to maintain the NCF free from humidity. Unfortunately, in the work presented in this thesis, it was not possible to test the transmission of the NCF for guidance at 3 µm due to the strong water absorption (present within the fibre) at that wavelength (Chapter 6). Therefore, it is crucial that further work should be carried out with completely dry fibre. This can be possible if the fibre is completely dry before packaging, maintaining it in a desiccator and during the analysis of the fibre this is performed in a completely sealed chamber, that could allow the control of the humidity and avoid the air humidity to enter the fibre.

The machining strategy presented in the thesis has the potential to enable the development of a range of novel topical devices and it is clear that prototype devices based around the gas sensors and LPGs discussed above would be the ideal showcase for this new processing route for hollow core microstructured fibres.

7.3 Contribution to Knowledge

The femtosecond laser machining methodology developed in this work, when compared to the work mentioned above in this field presents the following characteristics and adds the following contribution to knowledge:

- It is a robust method and not reported before on literature;
- It is a method to process microstructured optical fibres in a way that preserve the cladding web. This is of major importance for this fibre since the wavelengths that are guided are strongly dependent on the thickness of the core wall or capillaries. For example, for guidance at 1030 nm and 1064 nm a suitable wall thickness is in the range of 910 ± 50 nm [7]. This advantage opens the possibility to use the method with other fibres with much more complicated web cladding such as HC-PBGF or Kagome fibres;
- Presents novelty characteristics such as:
    - Overcomes the issues of tapering associated with drilling (as seen in reference [8]);
    - Uses a single technique (femtosecond laser machining), therefore there is no need of multi-step process such as laser machining with FIB milling (as in

[9]), water assisted femtosecond laser machining methods [12], or chemical etching method with laser machining (as in [10] and [11]);

- Produces larges slots than the ones presented in literature and still preserving the cladding web (larger than 50 μm diameter as in [13], for example);
- Provides a good and better depth control when compared to other laser processes, since it enables the process to be stopped exposing the core wall or breaking though the core due to the small increments in z;
- Enables the potential to modify the core wall which is not possible by other methods. This opens up a new path for chemical sensing, for example, combining the important guidance properties of NCF, allowing the infrared region detection and the detection of selective species, nor only by optical properties (wavelength) but also due to the possibility of incorporating selective membranes on the core walls or even Bragg gratings.

It was therefore possible to overcome the challenges mentioned in Chapter 1 regarding the issues of tapering, the issues of combined methods (which are not simple, expensive, time consuming and require handling of chemical substances) and to achieve a good control of the depth (since most of the structures in the literature are tapered or the depth is enhanced by chemical substances, so it is not always controllable).

In conclusion, the method showed the development of a strategy that potentially allows any shape to be machined in a microstructured optical fibre, since it is governed by a digital scanning pattern and provides a way to radically enhance the types of devices that might be developed using an NCF (and other microstructured fibres).

Appendix A– G Code for the scan of lines

This study was done in collaboration with Jacopo Siliprandi from the Institute of Photonics and Quantum Sciences.

```
; $depth1 will span ~15 mm
;Declare Position Variables
DVAR $posz1a $posz1b $posz1 $posx1 $posy1
DVAR $posz2a $posz2b $posz2 $posx2 $posy2
DVAR $posz3a $posz3b $posz3 $posx3 $posy3
DVAR $posz4a $posz4b $posz4 $posx4 $posy4
DVAR $startx $starty $startz
DVAR $realZ
;Declare Variables
DVAR $speed $numOfSpeeds $speed1 $speed2 $speed3 $speed4
DVAR $layers $numOfDiffLayers $layersT1 $layersT2 $layersT3 $layersT4
DVAR $numberOfPasses $numberOfLines
DVAR $length
DVAR $stepx $stepy $stepz $stepz1 $stepz2 $stepz3
DVAR $depth $depth1 $depth2 $depth3
DVAR $slopexSet1 $slopexSet2 $slopeySet1 $slopeySet2
DVAR $slopex $slopey
DVAR $jumpy $jumpz
DVAR $iii $jjj $kkk $lll $flip $ccc
DVAR $tens $marks $offsety $offsetz $markz $markStep $markStepZ
DVAR $hundred50 $tally $Ytally $Xtally
DVAR $resp $variable $terminate
;Set-up
;G71 ; Metric units
G108 ; No decel to zero
G76 ; SET TO UNITS/SECOND, fixed cycling fine boring
;G94 ; Normal federate
```

```
;G64 ; Set linear accel
G110 ; Norm circ interp, user macro ( Square root)
G90 ;Absolute value comand
dwell 0.1
Enable X Y Z
dwell 0.1
;SPEEDS
        $numOfSpeeds=4
        $speed1 = 0.45
        $speed2 = 1.0
        $speed3 = 1.5
        $speed4 = 2.0
        $speed = $speed1
; Initialise Variables
        $numberOfPasses = 1
        $stepx = 0.0500
        $stepy = 2.0000
        $stepz1 = 0.0001
        $stepz = $stepz1
        $depth1 = 0.0320 ; 0.0160 above and below the surface
        $depth = $depth1
        $jumpy = 1.5
        $jumpz = 0.0 ;beam height jump/leave it for now
        $flip = 1
        $numberOfLines = $depth/$stepz
        $offsety = 0.1000
        $Ytally = 0.0200 ; dimensions of the mark
        $Xtally = 0.0250
;Z Positions: This part of the code corrects for slope differences, because the slide might
not be perfectly flat ( imperfections or due to the glue underneath)
                $posx1  =  60.0000
                $posy1  =  -92.0000
                $posz1  =
```

```
$posx2  =  60.0000
$posy2  =  -70.0000
$posz2   =
$posx3  =  41.0000
$posy3  =  -92.0000
$posz3   =
$posx4  =  41.0000
$posy4  =  -70.0000
$posz4   =
$slopexSet1 = ($posz4-$posz2)/($posx4-$posx2) ; does the slope between positions 4 and 2 and 2 and 1
$slopeySet1 = ($posz2-$posz1)/($posy2-$posy1)
$slopexSet2 = ($posz3-$posz1)/($posx3-$posx1); does the slope between 3 and 1 and 4 and 3
$slopeySet2 = ($posz4-$posz3)/($posy4-$posy3)
$slopex = ($slopexSet1+$slopexSet2)/2
$slopey = ($slopeySet1+$slopeySet2)/2
$resp= MSGBOX DF_MSGBOX_YESNO + DF_ICON_QUESTION, "Current Slope Set Selected, Continue?"
MSGDISPLAY 1, "Resp =", $resp
IF ($resp==YES_BUTTON) THEN
    MSGDISPLAY 1, "Continuing."
    dwell 2
    $terminate = 0
ELSE
    MSGDISPLAY 1, "Terminating"
    dwell 2
    $terminate=1
ENDIF
IF $terminate EQ 0 THEN
;output slope info
$slopexSet1 = MSGINPUT DF_MSGBOX_OKONLY "Correction Slope; Slope X Set1;" $slopexSet1
```

```
        $slopexSet2 = MSGINPUT DF_MSGBOX_OKONLY "Correction Slope; Slope X Set2;" $slopexSet2
        $slopeySet1 = MSGINPUT DF_MSGBOX_OKONLY "Correction Slope; Slope Y Set1;" $slopeySet1
        $slopeySet2 = MSGINPUT DF_MSGBOX_OKONLY "Correction Slope; Slope Y Set2;" $slopeySet2

        $slopex = MSGINPUT DF_MSGBOX_OKONLY "Correction Slope; Slope X;" $slopex
        $slopey = MSGINPUT DF_MSGBOX_OKONLY "Correction Slope; Slope Y;" $slopey
dwell 2
; Writing Code
dwell 0.1
G90
G82
MSGCLEAR 1
$startx = $slopex ; corrected for slope
$starty = $slopey
$startx = MSGINPUT DF_MSGBOX_OKONLY "Start Position; Start X =;" $startx
$starty = MSGINPUT DF_MSGBOX_OKONLY "Start Position; Start Y =;" $starty
MSGDISPLAY 1, "Start X =", $startx
MSGDISPLAY 1, "Start Y =", $starty
dwell 5
$ccc = 1
WHILE $ccc LE 2 ;change to 1 next time
    MSGCLEAR 1
    MSGDISPLAY 1, "copy number ", $ccc
    $flip = 1
    $marks = 1
    $tens  = 10
    $hundred50 = 1
    G82
```

```
IF $ccc EQ 1 THEN
        $startx = $startx
        $starty = $starty
        $startz = -($depth/2) + $posz1 + $slopex*($startx - $posx1)+ $slopey*($starty-$posy1) ; correction for slope on z axis
        $offsetz = 0.0120          ; 0.018
        $markStepZ = 0.0060        ; 0.006
        $markz = 2*$offsetz/$markStepZ  ; 4 is number of markz
        $length = 0.5              ; lenght of the line
        $speed = $speed1           ; At speed determined here
ELSE IF $ccc EQ 2 THEN
        $startx = $startx
        $starty = $starty+$jumpy ; moves away in jumpy
        $startz = -($depth/2) + $posz1 + $slopex*($startx - $posx1)+ $slopey*($starty-$posy1)

        $offsetz = 0.0120          ; 0.012
        $markStepZ = 0.0060        ; 0.006
        $markz = 2*$offsetz/$markStepZ  ; 4 is number of markz
        $length = 0.5
        $speed = $speed1
ELSE IF $ccc EQ 3 THEN
        $startx = 65.0000
        $starty = -76.0000
        $startz = -($depth/2) + $posz1 + $slopex*($startx - $posx1)+ $slopey*($starty-$posy1)
        $offsetz = 0.0120          ; 0.0240
        $markStepZ = 0.0060        ; 0.0080
        $markz = 2*$offsetz/$markStepZ  ; 4 is number of markz
        $length = 1.0
        $speed = $speed2
ELSE IF $ccc EQ 4 THEN
        $startx = 65.0000
```

```
            $starty = -76.0000
            $startz =  -($depth/2) + $posz2 + $slopex*($startx - $posx2)+
$slopey*($starty-$posy2)
            $offsetz = 0.0120
            $markStepZ = 0.0060
            $markz = 2*$offsetz/$markStepZ ; 4 is number of markz
            $length = 1.0
            $speed = $speed2
        ENDIF
        F 3
        G1 X $startx Y $starty
        dwell 0.1
        F 0.05
        G1 Z $startz
        dwell 1
        G92 Z 0
        F $speed
        $iii=1
        WHILE $iii LE $numberOfLines
            ;Do Line
            G92 X 0 Y 0
             ;marks code
            IF $iii EQ $tens THEN ; This If does one mark when we reach 10 lines
                MSGDISPLAY 1, "line number  ", $tens
                IF $tens EQ 170 THEN ;
                    $hundred50 = -1
                    $marks = 1
                ENDIF
                    $tally = 1
                    WHILE $tally LE $marks
                        F 0.4
                         ;___mark on right hand side___
                        G1 Y +$offsety + 2*($tally-1)*$Ytally
```

```
                    G1 Z -$offsetz + $depth/2 + ($iii-1)*$slopex*(-
$stepx) +$slopey*$length + $offsety*$slopey +  2*($tally-1)*$Ytally*$slopey
                    $markStep=1
                    WHILE $markStep LE $markz
                        F 0.13
                        $DO0.X = 1    ;Open Shutter
                        dwell 0.1
                        G1 Y +$offsety + 2*($tally)*$Ytally ; goes
in Y direction
                        dwell 0.1
                        G1 X +($hundred50)*$Xtally ; goes in x
direction
                        dwell 0.1
                        G1 X 0
                        dwell 0.1
                        G1 Y +$offsety + 2*($tally-1)*$Ytally
                        dwell 0.1
                        $DO0.X = 0    ;Close Shutter

                        G1 Z -$offsetz + $depth/2 + ($iii-
1)*$slopex*(-$stepx) +$slopey*$length + $offsety*$slopey + 2*($tally-
1)*$Ytally*$slopey + $markStep*$markStepZ
                        $markStep = $markStep + 1
                    END WHILE
                    $tally = $tally + 1
                END WHILE
                    F 0.1
                    G1 X 0 Y 0
                    dwell 0.1
                    F 0.05
                    G1 Z ($iii-1)*$stepz + ($length)*$slopey + ($iii-
1)*$slopex*(-$stepx)
                    dwell 0.1
```

```
                    F $speed
                ;update $tens
                    $tens=$tens + 10
                    $marks=$marks + 1
            ENDIF
        ;end of marks code
        F $speed
        dwell 0.1
        $DO0.X = 1    ;Open Shutter
        dwell 0.1
        IF $flip EQ 1 THEN
            G1 Y ($flip)*$length Z ($iii-1)*$stepz + $flip*($length)*$slopey
+ ($iii-1)*$slopex*(-$stepx)
        ELSE IF $flip EQ -1 THEN
            G1  Y  ($flip)*$length  Z  ($iii-1)*$stepz  +  ($iii-1)*$slopex*(-
$stepx)
        ENDIF
        dwell 0.1
        $DO0.X = 0    ;Close Shutter
        ;Move X
        F 0.1
        G1 X -$stepx
        dwell 0.1
        ;Move Z
        F 0.005
        IF $flip EQ 1 THEN
            G1    Z    +($iii)*$stepz    +    ($iii)*$slopex*(-$stepx)    +
$flip*($length)*$slopey
        ELSE IF $flip EQ -1 THEN
            G1 Z +($iii)*$stepz + ($iii)*$slopex*(-$stepx)
        ENDIF
        dwell 0.1
        F $speed
```

```
                ;Reverse Line
                $flip = -$flip
                $iii  =  $iii+1
        END WHILE
        $DO0.X = 0
        $flip = 1 ;set $flip to original value
        dwell 1    ; END OF COPY
 $ccc=$ccc+1
END WHILE
MSGDISPLAY 1, "Program Terminated Correctly."
ELSE IF $terminate EQ 1 THEN
 MSGDISPLAY 1, "Program Terminated Incorrectly."
 dwell 1
ENDIF
MSGDISPLAY 1, "Program Ended. Change Power and Next Run ."
```

Appendix B– G Code example for the Square

This program was used to machine squares in fused silica and in fibre

```
; Declaring variables
DVAR $numberOfCopies $speed1 $speed2
DVAR $layers $layersT1 $layersT2 $numberoflayers  $numberOfSpeed
DVAR $speed1 $speed2
DVAR $speed3
DVAR $Xstepx $lengthy
DVAR $ccc $lll $ppp $vvv $iii
DVAR $stepy $lengthx
DVAR $EVEN $ODD $horVer
DVAR $stepx $stepy
DVAR $posx1 $posy1  $posz1a $posz1b  $posz1
DVAR $posx2 $posy2 $posz2a $posz2b   $posz2
DVAR $posx3 $posy3 $posz3a $posz3b  $posz3
DVAR $posx4 $posy4 $posz4a $posz4b  $posz4
DVAR $posz5 $posz6 $squareNo
DVAR $jumpy
DVAR $startx $starty $startz
DVAR $speed
;Set-up
G90 ; Absolute value command
Enable X Y Z
dwell 0.1
;initial commands
G82; Fixed cycle ( Drilling/ Counter Boring)
ENABLE X Y Z
;Initialise Variables
$jumpy=0.0405 ; distance between squares
$speed1=0.1
$speed2=0.05
```

$speed3=0.001

$numberOfCopies=1

$numberOfSpeed = 3

$numberoflayers = 1

$layersT1=1

$layersT2=2

$stepx = 0.000500 ; dividing 0.0175 by 35 spacing gives a spacing of 0.000500 mm

$stepy = 0.000500

$lengthy = 0.0175 ;length y is the square side

$lengthx = 0.0175

; Positions found. In this case, it is just needed one position and the other are defined by the distance between the squares and by the new z positions

$posx1 = 56.9845-0.00875 ; half of the size of the square to take positions in the middle of the holes

$posy1 = -78.5188-0.00875

$posz1 = 0.5914

;$posx2 =

;$posy2 =

$posz2 = 0.5914

;$posx3 =

;$posy3 =

$posz3 = 0.5914

;$posx4 =

;$posy4 =

$posz4 = 0.700

;$posx5 =

;$posy5 =

$posz5 = 0.700

;$posx6 =

;$posy6 =

$posz6 = 0.700

$startx = $posx1

$starty = $posy1

```
            $startz = $posz1
        dwell 1
;Code: moves the laser to the start position
F 2
G1 X $startx Y $starty
dwell 0.1
F 0.05
G1 Z $startz
dwell 0.1
$squareNo=0
$lll=1
WHILE $lll LE $numberOfSpeed ; This while cycle gives the chance to choose one of the three speeds determined in the initialise variables part
        IF $lll EQ 1 THEN
            $speed = $speed1
            F  $speed
        ELSE IF $lll EQ 2 THEN
            $speed = $speed2
            F  $speed
        ELSE IF $lll EQ 3 THEN
            $speed = $speed3
            F  $speed
        ENDIF
$ccc=1
WHILE $ccc LE $numberOfCopies ; TO DO 2 SQUARES each one with different layers, meaning more than one pass with the laser
        $ppp=1
        WHILE $ppp LE $numberoflayers    ;sets number of passes
            IF $ppp EQ 1 THEN
                $layers=$layersT1
            ELSE IF $ppp EQ 2 THEN
                $layers=$layersT2
            ENDIF
```

```
$vvv=1
    WHILE $vvv LE $layers
    $EVEN=2 ; The writing program will do lines in different directions in the vertical and horizontal directions so save traveling time
    $ODD=1
    G92 X 0 Y 0
    $horVer = 1
    WHILE $horVer LE 2
        $iii=1
        WHILE $iii LE 36  ;lines
            IF $horVer EQ 1 THEN ;
    IF $iii EQ $ODD; This part of the If does the lines in y
        $DO0.X = 1 ; opens shutter
        dwell 0.1 ; waits
        G1 Y $lengthy; does the distance defined in lenghty
        dwell 0.1
        F 0.001
        $DO0.X = 0; closes the shutter
        G1 X $stepx*$iii; does the increment defined in stepx
        dwell 0.1
        F $speed; writes with the speed defined by the while number of speed
    ELSE IF $iii EQ $EVEN
        $DO0.X = 1
        dwell 0.1
        G1 Y 0 ; with shutter open goes to the origin, meaning writing another line
        dwell 0.1
        F 0.001
        $DO0.X = 0
        G1 X $stepx*$iii;  does the increment defined in stepx
        $ODD=$ODD+2 ; and the counter continues
        $EVEN=$EVEN+2
```

```
                F $speed
            ENDIF
        ELSE IF $horVer EQ 2 THEN
            IF $iii EQ $ODD
                G1 X $lengthy ; This part of the  IF does the lines in x
                $DO0.X = 1 ; Opens shutter
                dwell 0.1
                G1 X 0 ; goes to the origin
                dwell 0.1
                F 0.001
                $DO0.X = 0
                G1 Y $stepy*$iii; gives increment in Y
                dwell 0.1
                F $speed
            ELSE IF $iii EQ $EVEN
                $DO0.X =1
                dwell 0.1
                G1 X $lengthx; moves X to length x
                dwell 0.1
                F 0.001
                $DO0.X = 0
                G1 Y $stepy*$iii; gives increment to stepy
                $ODD=$ODD+2; the counter continues
                $EVEN=$EVEN+2
                F $speed
            ENDIF
        ENDIF
                        $iii=$iii+1
                END WHILE
                $horVer=$horVer+1
                $EVEN=2
                $ODD=1
            END WHILE
```

```
                $vvv=$vvv+1
                G1 X 0 Y 0
            END WHILE
            $squareNo=$squareNo+1 ; This part of the Code redefines the new machining position
            G82 ; set the coordinate sistem
            ;move to new position
                ; move to new y
                G1 X $startx+$squareNo*$jumpy+$squareNo*$lengthy
                ; move to new z
                IF $squareNo EQ 1 THEN
                    ;G1 X $posx2 Y $posy2
                    G1 Z $posz2      ; When the Square one is finished, it goes to the new position, in this case number 2
                ELSE IF $squareNo EQ 2 THEN
                    ;G1 X $posx3 Y $posy3
                    G1 Z $posz3
                ELSE IF $squareNo EQ 3 THEN
                    ;G1 X $posx4 Y $posy4
                    G1 Z $posz4
                ELSE IF $squareNo EQ 4 THEN
                    ;G1 X $posx5 Y $posy5
                    G1 Z $posz5
                ELSE IF $squareNo EQ 5 THEN
                    ;G1 X $posx6 Y $posy6
                    G1 Z $posz6
                ENDIF
                    $ppp=$ppp+1
                END WHILE
                $ccc=$ccc+1
            END WHILE
        $lll=$lll+1
END WHILE
```

Appendix C –G Code for *Find the Fibre*

The find a fibre program runs from point A to point B with the shutter on with the focal position of the microscope slide. When the laser light passes through the fibre, the light disappears.

```
;Declare Variables
DVAR $pointAx $pointAy $pointAz
DVAR $pointBx $pointBy $pointBz
;Set-up
G90 ; Absolute value command
dwell 0.1
Enable X Y Z
dwell 0.1
;initial commands
G82; Fixed cycle (Drilling/ Counter Boring)
Enable X Y Z
dwell 0.1
;Point A and B
$pointAx  = 55.0000
$pointAy  = -86.0000
$pointAz  =  0.7290
$pointBx = 55.0000
$pointBy =  -74.0000
$pointBz  =  0.7030
;Code
; Go to Point A
F 2
G1 X $pointAx Y $pointAy
dwell 0.1
F 0.3
G1 Z $pointAz
dwell 0.1
```

```
; Go from Point A to Point B
F 0.1
$DO0.X = 1
dwell 0.1
G1 X $pointBx Y $pointBy  Z $pointBz
dwell 0.1
$DO0.X = 0
```

Appendix D– G Code for Planes Above the Surface

```
DVAR $speed  $speed1 $speed2 $speed3
DVAR $stepx  $lengthy $lengthx
DVAR $numberOfSpeed
DVAR  $lll $iii
DVAR $posx1 $posy1 $posz1
DVAR $totallines
DVAR $numberzplanes
DVAR $incrementz $squareNo
;Set-up
G90 ; Absolute value command
dwell 0.1
Enable X Y Z
dwell 0.1
;initial commands
G82; Fixed cycle ( Drilling/ Counter Boring)
;This part defines values to the variables. Here it is set the writing speed, the number of planes performed as well as the dimensions in x, y and z
$speed1=1.00
$speed2=0.05
$speed3=0.001
$incrementz=0.0025
$numberOfSpeed = 1
$stepx = 0.000500 ; This actually will determine the dimensions in y (it works differently from the conventional system)
$lengthx = 0.200
$totallines= 300 ; if the total of lines is 300 and it has 0.5 micron this means that the structures has 150 microns in y
;The position here is the one found after running the find the fibre program and adjusting the focal position
$posx1  =  55.0000
$posy1  =  -80.1224
```

$posz1 = 0.3383-0.005 ; the first increment is 0.005 but after this one the increment passes to 0.0025. In this program, the change in the focal position is manual. After this program, the Appendix 4.3 will run..

```
dwell 1
;Code
; Goes to the position determined above
F 2
G1 X $posx1 Y $posy1
dwell 0.1
F 0.05 ; with this speed
G1 Z $posz1
dwell 0.1
$squareNo=0
$lll=1
WHILE $lll LE $numberOfSpeed
        IF $lll EQ 1 THEN
                $speed = $speed1
                F  $speed
        ELSE IF $lll EQ 2 THEN
                $speed = $speed2
                F  $speed
        ELSE IF $lll EQ 3 THEN
                $speed = $speed3
                F  $speed
        ENDIF
        G92 X 0 Y 0
        $iii=1
        WHILE $iii LE $totallines
                $DO0.X = 0 ; With shutter of it will go in Y the distance lengthx
      G1 Y $lengthx
                dwell 0.1
        G1 X $stepx*$iii; It will do the step in x to start writing after the step x distance
                dwell 0.1
```

$DO0.X = 1 ; the shutter will open and it will go, from the distance determined in length x to -0.2000 passing though the zero position

G1 Y -0.200

dwell 0.1

F $speed ;this determines the writing distance

$DO0.X = 0 ; after the line as performed the shutter will close (safety procedure)

$iii=$iii+1 ;It will do this cycle according to this counter and determined by the total number of lines $totallines

END WHILE

$lll=$lll+1

G1 X 0 Y 0

END WHILE

Appendix E– G Code for Plane on Surface and Several Below

```
;Declaring variables
DVAR $speed  $speed1 $speed2 $speed3
DVAR $stepx  $lengthy $lengthx
DVAR $numberOfSpeed
DVAR  $lll $iii $aaa
DVAR $posx1 $posy1 $posz1
DVAR $totallines
DVAR $numberzplanes
DVAR $incrementz $squareNo
;Set-up
G90 ;Absolute value command
dwell 0.1
Enable X Y Z
dwell 0.1
;initial commands
G82; Fixed cycle ( Drilling/ Counter Boring)
ENABLE X Y Z
; This part defines values to the variables. Here it is set the writing speed, the number of planes performed as well as the dimensions in x, y and z
$speed1=1.00
$speed2=0.05
$speed3=0.001
$numberzplanes=58
$incrementz=0.0025
$numberOfSpeed = 1
$stepx = 0.000500 ; This actually will determine the dimensions in y (it works differently from the conventional system)
$lengthx = 0.200
$totallines= 300 ; if the total of lines is 300 and it has 0.5 micron this means that the structures has 150 microns in y
```

```
;The position here is the one found after running the find the fibre program and adjusting the focal position
$posx1  =  55.0000
$posy1  =  -80.1224
$posz1  =  0.3383
dwell 1
;Code
; Goes to the position determined above
F 2
G1 X $posx1 Y $posy1
dwell 0.1
F 0.05 ; with this speed
G1 Z $posz1
dwell 0.1
$squareNo=0
$lll=1
WHILE $lll LE $numberOfSpeed ; This while cycle gives the chance to choose one of the three speeds determined in the initialise variables part
        IF $lll EQ 1 THEN
        $speed = $speed1
        F  $speed
        ELSE IF $lll EQ 2 THEN
        $speed = $speed2
        F  $speed
        ELSE IF $lll EQ 3 THEN
        $speed = $speed3
        F  $speed
        ENDIF
        G92 X 0 Y 0
        $aaa=0
        WHILE $aaa LE $numberzplanes  ; This while does several planes in z, same y and x but displaced defined by the increment in z
                $DO0.X = 0
```

```
            G1 Z ($posz1+$incrementz*$aaa)
            dwell 0.1
      $iii=1
      WHILE $iii LE $totallines
            $DO0.X = 0 ; With shutter of it will go in Y the distance lengthx
   G1 Y $lengthx
            dwell 0.1
   G1 X $stepx*$iii; It will do the step in x to start writing after the step x distance
            dwell 0.1
            $DO0.X = 1 ; the shutter will open and it will go, from the distance determined in length x to -0.2000 passing though the zero position
            G1 Y -0.200
            dwell 0.1
            F $speed ;this determines the writing distance
            $DO0.X = 0 ; after the line as performed the shutter will close ( safety procedure)
            $iii=$iii+1 ;It will do this cycle according to this counter and determined by the total number of lines $totallines
      END WHILE
      $aaa=$aaa+1
      END WHILE
      $lll=$lll+1
      G1 X 0 Y 0
END WHILE
```

Appendix F - G Code for *Heat the Stages*

```
DVAR $speed  $speed1 $speed2 $speed3
DVAR $stepx $lengthy $lengthx
DVAR $numberOfSpeed
DVAR  $lll $iii $aaa
DVAR $posx1 $posy1 $posz1
DVAR $totallines
DVAR $numberzplanes
DVAR $incrementz $squareNo
;Set-up
G76 ; fixed cycle, fine boring
G90 ;Abs
dwell 0.1
Enable X Y Z
dwell 0.1
;initial commands
G90 ; Absolute value command
G82; Fixed cicle ( Drilling/ Counter Boring)
;This part defines values to the variables. Here it is set the writing speed, the number of planes performed as well as the dimensions in x, y and z
$speed1=1.00
$speed2=0.05
$speed3=0.001
$numberzplanes=1
$incrementz=0.0025
$numberOfSpeed = 1
$stepx = 0.000500 ; This actually will determine the dimensions in y (it works differently from the conventional system)
$lengthx = 0.500
$totallines= 200;
;The position here is the one found after running the find the fibre program and adjusting the focal position
```

```
        $posx1  =  55.0000
        $posy1  =  -80.1224
        $posz1  =  0.3383
    dwell 1
;Code
F 2
G1 X $posx1 Y $posy1
dwell 0.1
F 0.05 ; with this speed
G1 Z $posz1
dwell 0.1
        $squareNo=0
        $lll=1
        WHILE $lll LE $numberOfSpeed
                IF $lll EQ 1 THEN
                $speed = $speed1
                F  $speed
                ELSE IF $lll EQ 2 THEN
                $speed = $speed2
                F  $speed
                ELSE IF $lll EQ 3 THEN
                $speed = $speed3
                F  $speed
                ENDIF
                G92 X 0 Y 0
                        $aaa=0
                        WHILE $aaa LE $numberzplanes  ; This while does several planes
in z, in this case it is 2 planes
                        $DO0.X = 0
                        G1 Z ($posz1+$incrementz*$aaa)
                        dwell 0.1
                        $iii=1
```

WHILE $iii LE $totallines ; This while does several lines, always with shutter off just to allow the stages to move.

```
$DO0.X = 0
G1 Y $lengthx
dwell 0.1
G1 X $stepx*$iii
dwell 0.1
G1 Y -0.500
dwell 0.1
F $speed
$iii=$iii+1
END WHILE
$aaa=$aaa+1
END WHILE
$lll=$lll+1
G1 X 0 Y 0
END WHILE
```

Appendix G- Water IR Spectrum

Below there is the graphic of the Infrared Spectrum of the water from the NIST website (https://webbook.nist.gov/cgi/inchi?ID=C7732185&Type=IR-SPEC&Index=1#IR-SPEC). The absorbance is plotted against the wavenumber. The wavelength of 3 µm corresponds to a wavenumber of 3333 cm^{-1}.

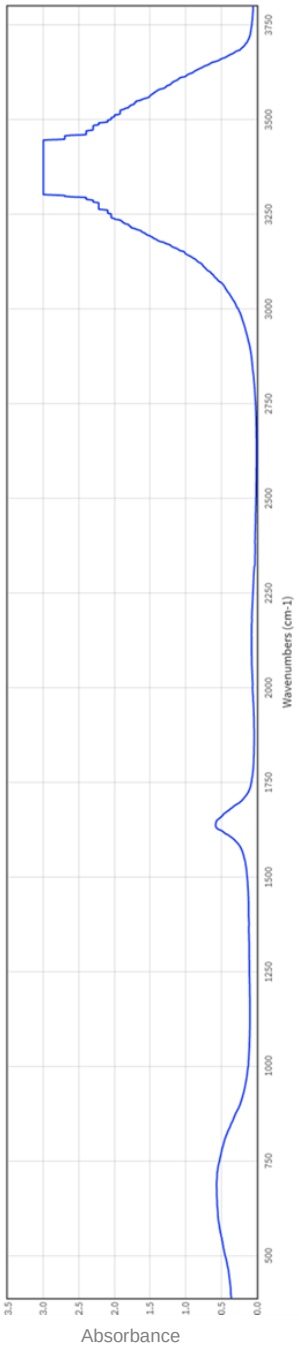

References

[1] J.M. W. M. Steen. Chapter 2 Basic Laser Optics. pp.106, 107 (2010)

[2] F. Yu, W.J. Wadsworth, J.C. Knight. *Low loss silica hollow core fibers for 3–4 μm spectral region*, Optics Express, **20**, 11153–8 (2012)

[3] F. Yu, J.C. Knight. *Spectral attenuation limits of silica hollow core negative curvature fiber*, Optics Express, **21**, 21466–71 (2013)

[4] C.C. Novo, A. Urich, D. Choudhury, R. Carter, D.P. Hand, R.R. Thomson, F. Yu, J.C. Knight, S. Brooks, S. Mcculloch, J.D. Shephard. *Negative curvature fibres: exploiting the potential for novel optical sensors*, Proceedings of SPIE, **9634**, 963454–5 (2015)

[5] A. Urich, R.R.J. Maier, F. Yu, J.C. Knight, D.P. Hand, J.D. Shephard. *Silica hollow core microstructured fibres for mid-infrared surgical applications*, Journal of Non-Crystalline Solids, **377**, 236–9 (2013)

[6] P. Jaworski, F. Yu, R.M. Carter, J.C. Knight, J.D. Shephard, D.P. Hand. *High energy green nanosecond and picosecond pulse delivery through a negative curvature fiber for precision micro-machining*, Optics Express, **23**, 8498–506 (2015)

[7] P. Jaworski, F. Yu, R.R.J. Maier, W.J. Wadsworth, J.C. Knight, J.D. Shephard, D.P. Hand. *Picosecond and nanosecond pulse delivery through a hollow-core Negative Curvature Fiber for micro-machining applications*, Optics Express, **21**, 22742–53 (2013)

[8] A. Van Brakel, C. Grivas, M.N. Petrovich, D.J. Richardson. *Micro-channels machined in microstructured optical fibers by femtosecond laser*, Optics Express, **15**, 8731–6 (2007)

[9] M. Amanzadeh, S.M. Aminossadati. *A New Approach for Drilling Lateral Microchannels in Photonic Crystal Fibres*, 2016 IEEE Photonics Conference (IPC), IEEE, 779–80 (2016)

[10] Y. Lai, K. Zhou, L. Zhang, I. Bennion. *Microchannels in conventional single-mode fibers*, Optics Letters, **31**, 2559–61 (2006)

[11] S. Rajesh, Y. Bellouard. *Towards fast femtosecond laser micromachining of fused silica: The effect of deposited energy*, Optics Express, **18**, 21490–7 (2010)

[12] I.-B. Sohn, Y.-S. Kim, Y.-C. Noh, J.-C. Ryu, J.-T. Kim. *Microstructuring of Optical Fibers Using a Femtosecond Laser*, Journal of the Optical Society of Korea, **13**, 33–6 (2009)

[13] J. Karp, W. Challener, M. Kasten, N. Choudhury, S. Palit, G. Pickrell, D. Homa, A. Floyd, Y. Cheng, F. Yu, J. Knight. *Fugitive methane leak detection using mid-infrared hollow-core photonic crystal fiber containing ultrafast laser drilled side-holes*, Proceedings of SPIE, **9852**, 985210-1–7 (2016)

[14] H. Lehmann, H. Bartelt, R. Willsch, R. Amezcua-Correa, J.C. Knight. *In-line gas sensor based on a photonic bandgap fiber with laser-drilled lateral microchannels*, IEEE Sensors Journal, **11**, 2926–31 (2011)

[15] A. Othonos, K. Kalli, D. Pureur, A. Mugnier. Chapter 5 Fiber Bragg gratings. *Wavelength Filters in Fibre Optics*. (H. Venghaus ed.) Vol. 123, Springer, Berlin, Heidelberg, pp.189–269 (2006)

[16] M. Hou, F. Zhu, Y. Wang, Y. Wang, C. Liao, S. Liu, P. Lu. *Antiresonant reflecting guidance mechanism in hollow-core fiber for gas pressure sensing*, Optics Express, **24**, 2827–30 (2016)

[17] C.K.Y. Leung, K.T. Wan, D. Inaudi, X. Bao, W. Habel, Z. Zhou, J. Ou, M. Ghandehari, H.C. Wu, M. Imai. *Review: optical fiber sensors for civil engineering applications*, Materials and Structures, **48**, 871–906 (2013)

[18] B. Lee. *Review of the present status of optical fiber sensors*, Optical Fiber Technology, **9**, 57–79 (2003)

[19] S. Ghetia, R. Gajjar, P. Trivedi. *Classification of Fiber Optical Sensors*, International Journal of Electronics Communication and Computer Technology (IJECCT), **3**, 442–5 (2013)

[20] C. Novo, L. Bilro, R. Ferreira, N. Alberto, P. Antunes, C. Leitão, R. Nogueira, J.L. Pinto. *Plastic optical fibre sensor for quality control in food industry*, Proceedings of SPIE, **8794**, 879411–4 (2013)

[21] C. Lafond, J.-F. Couillard, J.-L. Delarosbil, F. Sylvain, P. de Sandro. *Recent improvements on mid-IR chalcogenide optical fibers*, Proceedings of SPIE, **9070**, 90701C–90701C–7 (2014)

[22] M. Saad. *Fluoride glass fibers*, 2011 IEEE Photonics Society Summer Topical Meeting Series, **2**, 81–2 (2011)

[23] T.M. Monro, Y.D. West, D.W. Hewak, N.G.R. Broderick, D.J. Richardson. *Chalcogenide holey fibres*, Electronics Letters, **36**, 1998–2000 (2000)

[24] F. Berghmans, T. Geernaert, T. Baghdasaryan, H. Thienpont. *Challenges in the fabrication of fibre Bragg gratings in silica and polymer microstructured optical*

fibres, Laser and Photonics Reviews, **8**, 27–52 (2014)

[25] C. Wei, R.J. Weiblen, C.R. Menyuk, J. Hu. *Negative curvature fibers*, Advances in Optics and Photonics, **9**, 504–61 (2017)

[26] A.M.R. Pinto, M. Lopez-Amo. *Photonic crystal fibers for sensing applications*, Journal of Sensors, **2012**, (2012)

[27] R.R. Gattass, D. Rhonehouse, D. Gibson, C.C. McClain, R. Thapa, V.Q. Nguyen, S.S. Bayya, R.J. Weiblen, C.R. Menyuk, L.B. Shaw, J.S. Sanghera. *Infrared glass-based negative-curvature anti-resonant fibers fabricated through extrusion*, Optics Express, **24**, 546–7 (2016)

[28] K. Vlachos, T. Vasileiadis, V. Dracopoulos, C. Markos, G. Kakarantzas, S.N. Yannopoulos. *Development of hybrid solid and hollow core photonic crystal fiber with soft glass deposition for infrared light manipulation*, International Conference on Transparent Optical Networks, 1–6 (2014)

[29] L. Xiao, W. Jin, M.S. Demokan. *Photonic crystal fibers confining light by both index-guiding and bandgap-guiding: hybrid PCFs*, Optics Express, **15**, 15637–47 (2007)

[30] G.J. Pearce, G.S. Wiederhecker, C.G. Poulton, S. Burger, P.S.J. Russell. *Models for guidance in kagome-structured hollow-core photonic crystal fibres*, Optics Express, **15**, 12680–5 (2007)

[31] F. Benabid, P.J. Roberts. *Linear and nonlinear optical properties of hollow core photonic crystal fiber*, Journal of Modern Optics, **58**, 87–124 (2011)

[32] A.D. Pryamikov. *Negative curvature hollow core fibers : design, fabrication, and applications*, Proceedings of SPIE, **8961**, 1–11 (2014)

[33] J. Knight. *Photonic crystal fibres*, Nature, **424**, 847–51 (2003)

[34] F. Benabid, J.C. Knight, G. Antonopoulos, P.S.J. Russell. *Stimulated Raman Scattering in Hydrogen-Filled Hollow-Core Photonic Crystal Fiber*, Science, **298**, 399–402 (2002)

[35] F. Baldini, M. Brenci, F. Chiavaioli, A. Giannetti, C. Trono. *Optical fibre gratings as tools for chemical and biochemical sensing*, Analytical and Bioanalytical Chemistry, **402**, 109–16 (2012)

[36] A. Argyros. *Guided modes and loss in Bragg fibres*, Optics Express, **10**, 1411–7 (2002)

[37] M.N. Petrovich, F. Poletti, A. van Brakel, D.J. Richardson. *Robustly single mode*

hollow core photonic bandgap fiber, Optics Express, **16**, 4337–46 (2008)

[38] R. Barillé, P. Tajalli, P. Roy, S. Ahmadi-Kandjani, S. Kucharski, E. Ortyl. *Hollow-core grating fiber*, Optics Communications, **285**, 468–72 (2012)

[39] G. Bouwmans, F. Luan, J.C. Knight, P.S.J. Russell, L. Farr, B.J. Mangan, H. Sabert. *Properties of a hollow-core photonic bandgap fiber at 850 nm wavelength.*, Optics Express, **11**, 1613–20 (2003)

[40] F. Benabid. *Hollow-core photonic bandgap fibre: new light guidance for new science and technology*, Philosophical transactions. Series A, Mathematical, physical, and engineering sciences, **364**, 3439–62 (2006)

[41] A.D. Pryamikov. *The core modes of all solid photonic band gap fibers as bound states in the continuum*, eprint arXiv:1209.2280, 1–11 (2012)

[42] T. Engeness, M. Ibanescu, S. Johnson, O. Weisberg, M. Skorobogatiy, S. Jacobs, Y. Fink. *Dispersion tailoring and compensation by modal interactions in OmniGuide fibers*, Optics Express, **11**, 1175–96 (2003)

[43] F.B. B. Debord, M. Alharbi, T. Bradley, C. Fourcade-Dutin, Y.Y. Wang, L. Vincetti, F. Gérôme. *Hypocycloid-shaped hollow-core photonic crystal fiber Part I: Arc curvature effect on confinement loss*, Optics Express, **21**, 28597–21 (2013)

[44] B. Debord, M. Alharbi, A. Benoît, D. Ghosh, M. Dontabactouny, L. Vincetti, J.-M. Blondy, F. Gérôme, F. Benabid. *Ultra low-loss hypocycloid-core Kagome hollow-core photonic crystal fiber for green spectral-range applications*, Optics Letters, **39**, 6245–8 (2014)

[45] E. Coscelli, F. Poli, D. Passaro, A. Cucinotta, S. Selleri. *Guiding properties of kagome-lattice hollow-core fibers*, Proceedings of SPIE, **7714**, 771415 (2010)

[46] S.-J. Im, A. Husakou, J. Herrmann. *Guiding properties and dispersion control of kagome lattice hollow-core photonic crystal fibers*, Optics Express, **17**, 13050–8 (2009)

[47] A.D. Pryamikov, A.S. Biriukov, A.F. Kosolapov, V.G. Plotnichenko, S.L. Semjonov, E.M. Dianov. *Demonstration of a waveguide regime for a silica hollow--core microstructured optical fiber with a negative curvature of the core boundary in the spectral region > 3.5 μm*, Optics Express, **19**, 1441–8 (2011)

[48] F. Yu, J.C. Knight. *Negative Curvature Hollow-Core Optical Fiber*, IEEE Journal on Selected Topics in Quantum Electronics, **22**, (2016)

[49] Y.Y. Wang, F. Couny, P.J. Roberts, F. Benabid. *Low loss broadband transmission*

in optimized core-shape Kagome Hollow-Core PCF, Conference on Lasers and Electro-Optics 2010, OSA Technical Digest (CD) (Optical Society of America), (2010)

[50] R. Carter, W.N. MacPherson, P. Jaworski, F. Yu, R.J. Beck, J.D. Shephard, D.P. Hand. *Dispersion measurement of microstructured negative curvature hollow core fiber*, Optical Engineering, **55**, 116106-1–8 (2016)

[51] F. Yu, M. Xu, J.C. Knight. *Experimental study of low-loss single-mode performance in anti-resonant hollow-core fibers*, Optics Express, **24**, 12969–75 (2016)

[52] J.D. Shephard, A. Urich, R.M. Carter, P. Jaworski, R.R.J. Maier, W. Belardi, F. Yu, W.J. Wadsworth, J.C. Knight, D.P. Hand. *Silica hollow core microstructured fibers for beam delivery in industrial and medical applications*, Frontiers in Physics, **3**, 24 (2015)

[53] A.F. Kosolapov, A.D. Pryamikov, A.S. Biriukov, V.S. Shiryaev, M.S. Astapovich, G.E. Snopatin, V.G. Plotnichenko, M.F. Churbanov, E.M. Dianov. *Demonstration of CO2-laser power delivery through chalcogenide-glass fiber with negative curvature hollow core*, Optics Express, **19**, 25723–8 (2011)

[54] A.N. Kolyadin, A.F. Kosolapov, A.D. Pryamikov, A.S. Biriukov, V.G. Plotnichenko, E.M. Dianov. *Light transmission in negative curvature hollow core fiber in extremely high material loss region.*, Optics Express, **21**, 9514–9 (2013)

[55] W. Belardi, J.C. Knight. *Hollow antiresonant fibers with low bending loss*, Optics Express, **22**, 10091–6 (2014)

[56] W. Belardi, J.C. Knight. *Hollow antiresonant fibers with reduced attenuation*, Optics Letters, **39**, 1853–6 (2014)

[57] R.M. Carter, F. Yu, W.J. Wadsworth, J.D. Shephard, T. Birks, J.C. Knight, D.P. Hand. *Measurement of resonant bend loss in anti-resonant hollow core optical fiber*, Optics Express, **25**, 28609–16 (2017)

[58] *https://goo.gl/QhdR5w (accessed 22/12/2018)*, HPFS® Fused Silica Industrial Grade, Corning Website

[59] A. Urich, R.R.J. Maier, F. Yu, J.C. Knight, D.P. Hand, J.D. Shephard. *Flexible delivery of Er:YAG radiation at 2.94 μm with negative curvature silica glass fibers: a new solution for minimally invasive surgical procedures*, Biomedical Optics Express, **4**, 193–205 (2013)

[60] E. Popenda, M.A. Stawska, H.I. Mazur, L.M. Jakubowski, K. Kosolapov, A. Kolyadin, A. Bereś-Pawlik. *Application of Negative Curvature Hollow-Core Fiber in an Optical Fiber Sensor Setup for Multiphoton Spectroscopy*, Sensors, **17**, **2278**, (2017)

[61] B. Sherlock, F. Yu, J. Stone, S. Warren, C. Paterson, M.A.A. Neil, P.M.W. French, J. Knight, C. Dunsby. *Tunable fibre-coupled multiphoton microscopy with a negative curvature fibre*, Journal of Biophotonics, **9**, 715–20 (2016)

[62] C. Harvey, F. Yu, J.C. Knight, W. Wadsworth, P. Almeida. *Reducing Nonlinear Limitations of Ytterbium Mode-Locked Fibre Lasers with Hollow-Core Negative Curvature Fibre*, CLEO: 2015, OSA Technical Digest, STh1L.5 (2015)

[63] A. Urich, R.R.J. Maier, B.J. Mangan, S. Renshaw, J.C. Knight, D.P. Hand, J.D. Shephard. *Delivery of high energy Er:YAG pulsed laser light at 2.94 μm through a silica hollow core photonic crystal fibre*, Optics Express, **20**, 6677–84 (2012)

[64] A.N. Kolyadin, G.K. Alagashev, A.D. Pryamikov, L. Mouradian, A. Zeytunyan, H. Toneyan, A.F. Kosolapov, I.A. Bufetov. *Negative Curvature Hollow-core Fibers: Dispersion Properties and Femtosecond Pulse Delivery*, Physics Procedia, **73**, 59–66 (2015)

[65] C.J.S. de Matos, J.R. Taylor, T.P. Hansen, K.P. Hansen, J. Broeng. *All-fiber chirped pulse amplification using highly-dispersive air-core photonic bandgap fiber*, Optics Express, **11**, 2832–7 (2003)

[66] *https://www.corning.com/media/worldwide/coc/documents/Fiber/SMF-28%20Ultra.pdf (accessed 22/12/2018)*, Corning® SMF-28® Ultra Optical Fiber, Corning Website

[67] G.M. Ponzo, M.N. Petrovich, X. Feng, P. Horak, F. Poletti, P. Petropoulos, D.J. Richardson. *Fast and broadband fiber dispersion measurement with dense wavelength sampling*, Optics Express, **22**, 943–53 (2014)

[68] S.N. Turtaev, M.I. Belovolov, A.E. Levchenko, A.F. Kosolapov, A.D. Pryamikov, A.N. Kolyadin. *Acoustic sensitivity of the negative curvature hollow core fiber*, Proceedings - 2014 International Conference Laser Optics, LO 2014, **216**, 2011 (2014)

[69] A. Perveen, C. Molardi. *Chapter 2 - Machining of Glass Materials : An Overview*, Advanced Manufacturing Technologies, Springer International Publishing, 23–47 (2017)

[70] H. Huang, L.-M. Yang, J. Liu. *Micro-hole drilling and cutting using femtosecond fiber laser*, Optical Engineering, **53**, 51513 (2014)

[71] R.M. Hasan, X. Luo. *Nanolithography : Status and Challenges*, 2017 23rd International Conference on Automation and Computing (ICAC), IEEE, (2017)

[72] K.T.M. Tran, T.D. Nguyen. *Lithography-based methods to manufacture biomaterials at small scales*, Journal of Science: Advanced Materials and Devices, **2**, 1–14 (2017)

[73] W. Li, G. Lalev, S. Dimov, H. Zhao, D.T. Pham. *A study of fused silica micro/nano patterning by focused-ion-beam*, Applied Surface Science, **253**, 3608–14 (2007)

[74] L.B. and D.D. Pevec S. *Micromachining of All-Fiber Photonic Micro-Structures for Microfluidic Applications*, Journal of Microelectronics, Electronic Components and Materials, **46**, 113–9 (2016)

[75] R. Barbucha, M. Kocik, M. Tański, K. Garasz, T. Petrov, C. Radzewicz. *Femtosecond laser system for micromachining of the materials*, Proceedings of SPIE, **9447**, 94470J (2015)

[76] R.R. Gattass, E. Mazur. *Femtosecond laser micromachining in transparent materials*, Nature Photonics, **2**, 219–25 (2008)

[77] R.N. Oosterbeek, T. Ward, S. Ashforth, O. Bodley, A.E. Rodda, M.C. Simpson. *Fast femtosecond laser ablation for efficient cutting of sintered alumina substrates*, Optics and Lasers in Engineering, **84**, 105–10 (2016)

[78] G. Dearden, Z. Kuang, D. Liu, W. Perrie, S.P. Edwardson, K.G. Watkins. *Advances in Ultra Short Pulse Laser based Parallel Processing using a Spatial Light Modulator*, Physics Procedia, **39**, 650–60 (2012)

[79] E. Jäger, U. Rädel, C. Bischoff, U. Umhofer, S. Rung, R. Hellmann. *Laser micromachining – parallel processing with multiple top hat beams*, 8th International Conference on Photonic Technologies LANE 2014, 1–5 (2014)

[80] D.N. Wang, Y. Wang, C.R. Liao. 14 – Femtosecond laser micromachining on optical fiber. *Laser Surface Engineering, Processes and Applications*. pp.359–81 (2015)

[81] L. Cerami, E. Mazur, S. Nolte, C.B. Schaffer. Femtosecond Laser Micromachining. *Ultrafast Nonlinear Optics*. (Thomson Robert, Leburn Christopher, Reid Derryck ed.), Springer International Publishing, Heidelberg, pp.287–321 (2013)

[82] N. Varkentina, M. Dussauze, A. Royon, M. Ramme, Y. Petit, L. Canioni. *High repetition rate femtosecond laser irradiation of fused silica studied by Raman spectroscopy*, Optical Materials Express, **6**, 79–90 (2016)

[83] K.C. Vishnubhatla, N. Bellini, R. Ramponi, G. Cerullo, R. Osellame. *Shape control of microchannels fabricated in fused silica by femtosecond laser irradiation and chemical etching*, Optics Express, **17**, 8685–95 (2009)

[84] X. Liu, D. Du, G. Mourou. *Laser ablation and micromachining with ultrashort laser pulses*, IEEE Journal of Quantum Electronics, **33**, 1706–16 (1997)

[85] C.B. Schaffer, A. Brodeur, E. Mazur. *Laser-induced breakdown and damage in bulk transparent materials induced by tightly focused femtosecond laser pulses*, Measurement Science and Technology, **12**, 1784–94 (2001)

[86] B. Chimier, O. Utéza, N. Sanner, M. Sentis, T. Itina, P. Lassonde, F. Légaré, F. Vidal, J.C. Kieffer. *Damage and ablation thresholds of fused-silica in femtosecond regime*, Physical Review B - Condensed Matter and Materials Physics, **84**, 1–10 (2011)

[87] I.-B. Sohn, M.-S. Lee, J.-S. Woo, S.-M. Lee, J.-Y. Chung. *Fabrication of photonic devices directly written within glass using a femtosecond laser*, Optics Express, **13**, 4224–9 (2005)

[88] W. Ha, K. Oh, Y.M. Jung, K.K. Jun, W. Shin, I.B. Sohn, D.K. Ko, J.M. Lee. *Fabrication and Characterization of a Broadband Long-Period Grating on a Hollow Optical Fiber with Femtosecond Laser Pulses*, Journal of the Korean Physical Society, **53**, 3814–7 (2008)

[89] T. Wei, Y. Han, H.-L. Tsai, H. Xiao. *Miniaturized fiber inline Fabry-Perot interferometer fabricated with a femtosecond laser*, Optics Letters, **33**, 536–8 (2008)

[90] Y.-J. Rao, M. Deng, D.-W. Duan, X.-C. Yang, T. Zhu, G.-H. Cheng. *Micro Fabry-Perot interferometers in silica fibers machined by femtosecond laser*, Optics Express, **15**, 14123 (2007)

[91] B.X. Cao, M. Bae, H. Sohn, J. Choi, Y. Kim, J. Kim, J. Noh. *Design and Performance of a Focus-Detection System for Use in Laser Micromachining*, Micromachines, **7**, 1–8 (2016)

[92] S. Sun, M. Brandt. Chapter 2 Laser Beam Machining. *Nontraditional Machining Processes: Research Advances*. (Davim J Paulo ed.), Springer London, London,

pp.35–96 (2013)

[93] W. Osten (Ed.), B. Thompson, B. Zhao, G. Siegmund, A. Duparre, C. Furlong, I. De Wolf, A. Asundi, K. Korner, D. Vogel, C. Gorecki, L. Salbut, M. Serry, R. Hofling, M. Huttel, T. Wiesendanger, A. Ruprecht, B. Michel, H. Steger, J. Schmit, P. Aswendt, S. Petitgrand, C. Rembe, M. Wortge, P. Ferraro, A. Bosseboeuf, H. Xie. Chapter 9. *Optical Inspection of Mycrosystems*. (Osten Wolfgang ed.), CRC Press, Taylor & Francis Group, Boca, Raton, p.264 (2007)

[94] G. Palazzo, R. Pasquino, N. Bellomo. *Temperature Fields in Machining Processes and Heat Transfer Models*, Mathematical and Computer Modelling, **35**, 101–9 (2002)

[95] A. Dunn, J. V. Carstensen, K.L. Wlodarczyk, E.B. Hansen, J. Gabzdyl, P.M. Harrison, J.D. Shephard, D.P. Hand. *Nanosecond laser texturing for high friction applications*, Optics and Lasers in Engineering, **62**, 9–16 (2014)

[96] L. Sudrie, M. Franco, B. Prade, A. Mysyrowicz. *Study of damage in fused silica induced by ultra-short IR laser pulses*, Optics Communications, **191**, 333–9 (2001)

[97] S. Campbell, F.C. Dear, D.P. Hand, D.T. Reid. *Single-pulse femtosecond laser machining of glass*, Journal of Optics A: Pure and Applied Optics, **7**, 162–8 (2005)

[98] F. Madani-Grasset, Y. Bellouard. *Femtosecond laser micromachining of fused silica molds*, Optics Express, **18**, 21826–40 (2010)

[99] P. Yang, G.R. Burns, J. Guo, T.S. Luk, G.A. Vawter. *Femtosecond laser-pulse-induced birefringence in optically isotropic glass*, Journal of Applied Physics, **95**, 5280–3 (2004)

[100] X. Zhao, Y.C. Shin. *Femtosecond laser drilling of high-aspect ratio microchannels in glass*, Applied Physics A, **104**, 713–9 (2011)

[101] R.A. Shelby, D.R. Smith, S. Schultz. *Experimental Verification of a Negative Index of Refraction*, Science, **292**, 77–9 (2001)

[102] T. Chen, R. Fardel, C.B. Arnold. *Ultrafast z-scanning for high-efficiency laser micro-machining*, Light: Science & Applications, **7**, 17181–9 (2018)

[103] C. Li, S. Nikumb, F. Wong. *An optimal process of femtosecond laser cutting of NiTi shape memory alloy for fabrication of miniature devices*, Optics and Lasers in Engineering, **44**, 1078–87 (2006)

[104] Y. Kondo, J. Qiu, T. Mitsuyu, K. Hirao, T. Yoko. *Three-Dimensional Microdrilling of Glass by Multiphoton Process and Chemical Etching*, Japanese

Journal of Applied Physics, **38**, L1146–8 (1999)

[105] R. An, Y. Li, Y. Dou, H. Yang, Q. Gong. *Simultaneous multi-microhole drilling of soda- lime glass by water-assisted ablation with femtosecond laser pulses*, Optics Express, **13**, 1855–9 (2005)

[106] Y. Li, K. Itoh, W. Watanabe, K. Yamada, D. Kuroda, J. Nishii, Y. Jiang. *Three-dimensional hole drilling of silica glass from the rear surface with femtosecond laser pulses*, Optics Letters, **26**, 1912–4 (2001)

[107] R.R. Thomson, A.K. Kar, J. Allington-Smith. *Ultrafast laser inscription: an enabling technology for astrophotonics*, Optics Express, **17**, 1963–9 (2009)

[108] R.R. Thomson, H.T. Bookey, N.D. Psaila, A. Fender, S. Campbell, W.N. MacPherson, J.S. Barton, D.T. Reid, A.K. Kar. *Ultrafast-laser inscription of a three dimensional fan-out device for multicore fiber coupling applications*, Optics Express, **15**, 11691–7 (2007)

[109] J. Sun, X. Luo, J. Ritchie, T. Hrncir. *A predictive divergence compensation approach for the fabrication of three-dimensional microstructures using focused ion beam machining*, Proceedings of the Institution of Mechanical Engineers, Part B: Journal of Engineering Manufacture, **226**, 229–38 (2011)

[110] Y. Liao, J. Song, E. Li, Y. Luo, Y. Shen, D. Chen, Y. Cheng, Z. Xu, K. Sugioka, K. Midorikawa. *Rapid prototyping of three-dimensional microfluidic mixers in glass by femtosecond laser direct writing*, Lab on a Chip, **12**, 746–9 (2012)

[111] C. Hensley, D.H. Broaddus, C.B. Schaffer, A.L. Gaeta. *Photonic band-gap fiber gas cell fabricated using femtosecond micromachining.*, Optics Express, **15**, 6690–5 (2007)

[112] S. Nolte, C. Momma, G. Kamlage, A. Ostendorf, C. Fallnich, F. von Alvensleben, H. Welling. *Polarization effects in ultrashort-pulse laser drilling*, Applied Physics A, **68**, 563–7 (1999)

[113] H.Y. Zheng, W. Zhou, H.X. Qian, T.T. Tan, G.C. Lim. *Polarisation-independence of femtosecond laser machining of fused silica*, Applied Surface Science, **236**, 114–9 (2004)

[114] E. Toratani, M. Kamata, M. Obara. *Self-fabrication of void array in fused silica by femtosecond laser processing*, Applied Physics Letters, **87**, 171103 (2005)

[115] R.S. Taylor, C. Hnatovsky, E. Simova, D.M. Rayner, V.R. Bhardwaj, P.B. Corkum. *Femtosecond laser fabrication of nanostructures in silica glass*, Optics

Letters, **28**, 1043–5 (2003)

[116] S. Kim, G. Liu, A.M. Minor. *FIB Sample Preparation of Polymer Thin Films on Hard Substrates Using the Shadow-FIB Method*, Microscopy Today, **17**, 20–3 (2009)

[117] O. Olea-Mejía, O. Olea-Cardoso, R. Lopez-Castañares. *FIB-SEM Combination Technique for Characterizacion of Polymer Composites*, Current Microscopy Contributions to Advances in Science and Technology, 1060–5 (2012)

[118] X. Luo, J. Sun, J.M. Ritchie, W. Chang, W. Wang. *Deterministic fabrication of nanostructures for plasmonic lens by focused ion beam*, The International Journal of Advanced Manufacturing Technology, **57**, 1003–9 (2011)

[119] J. Sun, J. Li, R.R.J. Maier, D.P. Hand, W.N. MacPherson, M.K. Miller, J.M. Ritchie, X. Luo. *Fabrication of a side aligned optical fibre interferometer by focused ion beam*, Journal of Micromechanics and Microengineering, **23**, 105005 (2013)

[120] K. Nallapan, R. Morandotti, M. Skorobogatiy. *Feasibility Study for the Generation of High Power Continuous Wave Terahertz Radiation using Frequency Differenece Generation*, eprint arXiv: 1711.07830, (2017)

[121] J.M. Schmitt, A. Knüttel, M. Yadlowsky. *Confocal microscopy in turbid media*, Journal of the Optical Society of America A, **11**, 2226–35 (1994)

[122] *https://webbook.nist.gov/cgi/inchi?ID=C7732185&Typ (Accessed 06/07/2018)*, NIST Chemistry WebBook, SRD 69, Water, National Institute of Standards and Tehcnology Website

[123] P.S. Neelakanta. A textbook on ATM Telecommunications: Principles and Implementation. CRC Press, Boca Raton, Florida, p.231 (2000)

[124] S. Goel, X. Luo, A. Agrawal, R.L. Reuben. *Diamond machining of silicon : A review of advances in molecular dynamics simulation*, International Journal of Machine Tools and Manufacture, **88**, 131–64 (2015)

[125] S. Goel, X. Luo, R.L. Reuben, W. Bin Rashid. *Replacing diamond cutting tools with CBN for efficient nanometric cutting of silicon*, Materials Letters, **68**, 507–9 (2012)

[126] Z. Tong, X. Luo, J. Sun, Y. Liang, X. Jiang. *Investigation of a scale-up manufacturing approach for nanostructures by using a nanoscale multi-tip diamond tool*, The International Journal of Advanced Manufacturing Technology,

80, 699–710 (2015)

[127] S.J. Zhang, S. To, G.Q. Zhang. *Diamond tool wear in ultra-precision machining*, The International Journal of Advanced Manufacturing Technology, **88**, 613–41 (2017)

[128] W. Chang, J. Sun, X. Luo. *Comparison of diamond drilling and laser drilling techniques in glass drilling for fabrication of MEMS*, Proceedings of the Euspen International Conference, San Sebastian, (2009)

[129] S. Goel, X. Luo, R.L. Reuben. *Wear mechanism of diamond tools against single crystal silicon in single point diamond turning process*, Tribiology International, **57**, 272–81 (2013)

[130] F.Z. Fang, X.D. Liu, L.C. Lee. *Micro-machining of optical glasses – A review of diamond-cutting glasses*, Sadhana, **28**, 945–55 (2003)

[131] X. Luo, J. Sun, W. Chang, J.M. Ritchie. *Single Point Diamond Turning of Calcium Fluoride Optics*, Key Engineering Materials, **516**, 408–13 (2012)

[132] S.Y. Luo, Y.Y. Tsai, C.H. Chen. *Studies on cut-off grinding of BK7 optical glass using thin diamond wheels*, Journal of Materials Processing Technology, **173**, 321–9 (2006)

[133] X.P. Xu, Y. Li, W.Y. Zeng, L.B. Li. *Quantitative analysis of the loads acting on the abrasive grits in the diamond sawing of granites*, Journal of Materials Processing Technology, **129**, 50–5 (2002)

[134] C. Kong, X., Wang, X., Wu. *Diamond sawing process of 12 inch low-K silicon wafer applied in smart card*, 2014 Joint IEEE International Symposium on the Applications of Ferroelectric, International Workshop on Acoustic Transduction Materials and Devices & Workshop on Piezoresponse Force Microscopy, 885–7 (2014)

[135] D. Martin, S. Sullivan. Dicing of MEMS Devices. *Handbook of Silicon Based MEMS Materials and Technologies*. Elsevier Inc., pp.671–7 (2015)

[136] C. Holmes, A. Jantzen, A.C. Gray, L.G. Carpenter, P.C. Gow, S.G. Lynch, J.C. Gates, P.G.R. Smith. *Integrated Optical Fiber-Tip Cantilevers*, IEEE Sensors Journal, **17**, 6960–5 (2017)

[137] F. Albri, J. Li, R.R.J. Maier, W.N. MacPherson, D.P. Hand. *Laser machining of sensing components on the end of optical fibres*, Journal of Micromechanics and Microengineering, **23**, (2013)

[138] J. Li, F. Albri, J.N. Sun, M.M. Miliar, R.R.J. Maier, D.P. Hand, W.N. Macpherson. *Fabricating optical fibre-top cantilevers for temperature sensing*, Measurement Science and Technology, **25**, (2014)

[139] J. Li, F. Albri, R.R.J. Maier, W. Shu, J. Sun, D.P. Hand, W.N. MacPherson. *A Micro-Machined Optical Fiber Cantilever as a Miniaturized pH Sensor*, IEEE Sensors Journal, **15**, 7221–8 (2015)

[140] C. Guan, X. Tian, S. Li, X. Zhong, J. Shi, L. Yuan. *Long period fiber grating and high sensitivity refractive index sensor based on hollow eccentric optical fiber*, Sensors and Actuators B: Chemical, **188**, 768–71 (2013)

[141] Y. Wang, W. Jin, J. Ju, H. Xuan, H.L. Ho, L. Xiao, D. Wang. *Long period gratings in air-core photonic bandgap fibers*, Optics Express, **16**, 2784–90 (2008)